

**THE SUITABILITY OF THE IASI  
INSTRUMENT FOR OBSERVING CO FROM  
SPACE**

Thesis submitted for the degree of  
Doctor of Philosophy  
at the University of Leicester

by

Samuel Michael Illingworth  
Earth Observation Science Group  
Department of Physics and Astronomy  
University of Leicester

September 2010

© Samuel M. Illingworth, September 2010

This thesis is copyright material and no quotation from it may be published without proper acknowledgement.

## Declaration

I hereby declare that no part of this thesis has been previously submitted to this or any other University as part of the requirement for a higher degree. The work described herein was conducted by the undersigned except for contributions from colleagues as acknowledged in the text.

Samuel M. Illingworth

September 2010

# THE SUITABILITY OF THE IASI INSTRUMENT FOR OBSERVING CO FROM SPACE

Samuel M. Illingworth

## ABSTRACT

This thesis presents a methodological approach to developing the capability of the Infrared Atmospheric Sounding Interferometer (IASI) instrument to inform on the atmospheric concentrations of carbon monoxide (CO), focussing on three key studies: 1) an assessment of the radiometric accuracy of the instrument; 2) the development of the University of Leicester IASI Retrieval Scheme (ULIRS) to convert measured radiances into a CO product; and 3) an investigation into the reliability and possible use of the ULIRS product.

An intercomparison between the radiances as measured by the IASI and Advanced Along Track Scanning Radiometer (AATSR) instruments is performed, and absolute differences at 11  $\mu\text{m}$  of less than 0.1 K are observed. Given the radiometric behaviour across the IASI instrument as a whole, it is also concluded that the IASI instrument is radiometrically accurate to  $< 0.3\text{ K}$  in the 12 and 4.7  $\mu\text{m}$  spectral regions.

A retrieval scheme, the ULIRS, is developed with explicit digital elevation and emissivity information, and a correction for solar surface reflection with a high resolution solar spectrum. Typical random errors over the African region relating to the profiles are found to be  $\sim 10\%$  at 5 and 12 km, and on the total columns to be  $\sim 12\%$ .

The ULIRS dataset and the operational CO products from the Measurements Of Pollution In The Troposphere (MOPITT) are inter-compared. A methodology which uses the same a priori statistics, and which reduces the smoothing bias between the two sets of data shows that there is only a small bias between the ULIRS and MOPITT V4 products. A simplified top-down approach to estimating CO emissions from fires is also presented, highlighting the need for a better understanding of the correct detection of burnt area from space-based measurements.

# PUBLICATIONS

## Journal Articles

Illingworth S.M., Remedios J.J., Parker R.J. (2009), Intercomparison of integrated IASI and AATSR calibrated radiances, *Atmospheric Chemistry and Physics*, **9**, 6677-6683.

Atkinson N.C., Hilton F.I., Illingworth S.M. Eyre J.R., Hultberg T. (2010), Potential for the use of reconstructed IASI radiances in the detection of atmospheric trace gases, *Atmospheric Measurement Techniques*, **3**, 991-1003.

Illingworth S.M., Remedios J.J., Boesch H., Moore D.P., Sembhi H., Dudhia A., Walker J.C. (2010), A New Optimal Estimation Retrieval Scheme for Carbon Monoxide using IASI spectral radiances: Part I Sensitivity Analysis, Error Budget and Simulations, *Atmospheric Measurement Techniques Discussions*, **3**, 3747-3802.

Illingworth S.M., Remedios J.J., Boesch H., Deeter M.N., Edwards D.P., Palmer P.I., Gonzi S. (2010), A New Optimal Estimation Retrieval Scheme for Carbon Monoxide using IASI spectral radiances: Part II An Intercomparison with the MOPITT Instrument, *Atmospheric Measurement Techniques Discussions*, **3**, 4889-4930.

## Conference Proceedings

Illingworth S.M., Remedios J.J., Boesch H., Moore D.P., Sembhi H., Tansey K. (2010), Using IASI Retrieved CO Measurements to Characterise CO Emissions from Local African Fires, *Proceedings of the Second IASI International Conference*, Annecy, France, January 2010

Illingworth S.M., Remedios J.J., Boesch H., Moore D.P., Sembhi H., Tansey K. (2010), Using IASI to Investigate Carbon Monoxide and Volatile Organic Compounds Emissions from Local African Fires, *Proceedings of the 2010 ESA Living Planet Symposium*, Bergen, Norway, June 2010

# ACKNOWLEDGEMENTS

I would like to begin by thanking my primary supervisor Prof. John Remedios, who as well as offering me the PhD in the first instance, has been a constant source of inspiration, motivation, and, when necessary, perspiration! Thanks must also go to my secondary supervisor Dr. Hartmut Bösch, who has always provided me with answers, even when they were in the form of more questions. A big thank you to the post-docs in the Earth Observation Science (EOS) group, all of whom have helped me throughout my ‘journey’, with special thanks to Dr. David Moore and Dr. Harjinder Sembhi who have always offered me help, encouragement, and counselling. My fellow PhD students have made the whole ordeal a far more enjoyable one, and have been a never-ending source of amusement, knowledge, and above all support.

A big thank you to Leicester University Theatre (LUTheatre), with whom I rediscovered my love of the stage. Without LUTheatre I would be a poorer person, and I would have missed out on the most incredibly gifted and genuine set of people that I have ever met. Special mention to Nerissa, Shayna, Ali, and Dave; friends who will be with me forever. I am also indebted to my best friend Hilary, and to my house mate Fergus, whose role as my husband for the past few years has made my life that much sweeter.

Finally, I would like to thank my family: Gags and Grandad for their constant warmth and general hilarity; my sister Rebecca for abiding love, and her allergy to maps; and Josh, for being the best friend that I would have chosen as a brother, were it not already so. My last, and no doubt greatest thanks are to my mum, the most exceptional source of inspiration in my life, and without whom I would be nothing. This thesis is dedicated to her, and to all of the sacrifices that she has made so that I can stand here today, proud of my achievements.

*To mum*

# Table of Contents

<b>Table of Contents</b>	<b>I</b>
<b>1 Introduction</b>	<b>1</b>
1.1 The Troposphere . . . . .	1
1.2 Tropospheric Chemistry . . . . .	2
1.3 The Importance of CO in the Troposphere . . . . .	3
1.4 Sources and Sinks of CO . . . . .	6
1.5 The Distribution of CO . . . . .	8
1.6 The Transport of CO . . . . .	11
1.7 Techniques for Observing CO . . . . .	13
1.7.1 Ground Based Measurements of CO . . . . .	13
1.7.2 Aircraft In Situ Measurements of CO . . . . .	16
1.7.3 Satellite Measurements of CO . . . . .	19
1.8 Summary . . . . .	22
<b>2 Radiative Transfer and Retrieval Theory</b>	<b>24</b>
2.1 Introduction . . . . .	24
2.2 Radiative Transfer Theory . . . . .	24
2.2.1 The Spectrum of Radiation . . . . .	25
2.2.2 Black body radiation . . . . .	26
2.2.2.1 The Planck Function . . . . .	26
2.2.2.2 Kirchhoff's Law . . . . .	26
2.2.3 Physics of Scattering and Absorption and Emission . . . . .	28
2.2.3.1 Scattering by Air Molecules and Particles . . . . .	28
2.2.3.2 Absorption by Atmospheric Molecules . . . . .	29
2.2.4 Thermal Infrared Radiative Transfer In the Atmosphere . . . . .	32
2.3 Retrieval Theory . . . . .	33
2.3.1 Definitions . . . . .	34
2.3.1.1 The State and Measurement Vectors . . . . .	34
2.3.1.2 The Forward Model . . . . .	34
2.3.1.3 The Jacobian . . . . .	35
2.3.1.4 The Gain Matrix . . . . .	35
2.3.1.5 The Averaging Kernel Matrix . . . . .	35

2.3.2	Information Content . . . . .	36
2.3.2.1	The Shannon Information Content . . . . .	36
2.3.2.2	Degrees of Freedom for Signal . . . . .	37
2.3.3	Solution with Prior Data . . . . .	37
2.3.4	The Linear Problem . . . . .	39
2.3.5	The Non-linear Problem . . . . .	40
2.3.5.1	The Gauss-Newton Method . . . . .	41
2.3.5.2	The Levenberg-Marquardt Method . . . . .	42
2.3.5.3	Convergence . . . . .	42
2.3.6	Solution Without Prior Data . . . . .	43
2.3.6.1	The Twomey-Tikhonov Method . . . . .	43
2.3.6.2	The Backus-Gilbert Method . . . . .	44
2.3.7	Error Analysis . . . . .	44
2.3.7.1	The Smoothing Error . . . . .	46
2.3.7.2	The Forward Model Parameter Error . . . . .	46
2.3.7.3	The Forward Model Error . . . . .	46
2.3.7.4	The Measurement Error . . . . .	46
2.4	Summary . . . . .	47
<b>3</b>	<b>The IASI Instrument on MetOp-A</b>	<b>48</b>
3.1	Introduction . . . . .	48
3.2	The MetOp Mission . . . . .	48
3.3	Details of the IASI Instrument . . . . .	51
3.3.1	Fourier Transform Spectroscopy . . . . .	53
3.3.2	Viewing Geometry . . . . .	54
3.3.3	Detectors and Spectral Ranges . . . . .	56
3.4	Radiometric Calibration . . . . .	56
3.4.1	Noise Equivalent Spectral Radiance . . . . .	58
3.4.2	Instrument Line Shape . . . . .	59
3.5	Summary . . . . .	61
<b>4</b>	<b>Intercomparison of integrated IASI and AATSR calibrated radiances at 11 and 12 <math>\mu\text{m}</math></b>	<b>62</b>
4.1	Introduction . . . . .	62
4.2	AATSR . . . . .	63
4.3	Cross Calibration of IASI and AATSR . . . . .	64
4.3.1	Overview of Concept . . . . .	64
4.3.2	Cross-calibration Match-ups . . . . .	65
4.3.3	Flags for Homogeneity . . . . .	68
4.3.4	Cross-calibration Results . . . . .	69
4.4	Conclusions From the Radiometric Comparison Results . . . . .	75
4.5	Radiometric Accuracy of IASI in the 4.7 $\mu\text{m}$ Spectral Region . . . . .	77
4.6	Summary . . . . .	80

<b>5</b>	<b>The University of Leicester IASI Retrieval Scheme (ULIRS)</b>	<b>81</b>
5.1	Introduction . . . . .	81
5.2	Suitability of IASI to Retrieve CO . . . . .	82
5.3	ULIRS Methodology . . . . .	83
5.3.1	Retrieval Theory . . . . .	83
5.3.1.1	The Forward Model . . . . .	83
5.3.1.2	The Inverse Problem . . . . .	84
5.3.1.3	Characterisation and Error Analysis . . . . .	84
5.3.2	Retrieval Setup . . . . .	85
5.3.2.1	Choice of Spectral Window and State Vector . . . . .	85
5.3.2.2	Pressure Levels . . . . .	87
5.3.2.3	Iteration and Convergence . . . . .	89
5.3.3	A Priori Data . . . . .	90
5.3.3.1	Climatologies . . . . .	90
5.3.3.2	Temperature and Water Vapour Profiles . . . . .	91
5.3.3.3	CO Profile . . . . .	91
5.3.3.4	A Priori Error Covariance Matrix . . . . .	94
5.3.4	Auxiliary Data . . . . .	94
5.3.4.1	Emissivity . . . . .	94
5.3.4.2	Surface Elevation . . . . .	95
5.3.5	Pre-processing . . . . .	96
5.3.5.1	Instrument Noise . . . . .	96
5.3.5.2	Cloud Detection Algorithm . . . . .	97
5.4	Sensitivity Analysis . . . . .	99
5.4.1	Sensitivity of the RFM . . . . .	99
5.4.2	Radiometric Accuracy . . . . .	103
5.4.3	Information Content and Error Analysis . . . . .	104
5.4.3.1	DFS . . . . .	104
5.4.3.2	Errors . . . . .	105
5.4.4	Sensitivity of the ULIRS . . . . .	107
5.4.4.1	Retrievals with IASI Data . . . . .	112
5.5	Full Retrieval Simulations . . . . .	115
5.6	Summary . . . . .	119
<b>6</b>	<b>A comparison of CO Data sets from the IASI and MOPITT instruments</b>	<b>121</b>
6.1	Introduction . . . . .	121
6.2	MOPITT CO Retrievals . . . . .	122
6.2.1	MOPITT . . . . .	122
6.2.2	Retrieval Setup . . . . .	122
6.2.3	Comparison of MOPITT V3 and V4 Averaging Kernels . . . . .	125
6.2.4	Comparison of MOPITT V3 and V4 Retrievals . . . . .	127
6.3	Comparison of IASI and MOPITT CO . . . . .	129
6.4	Comparison of IASI and MOPITT CO Using the Same A Priori . . . . .	134

6.4.1	Smoothing Bias . . . . .	136
6.5	Comparison with Reduced Smoothing Error . . . . .	139
6.5.1	Methodology . . . . .	140
6.5.2	Results . . . . .	141
6.6	Summary . . . . .	146
<b>7</b>	<b>Top-down and Bottom-up Estimations of CO Emissions from Localised Fires</b>	<b>148</b>
7.1	Introduction . . . . .	148
7.2	Bottom-up Methodology . . . . .	149
7.2.1	Burnt Area . . . . .	149
7.2.2	Available Fuel Load . . . . .	152
7.2.3	Combustion Completeness . . . . .	152
7.2.4	Emission Factors . . . . .	153
7.3	Top-down Methodology . . . . .	154
7.3.1	Simplified Approach . . . . .	155
7.3.1.1	Detection of Fires . . . . .	157
7.3.1.2	Methodology . . . . .	158
7.3.1.3	Results . . . . .	161
7.4	Isolated Fire Event . . . . .	164
7.4.1	Top-down Estimate . . . . .	170
7.4.2	Bottom-up Estimate . . . . .	171
7.4.3	Discrepancies . . . . .	171
7.5	Comparison with Modelled Data . . . . .	174
7.6	Summary . . . . .	177
<b>8</b>	<b>Conclusions and Future Work</b>	<b>179</b>
8.1	Radiometric Accuracy of the IASI Instrument . . . . .	180
8.1.1	Future Work . . . . .	181
8.2	Retrieval of CO . . . . .	182
8.2.1	Future Work . . . . .	183
8.3	Satellite Intercomparison of CO . . . . .	184
8.3.1	Future Work . . . . .	185
8.4	Top-down and Bottom-up Estimates of CO Emissions . . . . .	186
8.4.1	Future Work . . . . .	186
8.5	Future Missions . . . . .	187
8.6	Closing Remarks . . . . .	190

# List of Figures

1.1	The thermal structure of the Earth's atmosphere. . . . .	2
1.2	The NOAA CCGG Air Sampling Network . . . . .	9
1.3	Three dimensional representation of the global distribution of CO in the remote marine boundary layer. . . . .	10
1.4	Location of NDACC global CO measurement sites . . . . .	15
1.5	MOZAIC flight paths. . . . .	17
1.6	Nominal flight tracks for the INTEX-B flight campaign. . . . .	18
1.7	Monthly averaged IASI CO total column measurements. . . . .	20
2.1	Black body Emission Spectra . . . . .	27
2.2	CO molecular absorption spectra . . . . .	31
3.1	The MetOp-A Satellite and its payload. . . . .	51
3.2	The geometry of the EUMETSAT Polar System ground segment. . .	52
3.3	The IASI interferometer. . . . .	53
3.4	A typical interferogram as measured by the IASI instrument. . . . .	55
3.5	The viewing geometry of the IASI instrument . . . . .	56
3.6	The IASI field of regard. . . . .	57
3.7	The IASI field of view. . . . .	58
3.8	The IASI Noise Equivalent Spectral Radiance . . . . .	59
3.9	The IASI instrument line shape. . . . .	60
4.1	Temporal and spatial coincidences for the IASI and AATSR instru- ments on 1 September 2007. . . . .	67
4.2	Spectral filter functions for the 11 and 12 $\mu\text{m}$ channels for the AATSR, in comparison to a typical IASI spectral measurement. . . . .	68

4.3	Comparison of clear sky 11 $\mu\text{m}$ AATSR BTs and IASI equivalent BTs for 1 September 2007. . . . .	70
4.4	Comparison of clear sky 12 $\mu\text{m}$ AATSR BTs and IASI equivalent BTs for 1 September 2007. . . . .	71
4.5	Comparison of clear sky 11 $\mu\text{m}$ AATSR BTs and IASI equivalent BTs for 1 September 2007, with no filtering for inhomogeneous scenes. . .	72
4.6	Comparison of clear sky 12 $\mu\text{m}$ AATSR BTs and IASI equivalent BTs for 1 September 2007, with no filtering for inhomogeneous scenes. . .	73
4.7	Comparison of clear sky and fully cloudy 11 $\mu\text{m}$ AATSR BTs and IASI equivalent BTs for 1 September 2007. . . . .	74
4.8	Comparison of clear sky and fully cloudy 12 $\mu\text{m}$ AATSR BTs and IASI equivalent BTs for 1 September 2007. . . . .	75
4.9	The internal radiometric accuracy of the IASI instrument. . . . .	78
4.10	Example IR spectral radiance inter-comparisons between NAST-I and IASI measurements, for the 2390 to 2490 $\text{cm}^{-1}$ spectral region. . . . .	79
5.1	The temporal frequency of the IASI instrument, on a 1° by 1° grid. . .	82
5.2	The spectral window used by the ULIRS to retrieve IASI CO. . . . .	86
5.3	The effect of an equidistant pressure grid on the Jacobian and averaging kernel matrices. . . . .	87
5.4	The effect that the number of retrieval levels has on the RFM. . . . .	88
5.5	The CO a priori profile used by the ULIRS. . . . .	92
5.6	The CO a priori error covariance used by the ULIRS. . . . .	93
5.7	The effect of the choice of HITRAN database on the RFM. . . . .	100
5.8	The effect of the choice of spectral resolution on the RFM. . . . .	101
5.9	The effect of the IASI ILS on the RFM. . . . .	102
5.10	The effect of the radiometric accuracy on the ability to retrieve a CO product. . . . .	104
5.11	Typical ULIRS averaging kernels over the Arctic Ocean and the Namibian mountain range. . . . .	105
5.12	Typical ULIRS errors over the Arctic Ocean and the Namibian mountain range. . . . .	106

5.13	The effect that the inclusion of a solar reflected component has on the retrieved CO product. . . . .	108
5.14	The effect of surface emissivity on the retrieved CO product. . . . .	109
5.15	The effect of surface elevation on the retrieved CO product . . . . .	110
5.16	The error terms introduced by not accounting for different parameters in the retrieval process. . . . .	111
5.17	The effect of different parameters on the retrieved CO profile. . . . .	113
5.18	ULIRS error budget for a retrieval over the Namibian mountain range, showing the error associated with the surface emissivity, solar reflected term, and scene topography. . . . .	114
5.19	ULIRS retrievals of simulated CAMELOT data, assuming that the temperature and water vapour profiles are well known. . . . .	117
5.20	ULIRS retrievals of simulated CAMELOT data, assuming a random error of $\pm 5\%$ in both the water vapour and temperature profiles. . .	118
6.1	IASI and MOPITT CO a priori profiles over Southern Africa for 1 September 2007. . . . .	124
6.2	Averaged MOPITT V3 and V4 daytime and oceanic averaging kernels for 1 September 2007 over Southern Africa. . . . .	126
6.3	MOPITT V3 and V4 mean CO profiles for 1 September 2007 for the daytime over the ocean, over the Southern Africa region. . . . .	128
6.4	IASI, MOPITT, and GEOS-Chem CO total column density over Southern Africa during the daytime of 1 September 2007. . . . .	130
6.5	IASI and MOPITT V3 daytime and ocean averaging kernels over the Southern Africa region for 1 September 2007. . . . .	131
6.6	IASI and MOPITT V4 daytime and ocean averaging kernels over the Southern Africa region for 1 September 2007. . . . .	132
6.7	MOPITT and IASI CO mean CO profiles for 1 September 2007 for the daytime over the ocean, over the Southern Africa region. . . . .	133
6.8	MOPITT and IASI CO mean profiles, retrieved using common a priori statistics, for 1 September 2007 for the daytime over the ocean, over the Southern Africa region. . . . .	137

6.9	The smoothing bias of MOPITT and IASI CO mean profiles, retrieved using common a priori statistics, for 1 September 2007 for the daytime over the ocean, over the Southern Africa region. . . . .	138
6.10	Daytime and ocean averaging kernels over the Southern Africa region for 1 September 2007, for adjusted MOPITT V3 averaging kernels converted onto the IASI pressure grid, and IASI averaging kernels at pressure levels closest to the MOPITT V3 pressure levels. . . . .	141
6.11	Daytime and ocean averaging kernels over the Southern Africa region for 1 September 2007, for adjusted MOPITT V4 averaging kernels converted onto the IASI pressure grid and IASI averaging kernels at pressure levels closest to the MOPITT V4 pressure levels. . . . .	142
6.12	MOPITT and smoothed IASI CO mean profiles, retrieved using common a priori statistics, for 1 September 2007 for the daytime, over the oceanic Southern Africa region. . . . .	143
6.13	The smoothing bias of MOPITT and smoothed IASI CO mean profiles, retrieved using common a priori statistics, for 1 September 2007 for the daytime, over the oceanic Southern Africa region. . . . .	144
7.1	ISAM estimated available fuel load for the year 2000. . . . .	151
7.2	1° × 1° gridded monthly combustion completeness for December 2005. . . . .	154
7.3	Illustration of a simplified approach to a top-down estimate of CO emissions from African wildfires. . . . .	159
7.4	HYSPLIT trajectory analysis for 1 September 2007 over the Southern Hemisphere Africa region. . . . .	160
7.5	CALIPSO vertical feature mask for 2 September 2007 over the Southern Hemisphere Africa region. . . . .	161
7.6	Globcover land type map over the Southern Hemisphere Africa region. . . . .	162
7.7	Backwards HYSPLIT trajectory analysis for 1 September 2007 over the Southern Hemisphere Africa region. . . . .	165
7.8	ULIRS daytime total CO total column density for 6 February 2009 over South Africa. . . . .	166
7.9	ULIRS daytime total CO total column density for 7 February 2009 over South Africa. . . . .	167

7.10 HYSPLIT trajectory analysis for 7 February 2009 over South Africa.	168
7.11 CALIPSO vertical feature mask for 7 February 2009 over South Africa.	169
7.12 Globcover land type map over South Africa. . . . .	169
7.13 Backwards HYSPLIT trajectory analysis for 7 February 2009 over South Africa. . . . .	170
7.14 Burnt Area map of the February 2009 fire in the Cederberg Wilderness Area of South Africa. . . . .	172
7.15 GEMS re-analysis CO total column density over the Western Cape region of South Africa, for 6 February 2009 on a $1.125^\circ \times 1.125^\circ$ grid.	174
7.16 GEMS re-analysis CO total column density over the Western Cape region of South Africa, for 7 February 2009 on a $1.125^\circ \times 1.125^\circ$ grid.	175
7.17 GEMS re-analysis CO total column density over the African region, for 7 February 2009 on a $1.125^\circ \times 1.125^\circ$ grid. . . . .	176

# List of Tables

1.1	Global turnover of tropospheric gases. . . . .	4
1.2	Estimates of the global budget of CO in the Troposphere. . . . .	8
1.3	Detection limits and precision of different ground based CO measurement techniques. . . . .	14
3.1	The 11 scientific instruments onboard the MetOp-A satellite . . . . .	50
3.2	The three spectral bands measured by the IASI instrument. . . . .	57
4.1	Comparison of AATSR BTs and IASI equivalent BTs at 11 $\mu\text{m}$ . . . . .	76
4.2	Comparison of AATSR BTs and IASI equivalent BTs at 12 $\mu\text{m}$ . . . . .	76
5.1	Mean and one sigma standard deviations of the retrieved CO product and associated a priori and error terms. . . . .	115
6.1	Mean and percentage biases for IASI and MOPITT V3 CO profiles for the daytime over the ocean. . . . .	135
6.2	Mean and percentage biases for IASI and MOPITT V4 CO profiles for the daytime over the ocean. . . . .	136
6.3	Mean and percentage biases for IASI and MOPITT V3 CO profiles for different scenarios. . . . .	145
6.4	Mean and percentage biases for IASI and MOPITT V4 CO profiles for different scenarios. . . . .	146
7.1	ISAM estimated AFL for forest ecosystems as well as totals for forest and non-forests ecosystems and regions for the year 2000. . . . .	153
7.2	Combustion Completeness (CC) for different land cover types. . . . .	155
7.3	Emission Factors (EFs) for different land cover types and regions for CO. . . . .	156

7.4	Estimates of CO emissions from a fire event in Southern Hemisphere Africa on 1 September 2007. . . . .	163
7.5	Estimates of CO emissions from an isolated fire event on 6 February 2009 in South Western South Africa. . . . .	171
7.6	In situ and MODIS derived Burnt Area and CO emissions for a fire in the Cederberg Wilderness Area of South Africa. . . . .	173

## LIST OF ABBREVIATIONS

AATSR	Advanced Along Track Scanning Radiometer
ACE	Atmospheric Chemistry Experiment
AFL	Available Fuel Load
AIRS	Atmospheric InfraRed Sounder
AMD	Average Mean Difference
ASL	Above Sea Level
ATSR-1	Along-Track Scanning Radiometer-1
ATSR-2	Along-Track Scanning Radiometer-2
AVHRR	Advanced Very High Resolution Radiometer
BB	Biomass Burning
BT	Equivalent Blackbody Brightness Temperature
CALIPSO	Cloud Aerosol Lidar and Infrared Pathfinder Satellite Observations
CAMELOT	Chemistry of the Atmosphere Mission concEpts and sentineL Observation Techniques
CC	Combustion Completeness
CCGG	Carbon Cycle Greenhouse Gases group
CTM	Chemical Transport Model
DEM	Digital Elevation Model
DFS	Degrees of Freedom for Signal
ECMWF	European Centre for Medium-Range Weather Forecasts
EDGAR	Emission Database for Global Atmospheric Research

EF	Emission Factor
EFOV	Effective Field Of View
EM	ElectroMagnetic
Envisat	Environmental satellite
EPS	EUMETSAT Polar System
ESA	European Space Agency
EUMETSAT	EUropean organisation for the exploitation of METeorological SATellites
FOV	Field of View
FT	Fourier Transform
FTIR	Fourier Transform Infrared Radiometry
FTS	Fourier Transform Spectrometer
FWHM	Full Width at Half Maximum
GC	Gas Chromatography
GCM	General Circulation Model
GEMS	Global and regional Earth-system Monitoring using Satellite and in-situ data
GEOS-Chem	Goddard Earth Observing System Chemical transport model
GFED	Global Fire Emissions Data Base
GOES	Geostationary Operational Environmental Satellite
HITRAN	HIgh-resolution TRANsmission molecular absorption database
HYSPLIT	Hybrid Single Particle Lagrangian Integrated Trajectory

IASI	Infrared Atmospheric Sounding Interferometer
IFOV	Instantaneous Field Of View
IHOS	Interferometer and Hot Optics Subassembly
IIS	Integrated Imaging Subsystem
ILS	Instrument Line Shape
IMG	Interferometer Monitor for Greenhouse gases
INTEX	Intercontinental Chemical Transport EXperiment
IR	InfraRed
ISAM	Integrated Science Assessment Model
LEO	Low Earth Orbit
LMC	Length Modulation Cell
LST	Local Solar Time
LUT	Look-Up Table
MAP	Maximum A posteriori Probability
MAPS	Measurement of Air Pollution from Satellites
MetOp	Meteorological Operational satellite
MIPAS	Michelson Interferometer for Passive Atmospheric Sounding
MLS	Microwave Limb Sounder
MODIS	MODerate resolution Imaging Spectroradiometer
MODTRAN	MODerate spectral resolution atmospheric TRANSmittance algorithm and computer model

MOPFAS	MOPITT operational fast forward model
MOPITT	Measurements of Pollution in the Troposphere
MOZAIC	Measurements of OZone, water vapour, carbon monoxide and nitrogen oxides by in-service AIRbus airCRAFT
MOZART	Model for OZone And Related chemical Tracers
MPD	Maximum Path Difference
NASA	National Aeronautics and Space Administration
NDACC	Network for the Detection of Atmospheric Composition Change
NE $\Delta$ R	Noise Equivalent $\Delta$ Radiance
NE $\Delta$ T	Noise Equivalent $\Delta$ Temperature
NESR	Noise Equivalent Spectral Radiance
NH	Northern Hemisphere
NIR	Near InfraRed
NMHC	Non-Methane HydroCarbon
NOAA	National Oceanic and Atmospheric Administration
NWP	Numerical Weather Prediction
OEM	Optimal Estimation Method
OPD	Optical Path Difference
PBL	Planetary Boundary Layer
PMC	Pressure Modulation Cell
PREMIER	PRocess Exploration through Measurements of Infrared and millimetre-wave Emitted Radiation

RFM	Reference Forward Model
RT	Radiative Transfer
SCIAMACHY	SCanning Imaging Absorption SpectroMeter for Atmospheric CHartographY
SH	Southern Hemisphere
SHA	Southern Hemisphere Africa
SNR	Signal to Noise Ratio
SST	Sea Surface Temperature
TES	Tropospheric Emission Spectrometer
TIR	Thermal InfraRed
TOA	Top Of Atmosphere
TOMCAT	Toulouse Off-line Model of Chemistry And Transport
TOMS	Total Ozone Mapping Spectrometer
TRMM	Tropical Rainfall Measuring Mission
ULIRS	University of Leicester IASI Retrieval Scheme
USGS	United States Geological Survey
UTLS	Upper Troposphere Lower Stratosphere
UV	UltraViolet
UW	University of Wisconsin
VMR	Volume Mixing Ratio
VOC	Volatile Organic Compound
WFA	World Fire Atlas

# Chapter 1

## Introduction

### 1.1 The Troposphere

The atmosphere can be considered as a series of layers, as shown in Fig. 1.1. The troposphere is the lowest of these layers; it contains approximately 75 % of the atmosphere's mass, and almost all of its water vapour and aerosols. It extends from the Earth's surface to around 15 to 20km in the tropics, and about 10 km in the polar regions (during the summer). The lowest part of the troposphere, where friction with the Earth's surface influences air flow, is referred to as the Planetary Boundary Layer (PBL); this layer is typically a few hundred metres to a couple of kilometres deep, depending on the landform and time of day. The border between the troposphere and the stratosphere is called the tropopause, and it is usually characterised by a temperature inversion; the free troposphere is defined as the region of the troposphere that lies between the PBL and the tropopause. The troposphere is well mixed, and its bulk composition is: 78 % nitrogen ( $N_2$ ), 21 % oxygen ( $O_2$ ), 1 % argon (Ar), and 0.036 % carbon dioxide ( $CO_2$ ). The chemical composition of the troposphere is essentially uniform, with the notable exception of water vapour, which varies depending upon the altitude and temperature.

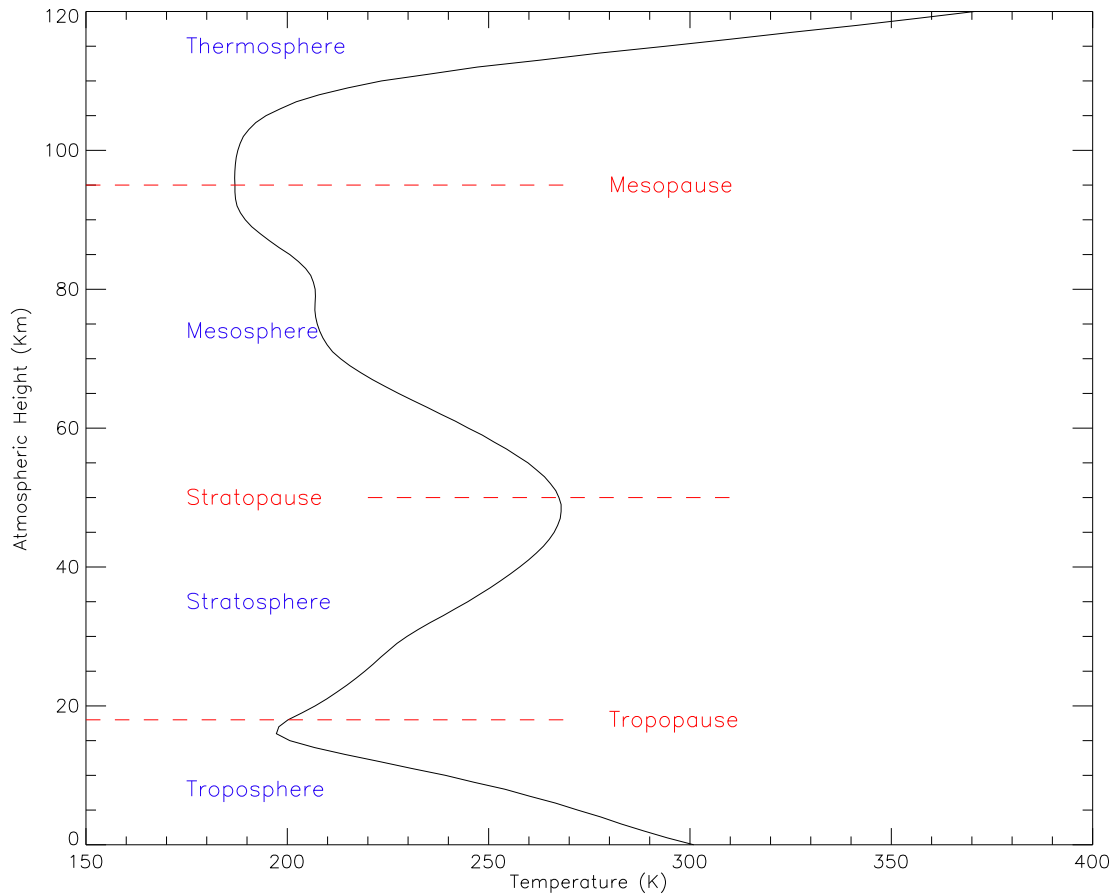


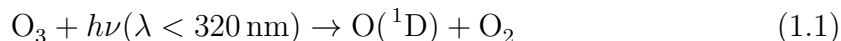
Figure 1.1: The thermal structure of the Earth's atmosphere. The curve shown represents the mean structure at the equator in the summer.

## 1.2 Tropospheric Chemistry

In the general case the chemistry of the troposphere is analogous to a low temperature combustion system, but instead of a thermally initiated process the reactions are controlled and initiated by photochemical processes [Monks, 2005].

One of the most dramatic and well documented changes in atmospheric composition over the past couple of decades is the depletion of stratospheric ozone ( $O_3$ ), with a global decrease of over 5% being observed since 1970 [IGAC, 2003].  $O_3$  exhibits very strong absorption from 230 to 290 nm, and is the only atmospheric species that is capable of attenuating solar radiation between these wavelengths. Radiation below 290 nm damages living cells, and so any decrease in stratospheric  $O_3$  is potentially

harmful for life on Earth. About 90 % of the  $O_3$  in the atmosphere resides in the stratosphere, with the remaining 10 % located in the troposphere where it behaves as a greenhouse gas. Recent estimates indicate that the increase in tropospheric  $O_3$  since pre-industrial times has resulted in a net positive radiative forcing effect of approximately  $0.35 \text{ W m}^{-2}$  [IPCC, 2007]. Any observed elevation in tropospheric  $O_3$  levels needs to be carefully monitored because of the heating effect it has on the atmosphere, and also because of its adverse effects when it is in direct contact with plants and animals. In addition, the photolysis of tropospheric  $O_3$  in the presence of water vapour is the primary source of the hydroxyl free radical (OH) in the troposphere viz:



OH is the major oxidising chemical in the troposphere. It is known to react with most trace gases, and as shown in Table 1.1, reactions with OH are the main removal mechanism for many of these trace gases in the troposphere. For this reason OH is often referred to as the “detergent” of the atmosphere, and the chemistry of the troposphere is thus much concerned with the production of OH radicals from  $O_3$  photolysis in the presence of water vapour, their reaction with other trace gases, and their subsequent removal.

### 1.3 The Importance of CO in the Troposphere

As outlined in section 1.2, the chemistry of the troposphere is controlled mainly by the relationship between tropospheric  $O_3$  and the OH free radical. Measuring the tropospheric concentrations of either  $O_3$  or OH directly is difficult:  $O_3$  because of the overburden of its stratospheric concentrations, and OH because of its low tropospheric concentrations and weak spectral signals. What is needed, in order to properly observe tropospheric chemistry, is a tropospheric constituent which is relatively easy to measure, and which acts as a good indicator of the tropospheric concentrations of OH.

Trace Gas	Global emission rate (Tg per year)	Removal by OH <sup>a</sup> (%)
CO	2800	85
CH <sub>4</sub>	530	90
C <sub>2</sub> H <sub>6</sub>	20	90
Isoprene	570	90
Tereprene	140	50
NO <sub>2</sub>	150	50
SO <sub>2</sub>	300	30
(H <sub>3</sub> CH <sub>3</sub> <sub>2</sub> S)	30	90

<sup>a</sup> Assuming mean global [OH] = 1 × 10<sup>6</sup> molecules cm<sup>-3</sup>

Table 1.1: Global turnover of tropospheric gases, and the percentage removed by reaction with the OH free radical [Monks, 2005].

Carbon monoxide (CO) is a colourless and odourless gas, which when absorbed into the lungs binds with haemoglobin to form carboxyhaemoglobin (COHb), reducing the oxygen-carrying content of the blood and impairing the release of oxygen from haemoglobin. Potential health effects of direct exposure to CO range from headaches and nausea to depressed heart and respiratory rates, to death at extremely high concentrations [IGAC, 2003]. For these reasons CO is an important component in urban and indoor pollution. In the troposphere CO is a key carbon-containing molecule, it has strong concentration levels in the troposphere (35 to 220 ppbv), and an average lifetime of approximately two months [Novelli et al., 1998b]. This makes CO an ideal tropospheric constituent to be measured by a range of techniques; the pronounced spectral features and concentrations result in a strong spectral signal, which makes detection via spectroscopic techniques more manageable, and its average lifetime is neither too short to result in low concentrations, nor too long to lead to a well-mixed tropospheric gas.

In much of the troposphere, the reaction between CO and OH accounts for 75 % of the OH sink [Thompson, 1992], and in relatively unpolluted regimes the main fate

of OH is the reaction with CO to produce the peroxy radical HO<sub>2</sub> viz:



where  $M$  is a third body which is required to stabilise the excited product. From Eq. 1.3 it is apparent that an increase in the concentrations of CO will result in a decrease in tropospheric concentrations of OH. Hence an increase in CO concentrations results in longer atmospheric lifetimes for those trace and greenhouse gases whose main removal mechanism is through their reactions with OH; e.g. Wigley et al. [2002] show that CO emissions indirectly affect changes in radiative forcing, and CO is often referred to as an indirect greenhouse gas.

On a regional scale, the presence of CO in the troposphere can lead to either the net formation or depletion of tropospheric O<sub>3</sub>, depending on the presence of NO<sub>x</sub> (NO and NO<sub>2</sub>). In regions where there is a high concentration of NO<sub>x</sub>, the HO<sub>2</sub> produced in Eq. 1.4 results in the net formation of O<sub>3</sub> viz:



Whereas in regions of low NO<sub>x</sub>, the HO<sub>2</sub> produced in Eq. 1.4 reacts with the O<sub>3</sub>, leading to O<sub>3</sub> depletion viz:

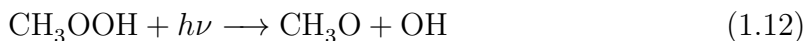
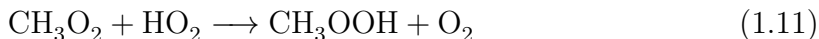
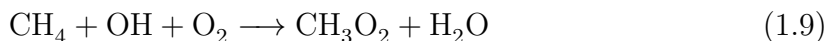


The direct effects of CO on human health only occur at high concentrations not observed on regional scales (e.g. 100 ppmv, Seinfeld [1986]); instead it is in its role as a precursor to tropospheric O<sub>3</sub>, and as the leading sink of the OH radical in which CO has the greatest air quality impact.

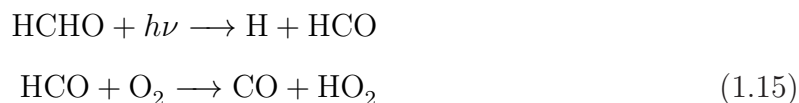
## 1.4 Sources and Sinks of CO

Our current knowledge of the global CO budget is limited by our understanding of the spatial and temporal variability of the CO sources and sinks. The three main sources of CO from surface emissions are the burning of fossil fuels, biofuels, and biomass. Fossil fuels are defined as hydrocarbon deposits which consist of the remains of organisms preserved in rocks in the Earth's crust. The burning of fossil fuels is considered to be one of the main causes for global warming, and the incomplete burning of these fuels are a major source of surface CO emissions. Biofuels differ from fossil fuels in that they are fuels which are produced from living organisms, or from metabolic by-products (organic or food waste products) in order to be considered a biofuel the fuel must contain over 80 % renewable materials. Again, it is the incomplete burning of these biofuels which results in the production of CO. A large source of surface CO emissions also comes from the incomplete combustion of living and dead plant organic matter (biomass) during the process of forest fires, the burning of agricultural wastes and the clearing of forests and savanna and brush lands by burning. As CO is emitted during any type of combustion; including those occurring during industrial processes and Biomass Burning (BB), the measurement of CO can be used to provide information about the impact of anthropogenic pollution.

As well as being produced by the incomplete combustion of fuels and biomass, which result in surface emissions, CO is also produced in the troposphere via a series of oxidation reactions with other gases. The major oxidation source of CO is the oxidation of methane ( $\text{CH}_4$ ) via formaldehyde (HCHO) viz:



or



Aside from  $\text{CH}_4$ , the other major oxidation sources of CO are biogenic and anthropogenic Non Methane Hydro Carbons (NMHCs). Anthropogenic NMHCs, such as those emitted during oil refining, or biogenic NMHCs emitted by vegetation, can react with either the OH radical or  $\text{O}_3$ , converting to oxygenated compounds and then partly to CO in the process.

In addition to the incomplete combustion of fuels and biomass, it has been suggested that the production of CO from plants is a significant contributor to CO surface emissions. Estimates of the emissions from plants and degrading organic matter range from 75 to 380 Tg per year [Kanakidou and Crutzen, 1999], with estimates for the amount of CO that is absorbed by soils ranging from 115 to 240 Tg per year [Sanhueza et al., 1998]. At the time of this thesis little is known in detail regarding the net production of CO from soils, and it is unknown whether or not the emissions balance that which is absorbed, over either global or regional scales. In regards to the oceans, studies [see e.g. Bates et al., 1995] have shown that the net flux of CO from the oceans to the atmosphere represents only 6 to 30 Tg per year, and as such cannot be considered to be a major source of CO surface emissions (see Table 1.2).

Globally the sources of CO vary both latitudinally and seasonally, with the incomplete combustion of fossil fuels providing the dominant source of CO in the northern midlatitudes, whilst the main sources in the tropics are emissions from BB, and the oxidation of  $\text{CH}_4$  and biogenic NMHCs [Holloway et al., 2000]. The main sink of CO is the reaction with OH in the free troposphere, which accounts for approximately 85 % of the total CO sink [Monks, 2005], whilst the flux of CO into the stratosphere accounts for approximately 5 % [Taylor et al., 1996]. Table 1.2 shows estimates of the global budget of CO derived by several research groups, and demonstrates the large degrees of uncertainties present in estimates of both the sources and sinks of CO.

Research Group	Bergamaschi et al.	Holloway et al.	Duncan et al.	Arellano Jr. and Hess
	2000	2000	2007	2006
Fossil Fuel (FF)	-	300	-	464-487
Biofuel (BF)	-	-	-	189
FF + BF	642	-	841	653-676
BB	722	748	501	451-573
<b>Total surface emission</b>	1364	-	1342	1104-1249
Anthropogenic NMHC oxidation	166	-	-	-
Biogenic NMHC oxidation	507	683	394	-
CH <sub>4</sub> oxidation	830	760	820	778-861
<b>Total oxidation source</b>	1503	-	-	1132-1240
<b>Total source</b>	2891	2491	2556	2236-2489
OH sink	2597	-	2618	-
CO deposition	294	-	-	-

Table 1.2: Estimates of the global budget of CO in the Troposphere (Tg per year).

## 1.5 The Distribution of CO

There exists a well-established monitoring program for observing surface CO concentrations, which is operated by the Carbon Cycle Greenhouse Gases group (CCGG) at the National Oceanic and Atmospheric Administration (NOAA). Since 1998 the global distribution of CO in the lower troposphere has been measured using this air sampling network, the geographical distribution of which is shown in Fig. 1.2; the instrumental techniques are described in Sec 1.7. As these site locations range from 82°N to 90°S and represent the free troposphere, regionally polluted atmosphere and marine boundary layer, the measurements from these sites present a unique, inter-calibrated and consistent data set that can be used to better define the spatial and temporal distribution of CO in the troposphere. These surface measurements reveal distinctive seasonal and latitudinal patterns in CO (see Fig. 1.3) that are affected by changes in surface emissions, meteorological effects, and photochemistry. As the

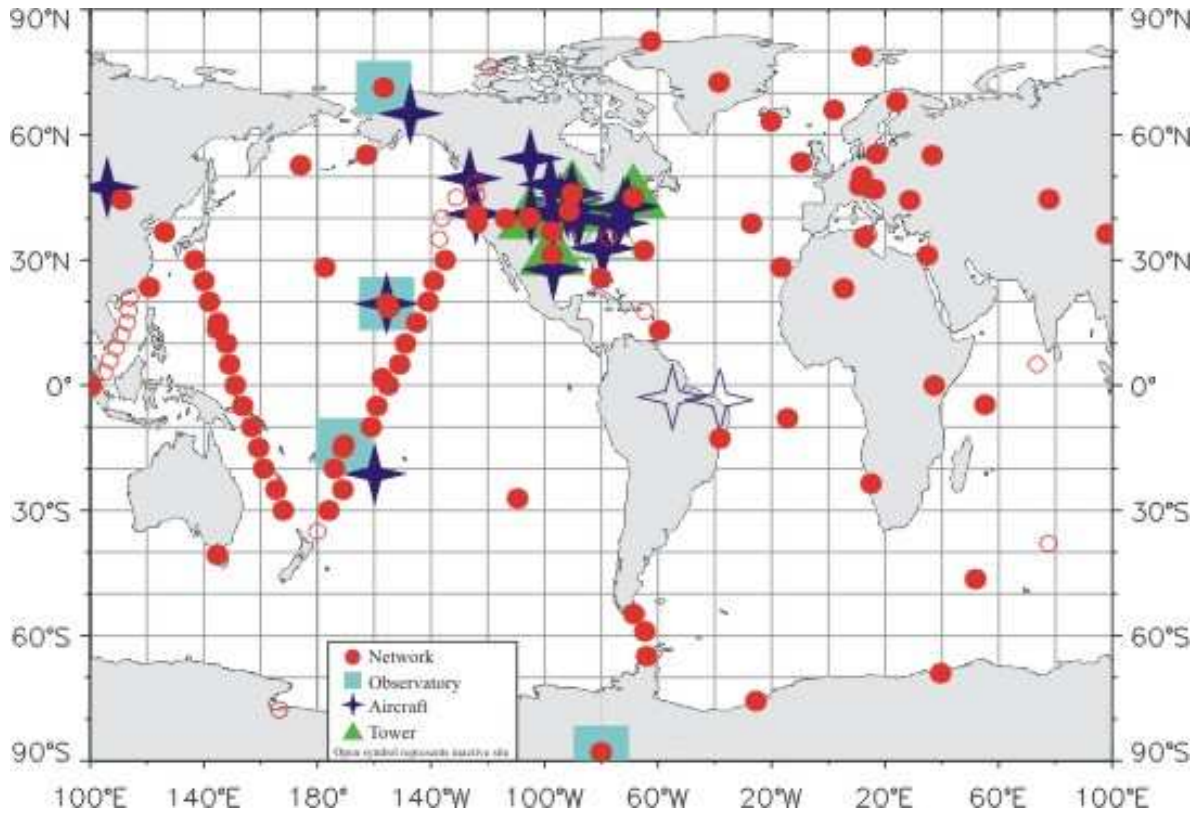


Figure 1.2: The NOAA CCGG Air Sampling Network. Figure taken from <http://www.esrl.noaa.gov/gmd/ccgg/iadv/>.

global distribution of CO is dependant upon the tropospheric concentrations of OH (see Sec. 1.4), the abundance of CO at the surface exhibits a strong interannual variability, which is strongly dependant upon the seasonal cycle of OH.

Novelli et al. [1998b] showed that the background tropospheric global distribution of CO is higher in the Northern Hemisphere (NH) than in the Southern Hemisphere (SH), with the greatest CO mixing ratios (220 to 225 ppbv) in the background troposphere being observed in the high NH during that hemisphere’s winter/early spring, and the lowest levels (35 to 40 ppbv) being observed in the SH, during that hemisphere’s summer months. This seasonal cycle is not symmetrical, but exhibits a gradual increase in mixing ratios during the NH autumn and winter, followed by a rapid decrease in the spring. As the seasonal variations in CO are driven by the seasonal cycle of OH there should be an inverse relationship observable between the OH and CO mixing ratios, and it is by comparing the offset of these two seasonal

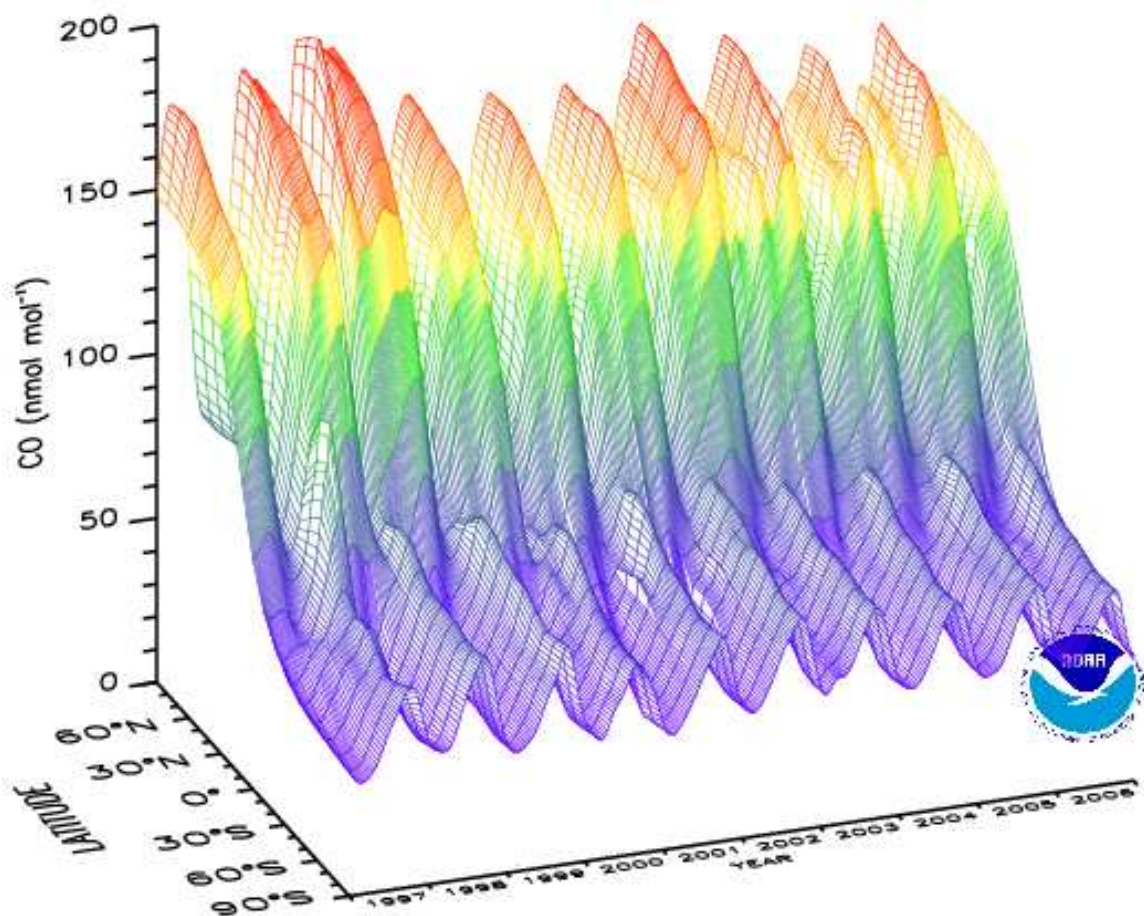


Figure 1.3: Three dimensional representation of the global distribution of CO in the remote marine boundary layer, using data from the cooperative air sampling network. The regular grid spacing of 7 days in time by  $10^\circ$  latitude was achieved by smoothing and interpolating the data. Figure taken from <http://www.esrl.noaa.gov/gmd/ccgg/iadv/>.

cycles that the influence of the anthropogenic sources of CO can be studied. In addition to the globally observable interannual variability, the CO seasonal cycles of the two hemispheres are out of phase by approximately six months. This results in an interhemispheric gradient which has a strong seasonality, with a maximum observed from February to March (160 to 180 ppbv) and a minimum from July to August (10 to 20 ppbv) [Novelli et al., 1998b]. During the NH winter, OH concentrations are low in the NH and high in the SH. Hence CO has a longer lifetime in the low-sink

high-source NH, compared to the high-sink low-source CO budget of the SH, resulting in the maximum in the interhemispheric gradient being observed in the NH winter. In the NH summer the OH sink for CO is greatest in the NH, thus the high-sink high-source CO budget of the NH almost balances the low-sink low-source CO budget of the SH, resulting in a minima in the interhemispheric gradient.

The temporal behaviour of CO is also well documented by the surface measurements from the NOAA network, with these sites observing a downward trend in CO tropospheric concentrations from the late 1980s until mid-1997 [Novelli et al., 1998b]. Recent anomalous events include the large increases in CO in the NH that were observed in 1998, 2002 and 2003, and were attributed to unusually large forest fires observed in these years [Duncan et al., 2007].

## 1.6 The Transport of CO

Transport is the mechanism that moves emissions from a source to a receptor, with the simplest source-receptor combination being that of an isolated point source and an isolated receptor. The transport of gases within the troposphere is a very important aspect of the tropospheric system, as it has a significant effect on the distributions and global budgets of the trace gases. In terms of the transport of trace gases the troposphere can be divided into three principal latitudinal zones: the tropics, and the two extratropics in the Northern and Southern hemispheres. Particles that are released in the extratropics disperse quickly, under the effects of large-scale transient eddies, whilst within the tropics the overturning Hadley cells are responsible for the rapid circulation. The transport of particles within these zones is rapid, and on a similar timescale within each zone (days to a few weeks), whilst the transport of particles between these zones is much slower (weeks to months) [Bowman, 2006]. The slow exchange between these zones results in the appearance of semi-permeable “barriers” to transport in the subtropics. As a result of this slow exchange between the tropics and the extratropics, the time required to transport particles from the extratropics of one hemisphere, through the central tropics and into the extratropics of the other hemisphere, is of the order of 1.8 years [Bowman and Cohen, 1997], with observations of the transport of CO helping to confirm the presence of these transport

barriers [Bowman, 2006].

In addition to the slow exchange across the physical equator because of the large semi-permeable barriers to transport in the subtropics, there is also the exchange of CO across the chemical equator to consider. A recent study by Hamilton et al. [2008] reported observations of a tropospheric chemical equator in the Western Pacific region during the Austral monsoon season. Unlike the physical equator (with which it is non-coincident), this chemical equator is defined as separating the polluted Northern Hemisphere from the cleaner Southern Hemisphere, and is thought to be approximately 50 km wide. Across this chemical equator, defined as a sharp gradient in the chemical background, CO mixing ratios were observed to increase rapidly within the boundary layer, from 40 ppbv to 160 ppbv within  $0.5^\circ$  latitude ( $\sim 50$  km); with transport across this boundary found to be restricted.

The extent to which a trace gas is affected by transport is determined by chemical processes in the troposphere, as well as by dynamical processes in the rest of the atmosphere. The chemical processes govern the extent to which a trace gas is affected by transport, as the lifetime (which determines if the trace particle is in a stable state for long enough so as to be affected by transport processes) is directly linked to the tropospheric photochemical loss, which in the case of CO is its reaction with OH. The longer a trace gas's tropospheric lifetime the more its distribution is governed by dynamical processes, such as the mixing and exchange between the PBL and the free troposphere. The depth of the PBL is dependent on many factors, including sensible heat and large temporal scale frictional drag [IGAC, 2003], and varies on a diurnal scale, with heights during the middle of the day (when heating is at a maximum) significantly higher than they are at night; these diurnal variations are less pronounced over the sea. At the top of the PBL there is a stable entrainment zone, and it is in this region where air can mix between the boundary layer and the free troposphere. Stability in this entrainment zone can create a capping inversion, thereby stopping this dynamical exchange and preventing any movement of air between the two regions. Within the PBL, ground based convective and turbulent processes control the CO mixing ratios, often causing emissions of CO to be brought back down to ground reasonably close to their source. A process called deep convection enables CO to be rapidly injected from below the PBL and into the upper troposphere, where it can

then travel for hundreds of miles, spreading horizontally due to winds, before being brought to Earth.

The strength and location of deep convection varies considerably from season to season. From winter to summer, the maximum migrates from the Western Pacific to South and Southeast Asia, whilst in the summer it is associated with the Asian summer monsoon, retreating southward to the ocean in mid-autumn [Jiang and Livesey, 2007]. There is also evidence to suggest that the meteorological processes that are responsible for the long-range transport processes in the troposphere are also responsible for the interannual variability of the CO that was discussed in section 1.5. In both the Southern and Northern high latitudes, the CO interannual variability is controlled in equal parts by the variations in BB emissions and atmospheric meteorology. In the tropics however, the meteorological variability is solely responsible for 50 to 90 % of the CO interannual variability [Szopa et al., 2007].

## **1.7 Techniques for Observing CO**

Several remote sensing and in situ techniques provide routine measurements to monitor the spatial and temporal changes in the concentration of atmospheric CO. The accuracy, sampling, vertical, horizontal, and temporal coverage of these measurements depend on the instrument and the observation technique. The three main observation techniques that are used to detect CO in the atmosphere are: ground based measurements; in situ sampling (usually from an aeroplane); and remote sensing from space. Each of these methods has different sensitivities. In order to measure the complex spatial and temporal variations in CO distribution, a combination of all three techniques is often implemented.

### **1.7.1 Ground Based Measurements of CO**

Ground based measurements of CO are useful for providing information about the temporal distribution of CO at a set location, and over a long time period. As climate change is defined as any long-term significant change in the average atmospheric conditions that a given region experiences, these ground based measurements provide

Technique	Detection limit (ppbv)	Precision (%)	Linear range	Other species measured
<i>(a) Gas Chromatographic techniques</i>				
GC-FID	35-50	2-8	Atmospheric	CH <sub>4</sub> , CO <sub>2</sub>
GC-ECD	10	2-3	Variable	H <sub>2</sub> , CH <sub>4</sub>
GC-HgO	1-2	0.5-2	Variable	H <sub>2</sub>
<i>(b) Spectroscopic techniques</i>				
NDIR	22-70	1-10	Atmospheric	-
FTIR	1	0.5	Atmospheric	CH <sub>4</sub> , CO <sub>2</sub> , others
TDLS	1	0.2	Atmospheric	CH <sub>4</sub> , CO <sub>2</sub> , N <sub>2</sub> O
RF	5	1	Atmospheric	-

Table 1.3: Detection limits and precision of different ground based CO measurement techniques [Novelli, 1998a].

an excellent source for monitoring climate change in terms of CO variability. Measurement systems normally consist of a network of fixed sites and observatories, but also include measurements made on ships [see e.g. Velazco et al., 2005]. Ground based CO measurement techniques can be divided into two main groups: remote sensing spectroscopic techniques, and those that are based upon Gas Chromatography (GC). The first measurements of atmospheric CO, which were made in the late 1940s and early 1950s, made use of spectroscopic techniques [see e.g. Migeotte, 1949], whilst GC methods were developed later in the 1970s [see e.g. Swinnerton et al., 1970]. A list of the most commonly used measurement techniques along with their detection limits and precision is given in Table 1.3.

The most commonly used types of GC for the detection of CO are flame ionisation (GC-FID), electron capture (GC-ECD), and mercuric oxide absorption (GC-HgO). All of these techniques involve taking flask measurements of CO at a given site, and then the analysis of these samples back at a laboratory. Here the CO and other gases from the sample are separated as they flow over a stationary surface, on which a liquid has been immobilised by chemical bonding or absorption. The separated gases are then injected into a detector, where they each generate a specific disruption of a controlled current. This response is recorded by a computer and compared to the

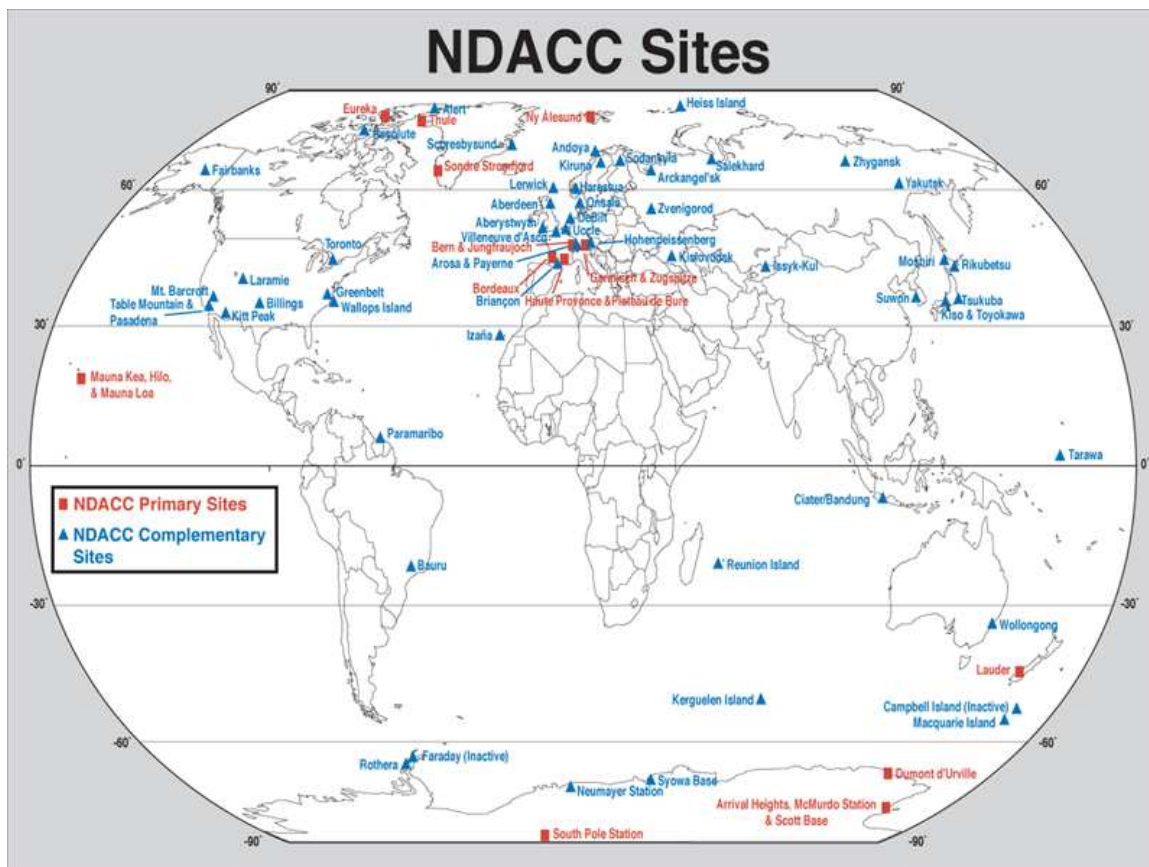


Figure 1.4: Location of NDACC global CO measurement sites. Figure taken from <http://www.ndacc.org>.

response that is generated by a standard sample of the gas, with this comparison then being quantified and converted into a concentration. As can be seen from table 1.3 these methods achieve a high precision (1 to 8 %) and have low detection limits (down to 1 ppbv); the main limitation of ground based GC as a measuring technique is its inability to give any detailed vertical information about the CO measurement. An example of a ground based network that makes measurements using GC is the NOAA CCGG cooperative air sampling network that was discussed in section 1.5, and whose sites are shown in Fig. 1.2.

CO atmospheric concentrations can also be determined by making remote measurements of the absorption of radiation by CO, and the physical processes underlying

this technique are discussed in Sec. 2.2. The most frequently used spectroscopic techniques in the ground based detection of CO are Non Dispersive Infrared Radiometry (NDIR), Fourier Transform Infrared Radiometry (FTIR), Tunable Diode Laser Spectroscopy (TDLA) and Resonance Fluorescence (RF). Spectroscopic techniques achieve a similarly high precision (1 to 10 %) and low detection limits (down to 1 ppbv) as GC techniques, but are also able to provide more detailed information about the vertical distribution of CO in the atmosphere. FTIR spectroscopic techniques are able to resolve 1 to 2 vertical layers of CO concentrations, and this is very important for satellite validation, as currently there are no satellites that are able to provide such vertical resolution [Peterson et al., 2008]. The Network for the Detection of Atmospheric Composition Change (NDACC, formerly the NDSC) has provided long-term atmospheric CO measurements using ground based remote sensing techniques since January 1991. Figure 1.4 shows the location of the sites for this network, and it can be observed that the location of these sites is sparse in global terms. As Fig. 1.2 shows, ground based GC measurements suffer from a similar problem, and as such ground based techniques alone cannot be used to build up a valid global dataset of CO concentrations.

### 1.7.2 Aircraft In Situ Measurements of CO

The English translation of the Latin phrase *in situ* is “in the place”, and in the context of atmospheric science it refers to measurements obtained through a direct contact with the respective subject. As such the measurements made by a radiosonde measuring a parcel of air, or an anemometer measuring wind speed, would be classed as *in situ* measurements, whereas the ground based spectroscopic techniques discussed in section 1.7.1 would be classed as remote sensing measurements. For tropospheric CO concentrations, the majority of *in situ* measurements are made using aircraft. There are two different types of aircraft *in situ* measurements of tropospheric CO: measurements that are made using specially designed aircraft in designated field missions, and measurements that are made using CO detectors that have been attached to commercial aircraft.

The European-funded MOZAIC (Measurements of OZone, water vapour, carbon monoxide and nitrogen oxides by in-service Airbus airCRAFT) programme has been

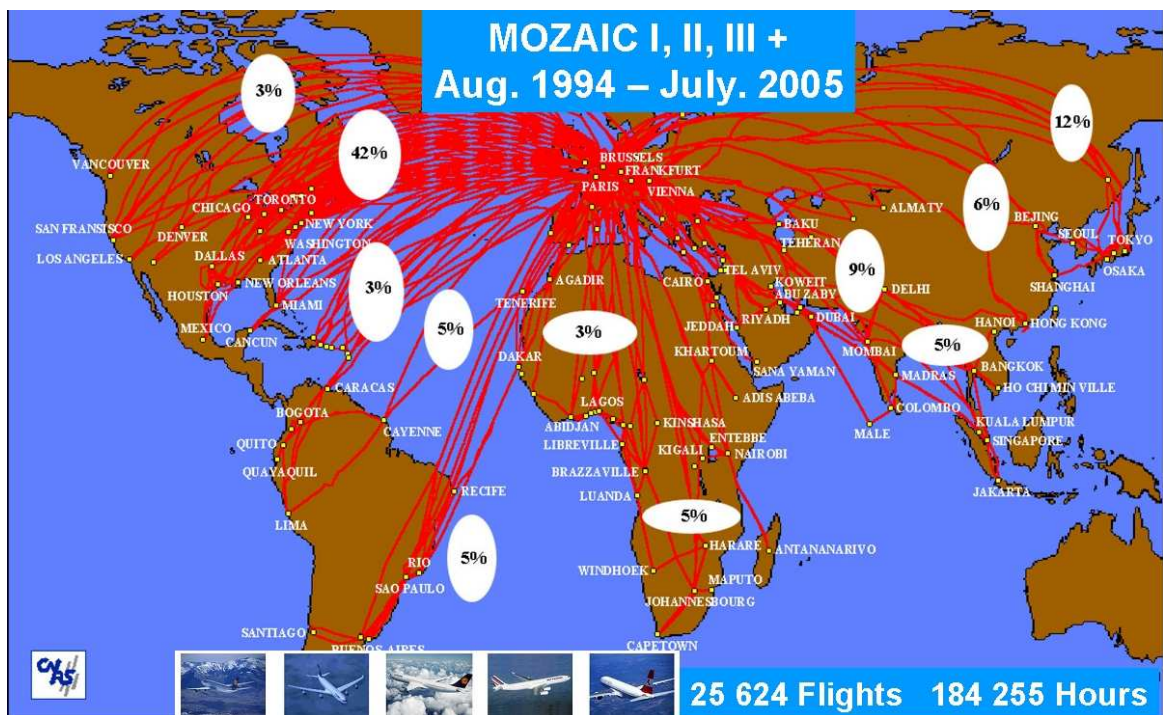


Figure 1.5: A global map of MOZAIC flight paths, from August 1994 to July 2005. Figure taken from <http://mozaic.aero.obs-mip.fr>.

running since 1994, aboard five commercial Airbus A340 aeroplanes. It was originally designed to measure  $O_3$  and water vapour, but as of December 2001 all aircraft were fitted with an infrared  $CO$  analyser, which achieves precision ( $\pm 5\%$ ) and detection limits ( $\pm 5$  ppbv) which are comparable to ground based measurements [Nedelec et al., 2003]. The MOZAIC aircraft now provide automatic  $CO$  measurements along the main routes operated by Lufthansa, Air France and Austrian airlines, providing in situ measurements of  $CO$  from over 900 flights per year. The benefits of commercial aircraft measurements are the relative low-cost involved, and the number of measurements that can be made. The major disadvantage with these types of measurements is that they can only be made along existing flight paths; thereby limiting the distribution of in situ measurements that can be made; Fig. 1.5 shows that whilst the MOZAIC campaign operates over a large number of flight paths, the flight tracks provide a biased sampling of  $CO$ .

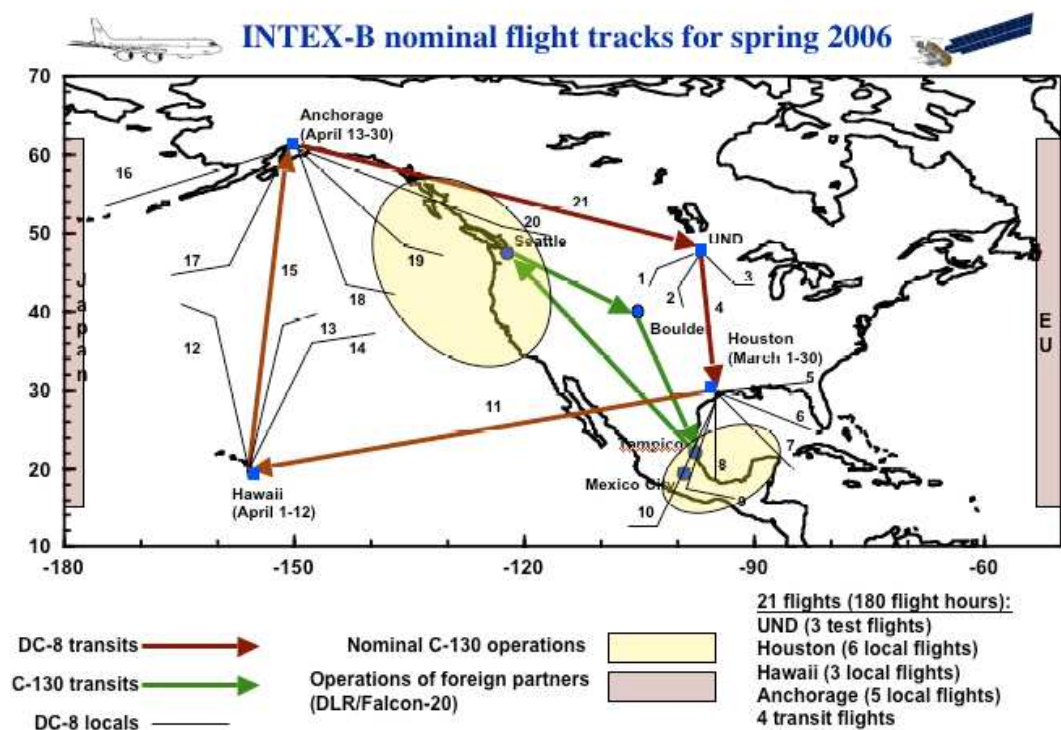


Figure 1.6: Nominal flight tracks for the INTEX-B flight campaign. Figure taken from <http://www.nserc.und.edu/images/missionmap.gif>.

The other type of in situ aircraft measurements that are made involve using specially designated aircraft and instrumentation to conduct a specific field study over a set period of time. An example of such a flight campaign was the INTEX-NA (Intercontinental Chemical Transport Experiment - North America) field study, a two phase experiment which aimed to better understand the transport and transformation of gases and aerosols on transcontinental/intercontinental scales, and to assess their impact on air quality and climate. It was completed in two stages, INTEX-A (during the summer of 2004) and INTEX-B (during spring of 2006), and made use of both high and low-flying airborne platforms to make measurements of  $O_3$  and its precursors, being able to detect concentrations of CO down to 3 ppbv [Singh et al., 2004]. The nominal flight tracks of the National Aeronautics and Space Administration (NASA) DC-8, C-130 and Falcon-8 aircraft used during this mission are shown

in Fig. 1.6. As is evident in Fig. 1.6, measurements made during a field campaign such as INTEX-B can be made over specified spatial regions, but offer very limited temporal information about CO distributions (INTEX-B totalled 143 flight hours over 8 weeks).

In situ measurements made using aircraft provide vertical and horizontal distributions of CO that are a useful supplement to measurements made using ground based techniques. Ultimately though the temporal and spatial information that is provided, by both ground based and aircraft measurements, is too restricted to offer a fully global picture of the distribution and transport of CO in the troposphere. In order to overcome these restrictions, measurements made by satellites are required.

### 1.7.3 Satellite Measurements of CO

Observations from space allow for fully global measurements of CO concentrations to be made over a reasonably short time period, as demonstrated in Fig. 1.7. When designing a space-borne instrument to measure CO concentrations, the spectral range, viewing geometry, orbit, and any bias that is introduced as a result of these choices, must be considered. CO has two strong spectral bands observable in the IR region, centred on  $2140\text{ cm}^{-1}$  ( $4.7\text{ }\mu\text{m}$ ) and  $4200\text{ cm}^{-1}$  ( $2.3\text{ }\mu\text{m}$ ), and so any instrument which wishes to observe CO in the IR must make measurements that incorporate at least one of these spectral bands. The spectral band centred on  $4.7\text{ }\mu\text{m}$  consists of a strong CO emission feature which is dependent on thermal emission in the Thermal InfraRed (TIR), whereas the features of the spectral band centred on  $2.3\text{ }\mu\text{m}$  are dependent upon scattered sunlight in the Near InfraRed (NIR), which is weaker than that from thermal emission. Current operational remote sensing measurements of CO are typically most sensitive to the middle troposphere for TIR measurements, and to a total column for NIR measurements. Under conditions with good thermal contrast (usually found in arid regions), sensitivity close to the surface is also obtainable with TIR measurements [see e.g. Deeter et al., 2007b]. Both the  $4.7\text{ }\mu\text{m}$  and the  $2.3\text{ }\mu\text{m}$  bands also contain other components which contaminate the spectra, and ideally a spectral window where these contaminants is minimised should be chosen. Any space instrumentation must also reach a compromise in terms of spectral resolution, as whilst a higher spectral resolution will result in more information being obtained, it will also result in a lower

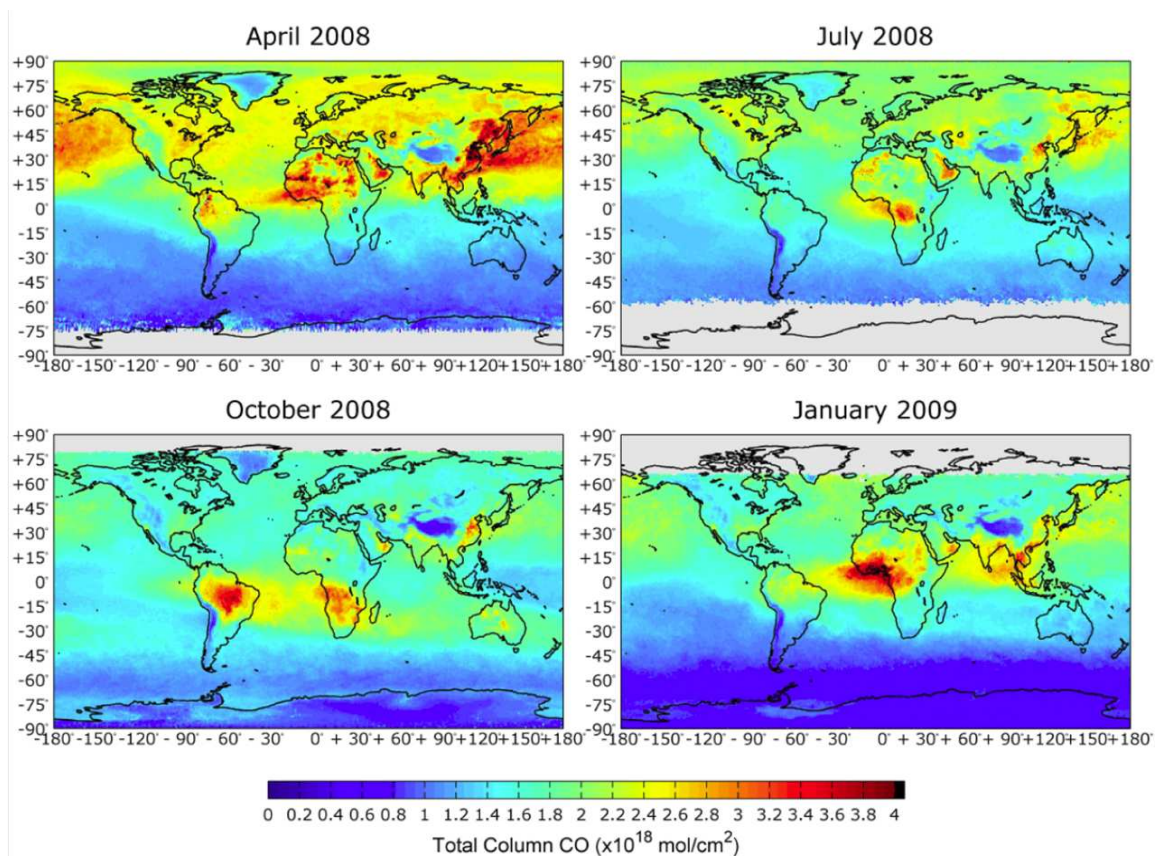


Figure 1.7: Monthly averaged IASI CO total column measurements. Figure taken from Clerbaux et al. [2009].

Signal to Noise ratio (SNR); both determine the amount of information that can be retrieved from a measurement.

The choice of viewing geometries for a satellite will determine to what degree tropospheric CO can be measured, as the nadir and limb/occultation viewing modes present contrasting benefits and limitations. Nadir-viewing instruments offer good horizontal resolution, and are able to probe the atmosphere down to the lower PBL, but have poor vertical resolution and are less sensitive than limb/occultation-viewing instruments, which offer high vertical, but low horizontal resolution. The actual orbit of any proposed CO measuring instrument is also important: in a Low Earth Orbit (LEO), satellite instrumentation is able to achieve repeat coverage times of less than one day, and planetary coverage of up to a few times a day, whilst their

location makes instrument and satellite design both relatively easy and cheap. In contrast to this, geostationary satellites offer repeat times of less than one hour, but due to them only offering coverage of approximately one fifth of the planet, and being very expensive to build, they are not yet used for the detection of tropospheric CO. All satellite instruments have biases that must be taken into consideration when processing any measurements: instruments in a LEO offer more polar than equatorial coverage; limb/occultation instruments are not able to make measurements at the ground; and instruments which operate in the 2.3  $\mu\text{m}$  band offer no nighttime coverage (as they make use of reflected sunlight). There is no such thing as an ideal CO measuring instrument, rather all CO measuring instruments are developed within these limitations, with each instrument having different strengths and weaknesses.

The first instrument to measure atmospheric CO from space was the Measurement of Air Pollution from Satellites (MAPS) instrument, which was flown onboard the Space Shuttle four times: in November 1981 (STS-2), as the first science payload on the Space Shuttle; in October 1984 (STS-41G); April 1994 (STS-59); and October 1994 (STS-68). The MAPS instrument was a selective chopper radiometer, employing a type of GC to determine the CO mixing ratio in the atmosphere [Reichle Jr. et al., 1999]. It was able to measure the distribution of CO in the Earth's lower atmosphere (3 to 10 km above the surface), from 57° N to 57°S, and the space-based data from the MAPS instrument was correlated with a global network of intercalibrated ground- and aircraft-based measurements.

Following on from MAPS, the MOPITT (Measurements of Pollution in the Troposphere) instrument is a nadir viewing GC radiometer which has been making TIR observations of CO for over a decade [Deeter et al., 2003]. IMG (Interferometer Monitor for greenhouse Gases) [Kobayashi et al., 1999], AIRS (Atmospheric InfraRed Sounder) [McMillan et al., 2005], and TES (Tropospheric Emission Spectrometer) [Rinsland et al., 2006] have also successfully exploited observations in the 4.7  $\mu\text{m}$  spectral band to increase the vertical information content of profiles and also global coverage. In the past decade, SCIAMACHY (SCanning Imaging Absorption SpectroMeter for Atmospheric CHartography) [Bovensmann et al., 1999] has added further sensitivity near the surface through the use of observations made in the 2.3  $\mu\text{m}$  spectral band. More recently, exploitation of the NIR channels in the MOPITT instrument have also been

possible, due to recent progress in characterising channel radiance errors [Worden et al., 2010]. These space-borne instruments can be used to provide consistent and long term global measurements, which can then be combined with accurate ground based and in situ data products to give a complete global picture of the atmospheric composition of CO.

The IASI (Infrared Atmospheric Sounding Interferometer) is the latest instrument in the TIR suite of tropospheric sounders, and is the instrument that will be used for the main focus of this thesis; it is described in detail in Chapter 3. As the first in a series of three instruments, to be launched in time intervals of 5 years, IASI aims to deliver continuous and high-quality global meteorological data until at least 2020.

## 1.8 Summary

This introduction has discussed the importance of CO in the troposphere and introduced methods for the observation of CO, both from an in situ and a remote sensing perspective. Because of its relationship with the main oxidising components in the troposphere (i.e. O<sub>3</sub> and OH), as well as its usefulness as an atmospheric tracer, there is a large demand for accurate global maps of the distribution of CO throughout the troposphere. Ground based and aircraft measurements, whilst making useful and precise measurements of tropospheric CO, are unable to offer a truly global perspective, so there is a need for satellite measurements to inform on these large spatial scales. In order to develop a true climatic record of the distribution of global CO it is necessary to make long term (10 years or more) measurements at a reasonable temporal resolution, using a consistent set of protocols to maximise the accuracy and validity of the measurements.

The aim of this thesis is to study the suitability of the IASI instrument to observe CO from space. By understanding the accuracy, bias, and reliability of the measurements that are used to do this, it is hoped that a better perception of the differences between ground based emission inventories and satellite derived products can be reached, and that a strong platform can be established for long-term, well characterised data sets of CO. The remainder of this thesis is structured as follows:

- Chapter 2 - The basics of radiative transfer are outlined, along with a summation

of retrieval theory, a technique which solves the inverse problem of how to use measurements of the Earth's radiation, e.g. from space, to estimate profiles of the constituent parts of the atmosphere.

- Chapter 3 - The IASI instrument is described in detail. The viewing geometry, spectral range and resolution, radiometric calibration, and temporal frequency of the instrument are discussed.
- Chapter 4 - A study is presented which demonstrates the radiometric stability of the IASI instrument at 11 and 12  $\mu\text{m}$ , by comparing measured radiances with those taken by the Advanced Along Track Scanning Radiometer (AATSR) on-board the Environmental satellite (Envisat). Also discussed are the implications that this study has for the radiometric stability of the IASI instrument across the spectral range used for observing CO.
- Chapter 5 - A new retrieval scheme that has been developed to retrieve tropospheric CO profiles using IASI measured radiances is presented. This scheme is differentiated by its incorporation of a solar reflected term, detailed surface emissivity, and precise scene topography. Sensitivity tests and full retrieval simulations which illustrate the accuracy and quantify the bias of the scheme are also discussed.
- Chapter 6 - An intercomparison between the IASI retrieved CO product discussed in Chapter 5, and that of the operational product from the MOPITT instrument is discussed. A full consideration of the use of different a priori information and retrieval pressure grids is given, and the consistency between the different MOPITT and IASI retrievals is assessed.
- Chapter 7 - A summary of the methodologies used to calculate CO emissions using both emission based inventories and satellite derived products is presented. These two techniques are then used to estimate CO emissions from a number of fires during the Southern Africa fire season, as well as from an isolated fire event; the results and discrepancies are discussed.
- Chapter 8 - Conclusions from the current work are presented, as well as suggestions for future work.

## Chapter 2

# Radiative Transfer and Retrieval Theory

### 2.1 Introduction

The work in this thesis is primarily concerned with using the IASI instrument (see Chapter 3) to observe atmospheric concentrations of CO (see Chapter 1). In order to do this a thorough understanding of how the radiative properties of CO under atmospheric conditions, and how this manifests itself in the signal measured by the IASI instrument at the Top Of the Atmosphere (TOA) in the TIR is needed. Section 2.2 discusses the fundamentals of atmospheric radiative transfer, whilst Sec. 2.3 presents the notion of retrieval theory, the process by which TOA measured radiances are converted into information pertaining to the relevant geophysical state of the atmosphere.

### 2.2 Radiative Transfer Theory

Radiative Transfer (RT) can be defined as the physical phenomenon of energy transfer in the form of electromagnetic radiation. It is an important branch of atmospheric physics which draws from many other branches of the physical sciences including, but not limited to: quantum physics; climatology; and electromagnetism. In order to satisfactorily solve any RT problem one must take into account not only the spectral

distribution of the radiation, but also the topography, homogeneity, and instrument viewing geometry of the scene. It is the purpose of this section to explain the fundamentals of atmospheric RT which are relevant to this thesis, and the theory and definitions are taken largely from Wallace and Hobbs [2006].

### 2.2.1 The Spectrum of Radiation

In its most simplistic terms, ElectroMagnetic (EM) radiation can be thought of as a collection of waves propagating at the speed of light. The fundamental properties of such a wave can be expressed in terms of the frequency  $\nu$ , wavelength  $\lambda$  and wavenumber  $\hat{\nu}$  in relation to the speed of light  $c^*$  ( $2.998 \times 10^8 \text{ m s}^{-1}$ ):

$$\nu = c^* \hat{\nu} = c^* / \lambda. \quad (2.1)$$

As demonstrated by Eq. 2.1,  $\lambda$ ,  $\hat{\nu}$ , and  $\nu$  are interchangeable; for simplicity the equations of RT used throughout Sec. 2.2 are expressed in terms of  $\lambda$ .

The EM spectrum is the range of all possible frequencies of EM radiation. The visible region (0.39 to 0.76  $\mu\text{m}$ ) of the EM spectrum corresponds to that part of the spectrum that can be “seen” by the human eye, whilst much of remote sensing technology concerns itself with the microwave, UltraViolet (UV) and InfraRed (IR) regions, with the IR region being of particular importance because it contains the distinctive spectroscopic features of many trace gases. The NIR and shortwave IR ( $\sim 0.8$  to 4  $\mu\text{m}$ ) are dominated by incoming solar radiation, with outgoing terrestrial radiation being prevalent throughout the rest of the IR region.

The monochromatic (or spectral) intensity  $I_\lambda$  is defined as the amount of energy that is transferred by EM radiation in a specific direction, passing through a unit area per unit time at a given wavelength. It can be expressed in units of watts per square metre per unit of solid angle per unit wavelength ( $\text{W m}^{-2} \text{sr}^{-1} \mu\text{m}^{-1}$ ).

The radiance (or intensity)  $I$  is defined as the integral of the monochromatic intensity over a finite range of the EM spectrum. It has units of  $\text{W m}^{-2} \text{sr}^{-1}$  and can be expressed mathematically as:

$$I = \int_{\lambda_1}^{\lambda_2} I_\lambda \text{d}\lambda. \quad (2.2)$$

The irradiance (or flux density) is defined as the rate at which radiant energy passes through a unit area on a plane surface; it is expressed in units of  $\text{W m}^{-2}$  and, is given as:

$$F = \int_{2\pi} I \cos \theta \, d\omega = \int_{\lambda_1}^{\lambda_2} \int_{2\pi} I_\lambda \cos \theta \, d\omega \, d\lambda, \quad (2.3)$$

where the  $2\pi$  limit on the integral indicates that the integration extends over the entire hemisphere of solid angles lying above the respective plane,  $\theta$  is the angle between the incident radiation and the direction normal to the plane (the zenith angle), and  $d\omega$  is representative of an elemental arc of solid angle.

## 2.2.2 Black body radiation

A black body is defined as an idealised object that absorbs all EM radiation that is incident upon it; no EM radiation passes through it and none is reflected. A black body appears black because it is unable to transmit or reflect any visible radiation, which as discussed in Sec. 2.2.1 is part of the EM spectrum.

### 2.2.2.1 The Planck Function

Whilst a black body does not transmit or reflect EM radiation, it does emit a temperature-dependent spectrum of light, the black body radiation, the intensity of which has been determined experimentally to be given by:

$$B_\lambda(T) = \frac{c_1 \lambda^{-5}}{\pi(e^{c_2/\lambda T} - 1)}, \quad (2.4)$$

where  $c_1 = 3.74 \times 10^{-16} \text{ W m}^2$ , and  $c_2 = 1.45 \times 10^{-2} \text{ m K}$ . Black body radiation is isotropic, that is to say that it exhibits properties with the same values when measured along axes in all directions.

### 2.2.2.2 Kirchhoff's Law

The monochromatic emissivity  $\epsilon_\lambda$  is defined as the ratio of the monochromatic radiance emitted by a body compared to the radiance emitted by a black body at the equivalent

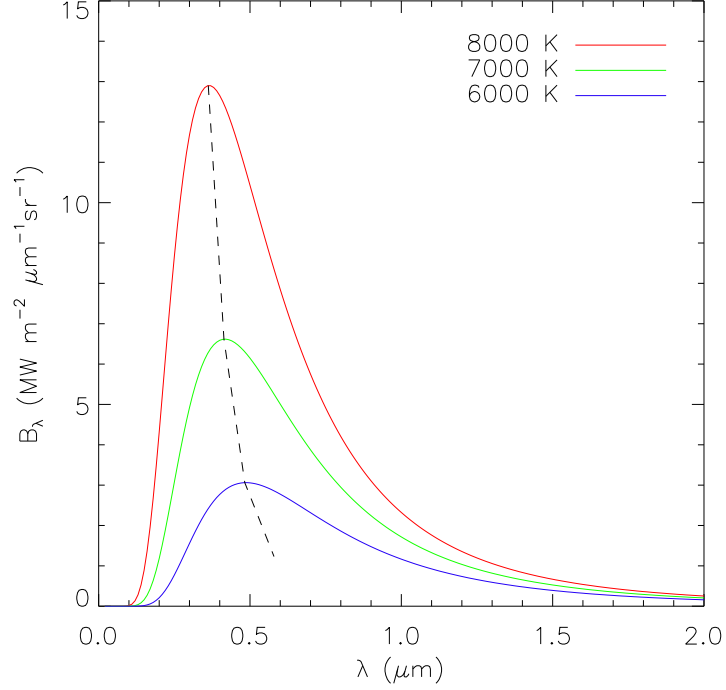


Figure 2.1: Emission spectra for blackbodies with a range of absolute temperatures, plotted as a function of wavelength. The dotted line indicates the peak emission for each of the blackbodies.

temperature. It can be expressed mathematically as:

$$\epsilon_{\lambda} = \frac{I_{\lambda}(\text{emitted})}{B_{\lambda}(T)}, \quad (2.5)$$

which is therefore equal to one for a black body. Kirchhoff's law states that the monochromatic emissivity and absorptivity  $\alpha_{\lambda}$  of a body are equivalent to one another, which can be written as:

$$\epsilon_{\lambda} = \alpha_{\lambda}, \quad (2.6)$$

with this relationship being true for any given body at any given wavelength. In the case of atmospheric gases, Eq. 2.6 is only valid when the frequency of collisions between atmospheric molecules is far greater than the rate of absorption/emission by that gas at the specified wavelength; when this condition is met the gas is said to be

in a state of Local Thermal Equilibrium (LTE).

### 2.2.3 Physics of Scattering and Absorption and Emission

As terrestrial and solar light passes through the Earth's atmosphere it can be either scattered, or absorbed by aerosols (a suspension of fine solid particles or liquid droplets in a gas) and gas molecules. These scattering and absorption processes are linearly proportional to: the concentrations of the scattering/absorbing medium; the effectiveness of the absorbers or scatterers; and the intensity of the radiation. For a beam of radiation passing through a thin layer of the atmosphere, the monochromatic radiance is decreased by an amount given by the rate of scattering/absorbing:

$$d I_{\lambda} = -I_{\lambda} K_{\lambda} N \sigma d s, \quad (2.7)$$

where  $I_{\lambda}$  is the monochromatic radiance,  $K_{\lambda}$  is the scattering/absorbing efficiency,  $N$  is the number of particles per unit volume of air,  $\sigma$  is the cross section of the particles, and  $d s$  is the differential path length along the beam of initial radiation. Equation 2.7 can also be written as:

$$d I_{\lambda} = -I_{\lambda} k_{\lambda} \rho r d s, \quad (2.8)$$

where:  $k_{\lambda}$  represents the mass absorption coefficient;  $\rho$  represents the air density; and  $r$  is the air mass ratio of the absorber/scatterer. The terms  $K_{\lambda} N \sigma$  and  $k_{\lambda} \rho r$  are referred to collectively as the extinction coefficients.

#### 2.2.3.1 Scattering by Air Molecules and Particles

Whilst scattering and absorbing air molecules and particles can assume a wide variety of both shape and size, it is helpful to consider these processes for particles with an assumed spherical radius  $r$ , in which case an appropriate size parameter is defined as:

$$x = \frac{2\pi r}{\lambda}. \quad (2.9)$$

A complex index of refraction can also be defined ( $\mathbf{m} = m_r + im_i$ ), whose real and imaginary parts relate to the scattering and absorption processes, respectively.

The Rayleigh scattering regime is defined as one for which  $x \ll 1$ , with a scattering efficiency of the form:

$$K_\lambda \propto \lambda^{-4}, \quad (2.10)$$

whilst Mie scattering occurs when  $0.1 < x < 50$ , and is characterised by an extinction efficiency with a damped oscillatory pattern around a mean value of approximately 2, with these oscillations being further damped by an increase in  $m_i$ . For  $x \geq 50$ , the geometric optic regime, the extinction efficiency displays almost no oscillatory behaviour, and is approximately equal to 2.

### 2.2.3.2 Absorption by Atmospheric Molecules

The absorption of radiation by idealised spherical particles is closely related to the scattering processes discussed in Sec. 2.2.3.1, with the imaginary part of the refractive index of such a particle strongly related to its absorption efficiency.

The absorption of radiation by air molecules is determined by the wavelength of the incident radiation. Extreme UV radiation is defined as radiation which has a wavelength of  $\leq 0.1 \mu\text{m}$ , the energy of which is large enough to strip the electrons from the atoms of any molecules that it may encounter; this process is known as photoionisation, and it is a process which occurs readily in the Earth's ionosphere (see Fig. 1.1). UV radiation with  $0.1 < \lambda \leq 0.24 \mu\text{m}$  is responsible for the photodissociation of  $\text{O}_2$  molecules into two separate O atoms in the Earth's upper atmosphere, whilst the photodissociation of  $\text{O}_3$  into  $\text{O}_2$  and O is a process which absorbs virtually all of the sun's UV radiation that is emitted with a wavelength of up to  $\sim 0.3 \mu\text{m}$ .

Photons at wavelengths greater than  $\sim 0.3 \mu\text{m}$  may not be of a sufficient energy to photo-dissociate or -ionise, but can be absorbed, depending upon the internal energy of the gas molecules:

$$E = E_o + E_v + E_r + E_t, \quad (2.11)$$

where  $E_o$  is the energy level of the electrons in orbit around the atoms,  $E_v$  is the vibrational energy,  $E_r$  is the rotational energy of the molecule, and  $E_t$  is the translational energy that is associated with the random motions of the molecule. The

frequency of the absorbed or emitted radiation is quantified by the change in energy level, which either increases (for absorption) or decreases (for emission);  $E$  is related to the wavelength of the radiation by  $E = h\nu$ . The absorption of radiation of visible or greater wavelengths for a given gas can therefore be described in terms of a line spectrum, which consists of very narrow absorption lines (where the frequency corresponds to the energy of a particular molecular transition) separated by much wider gaps, where the gas is transparent to the incident radiation because there are no relevant transitions. Pure rotational energy  $E_r$  is associated with the microwave region of the spectra; vibrational  $E_v$  and rotational energy are associated with the IR; and electron  $E_o$ , vibrational, and rotational energy are associated with the visible part of the spectra.

The atoms that make up a molecule are not immobile, but oscillate around their equilibrium position. These oscillations are grouped according to how they change the molecular geometry and are called vibrational modes. The number of possible vibrational modes depends on the exact molecular geometry and the number of atoms in the molecule, for a linear molecule with  $N$  atoms (such as CO) there are a total number of  $3N - 5$  allowed vibrational modes. In the case of CO therefore there is one allowed vibrational mode, which corresponds to a stretch of the molecule. At the same time, the molecules can also rotate around their various symmetry axes. Since the rotational properties depend on the geometry, each vibrational state has its own set of rotational states; the vibrational quantum states are generally denoted by  $\nu$ ; the rotational quantum states generally by  $J$ .

Figure 2.2 shows the molecular absorption spectra of CO over the 1 to 1000  $\mu\text{m}$  region. The 4.7  $\mu\text{m}$  region involves the 0-1 fundamental transition, i.e. by absorbing a photon with an energy corresponding to a wavelength in this region, the CO molecule is able to move from the vibrational ground state ( $\nu = 0$ ) to the first excited vibrational state ( $\nu = 1$ ); the different absorption lines centred around this transition are related to the change in the rotational state of the molecule, which are quantised by the selection rule  $\Delta J = \pm 1$ . Similarly, the lines centred around the 2.3  $\mu\text{m}$  region correspond to a transitions which are all characterised by  $\Delta\nu = 2$ . The microwave region of CO absorption (which is utilised by instruments making measurements in the microwave, such as Microwave Limb Sounder (MLS) instrument onboard the Aura

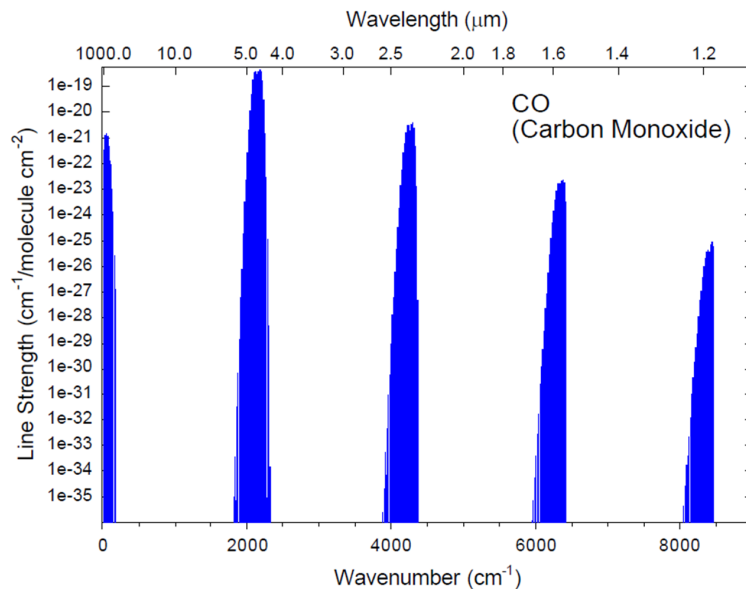


Figure 2.2: CO molecular absorption spectra, produced using HITRAN-96 data. Figure taken from <http://www.coe.ou.edu/sserg/web/Results/Spectrum/co.pdf>

satellite) involves the absorption of photons with a much lower energy than that in the IR region, and hence involves transitions that are purely rotational.

Spectral lines are not infinitesimally sharp. However, this natural broadening is negligible in comparison to the broadening caused by Doppler and pressure (or Lorentz) broadening. Doppler broadening is the broadening which is caused by the distribution of the velocities of the particles; different velocities of the absorbing/emitting particles result in different Doppler shifts, with these differences combining to produce line broadening. Pressure broadening is the result of an interaction with nearby particles, with the collision of other particles with the absorbing/emitting particle temporarily interrupting the absorption/emission process. The absorption spectrum  $k_\nu$  in the presence of these broadening effects can be mathematically described by:

$$k_\nu = S f(\hat{\nu} - \hat{\nu}_0), \quad (2.12)$$

where  $S$  is the line intensity,  $\hat{\nu}_0$  is the central wavenumber of the absorption line, and  $f$  is the line profile. The line profiles of the Doppler and pressure broadening are different, with the absorption lines caused by pressure broadening having “wings”

which extend further from  $\nu_0$  than those caused by Doppler broadening. Similarly the Full Width at Half Maximum (FWHM) of lines caused by Doppler broadening are proportional to  $T^{1/2}$  and independent of pressure  $P$ , whilst the FWHM of pressure broadening is inversely proportional to the  $T$ , and directly proportional to  $P$ . These inherent differences mean that above  $\sim 50$  km in the Earth’s atmosphere, where there are far fewer molecular collisions, Doppler broadening is the dominating factor in determining the absorption line width, whereas in the more densely populated lower atmosphere (below  $\sim 20$  km) pressure broadening dominates.

Theoretically or experimentally derived absorption line information, such as that available from the HIgh-resolution TRANsmission (HITRAN) spectroscopic data base [Rothman et al., 2009], can be used to calculate the absorption spectra for all of the absorbing gas molecules in any given spectral region.

## 2.2.4 Thermal Infrared Radiative Transfer In the Atmosphere

A remote sensing instrument measures all the radiation which passes through the atmosphere within its field of view, as well as the radiation emitted along the viewing path by atmospheric molecules, or scattered by clouds and aerosols. The true atmosphere is composed of continuous vertical profiles of gas, not just one layer, i.e. the atmosphere is separated into a number of layers, each of which absorb and re-emit radiation. In the TIR a reasonable assumption is to ignore scattering effects, because the particle size of atmospheric aerosols is such that they do not interact to a great extent with radiation at these wavelengths. Neglecting scattering effects, the radiative transfer through each of these atmospheric layers is given by the Schwarzschild Equation in LTE:

$$d I_\lambda = -k_\lambda I_\lambda dz + k_\lambda B_\lambda(T) \rho dz, \quad (2.13)$$

where  $I_\lambda$  is the intensity of radiation at wavelength  $\lambda$ ,  $k_\lambda$  is the absorption coefficient,  $\rho$  is the density of the medium,  $z$  is the distance travelled by the radiation, and  $B_\lambda(T)$  is the Planck Function (Eq.2.4).

For nadir viewing instruments (such as IASI), the observed intensity for a given wavelength, and at a particular height,  $z$ , is obtained by integrating Eq. 2.13 over the complete vertical path travelled by the radiation through the atmosphere:

$$I_\lambda = \epsilon_s B_\lambda(T_s) \tau_\lambda + \int B_\lambda(T_z) (d\tau_\lambda(T_z)/dz) dz, \quad (2.14)$$

where  $\epsilon_s$  is the surface emissivity,  $T_s$  is the surface temperature,  $\tau_\lambda$  is the transmittance of the atmosphere at the specified wavelength, and  $T_z$  is the temperature of the layer. The first term of the rhs of Eq. 2.14 represents the emission from the surface, attenuated by the transmission of the atmosphere between the surface and the TOA, where the measurement is made. The second term determines the additional contribution from the emission by each layer, with the function  $d\tau_\lambda(T_z)/dz$  defining the contribution to the TOA measurement due to the emission from each layer. This function is often referred to as the weighting function, the shape of which is determined by two main effects: 1) the concentrations of the absorbing gas with respect to height; and 2) the increase in transmission at higher altitudes because of the decrease in path length with respect to the satellite's altitude.

In the IR the TOA radiation measured by a satellite is composed of two main terms: the longwave radiation emitted by the Earth and its atmosphere (given by Eq. 2.14), and the back-scattered solar radiation. Neglecting the effects of scattering, the reflected solar radiation as detected at the TOA can be represented using the following equation, taken from Hobbs [2000]:

$$I_\lambda = A_s I_\lambda(0) \exp(-\gamma((1/\cos(\theta_{sat})) + (1/\cos(\theta_{sol})))), \quad (2.15)$$

where  $I$  is the reflected solar radiation term detected at the TOA,  $A_s$  is the surface Albedo,  $I_\lambda(0)$  is the solar radiance which is incident on the Earth,  $\gamma$  is the optical depth of the atmosphere,  $\theta_{sat}$  is the satellite zenith angle, and  $\theta_{sol}$  is the solar zenith angle.

## 2.3 Retrieval Theory

Earth observational satellites make measurements of the radiance spectra of the Earth. As was discussed in Sec. 2.2, the radiance that reaches the satellite corresponds to the sum of the radiances emitted and reflected at the Earth's surface, attenuated by the whole atmosphere, and the radiation emitted by each atmospheric layer attenuated by the atmosphere remaining above it. In essence, the radiation measured by the

satellites is an intricate function of all of the components that make up the atmosphere, as well as of the properties of the Earth’s surface; retrieval theory ascertains which of these constituents have changed from a starting assumption, and by how much, in order to reproduce the signal that has been observed. This section on retrieval theory introduces the “inverse problem”, its associated terminology and definitions, and some of the techniques that can be used to solve it; the theory and definitions are taken mainly from Rodgers [2000].

### 2.3.1 Definitions

In order to be concise in an explanation of retrieval theory, a consistent nomenclature is required; this section aims to define a number of variables and their constructs in a dependable manner.

#### 2.3.1.1 The State and Measurement Vectors

The state vector,  $\mathbf{x}$  has  $n$  elements,  $x_1, x_2, \dots, x_n$ . It represents a profile of some quantity, chosen at a finite number of levels so as to adequately represent the atmospheric variations for that quantity. In order to retrieve  $\mathbf{x}$ , the quantity that is actually measured is the measurement vector  $\mathbf{y}$ , with  $m$  elements  $y_1, y_2, \dots, y_m$ . The measurement vector should include all measured quantities which are a function of the state vector; all measurements have an error, or measurement noise associated with them, and this is represented by  $\epsilon$ . The primary aim of retrieval theory is to gain as much information about the properties of the atmosphere as possible, from the measurements made by the instrument, i.e. given  $\mathbf{y}$  and  $\epsilon$  how accurately can  $\mathbf{x}$  be retrieved.

#### 2.3.1.2 The Forward Model

For a discretised atmosphere, the analytical relationship between the measured radiance  $\mathbf{y}$  and the true atmospheric state  $\mathbf{x}$ , is given by:

$$\mathbf{y} = \mathbf{f}(\mathbf{x}; \mathbf{b}) + \epsilon, \tag{2.16}$$

where the forward function  $\mathbf{f}$  describes the complete physics of the measurement, and the vector of parameters  $\mathbf{b}$  represents all of the other fixed parameters which have an

impact on the measurement, but are not contained within the state vector. These are termed the forward function parameters, a typical example of which is the ILS (see Sec. 3.4.2).

Due to the detailed physics that it represents, accurately characterising the forward function can be a source of difficulty, and so instead an approximation is often used. This approximation is called the forward model  $\mathbf{F}$ , and Eq. 2.16 can be rewritten to give the relationship between the measurement and the state vector as:

$$\mathbf{y} = \mathbf{F}(\mathbf{x}; \mathbf{b}) + \epsilon. \quad (2.17)$$

### 2.3.1.3 The Jacobian

The Jacobian  $\mathbf{K}$  is a  $m \times n$  weighting function matrix, which describes the sensitivity of the forward model to the state vector:

$$\mathbf{K} = \frac{d\mathbf{F}(\mathbf{x})}{d\mathbf{x}}. \quad (2.18)$$

If  $m < n$ , then there are more quantities that need to be retrieved than there are measurements, and so the equations of the Jacobians are said to be underconstrained, and the inverse problem under-determined. Similarly if  $m > n$ , then there are more measurements than there are quantities to be retrieved, and the equations of the Jacobians are said to be overconstrained, and the inverse problem over-determined.

### 2.3.1.4 The Gain Matrix

The gain matrix, or measurement contribution function,  $\mathbf{G}$  represents the sensitivity of the retrieved state vector  $\hat{\mathbf{x}}$  to the measurement vector:

$$\mathbf{G} = \frac{d\hat{\mathbf{x}}}{d\mathbf{y}}. \quad (2.19)$$

The amplitude of the elements of the gain matrix essentially represents the weight given to the measurements in order to achieve the optimal solution.

### 2.3.1.5 The Averaging Kernel Matrix

The averaging kernel matrix  $\mathbf{A}$  is a representative of the sensitivity of the retrieved state to the true state:

$$\mathbf{A} = \frac{d\hat{\mathbf{x}}}{d\mathbf{x}}. \quad (2.20)$$

It can also be shown [Rodgers, 2000], that:

$$\mathbf{A} = \mathbf{G}\mathbf{K}. \quad (2.21)$$

The rows of  $\mathbf{A}$  are generally peaked functions, which have a half-width that is representative of the spatial resolution of the observing system. An ideal observing system would have  $\delta$ -function averaging kernels, peaking at the various levels over which the retrieval was performed, and no noise.

### 2.3.2 Information Content

The information content of a measurement is used to state what the measurement  $\mathbf{y}$  says about the state  $\mathbf{x}$ . There are many different ways to express the information content of a measurement, and here only two are dealt with in detail: the Shannon information content, and the Degrees of Freedom for Signal (DFS).

#### 2.3.2.1 The Shannon Information Content

The information content of a measurement can be expressed as the change in the entropy of the system, and the Shannon information content  $H$  of a random vector  $\mathbf{v}$  is defined as the change in entropy of the probability density function (pdf) of  $\mathbf{v}$ , where the entropy itself is defined as:

$$S\{P\} = - \int P(\mathbf{v}) \log_2 [P(\mathbf{v})M(\mathbf{v})] d v, \quad (2.22)$$

where  $M(\mathbf{v})$  is a measure function which can often be taken as constant. Qualitatively, entropy can be thought of as the log of the volume of state space occupied by the pdf.

The Shannon information content of a measurement  $\mathbf{y}$  can thus be defined as the change in entropy of the pdf of  $\mathbf{x}$ :

$$H = S\{P(\mathbf{x})\} - S\{P(\mathbf{x}|\mathbf{y})\}. \quad (2.23)$$

It can be shown [Rodgers, 2000] that, for Gaussian statistics,  $S(P) = \frac{1}{2} \log |\mathbf{S}|$ ; so  $H$  can be written as:

$$H = \frac{1}{2} \log |\mathbf{S}_a| - \frac{1}{2} \log |\hat{\mathbf{S}}| \quad (2.24)$$

where  $\mathbf{S}_a$  and  $\hat{\mathbf{S}}$  are the a priori and a posteriori covariance matrices, respectively.

The Shannon information content can also be written in terms of the averaging kernel matrix:

$$H = -\frac{1}{2} \ln |\mathbf{I}_n - \mathbf{A}| \quad (2.25)$$

where  $\mathbf{I}_n$  is a  $n \times n$  unit matrix.

### 2.3.2.2 Degrees of Freedom for Signal

The DFS are a measurement of the effective number of independent quantities whose uncertainty has been improved by the measurement. It can be thought of as a way of determining which of the  $n$  values of the state vector  $\mathbf{x}$  are independent quantities relating to the measurement signal, and not the noise. A solution which minimises a function that includes both measurement and prior assumed information, is called the Optimal Estimation Method (OEM). The function to be minimised is known as the joint cost function, and it can be expressed as:

$$\chi^2 = (\mathbf{y} - \mathbf{F}(\hat{\mathbf{x}}))^T \mathbf{S}_\epsilon^{-1} (\mathbf{y} - \mathbf{F}(\hat{\mathbf{x}})) + (\hat{\mathbf{x}} - \mathbf{x}_a)^T \mathbf{S}_a^{-1} (\hat{\mathbf{x}} - \mathbf{x}_a) \quad (2.26)$$

where  $\mathbf{S}_\epsilon$  is the measurement noise covariance matrix.

When  $\chi^2$  is at a minimum it is equal to the number of measurements  $m$ , the total number of degrees of freedom. This number has two components: the degrees of freedom for signal ( $d_s$ ) and the degrees of freedom for noise ( $d_n$ ), and it is the  $d_s$  term which describes the number of useful independent quantities that are in the measurement. The degrees of freedom for signal can be written in terms of the averaging kernel matrix:

$$d_s = \text{tr}(\mathbf{GK}) = \text{tr}(\mathbf{A}). \quad (2.27)$$

Thus by finding the trace of the averaging kernel matrix, one is able to determine how many elements of the retrieved state vector represent truly independent measurements, uncontaminated by the noise of the signal.

### 2.3.3 Solution with Prior Data

As was shown in section 2.3.1.3 the inverse problem can be either over or under-constrained. Building an instrument with a large number of  $n$  channels might be

impractical; similarly making  $\mathbf{x}$  have only  $m$  possible values does not lead to satisfactory solutions. What is needed is a solution that is able to solve the ill-determined nature of this inverse problem. In order to do this,  $\mathbf{x}$  and  $\mathbf{y}$  should be thought of as vector random variables with pdfs of  $P(\mathbf{x})$  and  $P(\mathbf{y})$  respectively. Once a measurement of  $\mathbf{y}$  has been made the pdf of  $\mathbf{x}$  is now given as  $P(\mathbf{x}|\mathbf{y})$ , i.e. the a posteriori pdf of the state vector. Bayes's theorem states that:

$$P(\mathbf{x}|\mathbf{y}) = \frac{P(\mathbf{y}|\mathbf{x})P(\mathbf{x})}{P(\mathbf{y})}. \quad (2.28)$$

$P(\mathbf{y})$  can be calculated using the forward model and information about  $\epsilon$ , which in this case is the measurement noise of the instrument. Eq. 2.28 will give a value for the pdf of the state vector  $\mathbf{x}$ , but what is actually required for the retrieval is a value for  $\mathbf{x}$ . A value of the retrieved state vector  $\hat{\mathbf{x}}$  which maximises  $P(\mathbf{x}|\mathbf{y})$  would represent the most probable value for  $\mathbf{x}$ , and the method that is used to find this value is known as the Maximum A posteriori Probability (MAP) method. The MAP solution is a form of OEM, and in order to make best use of the MAP method it is assumed that the various probability density functions are all Normal distributions or Gaussians. For a random vector  $\mathbf{v}$  the Normal distribution takes the following form:

$$P(\mathbf{v}) = \frac{1}{(2\pi)^{\frac{n}{2}}|\mathbf{S}|^{\frac{1}{2}}} \exp\left(-\frac{1}{2}(\mathbf{v} - \bar{\mathbf{v}})^T \mathbf{S}^{-1}(\mathbf{v} - \bar{\mathbf{v}})\right), \quad (2.29)$$

where  $\bar{\mathbf{v}}$  is the mean value of  $\mathbf{v}$ , and  $\mathbf{S}$  is its covariance matrix. The natural logarithm of Eq. 2.29 gives the following equation:

$$-2 \ln P(\mathbf{v}) = (\mathbf{v} - \bar{\mathbf{v}})^T \mathbf{S}^{-1}(\mathbf{v} - \bar{\mathbf{v}}) + c_1, \quad (2.30)$$

where  $c_1$  is a constant that is independent of  $\mathbf{v}$ . The MAP solution of this equation is when  $P(\mathbf{v})$  is maximised, and this occurs when  $\mathbf{v} = \bar{\mathbf{v}}$ , which corresponds to a minimum in  $-2 \ln P(\mathbf{v})$ . Substituting for the random vector  $\mathbf{v}$  in Eq. 2.30 with the state vector  $\mathbf{x}$  gives:

$$-2 \ln P(\mathbf{x}) = (\mathbf{x} - \mathbf{x}_a)^T \mathbf{S}_a^{-1}(\mathbf{x} - \mathbf{x}_a) + c_2, \quad (2.31)$$

where  $\mathbf{x}_a$  is the a priori measurement for  $\mathbf{x}$ , and  $\mathbf{S}_a$  is the a priori covariance matrix. The a priori measurement is the best possible estimate of the state vector from prior knowledge, with the covariance matrix representing the uncertainty in this estimate.

If  $P(\mathbf{y}|\mathbf{x})$  is substituted for  $\mathbf{v}$  in Eq. 2.30, then the following equation is acquired:

$$-2 \ln P(\mathbf{y}|\mathbf{x}) = (\mathbf{y} - \mathbf{F}(\mathbf{x}))^T \mathbf{S}_\epsilon^{-1} (\mathbf{y} - \mathbf{F}(\mathbf{x})) + c_3, \quad (2.32)$$

where the covariance of measurement noise  $\mathbf{S}_\epsilon$  specifies the uncertainty in the measurement. Equations 2.31 and 2.32 can be combined with Bayes's theorem (Eq. 2.28) to give:

$$-2 \ln P(\mathbf{x}|\mathbf{y}) + c_4 = (\mathbf{x} - \mathbf{x}_a)^T \mathbf{S}_a^{-1} (\mathbf{x} - \mathbf{x}_a) + (\mathbf{y} - \mathbf{F}(\mathbf{x}))^T \mathbf{S}_\epsilon^{-1} (\mathbf{y} - \mathbf{F}(\mathbf{x})), \quad (2.33)$$

where  $c_4$  is a combination of  $c_2$ ,  $c_3$  and  $P(\mathbf{y})$ , constants which are all independent of  $\mathbf{x}$ . The MAP solution is not normally one which makes either of the two terms on the right hand side of Eq. 2.33 equal to zero, and hence it is not an exact solution:  $\mathbf{F}(\hat{\mathbf{x}}) \neq \mathbf{y}$ . This is not a problem, providing that  $\mathbf{F}(\hat{\mathbf{x}}) - \mathbf{y}$  is comparable to the measurement error.

Minimising Eq. 2.33 achieves a balance between a solution which is like the a priori solution and one which agrees exactly with the measurements. This solution minimises a function that includes both measurement and a priori information; the joint cost function which needs to be minimised is given by Eq. 2.26, and it is reproduced below:

$$\chi^2 = (\mathbf{y} - \mathbf{F}(\hat{\mathbf{x}}))^T \mathbf{S}_\epsilon^{-1} (\mathbf{y} - \mathbf{F}(\hat{\mathbf{x}})) + (\hat{\mathbf{x}} - \mathbf{x}_a)^T \mathbf{S}_a^{-1} (\hat{\mathbf{x}} - \mathbf{x}_a). \quad (2.34)$$

### 2.3.4 The Linear Problem

A truly linear problem is one for which  $\mathbf{K}$  is invariant with  $\mathbf{x}$ , and for which any a priori information is Gaussian.

The sum of two quadratic equations is another quadratic equation, and so the posterior pdf of the state vector, given the measurement vector (Eq. 2.33) can also be written as:

$$-2 \ln P(\mathbf{x}|\mathbf{y}) + c_4 = (\mathbf{x} - \hat{\mathbf{x}})^T \hat{\mathbf{S}}^{-1} (\mathbf{x} - \hat{\mathbf{x}}), \quad (2.35)$$

where  $\hat{\mathbf{x}}$  is the retrieved MAP state vector, and  $\hat{\mathbf{S}}$  is its covariance matrix.

For the linear case,  $\mathbf{y} = \mathbf{K}\mathbf{x}$ , and so Eqs. 2.33 and 2.35 can be combined to give:

$$(\mathbf{x} - \hat{\mathbf{x}})^T \hat{\mathbf{S}}^{-1} (\mathbf{x} - \hat{\mathbf{x}}) + c_4 = (\mathbf{x} - \mathbf{x}_a)^T \mathbf{S}_a^{-1} (\mathbf{x} - \mathbf{x}_a) + (\mathbf{y} - \mathbf{K}\mathbf{x})^T \mathbf{S}_\epsilon^{-1} (\mathbf{y} - \mathbf{K}\mathbf{x}). \quad (2.36)$$

Multiplying out Eq. 2.36 and equating the quadratic terms in  $\mathbf{x}$  gives:

$$\mathbf{x}^T \hat{\mathbf{S}}^{-1} \mathbf{x} = \mathbf{x}^T \mathbf{S}_a^{-1} \mathbf{x} + \mathbf{x}^T \mathbf{K}^T \mathbf{S}_\epsilon^{-1} \mathbf{K} \mathbf{x}, \quad (2.37)$$

and hence:

$$\hat{\mathbf{S}}^{-1} = \mathbf{S}_a^{-1} + \mathbf{K}^T \mathbf{S}_\epsilon^{-1} \mathbf{K}. \quad (2.38)$$

By equating the  $\mathbf{x}^T$  terms in Eq. 2.36 it can be shown that:

$$\hat{\mathbf{x}} = (\mathbf{S}_a^{-1} + \mathbf{K}^T \mathbf{S}_\epsilon^{-1} \mathbf{K})^{-1} (\mathbf{S}_a^{-1} \mathbf{x}_a + \mathbf{K}^T \mathbf{S}_\epsilon^{-1} \mathbf{y}). \quad (2.39)$$

This equation can be rewritten in several forms, two of the most useful of which are:

$$\hat{\mathbf{x}} = \mathbf{x}_a + \mathbf{S}_a \mathbf{K}^T (\mathbf{K} \mathbf{S}_a \mathbf{K}^T + \mathbf{S}_\epsilon)^{-1} (\mathbf{y} - \mathbf{K} \mathbf{x}_a). \quad (2.40)$$

$$\hat{\mathbf{x}} = \mathbf{x}_a + (\mathbf{S}_a^{-1} + \mathbf{K}^T \mathbf{S}_\epsilon^{-1} \mathbf{K})^{-1} \mathbf{K}^T \mathbf{S}_\epsilon^{-1} (\mathbf{y} - \mathbf{K} \mathbf{x}_a) \quad (2.41)$$

Equation 2.40 is known as the  $m$ -form of the equation, because the matrix that needs to be inverted to find the solution is a  $m \times m$  matrix. Similarly Eq. 2.41, is known as the  $n$ -form of the equation, because in this case the matrix to be inverted is a  $n \times n$  matrix. The retrieved state vector can essentially be thought of as a weighted combination between the a priori state and the true state vector, with the gain matrix acting as the weight.

### 2.3.5 The Non-linear Problem

There are very few practical problems for which the inverse problem is truly linear. The linear solution can however be applied to problems that are nearly linear, providing that they are first appropriately linearised.

Most of the problems in inverse theory can be categorised as being moderately non-linear, that is problems for which linearisation is adequate for doing the error analysis, but not for finding the solution. The main difference in solving these moderately non-linear problems, in comparison to the linear and nearly linear problems, is that there are no explicit solutions for locating the optimal solution. The non-linear inverse problems that are discussed here are ones for which the pdf of the a priori are well described by a Gaussian, but for which a linear forward model is not appropriate. In order to solve these moderately non-linear problems, numerical methods must be introduced; two such methods are described here: the Gauss-Newton, and the Levenberg-Marquardt method.

### 2.3.5.1 The Gauss-Newton Method

Even in the non-linear case the Bayesian solution to the inverse problem can still be used to find the maximum probability state  $\hat{\mathbf{x}}$ , by equating the derivative of Eq. 2.33, i.e. the gradient of the cost function, to zero:

$$\nabla_{\mathbf{x}}\{-2 \ln(P(\mathbf{x}|\mathbf{y}))\} = -[\nabla_{\mathbf{x}}\mathbf{F}(\mathbf{x})]^T\mathbf{S}_{\epsilon}^{-1}[\mathbf{y} - \mathbf{F}(\mathbf{x})] + \mathbf{S}_{\mathbf{a}}^{-1}[\mathbf{x} - \mathbf{x}_{\mathbf{a}}] = 0. \quad (2.42)$$

Putting  $\mathbf{K}(\mathbf{x}) = \nabla_{\mathbf{x}}\mathbf{F}(\mathbf{x})$  gives the following implicit equation for  $\hat{\mathbf{x}}$ :

$$-\hat{\mathbf{K}}^T(\hat{\mathbf{x}})\mathbf{S}_{\epsilon}^{-1}[\mathbf{y} - \mathbf{F}(\hat{\mathbf{x}})] + \mathbf{S}_{\mathbf{a}}^{-1}(\hat{\mathbf{x}} - \mathbf{x}_{\mathbf{a}}) = 0. \quad (2.43)$$

This equation must be solved numerically, i.e. an iteration must be used, with the difficulty in finding a solution dependant upon the non-linearity of the forward model. If the problem is not too non-linear, then Newtonian iteration represents a straightforward numerical method. It is used here to find the zero of the gradient of the cost function and, in the case of the general vector equation  $\mathbf{v}(\mathbf{x}) = 0$ , it is analogous to the Newtonian iteration for the scalar case, that is:

$$\mathbf{x}_{i+1} = \mathbf{x}_i - [\nabla_{\mathbf{x}}\mathbf{v}(\mathbf{x}_i)]^{-1}\mathbf{v}(\mathbf{x}_i) \quad (2.44)$$

where the inverse is a matrix inverse. Using the l.h.s of Eq. 2.43 for  $\mathbf{v}$ :

$$\nabla_{\mathbf{x}}\mathbf{v}(\mathbf{x}) = \mathbf{S}_{\mathbf{a}}^{-1} + \mathbf{K}^T\mathbf{S}_{\epsilon}^{-1}\mathbf{K} - [\nabla_{\mathbf{x}}\mathbf{K}^T]\mathbf{S}_{\epsilon}^{-1}[\mathbf{y} - \mathbf{F}(\mathbf{x})], \quad (2.45)$$

where the first derivative of the cost function is represented by the function  $\mathbf{v}$ , and  $\nabla_{\mathbf{x}}\mathbf{v}(\mathbf{x})$  is the second derivative, or Hessian. As can be seen from Eq. 2.45, the Hessian is a function of both the Jacobian  $\mathbf{K}$ , or first derivative of the forward model, and  $\nabla_{\mathbf{x}}\mathbf{K}^T$ , the second derivative of the forward model. This latter term becomes smaller as the solution proceeds, and also as  $\mathbf{y} - \mathbf{F}(\mathbf{x})$  approaches the noise. The Gauss-Newton method involves ignoring the second derivative of the forward model completely, and then substituting Eqs. 2.43 and 2.45 into the Newtonian iteration (Eq. 2.44), to give:

$$\mathbf{x}_{i+1} = \mathbf{x}_i + (\mathbf{S}_{\mathbf{a}}^{-1} + \mathbf{K}_i^T\mathbf{S}_{\epsilon}^{-1}\mathbf{K}_i)^{-1}[\mathbf{K}_i^T\mathbf{S}_{\epsilon}^{-1}(\mathbf{y} - \mathbf{F}(\mathbf{x}_i)) - \mathbf{S}_{\mathbf{a}}^{-1}(\mathbf{x}_i - \mathbf{x}_{\mathbf{a}})], \quad (2.46)$$

where  $\mathbf{K}_i = \mathbf{K}(\mathbf{x}_i)$ . If  $\mathbf{x}_{i+1}$  is expressed as a departure from  $\mathbf{x}_{\mathbf{a}}$  rather than  $\mathbf{x}_i$ , then Eq. 2.46 can be rewritten in both the  $n$ -form (Eq. 2.47) and the  $m$ -form (Eq. 2.48):

$$\mathbf{x}_{i+1} = \mathbf{x}_{\mathbf{a}} + (\mathbf{S}_{\mathbf{a}}^{-1} + \mathbf{K}_i^T\mathbf{S}_{\epsilon}^{-1}\mathbf{K}_i)^{-1}\mathbf{K}_i^T\mathbf{S}_{\epsilon}^{-1}[\mathbf{y} - \mathbf{F}(\mathbf{x}_i) + \mathbf{K}_i(\mathbf{x}_i - \mathbf{x}_{\mathbf{a}})] \quad (2.47)$$

$$\mathbf{x}_{i+1} = \mathbf{x}_a + \mathbf{S}_a \mathbf{K}_i^T (\mathbf{K}_i \mathbf{S}_a \mathbf{K}_i^T + \mathbf{S}_\epsilon)^{-1} [\mathbf{y} - \mathbf{F}(\mathbf{x}_i) + \mathbf{K}_i (\mathbf{x}_i - \mathbf{x}_a)]. \quad (2.48)$$

### 2.3.5.2 The Levenberg-Marquardt Method

The Gauss-Newton method will find the optimal solution in one step for a cost function which is exactly quadratic in  $\hat{\mathbf{x}}$ , and will get close if the function is nearly quadratic; however, if the true solution is sufficiently far from the current iteration point then a quadratic may represent the surface so poorly that the next iteration or step is no nearer to the solution. Applying an extra factor  $\gamma$  (which can be tuned after each iteration so as to minimise the cost function) to Eq. 2.47 gives the Levenberg-Marquardt equation (the  $m$ -form of the Gauss-Newton method, given by Eq. 2.48, cannot easily be used in the Levenberg-Marquardt method):

$$\hat{\mathbf{x}}_{i+1} = \hat{\mathbf{x}}_i + [(1 + \gamma) \mathbf{S}_a^{-1} + \mathbf{K}_i^T \mathbf{S}_\epsilon^{-1} \mathbf{K}_i]^{-1} \{ \mathbf{K}_i^T \mathbf{S}_\epsilon^{-1} [\mathbf{y} - \mathbf{F}(\hat{\mathbf{x}}_i)] - \mathbf{S}_a^{-1} [\hat{\mathbf{x}}_i - \mathbf{x}_a] \}. \quad (2.49)$$

The purpose of the  $\gamma$  function is to allow  $\hat{\mathbf{x}}$  to converge as quickly as possible to the optimal solution. After each iteration the cost function (Eq. 2.34) is calculated, and this is used to calculate a value for the ratio  $R$ :

$$R = \frac{\chi_{i+1}^2 - \chi_i^2}{\chi_f^2 - \chi_i^2} \quad (2.50)$$

where  $\chi_f^2$  is the forecasted, or predicted, cost function calculated using  $\mathbf{F}(\hat{\mathbf{x}}_{i+1}) = \mathbf{F}(\hat{\mathbf{x}}_i) + \mathbf{K}_i \hat{\mathbf{x}}_i$ . This ratio indicates how appropriate it is to use the linear Gaussian approximation: if the linear approximation is satisfactory then  $R$  will be approximately unity. After each iteration  $R$  is calculated, and  $\gamma$  is adjusted so that  $\hat{\mathbf{x}}_{i+1}$  is restricted to lie within a linear range of  $\hat{\mathbf{x}}_i$ .

### 2.3.5.3 Convergence

As solutions to the non-linear problem involve the use of numerical methods, convergence analysis is required so that the correct criterion for stopping the iterations can be established. When testing for convergence it is first necessary to check if the solution has converged, and then to decide if this convergence represents a sensible solution. It is not necessary for the iterations to continue until there is no change in the solution at machine precision, and so a suitable criterion is defined as the point

at which the difference between  $\hat{\mathbf{x}}_{i+1}$  and  $\hat{\mathbf{x}}_i$  is an order of magnitude smaller than the estimated error. In the case of the  $n$ -form of the solution, Rodgers [2000] gives the following as a sensible test for convergence:

$$d_i^2 = (\hat{\mathbf{x}}_i - \hat{\mathbf{x}}_{i+1})^T \hat{\mathbf{S}}^{-1} (\hat{\mathbf{x}}_i - \hat{\mathbf{x}}_{i+1}) \ll n. \quad (2.51)$$

Once an iteration has converged, it is necessary to test if it has converged to the correct answer. An appropriate test for correct convergence is to calculate a value for  $\chi^2[\mathbf{y} - \mathbf{F}(\hat{\mathbf{x}})]$ ; this is the term of the joint cost function (Eq. 2.34) which represents the fit of the forward model to the measurement, and it is defined as:

$$\chi^2[\mathbf{y} - \mathbf{F}(\hat{\mathbf{x}})] = [\mathbf{y} - \mathbf{F}(\hat{\mathbf{x}})]^T \mathbf{S}_\epsilon^{-1} [\mathbf{y} - \mathbf{F}(\hat{\mathbf{x}})]. \quad (2.52)$$

If  $\chi^2[\mathbf{y} - \mathbf{F}(\hat{\mathbf{x}})]$  is  $\sim m$ , then this indicates that the convergence that has been reached represents a sensible solution.

## 2.3.6 Solution Without Prior Data

OEM is a well-established technique for solving the inverse model; one of the major drawbacks of using such a technique, however, is the reliance upon a priori information, with both a prior state vector and covariance matrix being required. Other formulae, which do not rely as much upon the a priori data, can also be applied to the inverse problem, two of which (for the sake of completeness) are presented here: the Twomey-Tikhonov and the Backus-Gilbert method.

### 2.3.6.1 The Twomey-Tikhonov Method

The Twomey-Tikhonov method is used in the case of an under-constrained problem, that is one for which  $m < n$ . It is very similar to the MAP technique, in that it involves minimising the following function to give the most probable solution for  $\mathbf{x}$ :

$$C(\mathbf{x}) = (\mathbf{x} - \mathbf{x}_a)^T \mathbf{H} (\mathbf{x} - \mathbf{x}_a) + \gamma (\mathbf{y} - \mathbf{K}\mathbf{x})^T (\mathbf{y} - \mathbf{K}\mathbf{x}), \quad (2.53)$$

where  $\mathbf{H}$  is usually taken to be a unit matrix. To find the formula which minimises Eq. 2.53,  $C(\mathbf{x})$  must be differentiated with respect to  $\mathbf{x}$ , and the result set to a vector of zeros. It can be shown [Twomey, 1977] that:

$$\hat{\mathbf{x}} = \mathbf{x}_a + (\gamma^{-1} \mathbf{H} + \mathbf{K}^T \mathbf{K})^{-1} \mathbf{K}^T (\mathbf{y} - \mathbf{K}\mathbf{x}). \quad (2.54)$$

The advantage that the Twomey-Tikhonov methodology has over the MAP technique is that it does not require an a priori covariance matrix in order to solve it, and in the case where  $\mathbf{H}$  is taken to be a unit matrix, no a priori information is required at all. The main disadvantage of the Twomey-Tikhonov method is that in order to achieve a satisfactory trade-off with the departure of  $\mathbf{x}$  from  $\mathbf{x}_a$  and  $\mathbf{K}\mathbf{x}$  from  $\mathbf{y}$ , the  $\gamma$  factor must be manually tuned.

### 2.3.6.2 The Backus-Gilbert Method

Both the MAP and Twomey-Tikhonov techniques rely upon a priori information to some extent. If there is no a priori information then it is not possible to retrieve the state vector as such, but it is possible to get a smoothed version of it, providing that there is enough information in the measurements. The Backus-Gilbert method concerns itself with trying to find a set of gain matrices which result in a set of averaging kernels with the lowest possible spread. It can be shown [Kirsch et al., 1988] that the rows of the required gain matrices  $\mathbf{g}$  are given by:

$$\mathbf{g} = \frac{(\mathbf{Q} + \mu\mathbf{S}_\epsilon)^{-1}\mathbf{k}}{\mathbf{k}^T(\mathbf{Q} + \mu\mathbf{S}_\epsilon)^{-1}\mathbf{k}}, \quad (2.55)$$

where  $\mathbf{k}$  are the rows of the Jacobian,  $\mathbf{Q}$  is a matrix of functions depending only on  $\mathbf{k}$ , and  $\mu$  is a tradeoff term between the vertical resolution and the instrument noise. The retrieved state vector is then calculated using:

$$\hat{\mathbf{x}} = \mathbf{G}\mathbf{y}. \quad (2.56)$$

The obvious advantage of using the Backus-Gilbert method instead of the MAP technique is that no a priori information is required. However, this is also the Backus-Gilbert method's biggest drawback, as the use of a priori information can help to constrain an ill-conditioned problem to one that is well posed.

### 2.3.7 Error Analysis

There are two different types of errors: random errors and systematic errors. Random errors are statistical fluctuations in the measured data due to the precision limitations

of the measurement device. Systematic errors on the other hand, are errors which result from some bias in the measurement process and, in contrast to random errors, are not due to chance. Random errors are always present in a measurement, but if the existence and cause of a systematic error can be identified then it can usually be eliminated. In practice the distinction between random and systematic errors is complicated by the fact that error sources may have time variability on a range of scales, and so a source which represents a random error on one scale may well represent a systematic error on another scale. In retrieval theory there are four major sources of error that must be considered:

- **The smoothing error.** The retrieval is an estimate of the true state which has been smoothed by an averaging kernel, the smoothing error accounts for this.
- **The forward model parameter errors.** These are the errors that are associated with the imperfect knowledge of the forward model parameters. They should be calculated separately for each of the forward model parameters which have not already been retrieved.
- **The forward model error.** This is the error that is associated with the forward model.
- **The measurement error.** The measurement error is the noise that is associated with the measurement.

An expression for the error in  $\hat{\mathbf{x}}$ , that incorporates all of these errors, can be written as:

$$\begin{aligned}
 \mathbf{x} - \hat{\mathbf{x}} = & (\mathbf{A} - \mathbf{I}_n)(\mathbf{x} - \mathbf{x}_a) \dots \text{smoothing error} \\
 & + \mathbf{G}_\epsilon \mathbf{K}_b(\mathbf{b} - \hat{\mathbf{b}}) \dots \text{forward model parameter error} \\
 & + \mathbf{G}_\epsilon \Delta \mathbf{f}(\mathbf{x}, \mathbf{b}, \mathbf{b}') \dots \text{forward model error} \\
 & + \mathbf{G}_\epsilon \epsilon \dots \text{measurement error}
 \end{aligned} \tag{2.57}$$

The error analysis in this section has been derived under the assumption that the inverse problem is not worse than nearly linear. However the same error analysis can be applied to the moderately non-linear case, as the prior state  $\mathbf{x}_a$  still appears only linearly in the retrieval method.

### 2.3.7.1 The Smoothing Error

The smoothing error represents the loss of fine structure in the retrieved state, as a consequence of the observing system. The covariance of the smoothing error about  $\hat{\mathbf{x}}$  is given as:

$$\mathbf{S}_s = (\mathbf{A} - \mathbf{I}_n)\mathbf{S}_a(\mathbf{A} - \mathbf{I}_n)^T \quad (2.58)$$

### 2.3.7.2 The Forward Model Parameter Error

The forward model parameter error is a combination of all of the errors that have been introduced by the forward function parameters  $\mathbf{b}$  in the forward model. The covariance of the forward model parameter error is:

$$\mathbf{S}_f = \mathbf{G}_\epsilon \mathbf{K}_b \mathbf{S}_b \mathbf{K}_b^T \mathbf{G}_\epsilon^T \quad (2.59)$$

where  $\mathbf{S}_b$  is the error covariance matrix of  $\mathbf{b}$ . However, as these errors may be either systematic or random, depending on the scales that are involved, it is best to evaluate them separately. Also, if the error due to  $\mathbf{b}$  is large and dominated by one particular forward function parameter, then it may be wise to retrieve that parameter, and to instead include it as part of the state vector.

### 2.3.7.3 The Forward Model Error

The modelling error, i.e. the error associated with the forward model itself, is defined as  $\mathbf{G}_y \Delta \mathbf{f} = \mathbf{G}_y [\mathbf{f}(\mathbf{x}, \mathbf{b}, \mathbf{b}') - \mathbf{F}(\mathbf{x}, \mathbf{b})]$ . The forward model error can be difficult to estimate, as it represents the errors that are introduced by approximating the forward function, and this can only be calculated entirely accurately if there is a perfect model with which to compare the forward model to.

### 2.3.7.4 The Measurement Error

The measurement error is the component of the error that is caused by the measurement noise  $\epsilon$ . The covariance of the measurement error is:

$$\mathbf{S}_m = \mathbf{G}_\epsilon \mathbf{S}_\epsilon \mathbf{G}_\epsilon^T \quad (2.60)$$

## 2.4 Summary

This chapter has described the basics of radiative transfer and retrieval theory, a technique which solves the inverse problem of how to use measurements of the Earth's radiation, e.g. from space, to estimate profiles of the constituent parts of the atmosphere. Particular focus has been paid to the OEM, which uses prior information to constrain the solution to an inverse problem. Chapter 3 details how the IASI instrument makes measurements of TOA radiances, whilst Chapter 5 describes how these TOA radiances are used to infer measurements about CO in the troposphere, using an OEM retrieval scheme whose underlying theory is characterised by the explanation given in section 2.3.

# Chapter 3

## The IASI Instrument on MetOp-A

### 3.1 Introduction

Chapter 2 discussed how satellite measurements of TOA radiances could be used to infer information about atmospheric CO. The work done in this thesis focuses on the TOA radiances as measured by the IASI space-borne instrument. In order to retrieve CO accurately from the IASI TOA radiances, a thorough understanding of how the IASI instrument makes these measurements is required. Section 3.2 discusses the Meteorological Operational (MetOp) satellite programme, in particular the MetOp-A satellite on which the IASI is currently operational. Section 3.3 describes in detail the mechanisms of the IASI instrument, and Sec. 3.4 outlines the process of radiometrically calibrating the IASI measured spectra.

### 3.2 The MetOp Mission

MetOp is the polar-orbiting constituent of Europe's operational meteorological satellite program, whose aim it is to provide weather data services that will be used to monitor climate and improve weather forecasts. The MetOp programme's series of three satellites (A, B, and C) has been jointly established by the European Space Agency (ESA) and the European organisation for the exploitation of METeorological SATellites (EUMETSAT); with EUMETSAT's Polar System (EPS) division charged with operating the system once the satellites are developed and launched by ESA

on behalf of EUMETSAT [Edwards et al., 2006]. The EPS is Europe’s first polar orbiting operational meteorological satellite program, and it is the European contribution to the Initial Joint Polar-orbiting operational satellite System (IJPS). In this joint European-US polar satellite system, EPS serves the midmorning (a.m.) orbit, and the NOAA operates the midafternoon (p.m.) orbit, as part of its Polar Orbit Environmental Satellites (POES) system.

MetOp-A was launched on 19 October 2006; it is the first in a series of three MetOp satellites, with the intention being that the MetOp-B and MetOp-C satellites be launched in time intervals of 5 years, thereby ensuring the delivery of continuous and high-quality global meteorological data until at least 2020. The MetOp suite of satellites are all polar orbiting satellites, which mean that they orbit the Earth at a lower altitude than geostationary satellites - typically 800 km compared with 36 000 km for a geostationary satellite - and can therefore observe the Earth in closer detail. The altitude of the MetOp-A satellite is  $\sim 817$  km, crossing the equator at 09:30 Local Solar Time (LST) on a descending orbit, and at an inclination of  $98.7^\circ$  [Clerbaux et al., 2009]. The repeat cycle of the reference orbit is 29 days; this corresponds to 412 orbits, each one taking 101 mins, meaning that for the onboard sensors with a wide swath range, complete global coverage is achieved twice daily. The payload mass of MetOp-A is 812 kg, with a total mass of 4093 kg [Edwards et al., 2006], and of the instruments on board, five are new-generation European instruments, whilst the others have a well-proven heritage and have been provided by NOAA and the French Space Agency (CNES); a list of these instruments and their applications is given in Table 3.1, and their locations on the MetOp-A satellite are shown schematically in Fig. 3.1.

The EPS includes extensive ground-based facilities to monitor and control the MetOp satellites, as well as to distribute the data from the satellites. The MetOp Direct Readout Service (DRS) provides real-time transmission of data to local user stations, with the Global Data Service (GDS) providing products generated from the MetOp and NOAA satellite data to the user community in near real-time. Data is transmitted by the satellite once per orbit to a EUMETSAT ground station at Svalbard, Norway. From here the data is then transmitted to the EUMETSAT headquarters in Darmstadt, Germany for processing, archiving and distribution, with global

Instrument	Application
<b>GRAS</b> (Global navigation satellite system Receiver for Atmospheric Sounding) <sup>b</sup>	A GPS which provides atmospheric temperature and humidity profiles.
<b>IASI</b> (Infrared Atmospheric Sounding Interferometer) <sup>b</sup>	An interferometer used to provide temperature, humidity and trace gas profiles.
<b>HIRS</b> (High resolution Infrared Radiation Sounder-4) <sup>a b</sup>	An infrared scanning radiometer, providing profiles of temperature and humidity.
<b>AVHRR</b> (Advanced Very High Resolution Radiometer-3) <sup>a b</sup>	A radiometer used for global monitoring of cloud cover and land type.
<b>MHS</b> (Microwave Humidity Sounder ) <sup>a b</sup>	A microwave radiometer that collects information on atmospheric water vapour.
<b>AMSU-A</b> (Advanced Microwave Sounding Unit A1 and A2 ) <sup>a b</sup>	A microwave radiometer for temperature sounding.
<b>A-DCS</b> (Advanced Data Collection System-2) <sup>a c</sup>	A data collection relay system.
<b>S &amp; R</b> (Search and Rescue satellite) <sup>a c</sup>	Collects distress signals and distributes these to search and rescue authorities.
<b>ASCAT</b> (Advanced SCATterometer) <sup>b</sup>	A radar which measures wind speed and direction over the oceans.
<b>SEM</b> (Space Environment Monitor) <sup>a c</sup>	A spectrometer that observes the intensity of the Earth's radiation belts.
<b>GOME-2</b> (Global Ozone Monitoring Experiment-2) <sup>b</sup>	An optical spectrometer that provides concentrations of atmospheric gases.

<sup>a</sup> Also flown on the NOAA satellites

<sup>b</sup> Instruments for observing the planet

<sup>c</sup> Communications and support services

Table 3.1: The 11 scientific instruments onboard the MetOp-A satellite, including the IASI. Further details on the other 10 instruments can be found on the EUMETSAT website: <http://www.eumetsat.int>.

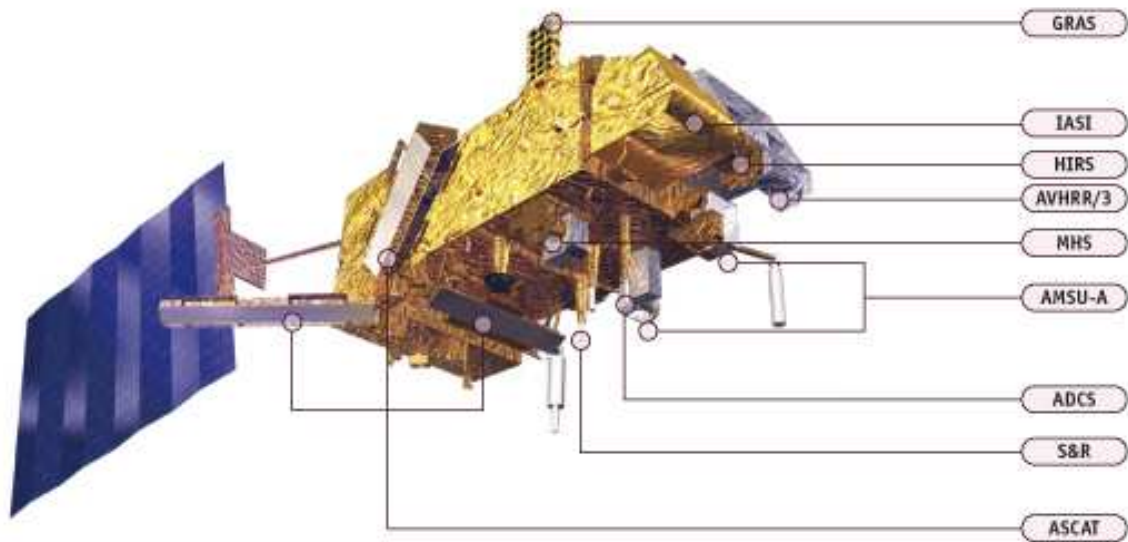


Figure 3.1: The MetOp-A Satellite and its payload. Figure taken from <http://www.eumetsat.int>. Not shown in this diagram are the GOME-2 and SEM instruments.

data from the NOAA satellites also being received and processed here. Operational level 1, as well as some level 2 products from the satellite data, are derived at the EUMETSAT headquarters, with the data and products being distributed to the users via the EUMETCast system, EUMETSAT’s broadcast system for environmental data. The delivery timeliness are between 135 and 180 minutes after the time of measurement, according to the level of processing. This whole downstream process, from the MetOp-A satellite to the user, is illustrated in Fig. 3.2. MetOp data is also available from EUMETSAT’s online archive, UMARF.

### 3.3 Details of the IASI Instrument

A summary of the main characteristics of the IASI instrument is given below; for a full description of the instrument see e.g. Blumstein et al. [2004]; Clerbaux et al. [2009]; Camy-Peyret and Eyre [1998]; Siméoni et al. [1997]; Chalon et al. [2001]; Phulpin et al. [2007]. IASI is a nadir viewing instrument flying operationally on the MetOp-A satellite, and which will operate also on the two subsequent satellites of the MetOp



Figure 3.2: The geometry of the EPS ground segment. Figure taken from <http://www.eumetsat.int>.

programme; the resulting record of spectrally resolved radiances should therefore span at least 15 years. IASI is composed of a Fourier Transform Spectrometer (FTS), and an associated Integrated Imaging Subsystem (IIS). The IIS enables accurate collocation between IASI and other MetOp sensors; it covers the IASI Effective Fields Of View (EFOV) with 6464 pixels, providing sub-kilometre spatial resolution at the sub-satellite point, and has a single channel over the 10.3 to 12.5  $\mu\text{m}$  IR region. When this thesis refers to the IASI instrument, it is referring to the FTS instrument alone.

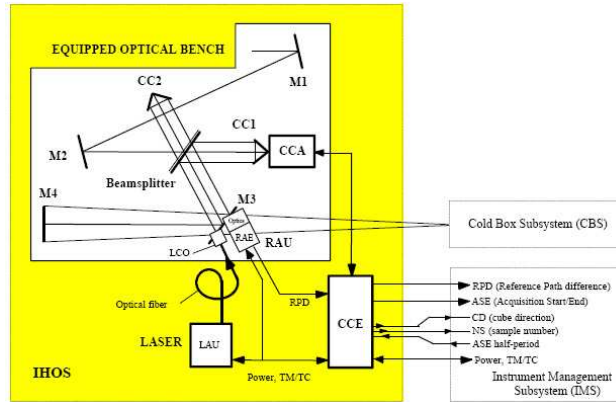


Figure 3.3: Block-diagram of the IASI interferometer. Figure taken from Henault et al. [1998].

### 3.3.1 Fourier Transform Spectroscopy

Fourier transform spectroscopy is a measurement technique whereby interference signals are collected based on the coherence of split radiation from the same source. The main advantages of an FTS compared to other techniques (e.g. a grating spectrometer or filter radiometer) are: the multiplex advantage in the Thermal Infra Red (TIR), i.e. the ability to make simultaneous measurements of a broad spectral region using a single detector; an instrument spectral response function which is a well-known function of measurable instrument parameters; and a highly accurate spectral calibration.

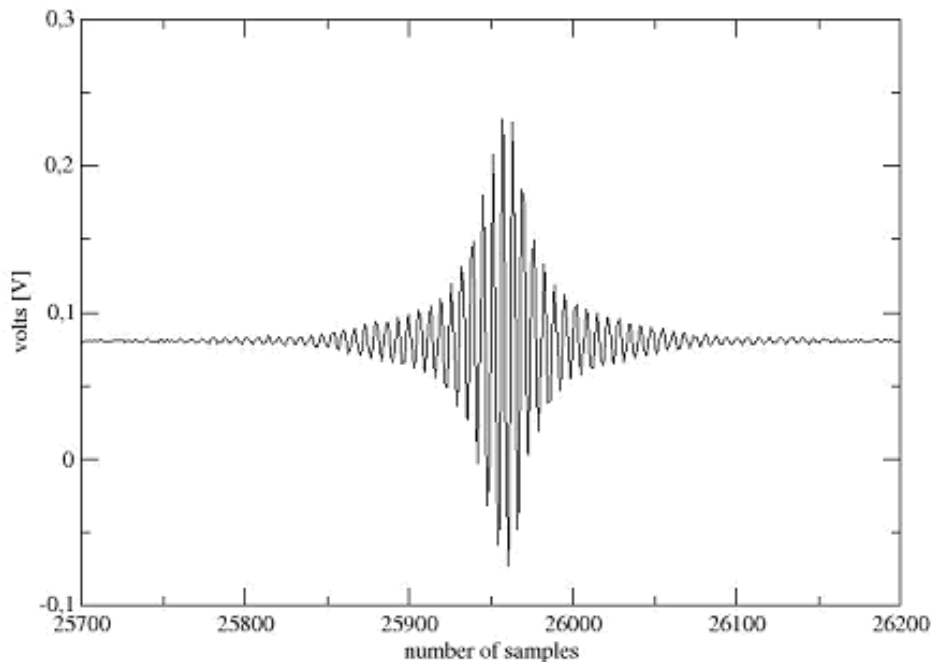
The principal mechanism of the IASI instrument is the Interferometer and Hot Optics Subassembly (IHOS) shown in Fig. 3.3. The IHOS is essentially a Michelson interferometer, but which uses hollow corner-cube retro-reflectors (CC) instead of flat mirrors, in order to create a modulated interferogram which will be recorded by a cooled focal plane array. The detected radiation enters the IHOS and is reflected by mirrors M1 and M2 onto CC1. The radiation then reaches a beam splitter, with half of the radiation being transmitted to the fixed retro-reflector CC2, and half of the radiation being reflected back to CC1; hollow corner-cube retro-reflectors are preferred to flat mirrors as they reduce the effects of stray radiation from the beam splitting. The two beams of radiation are then reflected from CC1 and CC2 towards mirror M3, where an Optical Path Difference (OPD) between the two beams has now been

introduced, by using a driving mechanism (CCA) controlled by an electronic module (CCE), to axially displace CC1. The beams are then reflected by mirror M4 into the optics detector. The energy of the beams when they recombine on the detector varies with the OPD, being at a maximum when the OPD is an even multiple of the wavelength of the incident radiation (the two beams are in phase), and zero when the OPD is an odd multiple of the wavelength of the incident radiation (the two beams destructively interfere with one another). As CC1 moves with an approximately constant speed, the energy on the detector will thus vary with time; this time varying signal that is received by the detector is called an interferogram. An interferogram, such as that shown in Fig. 3.4, is the Fourier Transform (FT) of the input radiation spectrum, and so by applying a mathematical inverse FT to the interferogram, the spectrum of the input radiation is produced. CC1 is being constantly driven by CCA, and in order to calculate the exact speed at which CC1 is travelling, and hence the time dependence of the interferogram, a Reference Laser Source (RLS) is used to generate a reference path difference. This RLS is a frequency controlled laser diode, operating at an emission frequency of  $1.56\ \mu\text{m}$ , which corresponds to an absorption line of  $\text{C}_2\text{H}_2$ . The IHOS has a Maximum Path Difference (MPD) of  $-2$  to  $2\ \text{cm}$ , with a spectral sampling of  $0.25\ \text{cm}^{-1}$ , and a spectral range of  $645$  to  $2760\ \text{cm}^{-1}$ , which is split into three overlapping bands ( $645$  to  $1240\ \text{cm}^{-1}$ ,  $1200$  to  $2040\ \text{cm}^{-1}$ , and  $1960$  to  $2760\ \text{cm}^{-1}$ ).

### 3.3.2 Viewing Geometry

The IASI instrument utilises a step by step scanning mirror to achieve a swath width of  $2200\ \text{km}$ , and twice daily global coverage ( $\sim 99\%$ ). The optical axis of the scanning mirror moves from  $-48.3^\circ$  to  $48.3^\circ$  w.r.t. the nadir, and the viewing geometry of the IASI instrument is shown in Fig. 3.5. As IASI moves forward in its orbit a scan line is made of 30 EFOV. Each EFOV consists of a matrix of  $2 \times 2$  IFOVs (Instantaneous Field of View), each with a diameter of  $0.84^\circ$  ( $11\ \text{mrad} \leq d \leq 14.65\ \text{mrad}$ ) and with centres located at  $15.3\ \text{mrad}$  ( $0.88^\circ$ ) from the instrument optical axis (see Figs. 3.6 and 3.7). On the ground the EFOV is  $50\ \text{km}$  by  $50\ \text{km}$  at nadir, and the distance between two EFOV is approximately  $50\ \text{km}$ . Each cell of the  $2 \times 2$  matrix corresponds to a circular pixel of  $12\ \text{km}$  diameter at the sub-satellite point, and at the edge of the

### First IASI Interferogram



METOP A: Orbit 552; 27/11/2006, 13:13:07.086 UTC; Band 3, Pixel 1, Cold Space View

Figure 3.4: One of the first raw interferograms in orbit which was received by the EUMETSAT Ground Segment on 27 November 2006. Figure taken from <http://smc.cnes.fr/IASI>.

scan the across-track and along-track sizes of the individual pixel are 39 km and 20 km respectively, with each of the 4 simultaneously imaged pixels utilising its own detector.

The scan starts on the left side with respect to the flight direction, and each scan line takes 8 sec to complete, during which time IASI makes 37 independent measurements: 30 Earth views, 2 cold space views, 2 black body views and 3 which remain unused. These views are at equally spaced time intervals of  $8/37$  sec (216 m sec), with an interferogram acquisition time of 151 m sec. The step-by-step scanning of Earth views is corrected by satellite velocity compensation, so that the position of the IFOV at ground does not move during the interferogram acquisition time.

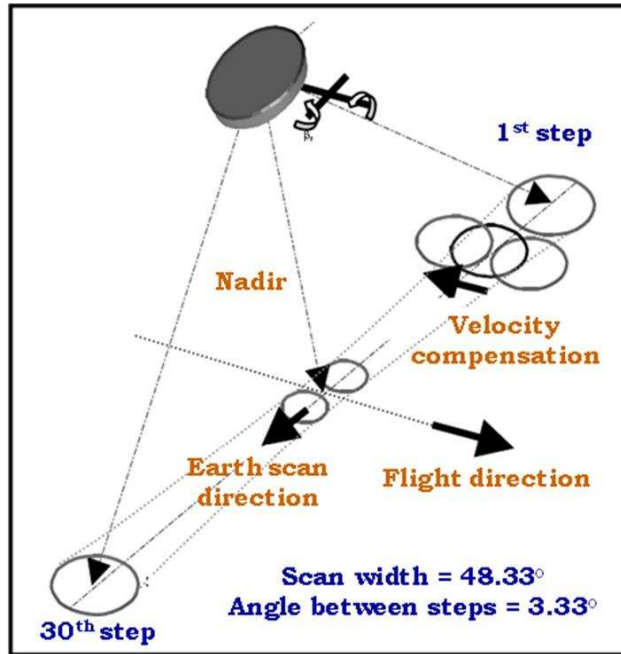


Figure 3.5: The viewing geometry of the IASI instrument: the instrument measures the TOA infrared radiation, from a low altitude sun-synchronous orbit, over a swath width of  $\sim 2200$  km, every 50 km at nadir (with 4 footprints of 12 km in diameter). Figure taken from Siméoni et al. [2004].

### 3.3.3 Detectors and Spectral Ranges

The full spectral range of the IASI instrument extends from  $645$  to  $2760\text{ cm}^{-1}$  ( $15.5$  to  $3.6\text{ }\mu\text{m}$ ), with this range having been chosen because it includes: the  $15\text{ }\mu\text{m}$   $\text{CO}_2$  absorption band which is used for temperature profile retrievals; the  $9.6\text{ }\mu\text{m}$   $\text{O}_3$  absorption band; the strong water vapour  $\nu_2$  absorption band; and up to the edge of the TIR in the  $\text{CH}_4$   $\nu_3$  absorption band. This spectral range is made up of three bands, which are separated by dichroics (colour filters), and the characteristics of these bands are given in Table 3.2.

## 3.4 Radiometric Calibration

Radiometric calibration is the process by which physical units are attributed to the raw spectrum as derived from the measured interferogram, using measurements of

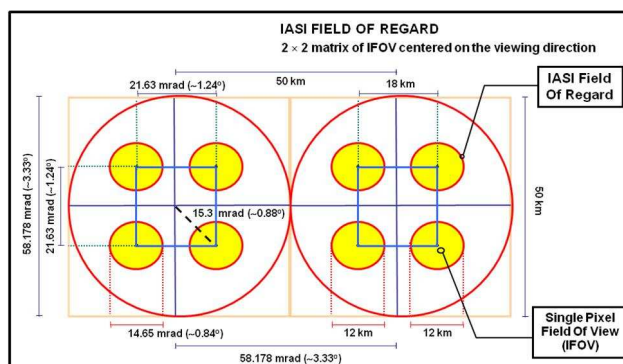


Figure 3.6: The IASI field of regard (EFOV), relative to the sub-satellite position. Figure taken from <http://ga.ifac.cnr.it/>.

Band	Spectral Range ( $\text{cm}^{-1}$ )	Type
1	645 to 1210	HgCdTe photoconductor
2	1210 to 2000	HgCdTe photovoltaic
3	2000 to 2760	InSb photovoltaic

Table 3.2: The three spectral bands measured by the IASI instrument.

well-defined targets. To calibrate radiometrically the spectra generated by the IASI instrument, two separate sets of measurements are made, the first from an internal calibration black body, and the second from deep space where the radiance emission is negligible. These two measurements are necessary to determine the effective gain and offset of the instrument.

Offset information is derived from the 2 cold space views that are made during every scan by the IASI to determine the instrument's offset value, that is the contribution of the measured signal which can be attributed to the self-emission of the instrument. The gain measurements are derived from the 2 black body views that are made during every scan of the internal black body, which has a temperature of between 290 and 295 K (Denis Blumstein, personal communication, 2010); like the offset measurements, these are made during every scan along the IASI track.

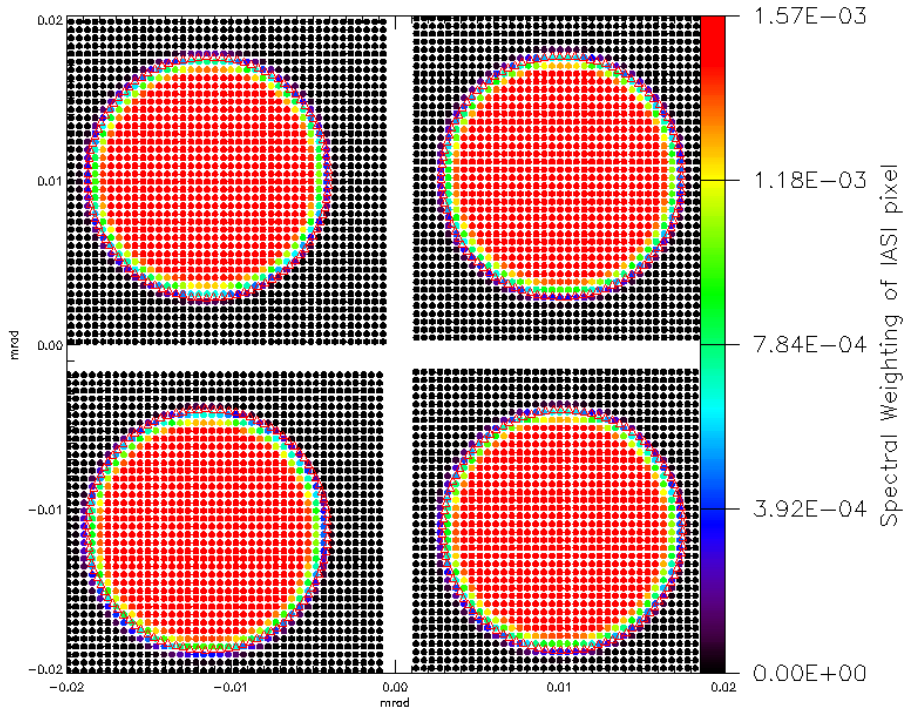


Figure 3.7: Each IASI EFOV is made up of four IFOV. The IFOV diameter is defined so that the integral of the Point Spread Function (PSF) over the circular area (red triangles) is larger than 95 %, and it can be seen that the non-uniformity within the inner 80 % of the IFOV is not larger than  $\pm 5 \%$

### 3.4.1 Noise Equivalent Spectral Radiance

In order to successfully retrieve trace gases from atmospheric measurements a large SNR is required, so that the results are not limited by random noise errors. The sensitivity of the IASI to noise can be expressed in terms of the Noise Equivalent Spectral Radiance (NESR), which is defined as the Root Mean Square (RMS) noise of a given measurement, expressed in units of radiance. The noise can also be defined in terms of the Noise Equivalent Delta Radiance ( $NE\Delta R$ ), which in a thermal imaging system is defined as the change in radiance that yields a SNR of unity. The  $NE\Delta R$  is often given in terms of the Noise Equivalent Delta Temperature ( $NE\Delta T$ ), which is converted from  $NE\Delta R$  at a given reference temperature. The IASI level 1c spectra obtained so far are of a high radiometric quality, with [Clerbaux et al., 2009] reporting a current in-flight  $NE\Delta T$  (at 280 K) of less than 0.2 K observed for wavenumbers

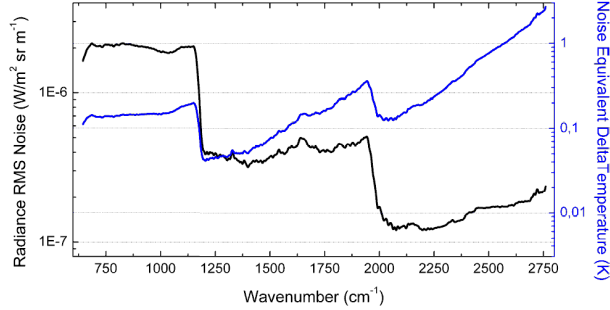


Figure 3.8: The IASI NESR and NE $\Delta$ T, as established from a set of representative spectra covering a wide range of latitudes. The NE $\Delta$ T were converted at a reference temperature of 280 K. Figure taken from Clerbaux et al. [2009].

lower than  $2200\text{ cm}^{-1}$ , except for the spectral region between  $1800$  and  $2000\text{ cm}^{-1}$ , where the NE $\Delta$ T is nearer to  $0.3\text{ K}$ . These values are illustrated in Fig. 3.8, which also demonstrates how the NE $\Delta$ T is well below  $0.1\text{ K}$  between  $1150$  and  $1500\text{ cm}^{-1}$ , and starts to increase above  $2500\text{ cm}^{-1}$ , where the signal from the TIR emission is weaker. In comparison to the preflight specifications, and ground-based calibration assessments (see e.g. Blumstein et al. [2004]), these radiometric performances are an improvement by approximately a factor of two.

### 3.4.2 Instrument Line Shape

An important factor when using instruments for the remote sensing of the Earth’s atmosphere is the spectral response that the instrument itself imposes on the observed atmospheric spectrum. For a FTS such as the IASI, the spectral response is defined by the Instrument Line Shape (ILS) of the instrument. The ILS is a polynomial function that describes how the instrument “sees” a spectral line of negligible width. For the IASI instrument, the main contributor to the ILS is the MPD between the two mirrors of the IHOS, with a longer MPD resulting in an ILS of narrower width. Other contributors to the ILS include the finite optical resolution of the instrument, and also any misalignment of the optical components. The level 1c ILS for the IASI instrument is shown in Fig. 3.9(b), and it can be seen to extend over a wide wavenumber range; Fig. 3.9(a) shows a truncated  $1\text{ cm}^{-1}$  wide apodised IASI ILS.

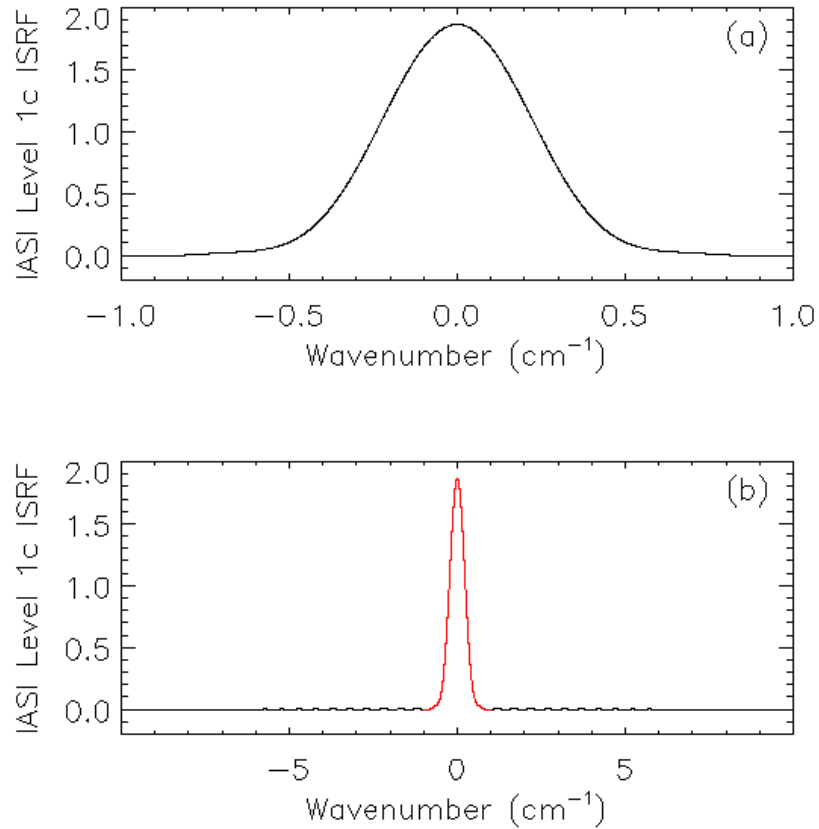


Figure 3.9: (a) The modified ( $1 \text{ cm}^{-1}$  wide) IASI ILS; and (b) The ILS for the IASI instrument, as provided by the EPS (black), and the modified ILS (red).

As discussed in Sec. 3.3.1, the spectral resolution is driven by the FTS MPD, which ranges from  $-2 \text{ cm}$  to  $2 \text{ cm}$ . This leads to a spectral resolution (FWHM) varying between  $0.35$  and  $0.5 \text{ cm}^{-1}$  depending on the wavelength. The level 1c products used in this thesis are apodised by a Gaussian function of  $0.5 \text{ cm}^{-1}$  FWHM; thus the apodised spectral resolution of IASI is considered to be  $0.5 \text{ cm}^{-1}$ . The processing that occurs between level 1B and level 1C also corrects for differences in the ILS between the four IASI IFOV.

## 3.5 Summary

This chapter has given a general overview of the ESA and EUMETSAT MetOp mission, as well as a description of the IASI. The large spatial and spectral sampling and high resolution of the IASI instrument make it ideal for making measurements in the TIR, where CO absorption takes place. A discussion of both the spectral and the radiometric calibration of the IASI have been given, as relevant to this thesis, and it is apparent that the IASI instrument is well set up to make measurements of a sufficient accuracy, and over such a time-scale as to allow for the observations of real climate trends. Chapter 4 presents a study of the radiometric accuracy of the IASI instrument, which must be well characterised in order for a meaningful retrieval of atmospheric concentrations from the TOA measured radiances, as will be discussed more fully in Chapter 5.

# Chapter 4

## Intercomparison of integrated IASI and AATSR calibrated radiances at 11 and 12 $\mu\text{m}$

### 4.1 Introduction

The purpose of this thesis is to determine the suitability of the IASI instrument to make observations of atmospheric CO from space. As was discussed in Chapters 2 and 3, the IASI instrument makes measurements of TOA radiances, and it is from these measurements that information about the composition of the atmosphere can be retrieved, as will be shown in Chapter 5. It is therefore important to determine the radiometric accuracy of the IASI instrument, as in order for a meaningful retrieval of atmospheric CO, it is important that the accuracy of the raw TOA radiances are themselves well characterised.

This chapter presents a study into the radiometric accuracy of the IASI TOA measured radiances, by performing an intercomparison with a set of accurate and well defined radiance measurements from another space-borne instrument. In order for such an intercomparison to be worthwhile, it is important that the measurements to be compared with achieve the following criteria: well defined and high radiometric accuracy; temporal and spatial coincidence with IASI measurements; and a high spatial resolution (i.e. one which is significantly more resolved than IASI), for reasons

which will become apparent in the discussion of the methodology (Section 4.3). Two instruments which satisfy these criteria are the AATSR onboard Envisat, and the AVHRR flown on MetOp-A.

The major limitation with the AVHRR data is that it is limited to accuracies of approximately  $\sim 1$  K due to dependencies on scene temperature and scan angle. In order for these accuracies to be improved upon, corrections via IASI (which would be circular in this case) or through a reference model would be required, and even then a significant improvement in the accuracies will only be observed at the sub-satellite point [Mittaz and Harris, 2009]. For these reasons, and for those discussed in Sec. 4.2, which presents a description of the AATSR instrument, the AATSR has been chosen as the instrument for performing an intercomparison with the IASI measured radiances. Section 4.3 describes the cross-calibration technique used to radiometrically calibrate the IASI instrument, and presents the results of this process, and Sec. 4.4 concludes the intercomparison of the IASI and AATSR at 11 and 12  $\mu\text{m}$ .

As was discussed in Sec. 1.7.3, it is the IASI TOA radiances in the 4.7  $\mu\text{m}$  spectral window that will be used in the retrieval of atmospheric CO information. The original scientific aim of the IASI instrument was to obtain a radiometric accuracy of 0.5 K [Camy-Peyret and Eyre, 1998], but as will be shown in Chapter 5, this degree of accuracy will result in large uncertainties in the retrieved CO product. One limitation in using the AATSR instrument to perform an intercomparison study with the IASI measured radiances is that it does not have a channel that is suitable for comparison at the 4.7  $\mu\text{m}$  spectral region. Because of this limitation, careful consideration is needed in determining how the intercomparison relates to the radiometric accuracy of IASI at 4.7  $\mu\text{m}$ ; Sec. 4.5 discusses the internal radiometric calibration of the IASI instrument in relation to the work presented here, and that of other studies, in order to ascertain the radiometric accuracy of IASI in this spectral region.

## 4.2 AATSR

The AATSR, on Envisat, is used in this study as the reference inter-comparison instrument; the Envisat equator crossing time is 10:00 LST. The AATSR is a dual-view, scanning radiometer with a 1  $\text{km}^2$  footprint for the nadir view at the sub-satellite

point. It has seven channels, including three thermal channels: the two split-window channels at 11 and 12  $\mu\text{m}$ , and a third infrared channel at 3.7  $\mu\text{m}$ , which is only used at night as it is contaminated by reflected solar radiation during the day. Due to the channel at 3.7  $\mu\text{m}$  not providing both day and night data, and also because the full AATSR bandpass for this channel does not fall completely within the IASI spectral range (3.6 to 15.5  $\mu\text{m}$ ), only the nadir-view AATSR data in the 11 and 12  $\mu\text{m}$  channels are considered in this study. More details about the AATSR instrument are given in e.g. Llewellyn-Jones et al. [2001]; Smith et al. [2001]; ESA [2008].

The AATSR instrument uses a very stable on-board calibration system for its infrared channels, resulting in a high intrinsic radiometric sensitivity and accuracy. Two targets (“hot” and “cold” at approximately 305 K and 265 K, respectively) are viewed every scan for calibration, and the detectors are cooled to 80 K by a Stirling Cycle cooler to ensure that the radiometric noise of these channels at 270 K is  $< 0.05$  K. The AATSR is radiometrically calibrated to a high accuracy; pre-launch calibration using high-accuracy external black bodies indicated that the AATSR Brightness Temperatures (BTs) were within 30 mK of target temperatures for the 11 and 12  $\mu\text{m}$  channels [Smith et al., 2001]. The heritage of the instrument design is well proven since AATSR is the third instrument (for results for radiometric design and accuracy of the earlier Along-Track Scanning Radiometer-1 (ATSR-1) and Along-Track Scanning Radiometer-2 (ATSR-2) instruments see e.g., Mutlow et al. [1994]) founded on well-designed black bodies for radiometers [Mason et al., 1996]. During the time frame of this work it emerged that the spectral response function of the AATSR’s 12  $\mu\text{m}$  channel was potentially not as well characterised as expected resulting in additional BT uncertainties of 0.2 K; the analysis in this chapter is consistent with this concern.

## 4.3 Cross Calibration of IASI and AATSR

### 4.3.1 Overview of Concept

Sensor radiometric calibration involves well-known processes such as pre-flight calibration, on-board calibration and, in the case of optical sensors, vicarious calibration against well-known targets, with all of these approaches being well documented [e.g,

Dinguirard and Slater, 1999]; for the TIR, pre-flight and on-board calibration are also standard. However the cross-calibration of satellite instruments against “well-known” targets has proved to be more of an issue, because scene temperature and atmospheric state variability are critical parameters, and a mismatch in time (for example), can cause significant differences in observed TOA radiances. Further issues arise because of different spectral filter functions and differing views of the instruments to be compared. Some of these issues have been examined, for example, by Merchant et al. [2003], who developed radiance correction factors for the Visible Infrared Spin-Scan Radiometer (VISRR) on-board the Japanese Geostationary Meteorological Satellite (GMS-5), using equivalent data from the ATSR-2 instrument. The study presented in this chapter compares the IASI and AATSR instruments. Particular attention is given to how well such a comparison can be carried out by focussing on the intercomparison for surfaces with well understood characteristics, in a manner analogous to the vicarious calibration of visible sensors.

### **4.3.2 Cross-calibration Match-ups**

TIR TOA radiances vary strongly with wavelength, surface temperature and emissivity, atmosphere temperatures, atmosphere composition (particularly humidity), and clouds. Therefore, for the most accurate intercomparison of radiances, it is ideal to consider surfaces of largely uniform emissivity, close matches in time and space, and similar view angles. These factors are now considered in turn. Since thermal emission at 11 and 12  $\mu\text{m}$  does not substantially change its characteristics diurnally, both day and night data are used in the comparison.

The AATSR thermal channels at 11 and 12  $\mu\text{m}$  are designed to be able to determine surface temperature, particularly over the oceans, with very good accuracy. For the present purpose, scenes with both a uniform surface emissivity and small changes of surface temperature with time are ideal. Oceans satisfy both criteria in general (rather than land), and thick clouds may at least satisfy the first criterion but quite possibly the second. Therefore, this work focusses firstly on clear sky ocean scenes and subsequently considers results for cloudy scenes (see Sect. 4.3.4 for the classification system) over the ocean. Surface temperatures (and cloud fields) change more rapidly over land than ocean, and the radiance is more view angle dependent over land, thus

precluding the use of land data for accurate radiometric calibration work.

In order for a very good cross-calibration to be performed, the measured BTs for both instruments need ideally to be taken from the same geographic location (co-located view), and measured at similar times. The AATSR achieves global coverage approximately once every three days, with a repeat cycle of 35 days [ESA, 2008]. In comparison IASI achieves twice daily coverage with a 29 day repeat cycle [Clerbaux et al., 2009]. As the two instruments have equator crossing times that differ by on average half an hour, there will be some measurements where the two orbits become coincident at approximately the same time. Figure 4.1 shows that on 1 September 2007 the views of the two instruments coincided on both a spatial and temporal scale.

Considering the temporal domain, the match ups were limited to only those occurring within 30 min, in order to limit the possibility that the cloud scene will have changed between the IASI and AATSR views of the same scene. Thirty minutes was chosen as a threshold value in order to give a reasonable time constraint allowing match-ups, whilst ruling out the vast majority of cloud formation in the very homogeneous ocean scenes chosen for analysis. This threshold difference is similar to that adopted by Merchant et al. [2003], who applied a mean time difference between two co-located satellite data sets of 24 min.

In nadir mode the AATSR instrument scans between  $\pm 21.433^\circ$ , whilst the IASI instrument makes measurements with viewing angles ranging from  $-48.3^\circ$  to  $48.3^\circ$  across the swath. A difference in the viewing angles between the measurements made by the two instruments will introduce an offset, caused by the different atmospheric path lengths that radiation from the measured scene must travel to the detector. This offset will principally depend on the amount of water vapour in the atmosphere: for a polar winter, this difference could be close to zero, whereas for a large angular difference in a tropical atmosphere, this difference could be as much as 0.4 K at  $12 \mu\text{m}$  [Noyes, 2005]. Due to this offset, only match-ups where the absolute difference of the satellite zenith angles is less than  $1^\circ$ , and where the absolute satellite zenith angles themselves are less than  $15^\circ$ , are considered.

Having defined the match-ups between the IASI and AATSR data sets, the IASI spectrally resolved TOA radiances were integrated to “AATSR-like” radiances, and then converted to radiometric BTs, which are the equivalent form of the AATSR TOA

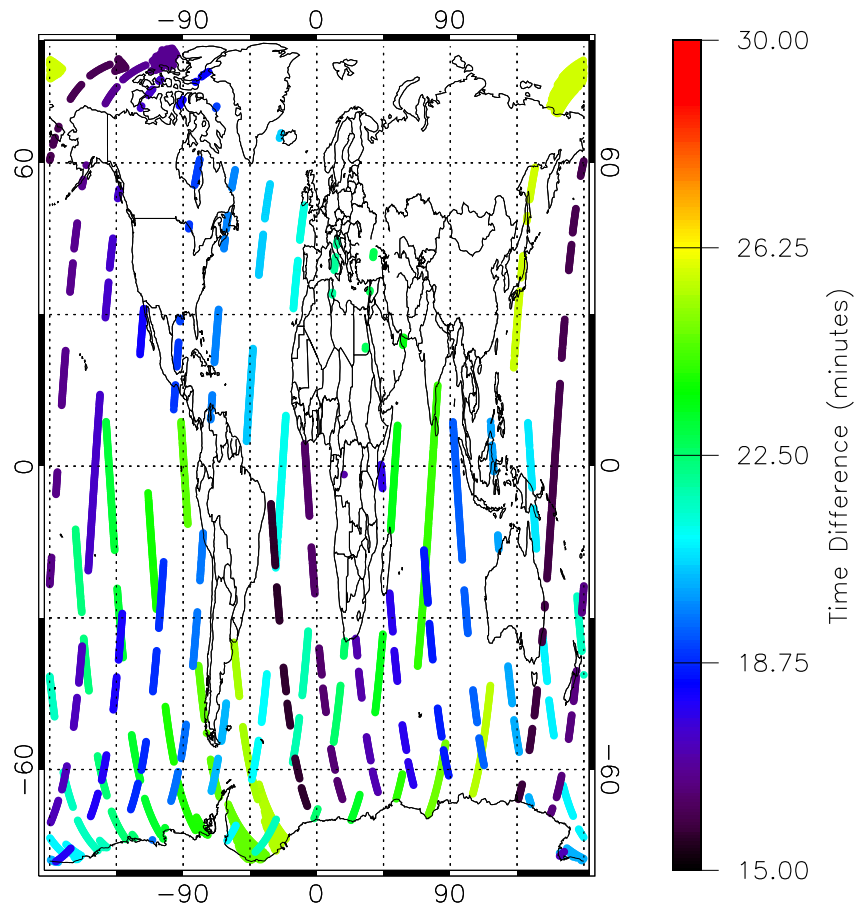


Figure 4.1: Temporal and spatial coincidences for the IASI and AATSR instruments on 1 September 2007. Only measurements which are temporally coincident within 30 minutes, which have absolute satellite zenith angles of less than  $15^\circ$ , and an absolute difference in the satellite zenith angles of less than  $1^\circ$  are shown.

radiances. The AATSR spectral filter functions for the  $11$  and  $12\ \mu\text{m}$  channels are shown in Fig. 4.2, in comparison to a typical IASI measurement of spectral radiance. For the selected regions, the mean and standard deviation of the AATSR BTs within each IASI pixel were then calculated. The standard deviations are subsequently used to illustrate the homogeneity of the scenes, and for the cloud scenes to perform a cross-calibration consistent with the clear sky comparisons (see Sec. 4.3.3).

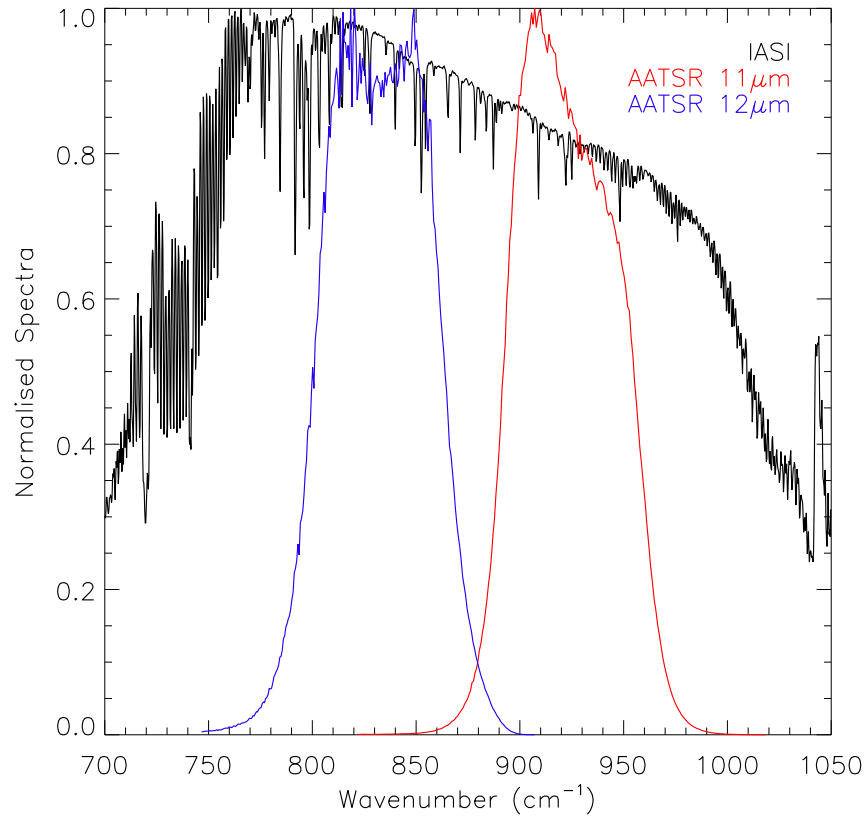


Figure 4.2: Spectral filter functions for the 11 and 12  $\mu\text{m}$  channels for the AATSR on Envisat [ESA, 2008], in comparison to a typical IASI spectral measurement. The broad background is governed by sea surface temperature, clouds, aerosols, and broad trace gas continua, whereas the sharp lines are entirely due to trace gases in the atmosphere.

### 4.3.3 Flags for Homogeneity

Further classification was performed using the flags associated with the AATSR land and cloud masks, since the AATSR instrument has a higher spatial resolution than the IASI. The land filters of the AATSR data set within each IASI coincident view were used to separate the match-ups into different sub-groups which could be further analysed. IASI pixels containing only “land” AATSR pixels were assumed to have been taken over the land, whilst those containing only “sea” AATSR pixels were

assumed to have been taken over the sea; for reasons outlined in Sec. 4.3.2 land pixels were not subsequently used in the analysis. Any IASI pixels which were deemed as being over both land and sea (such as a coastline) were also discarded, as they were too few in number to draw any significant statistical conclusions from.

The clear sky scenes were identified quite conservatively. The AATSR contains a detailed cloud-filtering system which labels each AATSR pixel as being either “clear sky” or “cloudy”; the cloud processor is described in Zavody et al. [2000]. This was then used to perform an initial classification of the scene into clear and cloudy scenes. A 100 % clear set of flags was required for a clear scene and 100 % cloud flags was required to identify fully-cloudy scenes. The clear scenes were further filtered to ensure homogeneity by insisting that there were no outliers in the AATSR BTs that were more than three sigma from the mean AATSR BT for that IASI scene. A final test was performed to assess even more rigorously the cloudiness of the scene. For each IASI pixel, a cluster flag is provided which indicates the degree of homogeneity of the scene as identified by coincident AVHRR-3 (onboard MetOp-A) observations. The criterion employed here is that the AVHRR cluster flag should be set to 1, indicating a fully homogeneous scene.

The clear sky comparisons for any given day are limited in their temperature range. However, the real criterion for conducting a comparison is a uniform scene rather than requiring the scene to be free of clouds. Therefore, the comparisons were extended to include fully-cloudy pixels. The approach that was adapted is similar to that for clear sky, except that the maximum standard deviation observed for the clear sky match-ups was applied as a limit to variations on AATSR BTs within each fully-cloudy IASI pixel. The order of filtering invoked was therefore: AATSR cloud flags (100 %); limit of the maximum AATSR BT standard deviation observed within one IASI clear sky pixel on a given day; three sigma intra-pixel AATSR BT test; and AVHRR cluster flag set to 1 for each IASI pixel. The fully-cloudy results could then be analysed separately or combined with the clear sky data.

#### **4.3.4 Cross-calibration Results**

To date, four days with good AATSR and IASI overlaps have been analysed: 13 August 2007, 1 September 2007, 5 March 2008, and 9 May 2008. Figures 4.3 and

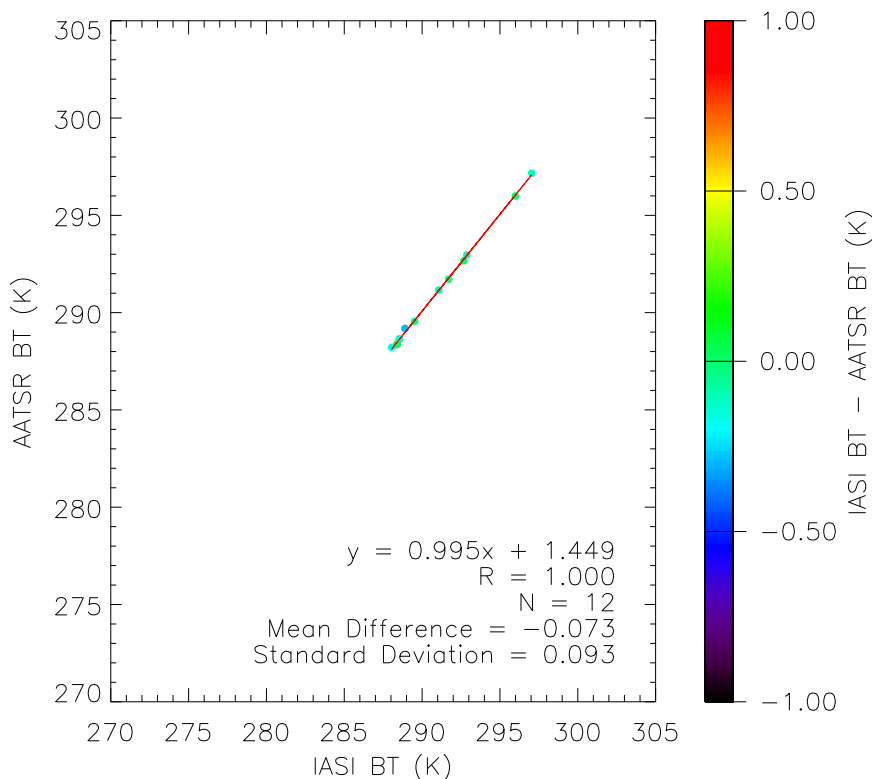


Figure 4.3: Comparison of  $11\ \mu\text{m}$  IASI equivalent BTs minus mean AATSR BTs in each IASI pixel for 1 September 2007. All match-ups have been selected over the oceans and represent clear sky conditions.

4.4 show results for the cross-calibration in clear sky conditions of the  $11$  and  $12\ \mu\text{m}$  channels, respectively on 1 September 2007. These plots shows that there is a very strong correlation between the AATSR and IASI BTs, in both the  $11$  and  $12\ \mu\text{m}$  spectral regions, over a temperature range of just greater than  $10\ \text{K}$ . For the  $11\ \mu\text{m}$  spectral region, a mean IASI-AATSR BT difference of  $-0.07\ \text{K}$  can be observed compared to  $0.22\ \text{K}$  in the  $12\ \mu\text{m}$  region; it is interesting to note that by applying the more rigorous criteria outlined here produces differences of only  $0.02\ \text{K}$  at  $11\ \mu\text{m}$  and  $0.01\ \text{K}$  at  $12\ \mu\text{m}$  from the initial results of this study which were presented in Illingworth et al. [2009]. In both spectral regions, the mean BT difference is less than  $0.3\ \text{K}$ ,

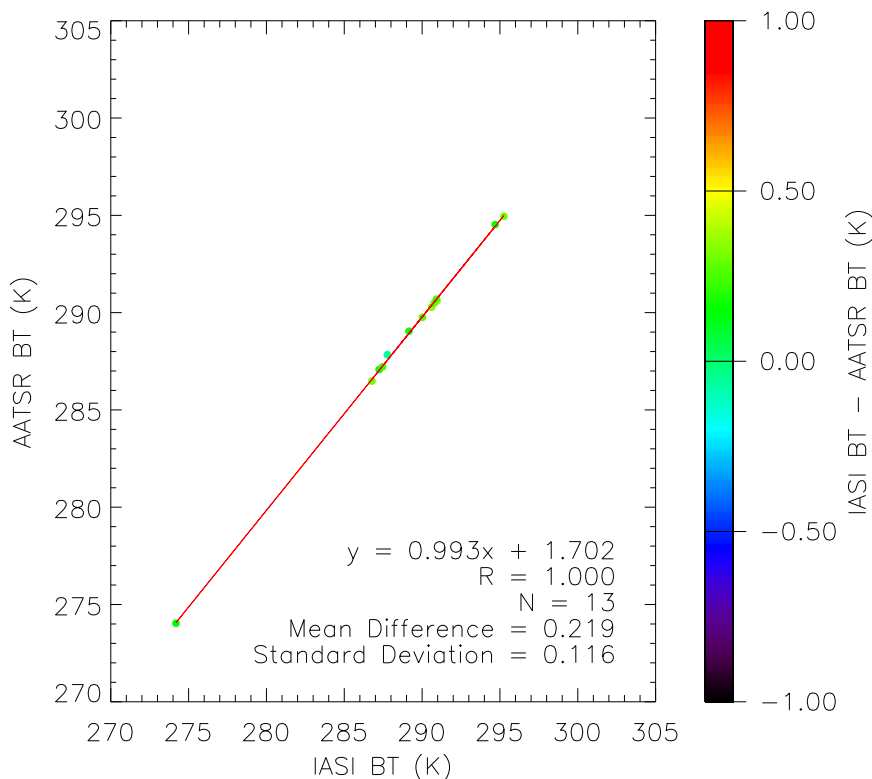


Figure 4.4: Same as Fig.4.3, but for 12  $\mu\text{m}$ .

with a small standard deviation, indicating that the IASI instrument is in agreement with the AATSR instrument to at least this level, in cloud-free scenes. Therefore the indication would be that IASI is likely to be meeting its target objective over ocean clear sky conditions. More importantly, the standard deviation on the mean for both channels is on the order of 0.03 to 0.04 K suggesting that at 11  $\mu\text{m}$ , the comparison is very good but that there is a larger and significant offset occurring at 12  $\mu\text{m}$ .

For comparative purposes, Figs.4.5 and 4.6 show the comparison of clear sky IASI and AATSR BTs at 11 and 12  $\mu\text{m}$ , respectively, for the case of no filtering in regards to the homogeneity of the scene. That is to say that neither the three sigma intra-pixel AATSR BT test, nor the AVHRR cluster flag have been applied to this data set. As can be seen from these plots, the number of coincident points is greatly increased,

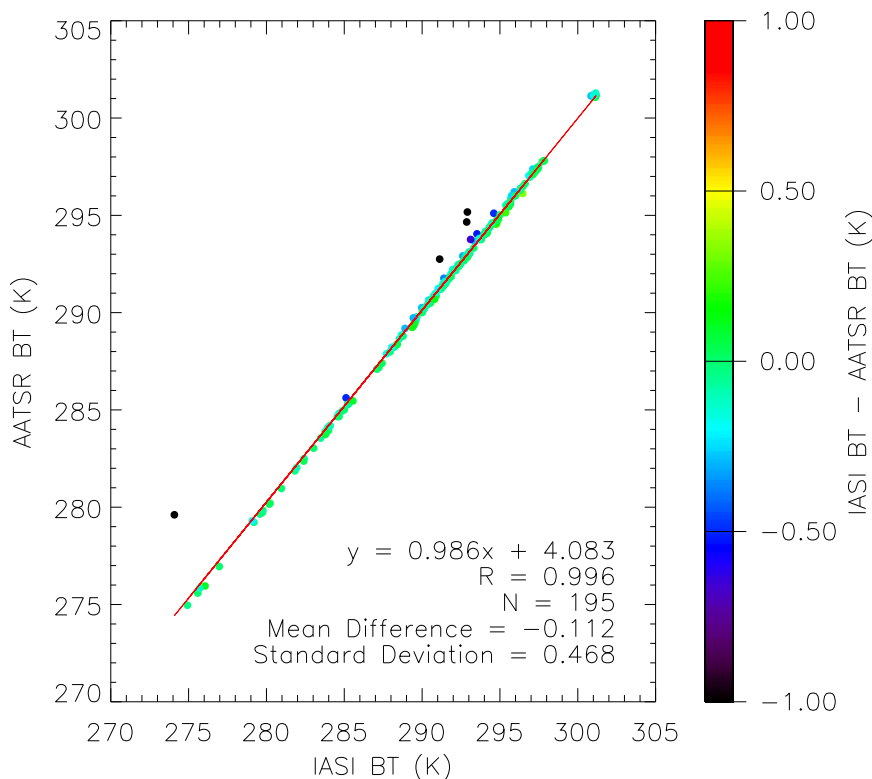


Figure 4.5: Comparison of 11  $\mu\text{m}$  IASI equivalent BTs minus mean AATSR BTs in each IASI pixel for 1 September 2007, with no filtering for inhomogeneous scenes. All match-ups have been selected over the oceans and represent clear sky conditions.

but this is offset by an increase in the standard deviation from the AMD (i.e. the spread of the data), as well as the introduction of spurious data, where the absolute AMD is much greater than 1 K. This comparison is likely to be limited by geophysical variability; by comparing Figs. 4.5 and 4.6 with Figs. 4.3 and 4.4, it is observed that the strict filtering for homogeneity discussed in Sec. 4.3.3 removes the anomalous data from the comparison, and whilst these filtering techniques are quite conservative, they ensure that reasonable conclusions can be drawn from the data.

It is also possible to look at the combination of clear sky and fully-cloudy data sets. Figures 4.7 and 4.8 show the corresponding relationships between the IASI and

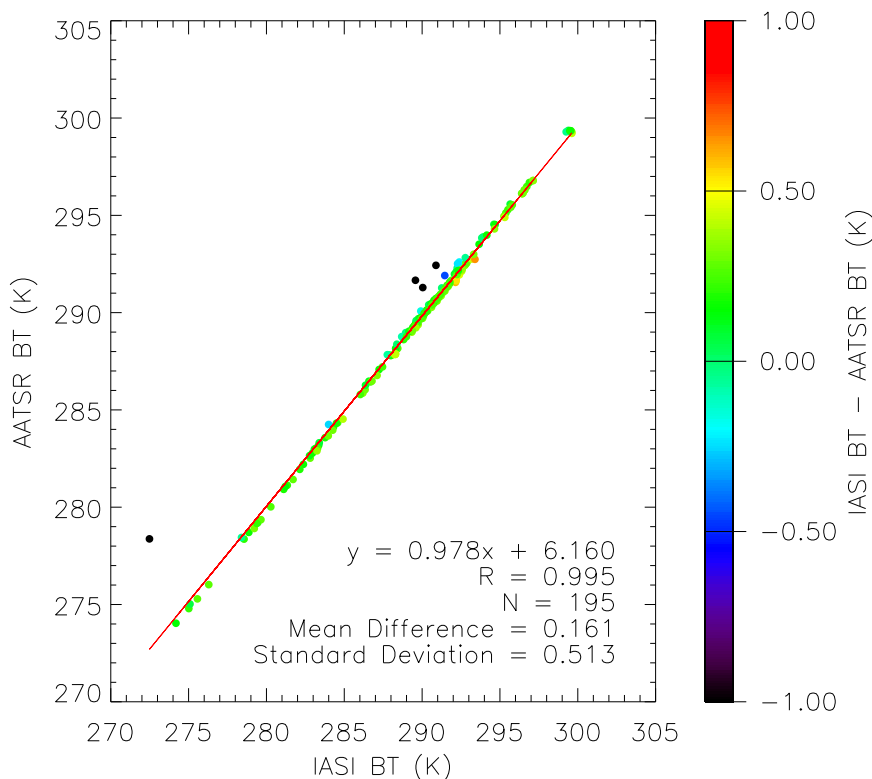


Figure 4.6: Same as Fig.4.5, but for 12  $\mu\text{m}$ .

AATSR BTs for all such data points, for the 11 and 12  $\mu\text{m}$  regions respectively, again for the 1 September 2007. It is immediately clear that the temperature range is now larger; the correlation coefficients are identical. The mean differences between IASI equivalent BTs and AATSR mean BTs for this particular day are now  $-0.08\text{ K}$  for the 11  $\mu\text{m}$  channel and  $0.34\text{ K}$  for the 12  $\mu\text{m}$  channel.

The intercomparisons for all four days are summarised in Tables 4.1 and 4.2 for 11 and 12  $\mu\text{m}$  respectively. The results show a remarkable consistency, particularly for the combination of clear sky and fully-cloudy data for which there are a larger number of matches and a wider temperature range. Absolute differences at 11  $\mu\text{m}$  are less than  $0.1\text{ K}$  for all cases, and for 12  $\mu\text{m}$  shift from approximately  $0.2\text{ K}$  for clear sky, to  $0.34\text{ K}$  for all match-ups; however one should bear in mind that the coldest

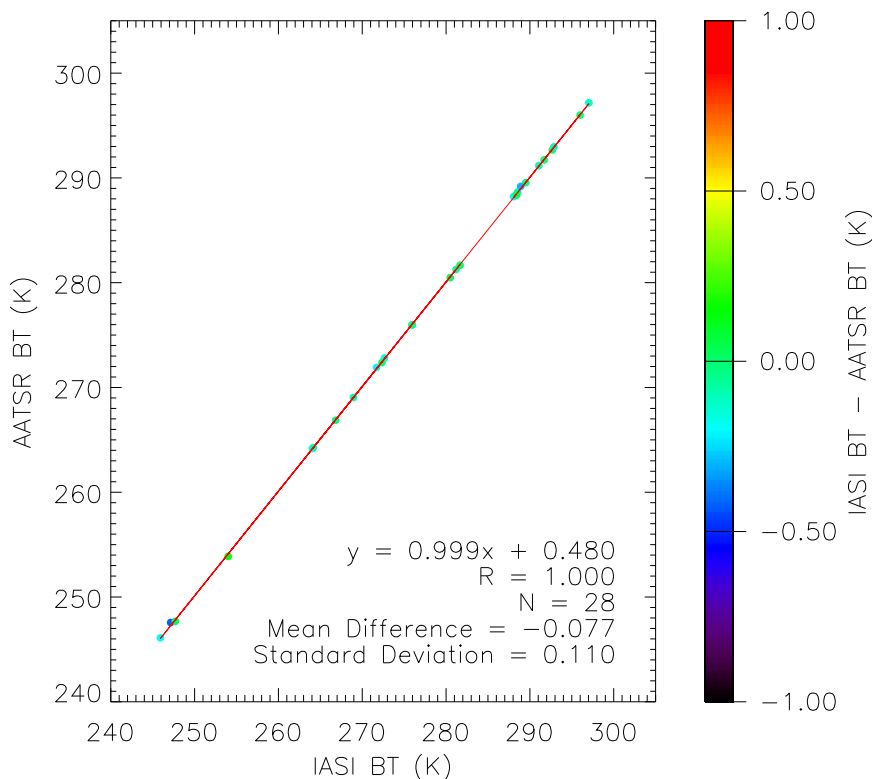


Figure 4.7: Comparison of  $11\ \mu\text{m}$  IASI equivalent BTs minus mean AATSR BTs in each IASI pixel on 1 September 2007. All clear sky and fully cloudy match-ups have been selected over the oceans and represent homogenous conditions.

cloud match-ups are slightly cooler than range for which the AATSR instrument is known to have a linear radiometric calibration, i.e. 265 to 305 K [Llewellyn-Jones et al., 2001; Smith et al., 2001].

The offset at  $12\ \mu\text{m}$  is in the same direction as the AATSR offset from ATSR-2, i.e., AATSR is cooler than IASI equivalent-BTs, thus adding to the evidence for the need for a correction to the AATSR  $12\ \mu\text{m}$  spectral response function. Based on the assumption that the AATSR is intrinsically calibrated to a radiometric accuracy of 30 mK, these results would seem to indicate that the IASI instrument is itself radiometrically calibrated to an accuracy of better than 0.1 K at  $11\ \mu\text{m}$ . At the same

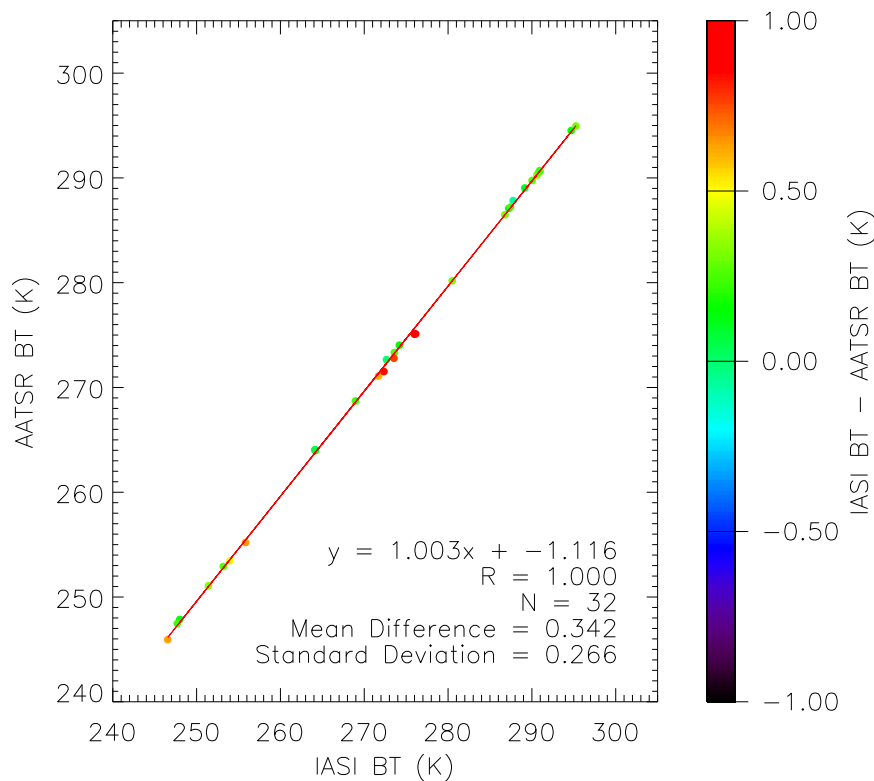


Figure 4.8: Same as Fig.4.7, but for 12  $\mu\text{m}$ .

time, the results emphasise the importance of knowledge of the AATSR spectral filter functions.

## 4.4 Conclusions From the Radiometric Comparison Results

Based on the cross-calibration results in this study, integrated IASI radiances agree very well with AATSR BTs at 11 and 12  $\mu\text{m}$ , and indicate that IASI is achieving accuracies of better than 0.1 K at 11  $\mu\text{m}$ , over the 245 to 300 K temperature range for which this intercomparison was conducted. The differences between IASI and AATSR at 12  $\mu\text{m}$  are of the same sign and magnitude as the differences between

Date	“Clear” (K)	“Clear” N	“All” (K)	“All” N
13 August 2007	-0.05 (0.11)	8	-0.05 (0.17)	19
1 September 2007	-0.07 (0.10)	12	-0.08 (0.11)	28
5 March 2008	-0.02 (0.14)	21	-0.05 (0.29)	39
9 May 2008	-0.05 (0.10)	20	-0.08 (0.16)	34

Table 4.1: AMD at 11  $\mu\text{m}$  for IASI-AATSR BTs. “Clear” refers to only clear pixels, and “All” refers to cloudy and clear pixels combined. The standard deviations relative to the AMD are given in parentheses, and **N** corresponds to the total number of measurements.

Date	“Clear” (K)	“Clear” N	“All” (K)	“All” N
13 August 2007	0.20 (0.04)	7	0.34 (0.27)	19
1 September 2007	0.22 (0.12)	13	0.34 (0.27)	32
5 March 2008	0.23 (0.17)	27	0.340 (0.420)	46
9 May 2008	0.25 (0.14)	19	0.34 (0.21)	36

Table 4.2: Same as Table 4.1, but for 12  $\mu\text{m}$ .

ATSR-2 and AATSR, i.e. approximately 0.2 K, with AATSR being cooler than the other ATSR instruments. The random component to the uncertainties on the Average Mean Difference (AMD), i.e. the standard deviation divided by the square root of the number of measurements, is relatively small (typically of the order of 0.02 K and 0.06 K for 11 and 12  $\mu\text{m}$ , respectively) and so the larger question concerns uncertainties in any bias terms. The spread of mean differences was observed to be only just consistent with the errors and so a conservative estimate of the bias uncertainty in the AMD was taken to be 0.04 K for both channels.

Despite dealing with a limited set of data (four days of AATSR-IASI measurement coincidences were analysed) the results of this study depend more on the details of the comparison and methodology so that analysis of further days, whilst valuable, is not as important as establishing a quality comparison for a small number of days. It

can be seen from the standard deviations on the mean that the random errors are already quite small for each of the four days of comparisons.

The results presented in this chapter are corroborated by a recent intercomparison study by Wang L. and Cao [2009], which used the Geostationary Operational Environmental Satellite (GOES) Imagers as transfer radiometers to compare AIRS and IASI radiances over warm scenes in the tropical regions, for a time period of 16 months. The double differences between AIRS and IASI radiance biases relative to the GOES-11 and -12 Imagers proved that, at the 95 % confidence level, the mean values of the IASI-AIRS BT differences for warm scenes are very small (typically less than 0.1 K, over the 245 to 300 K temperature range for which this intercomparison was conducted).

## 4.5 Radiometric Accuracy of IASI in the 4.7 $\mu\text{m}$ Spectral Region

By performing an intercomparison between the IASI and AATSR instruments it has been demonstrated that the IASI instrument is radiometrically accurate at 11  $\mu\text{m}$  to at worst 0.1 K. However, this intercomparison can only state anything directly quantitative about the radiometric accuracy in this spectral region, and by extension in band 1 (8.26 to 15.5  $\mu\text{m}$ ) of the IASI instrument. Channel characteristics, geometric factors (such as the effects of stray light on the instrument), and the issue of non-linearity, mean that the conclusions that have been ascertained in relation to the radiometric accuracy in band 1 of IASI, cannot simply be used to infer that for the 4.7  $\mu\text{m}$  region, which is located in third band (3.62 to 5.0  $\mu\text{m}$ ) of the instrument, and which is the region that will be used for retrieving information about the atmospheric composition of CO (see Chapter 5).

Although the radiometric accuracy of any one band of the IASI instrument does not transfer directly over to that of another band, Blumstein et al. [2004] showed that the radiometric calibration error between any 2 channels of the IASI instrument, for any scene temperature between 200 and 300 K, was  $< 0.1$  K. The on-ground calibration of the IASI instrument concluded that the “raw” (i.e. produced by onboard computation) calibration error was largely less than 0.1 K. The top plot in Fig. 4.9

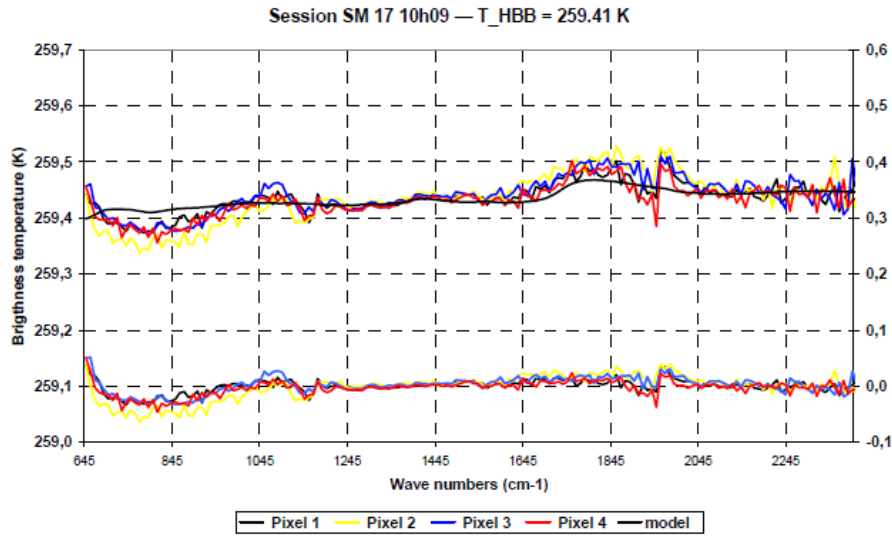


Figure 4.9: The internal radiometric accuracy of the IASI instrument. The top plot demonstrates the very good agreement between observations (pixels 1 to 4) and the model (isolated smooth curve). The bottom plot shows the differences between observations and model, scaled to 280 K; the scale for this plot is on the right of the figure. Figure taken from Blumstein et al. [2004].

demonstrates the differences observed between measured BTs and the actual temperature of the reference blackbody at a scene temperature of 259.4 K. The bottom plot in Fig. 4.9 shows that the relative accuracy between channels varies by no more than 0.1 K across the spectral range of the entire IASI instrument, with similar results being observed at a scene temperature of 299.65 K. Whilst bands 2 and 3 are believed to behave fairly linearly, band 1 of IASI requires a non-linearity correction, potentially affecting the ability to translate results from the AATSR comparisons to 4.7  $\mu\text{m}$ ; Fig. 4.9 indicates that the relation is reasonable.

The work carried out by Wang L. and Cao [2009] in comparing the radiometric performances of AIRS and IASI is in good agreement with the results presented in Sec. 4.3.4.; however, it is only able to offer quantitative information about the radiometric accuracy in bands 1 and 2 of the IASI instrument, as it did not extend into the spectral region covered by band 3. Aumann and Pagano [2008] used Real-Time, Global, Sea Surface Temperatures (RTGSST) as a transfer standard to demonstrate

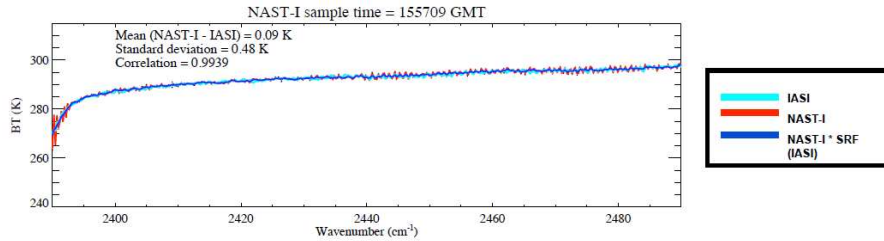


Figure 4.10: Example IR spectral radiance inter-comparisons for the 2390 to 2490  $\text{cm}^{-1}$  spectral region, showing space and time coincident NAST-I relative to measurements made in band 3 of the IASI instrument. Figure taken from Larar et al. [2010].

a 60 mK difference between the AIRS and the IASI calibration at  $2616 \text{ cm}^{-1}$  and 300 K, with a statistically nonsignificant 20 mK shift in six months, thereby establishing a similar radiometric accuracy of band 3 in comparison to band 1 for the IASI instrument. As part of the Joint Airborne IASI Validation Experiment (JAIVEx) field campaign, [Larar et al., 2010] demonstrated a mean difference between the National Polar-orbiting Operational Environmental Satellite System (NPOESS) Airborne Sounder Testbed Interferometer (NAST-I) and IASI, in band 3 of the IASI instrument of 0.09 K, thereby further indicating the relative stability of the radiometric accuracy across the entire spectral range of the IASI instrument. A typical example of an aircraft vs. spacecraft measurement from this study is shown in Fig. 4.10.

Biases across the IASI spectra may also be identified by comparing the observed data with radiances calculated from Numerical Weather Prediction (NWP) model data. Daily monitoring reports are available on the EUMETSAT website (<http://oiswww.eumetsat.org/epsreports/html/index.php?instrument=IASI>), with the available radiance monitoring comparing the IASI measurements obtained under clear sky conditions, over the sea, with modelled radiances. Whilst these daily monitoring reports are useful in determining the radiance anomaly (defined as the difference between the quarter daily average observed - modelled bias and the average bias of the last 30 days), the relative uncertainty in the modelled data means that this information cannot be used to comment on the radiometric relationship between the 3 bands of the IASI instrument to a degree of accuracy that is sufficient for this study.

To summarise, by taking into consideration the results of Sec. 4.4 and the radiometric calibration error that is introduced between any 2 channels of the IASI instrument, as well as the studies that have been carried out into the radiometric accuracy of the IASI instrument by other groups, it can be concluded that the radiometric accuracy of the IASI instrument in and around the  $4.7\ \mu\text{m}$  region is at worst 0.3 K, over the 245 to 300 K temperature range for which this intercomparison was conducted.

## 4.6 Summary

This chapter has discussed in detail work that has been carried out to demonstrate the radiometric stability of the IASI instrument. An intercomparison of the IASI and AATSR instruments found the AMD over the four days of study to be  $-0.04\ \text{K}$  and  $0.22\ \text{K}$  for the  $11\ \mu\text{m}$  and  $12\ \mu\text{m}$  channels respectively for clear sky. The random component to the uncertainties on the mean differences is relatively small (typically of the order of  $0.02\ \text{K}$  and  $0.06\ \text{K}$  for  $11\ \mu\text{m}$  and  $12\ \mu\text{m}$  respectively) and so the larger question concerns uncertainties in any bias terms. The results were consistent with a bias at  $12\ \mu\text{m}$ , most likely due to systematic error in the AATSR spectral filter function, which is currently under investigation.

The AATSR and IASI intercomparison yielded a quantitative statement about the behaviour of the radiometric accuracy in band 1 of the IASI instrument. By considering work done by other studies, and also by studying the behaviour of the radiometric accuracy across the instrument as a whole, it was concluded that around the  $4.7\ \mu\text{m}$  region the IASI instrument is radiometrically accurate to  $< 0.3\ \text{K}$ , over the 245 to 300 K temperature range for which this intercomparison was conducted. This is better than the  $0.5\ \text{K}$  originally stipulated in the IASI Science Plan and, as will be discussed in Chapter 5, has important consequences for the correct retrieval of an atmospheric CO product from IASI TOA radiances.

# Chapter 5

## The University of Leicester IASI Retrieval Scheme (ULIRS)

### 5.1 Introduction

This chapter discusses the University of Leicester IASI Retrieval Scheme (ULIRS), which has been developed to determine CO profile and tropospheric total column amounts, under clear sky conditions, using IASI measured TOA radiances. The ULIRS utilises an OEM to retrieve CO for a set of atmospheric layers. Whilst this particular study investigates the sensitivity and accuracy of the retrieval over a localised region, in this case Africa, the ULIRS could easily be applied to a global dataset, providing that the a priori and surface properties were constructed accordingly.

Section 5.2 discusses why the IASI instrument is ideal for observing CO in the Earth's troposphere. A quantitative discussion of factors which affect the retrieval process, and the justification for the selection of parameters used by the ULIRS, is reasoned in Sec. 5.3, with Sec. 5.4 outlining the sensitivity of the ULIRS to both the a priori and auxiliary data sets used in the retrieval scheme. Finally, Sec. 5.5 presents a series of simulations which demonstrate the capability of the ULIRS to retrieve tropospheric CO profiles for a wide range of scenarios.

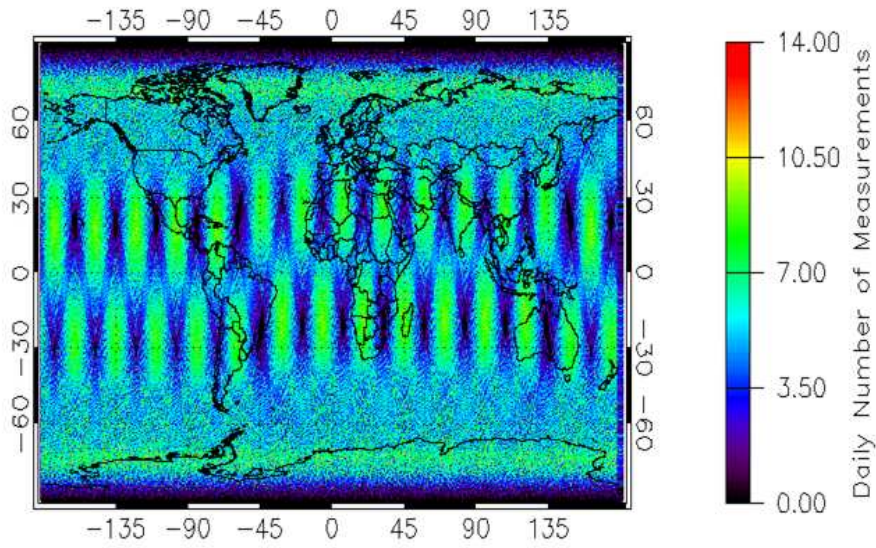


Figure 5.1: The number of measurements made by the IASI instrument, on a  $1^\circ$  by  $1^\circ$  grid.

## 5.2 Suitability of IASI to Retrieve CO

The IASI instrument's spectral range of  $645$  to  $2760\text{ cm}^{-1}$ , spectral sampling of  $0.25\text{ cm}^{-1}$  (unapodised), and low noise in the  $4.7\text{ }\mu\text{m}$  region (see Sec. 5.3.5) mean that it is well qualified to observe the CO spectral band centred on  $2140\text{ cm}^{-1}$ . The radiometric accuracy of the IASI instrument in and around this spectral band, as demonstrated in Chapter 4 is at worst  $0.3\text{ K}$ , over the  $245$  to  $300\text{ K}$  temperature range; the implications of the radiometric accuracy on the retrieved CO product are discussed in Sec. 5.4.2. In order to observe how the atmospheric composition of CO changes on a daily scale, it is necessary to use an instrument which is able to make global measurements at least once a day. As demonstrated in Fig. 5.1, the large swath width of the IASI instrument ( $2200\text{ km}$ ), means that it is able to achieve a twice daily global coverage ( $\sim 99\%$ ). As the first of a series of three instruments to be launched every five years, IASI will allow for the monitoring of long-term climatological trends at a very high temporal resolution.

## 5.3 ULIRS Methodology

### 5.3.1 Retrieval Theory

#### 5.3.1.1 The Forward Model

As outlined in Sec. 2.3, the forward model  $\mathbf{F}$  describes the relationship between the measurement  $\mathbf{y}$  and the state vector  $\mathbf{x}$ , and is repeated here as:

$$\mathbf{y} = \mathbf{F}(\mathbf{x}; \mathbf{b}) + \epsilon. \quad (5.1)$$

The ULIRS employs the Reference Forward Model (RFM) as a forward model. The RFM is a line-by-line RT model, which was developed at the University of Oxford (UK), and can be used to simulate the TOA signal as measured by a space-borne sensor [Dudhia, 2000]. The RFM is based on the GENLN2 RT model [Edwards, 1992], and was designed to provide reference spectral calculations for the Michelson Interferometer for Passive Atmospheric Sounding (MIPAS), a high spectral resolution limb-sounding instrument on board the Envisat satellite; it can be operated for any spectral range between  $0.001 \text{ cm}^{-1}$  and  $2000 \text{ cm}^{-1}$  ( $10 \text{ m}$  to  $0.5 \text{ }\mu\text{m}$ ) at a spectral resolution of  $0.0005$  to  $1.0 \text{ cm}^{-1}$ . The spectral coverage and resolution of the RFM makes it ideal for simulating IASI TOA measured radiances, which have a spectral sampling of  $0.25 \text{ cm}^{-1}$  (see Sec. 3.3.1). The RFM computes a jacobian product as part of its output. It does this by calculating the result of a 1% perturbation to the profile level for trace gases and a 1 K perturbation for atmospheric temperature.

The TOA radiation measured by the IASI instrument is composed of two main terms: the longwave radiation emitted by the Earth, and the back-scattered solar radiation. The RFM is able to very accurately simulate the longwave radiation emitted by the Earth, but it has no component to model the back-scattered solar radiation. Ignoring scattering effects (a reasonable assumption in the TIR, because of the particle size of atmospheric aerosols) the reflected solar radiation, as detected by the IASI instrument, is represented in the ULIRS by Eq.2.15, which is here repeated:

$$I = A I_0 \exp(-\gamma((1/\cos(\theta_{\text{sat}})) + (1/\cos(\theta_{\text{sol}}))))), \quad (5.2)$$

where  $I$  is the reflected solar radiation term detected at the TOA by IASI,  $A$  is the surface Albedo,  $I_0$  is the solar radiance which is incident on the Earth,  $\gamma$  is the

optical depth of the atmosphere,  $\theta_{\text{sat}}$  is the IASI satellite zenith angle, and  $\theta_{\text{sol}}$  is the solar zenith angle.  $I_0$  is calculated using the solar irradiance and the Atmospheric Chemistry Experiment (ACE) FTS atlas of the infrared solar spectrum [Hase et al., 2010],  $A$  is calculated from the a priori emissivity of the scene, and  $\gamma$  is calculated using the RFM.

### 5.3.1.2 The Inverse Problem

As discussed in Sec. 2.3, Earth observational satellites make measurements of the radiance spectra of the Earth, which is an intricate function of all of the components that make up the atmosphere, as well as of the properties of the Earth’s surface; retrieval theory ascertains which of these constituents could have changed, and by how much, in order to reproduce the signal that has been observed.

In order to determine the state vector (true atmospheric state) from the measurement vector (measured radiance), the solution to Eq. 5.1 needs to be inverted. This problem may be “ill-conditioned”, meaning that the inversion needs some form of regularisation. The ULIRS uses an OEM, which is described in detail in Sec. 2.3, and by Rodgers [2000], and which constrains the inversion with a priori information relating to the variables to be retrieved. This a priori information consists of a mean prior state  $\mathbf{x}_a$  and an a priori error covariance matrix  $\mathbf{S}_a$ , which represent the best statistical knowledge that is available of the state prior to any measurement being made. The a priori information must come from an independent source, with the choice of a priori used by the ULIRS discussed in detail in Sec. 5.3.3.

### 5.3.1.3 Characterisation and Error Analysis

As described in Sec. 2.3.1.5, the averaging kernel matrix  $\mathbf{A}$  is a representative of the sensitivity of the retrieved state to the true state. Recent work done by Ceccherini and Ridolfi [2010] proposed a new method to estimate  $\mathbf{A}$ , when using a retrieval scheme that incorporated the Levenberg-Marquardt iterative technique (see Sec. 2.3.5.2). This work concluded that  $\mathbf{A}$  was best represented by the following equation:

$$\mathbf{A} = \mathbf{TK}. \tag{5.3}$$

Where  $\mathbf{K}$  is the Jacobian and  $\mathbf{T}$  is defined as:

$$\mathbf{T}_{i+1} = \mathbf{G}_i + (\mathbf{I} - \mathbf{G}_i\mathbf{K}_i - \mathbf{M}_i\mathbf{S}_a^{-1})\mathbf{T}_i, \quad (5.4)$$

where:

$$\mathbf{M}_i = (\mathbf{K}_i^T\mathbf{S}_\epsilon^{-1}\mathbf{K}_i + (1 + \lambda)\mathbf{S}_a^{-1}) \quad (5.5)$$

$$\mathbf{G}_i = \mathbf{M}_i\mathbf{K}_i^T\mathbf{S}_\epsilon^{-1}, \quad (5.6)$$

where  $\lambda$  is a damping factor (see Sec. 5.3.2.3), and  $\mathbf{T}$  takes into account all of the iterations required by the minimisation process of the OEM, from the initial guess to the solution. Ceccherini and Ridolfi [2010] concluded that this new methodology resulted in the best possible agreement with accurate estimates derived a posteriori, and as such this methodology is adopted by the ULIRS.

The ULIRS assumes a linear approach for the error analysis, as outlined in Sec. 2.3.7, in conjunction with a new methodology proposed by Ceccherini and Ridolfi [2010] for calculating the measurement error covariance matrix  $\mathbf{S}_m$ , defining it to be given by:

$$\mathbf{S}_m = \mathbf{TS}_\epsilon\mathbf{T}^T. \quad (5.7)$$

## 5.3.2 Retrieval Setup

### 5.3.2.1 Choice of Spectral Window and State Vector

The spectral domain of the IASI instrument includes the (0-1) vibration-rotation band of CO at 4.7  $\mu\text{m}$ , with the strongest absorption lines of this band being spread from 2040 to 2190  $\text{cm}^{-1}$ , and well spaced across this region. This band also contains other absorbers which act to contaminate the spectra, and ideally a spectral window where these contaminants is minimised should be chosen. Figure 5.2 represents a simulated IASI radiance spectrum for the 2040 to 2190  $\text{cm}^{-1}$  spectral region, corresponding to tropical atmospheric conditions, together with the individual contributions of the strongest absorbers in this domain:  $\text{H}_2\text{O}$ ,  $\text{CO}_2$ ,  $\text{O}_3$ ,  $\text{N}_2\text{O}$ , and CO. Water vapour absorbs irregularly throughout the region and its contribution cannot be avoided. The  $\text{O}_3$  signature extends from 2060 to 2135  $\text{cm}^{-1}$ , whilst  $\text{N}_2\text{O}$  saturates the signal above 2180  $\text{cm}^{-1}$ . In order to avoid interferences due to  $\text{O}_3$  and  $\text{N}_2\text{O}$ , the spectral region used for the ULIRS CO retrieval is limited to the R branch of the TIR CO absorption

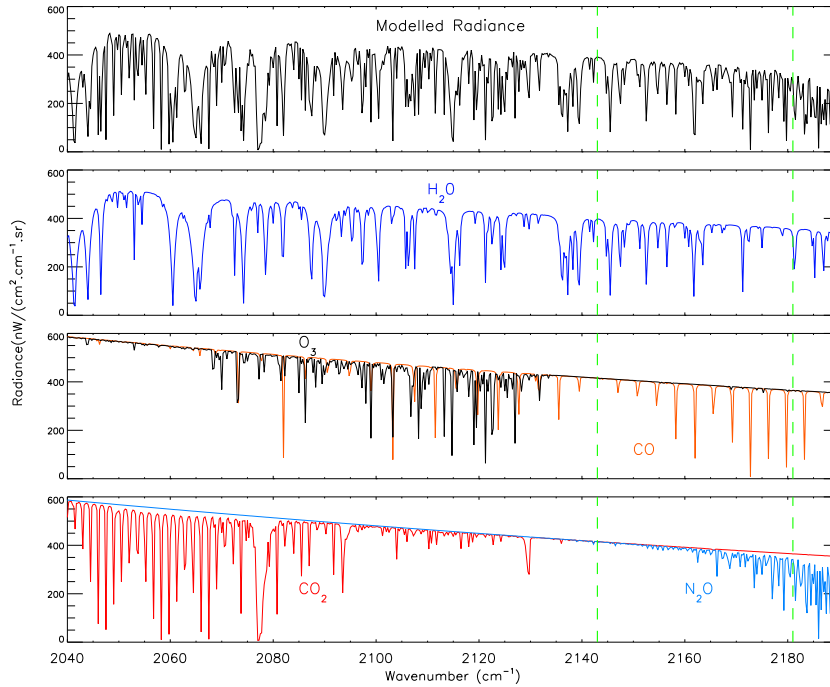


Figure 5.2: Simulated IASI radiances for the 2040 to 2190  $\text{cm}^{-1}$  spectral range (top panel). The contributions of the main absorbers in this spectral range are provided in the bottom three panels. The spectral window selected for the CO profile retrieval (2143 to 2181  $\text{cm}^{-1}$ ) is indicated by the vertical green lines.

band from 2143 to 2181  $\text{cm}^{-1}$ ; such a window has also been used to successfully retrieve CO by other retrieval schemes using space-borne high-resolution FTIR nadir measurements [see e.g. Barret et al., 2005; Turquety et al., 2009].

As can be seen from Fig. 5.2,  $\text{H}_2\text{O}$  and CO are the dominant absorbers in this spectral region, and delineating between the effect of the two of them is a non-trivial task. The errors that would otherwise be introduced to the retrieved CO profiles mean that water vapour is included in the state vector to give a more accurate retrieval. For a similar reason the temperature profile is also retrieved, hence the state vector  $\mathbf{x}$  retrieved by the ULIRS comprises of tropospheric CO,  $\text{H}_2\text{O}$  and temperature profiles, as well as a surface temperature term.

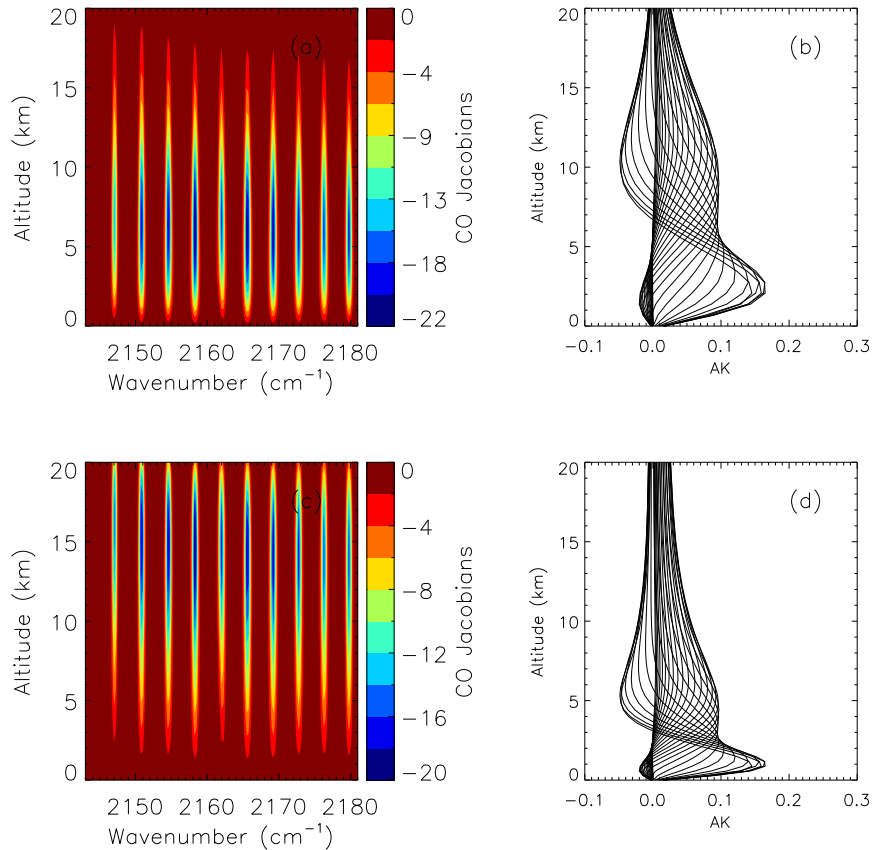


Figure 5.3:  $\mathbf{K}$  and  $\mathbf{A}$  calculated using a 30 level retrieval grid, and which is equidistant in either altitude (0 to 20 km) or pressure (1000 to 50 hPa): (a)  $\mathbf{K}$  for a retrieval grid that is equidistant in altitude; (b)  $\mathbf{A}$  for a retrieval grid that is equidistant in altitude; (c)  $\mathbf{K}$  for a retrieval grid that is equidistant in pressure; and (d)  $\mathbf{A}$  for a retrieval grid that is equidistant in pressure. The units of the Jacobians are radiances per VMR.

### 5.3.2.2 Pressure Levels

The choice of the pressure levels in the retrieval grid is an important one, as they will determine to some extent the sensitivity of  $\mathbf{K}$  and  $\mathbf{A}$  to different parts of the atmosphere. If a retrieval grid with levels equidistant in altitude (and which therefore had different “masses” of air associated with them) were chosen then this characteristic would produce results that were dependent upon the retrieval grid itself, and would therefore make a direct physical interpretation of  $\mathbf{K}$  difficult. The apparent artifacts

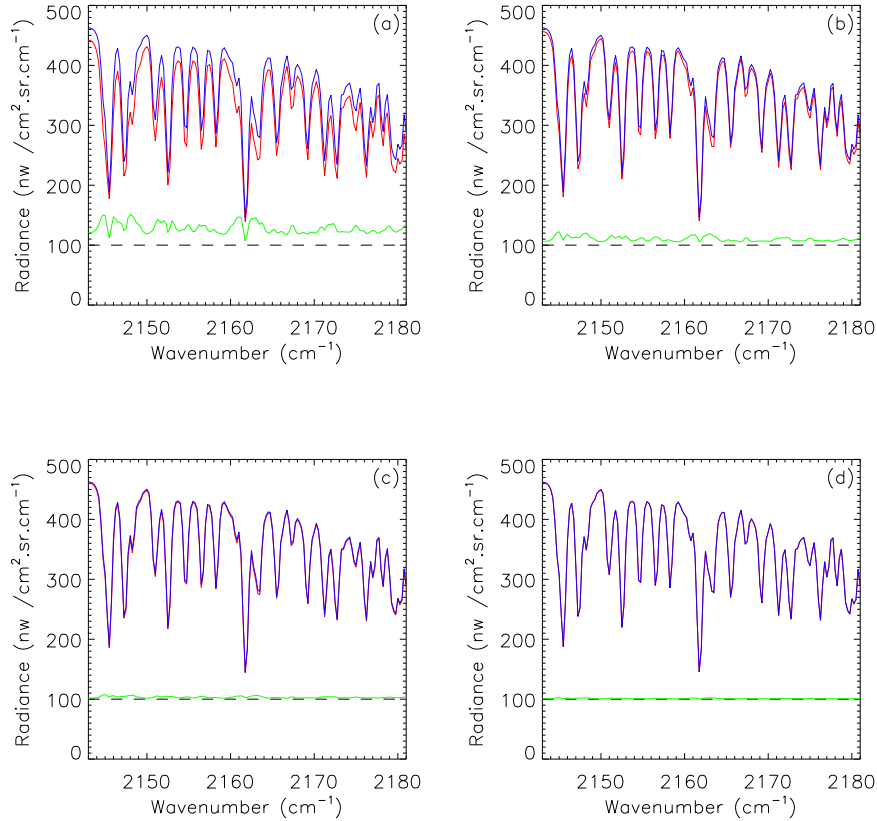


Figure 5.4: The effect that the number of retrieval levels has on the RFM’s accuracy in generating spectra at: (a) 5 levels (red), 40 levels (blue), and the residual + 100 (green); (b) 10 levels (red), 40 levels (blue), and the residual + 100 (green); (c) 20 levels (red), 40 levels (blue), and the residual + 100 (green); and (d) 30 levels (red), 40 levels (blue), and the residual + 100 (green). In the cases of (a), (b) and (c) the residual is higher than the noise in this spectral region (dashed line).

in the Volume Mixing Ratio (VMR)-based values for  $\mathbf{K}$ , caused by the nonuniform spacing of retrieval grid pressure levels, would also lead to the calculation of VMR-based  $\mathbf{A}$  that were proportionally larger for levels in the true profile associated with thicker layers, and smaller for levels associated with thinner layers; this was also found to be the case by Deeter et al. [2007a] who, in the V3 product of their retrieval algorithm, used a retrieval grid with layers that were non-equidistant in pressure to observe CO using the MOPITT instrument. Figure 5.3 illustrates the differences in

**K** and **A** when using a 30 level retrieval grid, which is equidistant in either pressure or altitude.

The retrieval grid was chosen to consist of a fixed number of levels which varied between the surface pressure and 50 hPa (approximately 20 km). This means that the minimum pressure will always be 50 hPa, but the surface pressure will depend upon the surface elevation of the IASI IFOV (see Sec. 5.3.4.2). By using this particular methodology (rather than choosing a fixed set of pressure levels, as is done in the case of the MOPITT operational CO product), the problem of having a retrieval pressure level which is greater than that of the surface pressure, as would be the case over (for example) a mountain, does not arise.

Figure. 5.4 illustrates the effect that the number of levels in a retrieval grid has on the RFM's ability to accurately simulate TOA radiances. By choosing 40 levels, spaced equidistantly in pressure, it was found that the RFM was able to simulate any spectral features that would be observed by the IASI instrument in the selected spectral window, given the spectral sampling and resolution of the instrument. By choosing to perform the retrieval over 30 levels instead of 40 the processing time of the RFM is decreased by a factor of 1.5, without any significant degradation in the accuracy of the simulation (see Fig. 5.4). To summarise, the ULIRS incorporates a retrieval grid with 30 levels that are equidistant in pressure, and which ranges from the surface pressure to 50 hPa.

### 5.3.2.3 Iteration and Convergence

The ULIRS uses a Levenberg-Marquardt iterative technique, which makes use of a damping factor  $\lambda$ , chosen so as to minimise the cost function at each step of the iteration [Rodgers, 2000]. After each iteration the cost function is calculated, and compared to the cost function of the previous iteration, if there has been an increase in the cost function then the damping factor is increased by a factor of 8, and if there has been a reduction in the cost function, then the damping factor is reduced by a factor of 4. These values, along with an initial damping factor of 0.1 were chosen based on the work done by Ceccherini and Ridolfi [2010].

Convergence analysis is needed to establish the correct criterion for stopping the iterations for each retrieval. In order to make sure that an accurate convergence is

reached, the iterations are stopped when one of the following two criteria are reached: (i) the number of iterations exceeds 10; (ii) the relative variation of the cost function is less than 0.01. These two criteria have been chosen as they are consistent with the literature [see e.g. Ceccherini and Ridolfi, 2010], with the ULIRS typically reaching convergence in 3 to 4 iterations.

Once an iteration has converged, it is necessary to test if this retrieved spectra is a sensible representation of the real spectra, as measured by the IASI instrument. A suitable test for a correct convergence is to calculate a value for the normalised cost function [Rodgers, 2000]. If the normalised cost function is approximately unity then the retrieved spectra can be assumed to be a good representation of the real spectra. The ULIRS calculates a value of the normalised cost function for each retrieved scene, therefore giving an indication of the reliability of the retrieval.

### **5.3.3 A Priori Data**

Being an OEM retrieval scheme, the ULIRS makes use of a priori knowledge relating to the quantities that are to be retrieved, with the posterior retrieval weighted by the choice of the inputted data.

#### **5.3.3.1 Climatologies**

Aside from CO, the principal absorbing atmospheric gases in the TIR CO absorption band are H<sub>2</sub>O, CO<sub>2</sub>, N<sub>2</sub>O, and O<sub>3</sub> (see Fig. 5.2). In order to correctly simulate TOA radiances in this region, an accurate representation of the climatology, i.e. the atmospheric concentrations of the relevant gases is required, with water vapour considered separately (see Sec. 5.3.3.2). The ULIRS makes use of a set of reference atmospheres, or climatologies, that were designed by Remedios et al. [2007] for use in IR sounding. Five atmospheres corresponding to tropical, mid-latitude day/night and polar summer/winter atmospheric conditions are available, with these profiles describing the concentrations of 30 atmospheric species, including CO<sub>2</sub>, N<sub>2</sub>O, and O<sub>3</sub> between the surface and a height of 120 km, with a vertical step size of 1 km.

### 5.3.3.2 Temperature and Water Vapour Profiles

The tropospheric temperature and water vapour are so highly variable, on such relatively short time and spatial scales, that they must be represented by a more accurate a priori data set than those given by the static reference atmospheres. The a priori tropospheric temperature and water vapour profiles used in the ULIRS algorithm are taken from the ECMWF operational data set, courtesy of the British Atmospheric Data Centre (BADC). This data set is on a  $1.125^\circ \times 1.125^\circ$  grid with 91 pressure levels, and a 6 hourly time resolution.

The ECMWF a priori tropospheric temperature and water vapour profiles associated with each retrieval scene is calculated by first finding the ECMWF data set which is closest in time to when the IASI measurement was made, the four ECMWF grid points that encompass each geolocated IASI pixel are then located. The profiles at these grid points are then linearly interpolated onto the same pressure grid as that used by the ULIRS (see Sect. 5.3.2.2); a spatial bilinear interpolation is then performed, resulting in a set of a priori tropospheric temperature and water vapour profiles.

### 5.3.3.3 CO Profile

In order to ensure that any spatial or temporal features observed in the retrieved CO product are not symptomatic of features in the a priori, the ULIRS employs a constant a priori CO profile. This profile is constructed using the Toulouse Off-line Model of Chemistry And Transport (TOMCAT) Chemical Transport Model (CTM) [Chipperfield, 2006], run over an entire year for a specified location. The TOMCAT CO emissions are climatological emissions based on the IPCC (Intergovernmental Panel on Climate Change) third assessment report. For the African region which is considered in this work, the TOMCAT model was run for one year (2004) over a grid box bounded longitudinally from  $-20$  to  $50^\circ\text{E}$ , and latitudinally from  $-30$  to  $30^\circ\text{N}$ , and to avoid the a priori being heavily biased by background concentrations of CO, only profiles where the surface concentration of CO was greater than 100 ppbv were considered. Once this selection criteria had been established there were approximately 8000 available TOMCAT profiles, from which a mean a priori profile was calculated.

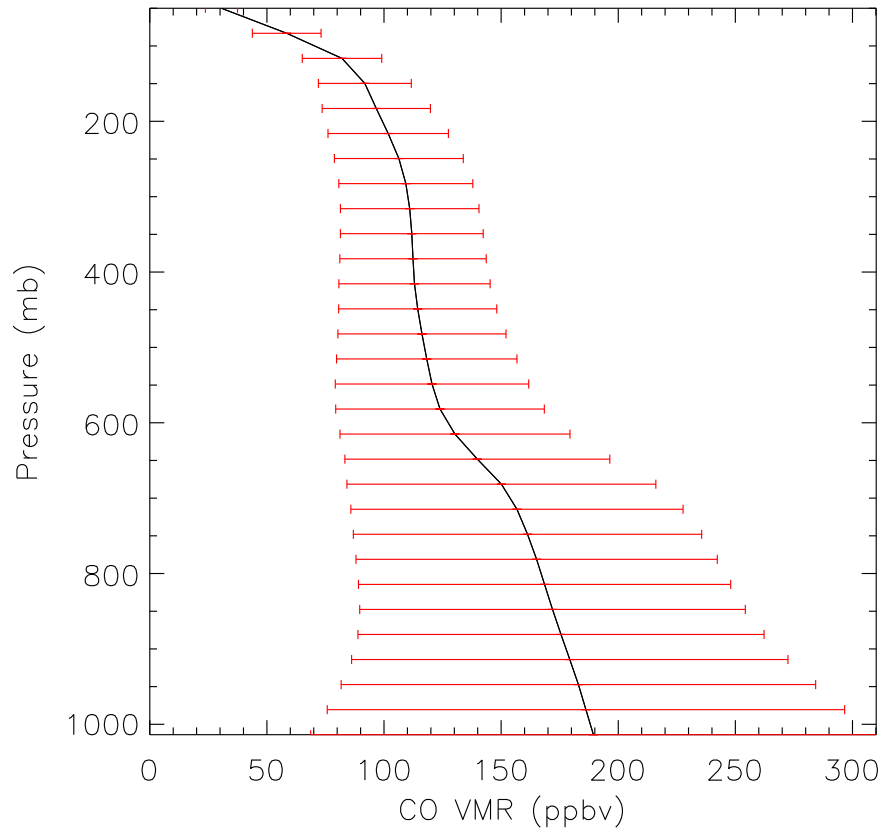


Figure 5.5: The CO a priori profile used by the ULIRS. The red error bars represent the diagonal elements of the a priori error covariance matrix as calculated by determining the covariance between the different TOMCAT CO profiles that were used to construct the a priori profile. The mean profile in this plot corresponds to an a priori in the total column of  $4.05 \times 10^{18}$  Molec  $\text{cm}^{-2}$ , and a range of  $1.49$  to  $6.61 \times 10^{18}$  Molec  $\text{cm}^{-2}$ .

The a priori profile for tropospheric CO that was used by the ULIRS in this study is shown in Fig. 5.5.

Whilst this chapter deals with investigating the sensitivity and accuracy of the retrieval over a localised region, in this case the African region, the ULIRS could easily be applied to a global dataset, providing that the a priori and surface properties were constructed accordingly. Were the ULIRS to be used for a truly global retrieval a careful consideration of the choice of a priori for the CO atmospheric profile would

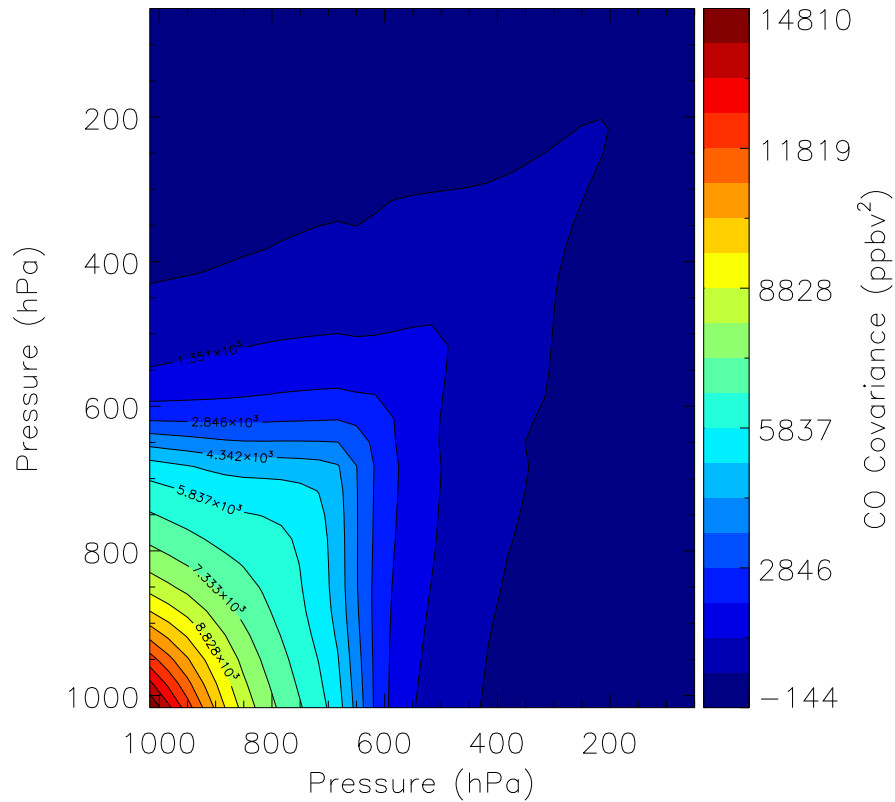


Figure 5.6: The CO a priori error covariance used by the ULIRS.

be necessary. The use of a single global a priori would ensure that any features in the retrieval could not be traced back to features in the a priori, however at levels where the weighting functions exhibit low sensitivity, the use of a single global profile can result in large systematic differences between the “true” CO concentration and the retrieved values. As this chapter deals with optimising the ULIRS over a localised region this issue is not dealt with here; for a more detailed discussion of the relative strengths and weaknesses of a global vs. a spatially dependant a priori please refer to Deeter et al. [2010].

### 5.3.3.4 A Priori Error Covariance Matrix

The a priori error covariance matrix  $\mathbf{S}_a$  determines the uncertainty in the a priori information used in the retrieval. Apart from surface temperature, each of the retrieved parameters has a  $n \times n$  covariance matrix associated with it, where  $n$  is the number of retrieval levels (30), and which in the case of the ULIRS have been deemed to be independent from one another, i.e. an uncertainty in one retrieved parameter has no direct effect on the uncertainty of any of the other retrieved parameters.

Similarly to the selection of the a priori profile of CO, the choice of  $\mathbf{S}_a$  for CO has a direct effect on the retrieved products, and for this reason it was decided that the  $\mathbf{S}_a$  used to represent CO should remain fixed. In the construction of the CO a priori profile (see Sec. 5.3.3.3), the covariance of the atmospheric CO between each of the retrieval pressure levels of the ULIRS was also calculated from the TOMCAT modelled values, and these values were used to construct the CO a priori error covariance matrix, as shown in Fig. 5.6.

The square root of the diagonal elements  $\mathbf{S}_a$  for the water vapour are set to 10 % of the ECMWF water vapour profile, whilst for the temperature the diagonal elements are set to 1 % of the ECMWF temperature profile. The off-diagonal elements of the water vapour and temperature sections of the a priori error covariance matrix are calculated using the Gauss-Markov equation:

$$\mathbf{S}_{ij} = \sqrt{\mathbf{S}_{ii}\mathbf{S}_{jj}} \exp\left(\frac{-(\mathbf{z}_i - \mathbf{z}_j)^2}{\mathbf{z}_s^2}\right) \quad (5.8)$$

where  $\mathbf{z}_i$  and  $\mathbf{z}_j$  are the altitudes of the  $i$ th and  $j$ th elements of the profile, and  $\mathbf{z}_s$  is a “smoothing length”. A smoothing length of 3 km was chosen for both the water vapour and the temperature. An uncertainty in the surface temperature of 5 K is assumed, resulting in a surface temperature variance of 25 K<sup>2</sup> being used.

## 5.3.4 Auxiliary Data

### 5.3.4.1 Emissivity

The parameters of surface emissivity and surface temperature play an important role in determining the TOA radiances that are detected by the IASI instrument, hence it is important that they are accurately represented in the retrieval scheme, and ideally

both should be retrieved in addition to the tropospheric CO profiles. However, the separation of the surface emissivity and the surface temperature in the chosen spectral window is not possible because of the nonlinearity of the relationship between radiance and surface temperature. The ULIRS includes a surface temperature term as part of its state vector (see Sec. 5.3.2.1) and so it is important that each retrieval uses an emissivity for the IFOV that is as representative of the true emissivity of that scene as is possible. As emissivity is a function of both land type and wavenumber, both of these must be factored into any auxiliary dataset that is used to represent the surface emissivity.

The MODerate resolution Imaging Spectroradiometer (MODIS) instrument was designed to provide improved monitoring for land, ocean, and atmosphere research; it was launched by NASA in 1999 on board the Terra (EOS AM) Satellite, and in 2002 on board the Aqua (EOS PM) satellite [Justice et al., 1998]. Seemann et al. [2008] have developed a global database of infrared land surface emissivity, derived using input from the MODIS operational land surface emissivity product (MOD11), and constructed using a baseline fit method developed from laboratory measurements of surface emissivity. This University of Wisconsin (UW) Baseline Fit Emissivity database has: a spatial resolution of  $0.05^\circ$ ; a monthly temporal resolution; and a spectral resolution of better than  $5\text{ cm}^{-1}$ , and has been shown by Seemann et al. [2008] to improve the validity of retrievals, in comparison to those made with a typical assumption of constant emissivity. The ULIRS calculates the surface emissivity for each IFOV by using the UW database to find the mean surface emissivity.

#### **5.3.4.2 Surface Elevation**

In order to ascertain the correct surface pressure of each IFOV, information about the surface elevation is needed. GTOPO30 is a global Digital Elevation Model (DEM) developed by the United States Geological Survey (USGS), with elevations in GTOPO30 regularly spaced at  $30''$  (approximately 1 km). When calculating the surface elevation of the IASI IFOV, the ULIRS calculates the surface elevation at the exact (to within  $30''$ ) geolocation given by the IASI level 1c data, with the topographic standard deviation within each IFOV also being recorded, so as to give an indication of the homogeneity of the scene.

The initial surface pressure for each IFOV is obtained from the ECMWF pressure profiles, which have been calculated for each scene in a manner identical to that of the a priori temperature and water vapour profiles (see Sec. 5.3.3.2). This surface pressure corresponds to a geopotential height that is also part of the ECMWF product, and which is then converted to a geometric surface elevation, before being compared to the elevation given by the USGS DEM, and interpolated accordingly. This surface elevation is then used, along with the equation of hydrostatic equilibrium and a latitudinally and vertically dependent gravitational acceleration, to compute the associated height (altitude) grid used by the ULIRS.

### 5.3.5 Pre-processing

The ULIRS retrieves tropospheric CO profiles from IASI level 1C radiances. These level 1C data products represent geolocated and calibrated IASI spectra, which are sampled onto a spectral grid, and have been apodised. As part of the data product a quality flag is associated with the level 1C spectra for each IASI pixel [Camy-Peyret and Eyre, 1998], and is used to filter the data before the level 1C radiances are processed by the ULIRS.

#### 5.3.5.1 Instrument Noise

The noise of the IASI instrument is a random measurement effect, which must be taken into account when the retrieval by the ULIRS is performed. This random component is represented in the retrieval process by the noise covariance matrix  $\mathbf{S}_\epsilon$ , which is calculated depending upon the noise  $\epsilon$  of the IASI instrument, and which has a standard deviation equal to the inverse of the SNR. A simplification of  $\mathbf{S}_\epsilon$  would be to assume that the errors in the different channels are uncorrelated and uniform, resulting in  $\mathbf{S}_\epsilon$  being a  $m \times m$  diagonal matrix, where  $m$  is the number of measurement vectors, with the diagonal elements corresponding to the expected radiometric noise in the spectral region used, which in the case of the TIR absorption band of CO (2040 to 2190  $\text{cm}^{-1}$ ) is approximately  $\pm 2 \text{ nW}/(\text{cm}^2\text{cm}^{-1}\text{sr})$ . Whilst this simplification has been used successfully by other studies [see e.g. Turquety et al., 2009], it is not an approach that is used in this work, as by incorporating non-diagonal elements into  $\mathbf{S}_\epsilon$

for the specified spectral region the effects of the apodisation can be accounted for.  $\mathbf{S}_e$  is constructed using the noise covariance matrix that is supplied as part of the IASI level 1c radiances, with apodisation meaning that the noise in each channel has a non-negligible effect on the five channels surrounding it.

### 5.3.5.2 Cloud Detection Algorithm

If a cloud occurs within the IASI instrument's field of view then the photon path length of the Earth's radiation can be dramatically altered. If single scattering occurs then the optical path length is shortened, with the cloud effectively shielding a significant fraction of the atmosphere below it. However, if there is multiple scattering then the optical path length will be increased. In this case, the light reaching the instrument will have deeper absorption features which are systematic of the longer path it has traversed rather than because of a greater amount of CO in the atmosphere.

The ULIRS has been developed to be optimal in cloud-free scenes, as such part of the pre-processing of the IASI level 1c spectra includes a cloud detection algorithm, so that the retrieval processes only cloud free scenes. No single cloud detection method is able to detect clouds in all situations, and so the cloud detection algorithm used by the ULIRS considers two different cloud detection methods, and uses them concurrently, i.e. if either cloud-detection technique classifies an IASI IFOV as being cloudy, then the ULIRS treats it as such.

The first cloud-detection method that is applied is a simple threshold test, which compares IASI measured BTs to the Earth's skin temperature (the temperature of a very thin layer of about  $10\ \mu\text{m}$  above the Earth's surface), as outlined by Hadji-Lazaro et al. [2001]. One of the products that is available from the ECMWF dataset is the  $2.5^\circ$  gridded skin temperature, which is calculated every 6 h. The ECMWF skin temperature associated with each IASI IFOV is computed by first finding the four ECMWF grid points that encompass the geolocation of each IASI pixel, and then performing a bilinear interpolation of these four grid points onto the geolocation of the IASI pixel; it is this value for the skin temperature which is used for the cloud detection threshold test.

The BTs for the IASI spectra are computed at  $2133.25$ ,  $2143$  and  $2150\ \text{cm}^{-1}$  (these

values differ slightly from the 2133.28, 2143 and 2150.11  $\text{cm}^{-1}$  values used by Hadji-Lazaro et al. [2001], as they have been rounded to the nearest 0.25  $\text{cm}^{-1}$  to account for the spectral sampling of the IASI instrument), assuming a surface emissivity of 0.9788 over water, and 0.9677 over land (for those IASI pixels which lay over both land and water, a surface emissivity of 0.9677 was used). These BTs are then compared to the ECMWF skin temperature computed for each IFOV, and if there is a difference between the two products of greater than 8 K over the sea, or 15.3 K over the land, then the pixel is flagged as being cloudy.

The second cloud detection method that is applied to the data set is a 8 - 11  $\mu\text{m}$  delta BT threshold test, which has been adapted from the tri-spectral brightness temperature method developed by Strabala et al. [1994]. Absorption by water vapour in the atmosphere in the 8 to 9  $\mu\text{m}$  region is moderate, but is at a minimum for ice-water particle absorption. In the 11 to 12  $\mu\text{m}$  region the opposite is true, i.e. water vapour absorption is relatively small, whilst absorption by ice and water particles is at a maximum. In the presence of a cloud, absorption in the 11  $\mu\text{m}$  region will be relatively larger than the absorption by water vapour in the 8  $\mu\text{m}$  region (because there is a sharper increase in the imaginary refractive index of ice and water, especially ice), and so if 8 - 11  $\mu\text{m}$  delta BT values are calculated a large positive value will be found. This is because there is more absorption in the 11  $\mu\text{m}$  region, and so the BT is lower than it is in the 8  $\mu\text{m}$  region. However, if the 8 - 11  $\mu\text{m}$  delta BT value is negative, then this indicates that there is more absorption by water vapour at 8  $\mu\text{m}$  than there is by ice and water particles (clouds) at 11  $\mu\text{m}$ , hence implying a cloud free region. Water-particle absorption increases more between 11 and 12  $\mu\text{m}$  than it does between 8 and 11  $\mu\text{m}$ , whilst ice particle absorption increases more between 8 and 11  $\mu\text{m}$  than it does between 11 and 12  $\mu\text{m}$ . This means that in the presence of water clouds, the 11 - 12 delta BTs are greater than 8 - 11 delta BTs, and for ice clouds the 8 - 11  $\mu\text{m}$  delta BTs are greater than the 11 - 12  $\mu\text{m}$  delta BTs. Therefore, on a scatter diagram of 11 - 12  $\mu\text{m}$  delta BTs (x) vs 8 - 11  $\mu\text{m}$  delta BTs (y), a steep slope (greater than one) would be indicative of ice-particle clouds, whilst a shallow slope (less than one) would represent a water-particle cloud. The essence of the trispectral method consists of interpreting this scatter diagram: the clear region is expected to be represented by small or negative values for the 8 - 11  $\mu\text{m}$  delta BTs, and small 11

- 12  $\mu\text{m}$  delta BTs. Ideally the 8  $\mu\text{m}$  band should be chosen so that it lies on a water vapour absorption line, and the 11  $\mu\text{m}$  region chosen so as to exclude water vapour effects, as this ensures that there will be a negative difference for clear conditions even in a tropical atmosphere (where the slope of the transmittance as a function of wavelength is very steep over the 11  $\mu\text{m}$  region).

The ULIRS is only sensitive to if there is or is not cloud, and hence only makes use of the 8 - 11  $\mu\text{m}$  delta BT threshold test. However, the 11 - 12  $\mu\text{m}$  delta BT test, could be used to distinguish between optically thick and optically thin clouds. Based on the work done by Strabala et al. [1994], wavelength intervals of 8.3 to 8.4  $\mu\text{m}$  and 11 to 11.25  $\mu\text{m}$  were used, and if the 8 - 11  $\mu\text{m}$  delta BTs were less than  $-0.4\text{ K}$  then the data was flagged as being cloud-free.

## 5.4 Sensitivity Analysis

### 5.4.1 Sensitivity of the RFM

As discussed in Sec. 5.3.1.1, the Oxford RFM is used by the ULIRS to model the forward function. The use of the RFM to simulate IASI spectra has been investigated in detail, and a summary of the optimisation of the RFM for use by the ULIRS is now discussed.

As the RFM generates synthetic spectra by using spectral line parameters to derive the absorption features of a given trace gas, parameters such as the line position, absorption strength and broadening coefficients need to be quantified very accurately, in order to avoid serious errors in the modelled spectra (see, e.g. Fig. 5.7). To ensure that simulated spectra are as realistic as possible the latest version of the HITRAN spectroscopic data base [Rothman et al., 2009] has been implemented by the ULIRS. The resolution at which the RFM is run is also a key parameter, and a series of sensitivity tests (see Fig. 5.8) which aimed to determine the most economical and accurate processing resolution for the RFM, in relation to the retrieval of CO, were performed, resulting in an RFM spectral resolution of  $0.01\text{ cm}^{-1}$  being used by the ULIRS.

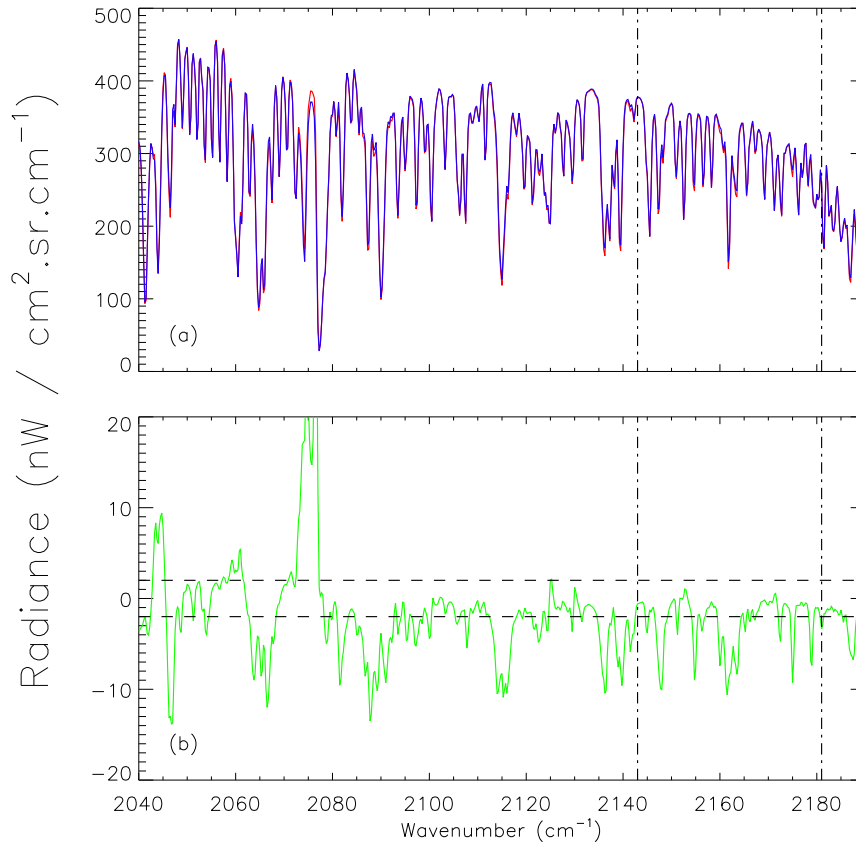


Figure 5.7: (a) Synthetic spectra generated using HITRAN 1994 (red line) and 2008 (blue line) spectroscopic data; and (b) substantial differences occur between the two spectra, the IASI noise in this spectral window is indicated by the dashed lines. The dashed vertical lines indicate the limits of the fitting interval.

The RFM was originally designed for retrievals of atmospheric products using MI-PAS measured radiances, and as such has a full limb viewing capability, however it can also be run in “nadir” mode, in which case a Plane-Parallel (PP) approximation is assumed. Walker and Dudhia [2009] examined the impact of neglecting the curvature of the Earth, and found that the PP method is only recommended for small satellite zenith angles up to approximately 18°, and that at higher viewing angles, the RFM nadir mode should be avoided, instead dealing explicitly with the curvature of the Earth in the radiative transfer calculations. As such the ULIRS uses the limb viewing capability of the RFM, configured so that the line-of-sight intersects the Earth’s

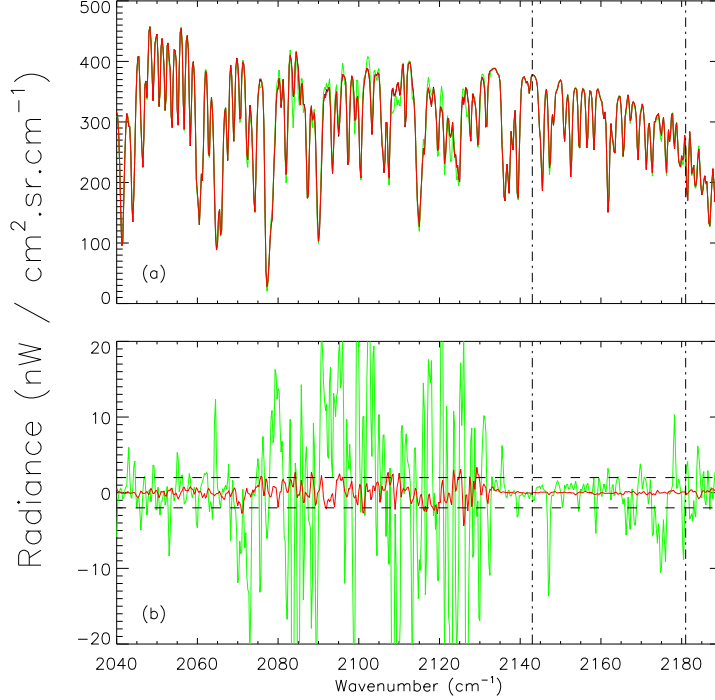


Figure 5.8: (a) Synthetic spectra generated using an RFM resolution of  $0.0005 \text{ cm}^{-1}$  (black),  $0.01 \text{ cm}^{-1}$  (red), and  $0.1 \text{ cm}^{-1}$  (green); and (b) the residual difference between the  $0.0005 \text{ cm}^{-1}$  and  $0.01 \text{ cm}^{-1}$  (red), and between the  $0.0005 \text{ cm}^{-1}$  and  $0.1 \text{ cm}^{-1}$  (green) resolutions. The differences between the  $0.0005 \text{ cm}^{-1}$  and the  $0.1 \text{ cm}^{-1}$  resolutions are significant (i.e. larger than the noise of the IASI instrument, which is indicated by the dashed lines), but this is not the case between the  $0.0005 \text{ cm}^{-1}$  and the  $0.01 \text{ cm}^{-1}$  resolutions. The dashed vertical lines indicate the limits of the fitting interval. It was decided that the RFM should be performed using a resolution of  $0.01 \text{ cm}^{-1}$ , resulting in simulations that represented the most efficient balance between accuracy and computational processing time.

surface appropriately.

As was discussed in Sec. 3.3.2, the EFOV of the IASI instrument is the useful field of view at each scan position, with each EFOV consisting of a  $2 \times 2$  matrix of IFOVs. Walker and Dudhia [2009] found that modelling the IASI IFOV as an infinitesimal beam for the purposes of the forward model is a very good approximation in the TIR

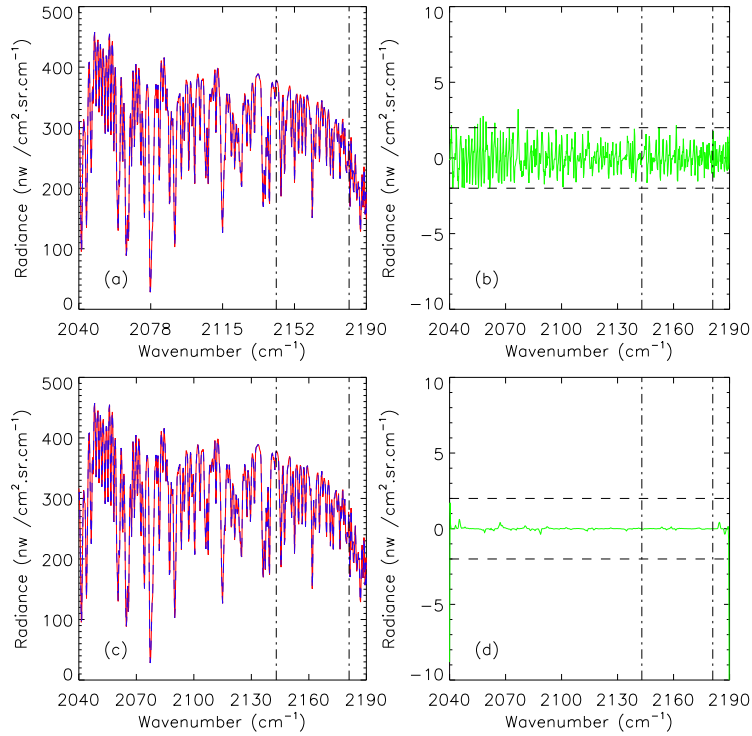


Figure 5.9: (a) Synthetic spectra generated by applying the full 10 cm<sup>-1</sup> wide ILS function (blue), and truncated 1 cm<sup>-1</sup> wide ILS function (red); (b) the residual difference between the 1 and 10 cm<sup>-1</sup> wide ILS functions, and IASI noise in this spectral window (dashed black line). (c) Synthetic spectra generated by applying the truncated 1 cm<sup>-1</sup> wide ILS function both during the RFM calculations (red) and afterwards (blue); and (d) the residual difference, and IASI noise in this spectral window (dashed black line). The dashed vertical lines indicate the limits of the fitting interval.

CO absorption region, and that in this region any errors introduced by making this approximation remain below the noise level, for all satellite zenith angles.

The RFM can incorporate the effect of the instrument response by specifying a file which accurately describes the ILS, and onto which the simulated spectra can be convolved, thereby ensuring that the simulated TOA radiances are characteristic of the instrument; the ILS for the IASI instrument is shown in Fig. 3.9(b), and it can be seen to extend over a wide wavenumber range. Figure 5.9 shows that the application of a truncated 1 cm wide apodised IASI ILS (see. Fig. 3.9(a)), has a negligible effect

in comparison to applying the full ILS, and in doing so the RFM calculations was found to be more computationally efficient, thus this methodology was adopted for use by the ULIRS. Figure 5.9 also shows that the difference between applying the ILS during the RFM simulation and afterwards is non-negligible at the edges of the spectral window. If the ILS needs to be applied after the RFM has performed a simulation (for example in the case where the RFM is used to simulate optical depths for the solar reflectivity term), then a slightly larger spectral window region is selected for the simulation, in order to correct for these edge effects.

### 5.4.2 Radiometric Accuracy

As was discussed in Chapter 4 the radiometric accuracy of the IASI instrument in the  $4.7\ \mu\text{m}$  spectral window is at worst 0.3 K, over the 245 to 300 K temperature range for which this intercomparison was conducted, which is significantly better than the 0.5 K that was originally stipulated in the IASI Science Plan. Figure 5.10 shows the effect that an inaccuracy in the measured spectra of 0.3 and 0.5 K can have on the retrieved CO profile. This figure was generated by retrieving simulated spectra with a surface emissivity of 0.98, a surface elevation of 0 m, and for conditions which represent a typical mid-latitude atmosphere with an enhanced CO concentration during the daytime. The black line represents the retrieved CO profile from the unperturbed simulated spectra, the red line represents the CO profile that was retrieved from the same simulated spectra, but with each measured radiance perturbed by a random noise of magnitude 0.5 K (converted into radiance units at a reference temperature of 280 K), and the blue line represents the retrieved CO profile using a simulated spectra, perturbed with a random noise of magnitude 0.3 K. As can be seen from Fig. 5.10, an inaccuracy in the spectra of 0.3 K results in a negligible difference (less than 2% across the profile) in the CO profile, whereas an inaccuracy of 0.5 K introduces significant differences of up to 8%. The radiometric accuracy of the IASI instrument at  $4.7\ \mu\text{m}$ , which was shown in Chapter 4 to be at worst 0.3 K (over the 245 to 300 K temperature range for which this intercomparison was conducted), thus allowing for confidence in the retrieved CO product.

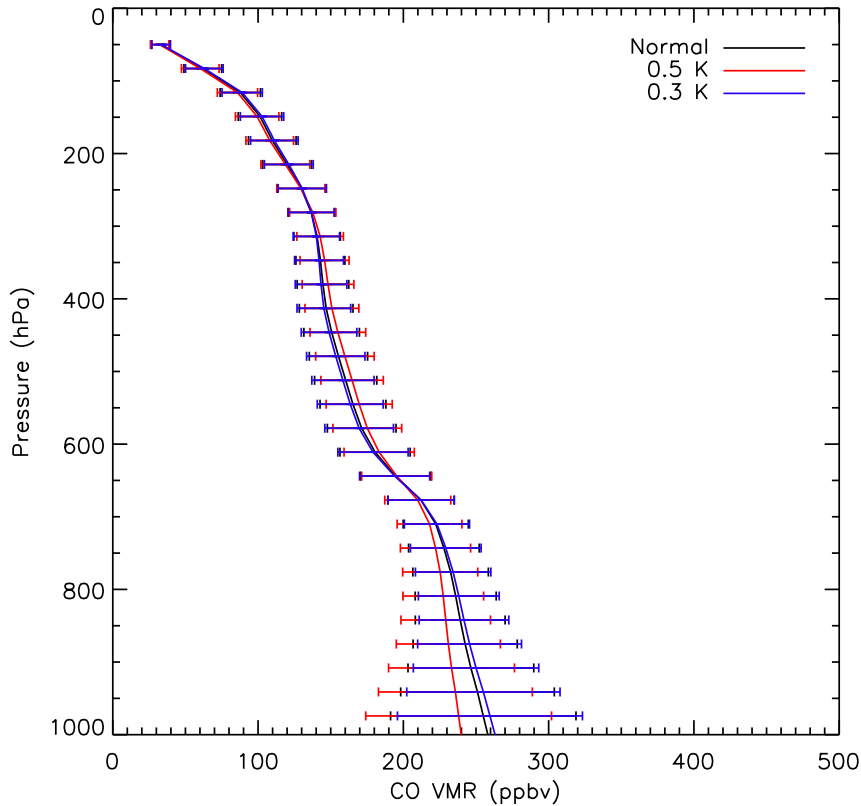


Figure 5.10: The effect of the radiometric accuracy on the ability to retrieve a CO product. The CO profiles in this plot have been retrieved from simulated spectra which have been generated for a typical mid-latitude atmosphere during the daytime, using a surface emissivity of 0.98 and a surface elevation of 0 m.

### 5.4.3 Information Content and Error Analysis

An error analysis, and characterisation of the retrievals, using the methodology outlined in Sec. 2.3.7 is now discussed.

#### 5.4.3.1 DFS

Two spectra corresponding to a low (DFS = 1.21) and a high (DFS = 1.91) information content have been selected for a detailed characterisation. They correspond to simulated retrievals over the Arctic Ocean and the Western Namibian mountain

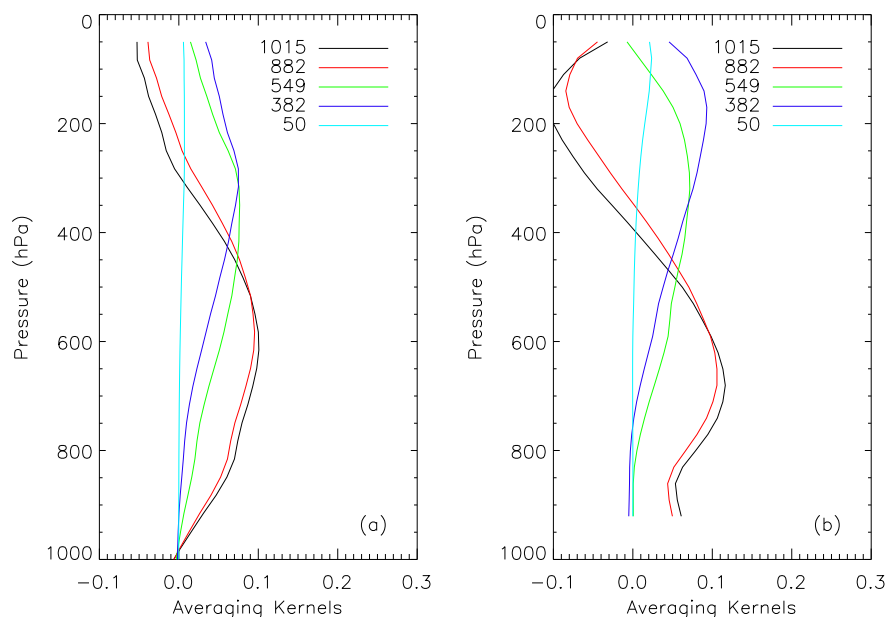


Figure 5.11: ULIRS CO averaging kernels for two selected IASI pixels: (a) Arctic Ocean ( $75.21^\circ$  N,  $115.97^\circ$  E, DFS=1.21); and (b) Namibian Mountains ( $17.67^\circ$  S,  $12.29^\circ$  E, DFS=1.91).

range, for the nighttime and daytime respectively; Fig. 5.11 plots the averaging kernels for each of these two scenes. In the case of the Arctic Ocean, the measurement only allows the retrieval of a single piece of information about the CO vertical distribution, covering the middle-upper troposphere at approximately 500 hPa, whereas over the Namibian mountains it is almost possible to separate the CO content in the middle troposphere from that in the Upper Troposphere Lower Stratosphere (UTLS), at approximately 200 hPa.

Strictly speaking only retrievals made with the same a priori are directly comparable. However, the variability that is observed in the DFS is comparable to that which has been observed for IASI by George et al. [2009].

#### 5.4.3.2 Errors

The vertical profiles for the simulated retrieval errors together with the vertical profile of the a priori variability are displayed in Fig. 5.12. In both cases the dominant

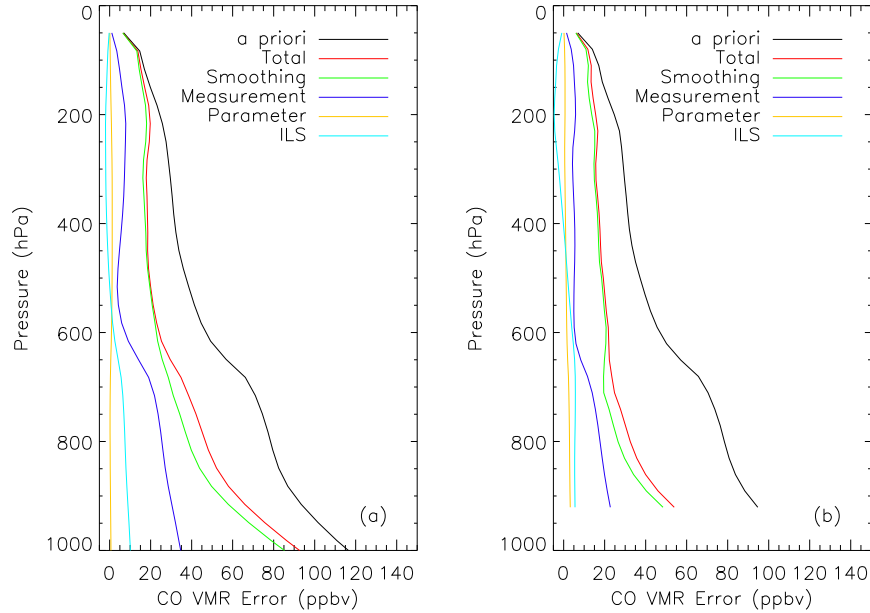


Figure 5.12: Same as Fig. 5.11 for the ULIRS CO tropospheric error profiles: (a) Arctic Ocean; and (b) Namibian Mountains

error at all altitudes is the smoothing error ( $\epsilon_{\text{smooth}}$ ). The other main contributing error is the measurement error  $\epsilon_{\text{meas}}$ , which contributes mainly below about 5 km. In addition to these two errors there is also a forward model parameter error  $\epsilon_{\text{param}}$ , which constitutes the errors in the parameters that are considered to be important in the retrieval but are not themselves retrieved; here this represents the errors in the trace gases that are absorbers in the spectral region (see Sec. 5.3.3.1), but are not retrieved. The total random error  $\epsilon_{\text{ran}}$  is defined here as the total error from the measurement, smoothing and forward model parameter error terms. As could be anticipated from the information content analysis, and due to the fact that the smoothing error is dominant above all the other errors, the total error is higher for the Arctic Ocean simulated retrieval, than for that over the Namibian mountains. In general there is a large reduction in total error in comparison to the a priori variability: up to 59% over Namibia, and 47% over the Arctic Ocean. However, the reduction of uncertainty about the CO vertical distribution is not significant above approximately 15 km.

For each retrieval a total systematic error is also calculated ( $\epsilon_{\text{sys}}$ ). This is defined

as the RMS of three terms: the ILS error, the radiometric stability error, and the radiometric accuracy error. The IASI Science Plan [Camy-Peyret and Eyre, 1998] states that the IASI instrument aims for a maximum error of 1 % in the ILS, a relative error of 0.3 K at 280 K for the radiometric stability error (approximately 1.2 %), and a relative error of 0.2 K at 280 K for the radiometric accuracy error (approximately 0.8 %); these values are used in the derivation of the systematic error for each retrieval.

#### 5.4.4 Sensitivity of the ULIRS

The three main features that exemplify the ULIRS are now characterised, so as to give a good indication as to the sensitivity of the retrieval scheme to these three parameters, namely: surface elevation, surface emissivity, and a quantified solar component. This section aims to enumerate the differences that are introduced into the retrieved CO product by varying these parameters. It should be noted however, that even for a perfect retrieval scheme the retrieved state vector will not be equal to the true state vector, i.e.  $\hat{\mathbf{x}} \neq \mathbf{x}_t$ . This is because of the smoothing that has been introduced by the limited resolution of the retrieval. As such, for a perfect retrieval (i.e. a retrieval for which there is no source of error, apart from that introduced by the discretising of the atmosphere), Rodgers and Connor [2003] states that  $\hat{\mathbf{x}}$  would be given as:

$$\hat{\mathbf{x}} = \mathbf{x}_a + \mathbf{A}(\mathbf{x}_t - \mathbf{x}_a) \neq \mathbf{x}_t. \quad (5.9)$$

As discussed in Sec. 5.3.1.1, the ULIRS includes a solar reflected component in its approximation of the forward function, and a quantification as to the effect that this inclusion has on the retrieved CO product is now demonstrated. Simulated radiances were produced using a solar reflected term, mid-latitude atmospheric conditions with an enhanced CO concentration, a surface emissivity of 0.84, and a surface elevation of 0 m; two different retrievals were then performed on these simulated radiances, one of which included a solar reflected component, and one which did not. As can be seen from Fig. 5.13, the effect of not including a solar term means that the retrieved profile deviates significantly from that of the smoothed truth, which represents the best possible retrieval. The total column densities for the retrieved product with and without a solar term are  $5.48 \times 10^{18}$  Molec cm<sup>-2</sup> and  $6.43 \times 10^{18}$  Molec cm<sup>-2</sup>, respectively, compared to a value of  $5.61 \times 10^{18}$  Molec cm<sup>-2</sup> for the smoothed truth. The

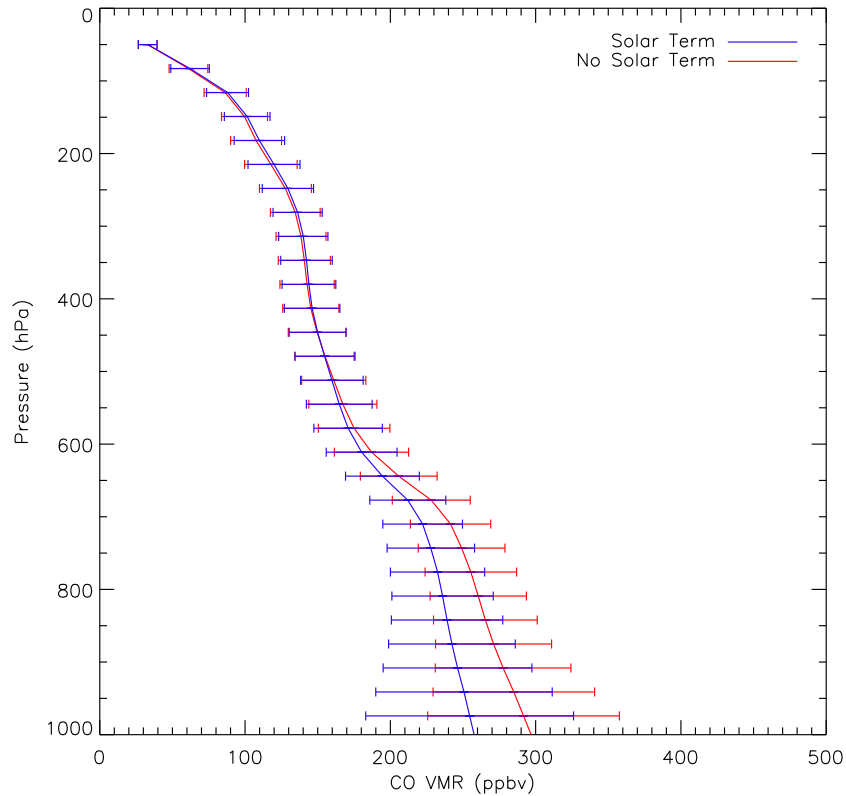


Figure 5.13: The effect that the inclusion of a solar reflected component has on the retrieved CO product. These retrievals were performed on radiances which were simulated under daytime mid-latitude atmospheric conditions, with a surface emissivity of 0.84 (representative of a desertified region), and a surface elevation of 0 m.

effect of neglecting a surface solar reflected term is much more pronounced over a desertified region than a water mass, which can largely be explained by the difference in the albedos (see Eq. 5.2).

Another feature of the ULIRS is its use of a surface emissivity, selected for each IASI IFOV using both spectral and spatial parameters (see Sec. 5.3.4.1); a sensitivity test was performed so as to investigate the effect that surface emissivity had on the retrieved CO product. A set of radiances were simulated using mid-latitude atmospheric conditions with an enhanced CO concentration, a surface elevation of 0 m, nighttime conditions (hence no solar reflected component), and a surface emissivity of

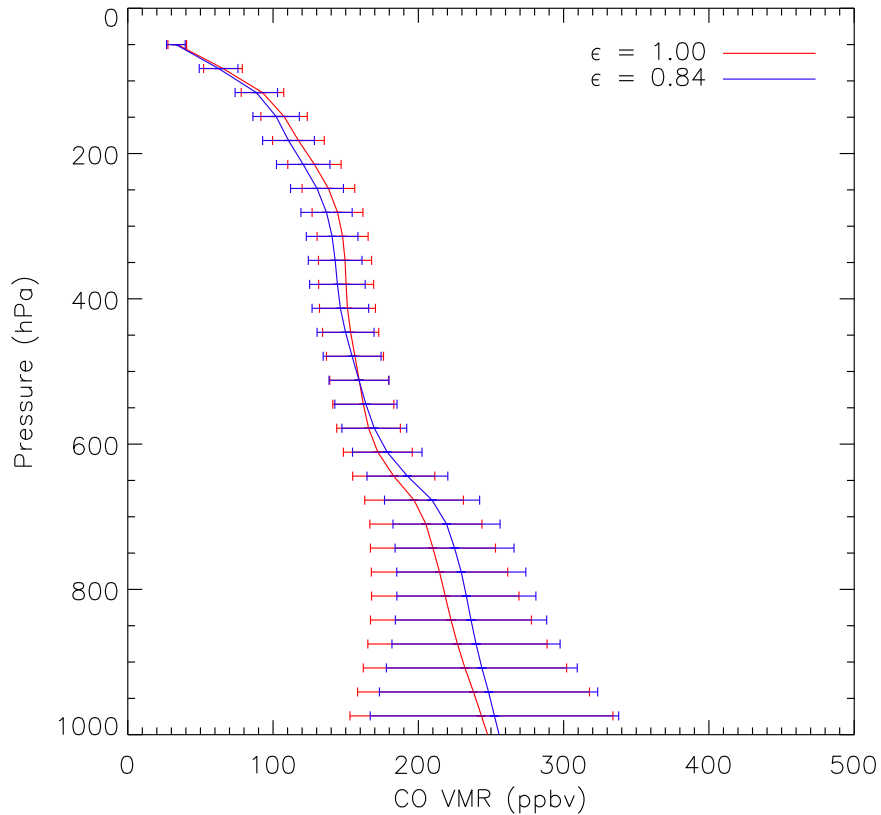


Figure 5.14: The effect of surface emissivity on the retrieved CO product. These retrievals were performed on radiances which had been simulated using mid-latitude atmospheric conditions during the nighttime, a surface emissivity of 0.84, and a surface elevation of 0 m.

0.84, chosen because it is representative of a desertified landscape in the CO TIR spectral window. Two separate retrievals were then performed using the ULIRS, identical in every respect apart from their assumed surface emissivities, which were chosen to be 0.84, and 1.0. Figure 5.14 demonstrates the effect that an incorrect knowledge of the surface emissivity can have on the retrieved CO product. The total column densities are  $5.76 \times 10^{18}$  Molec  $\text{cm}^{-2}$  for the case of an assumed surface emissivity of 1,  $5.52 \times 10^{18}$  Molec  $\text{cm}^{-2}$ , for a surface emissivity of 0.84, and  $5.52 \times 10^{18}$  Molec  $\text{cm}^{-2}$  for the smoothed truth (which used a surface emissivity of 0.84). The results of this sensitivity analysis demonstrate the importance of using a surface emissivity which

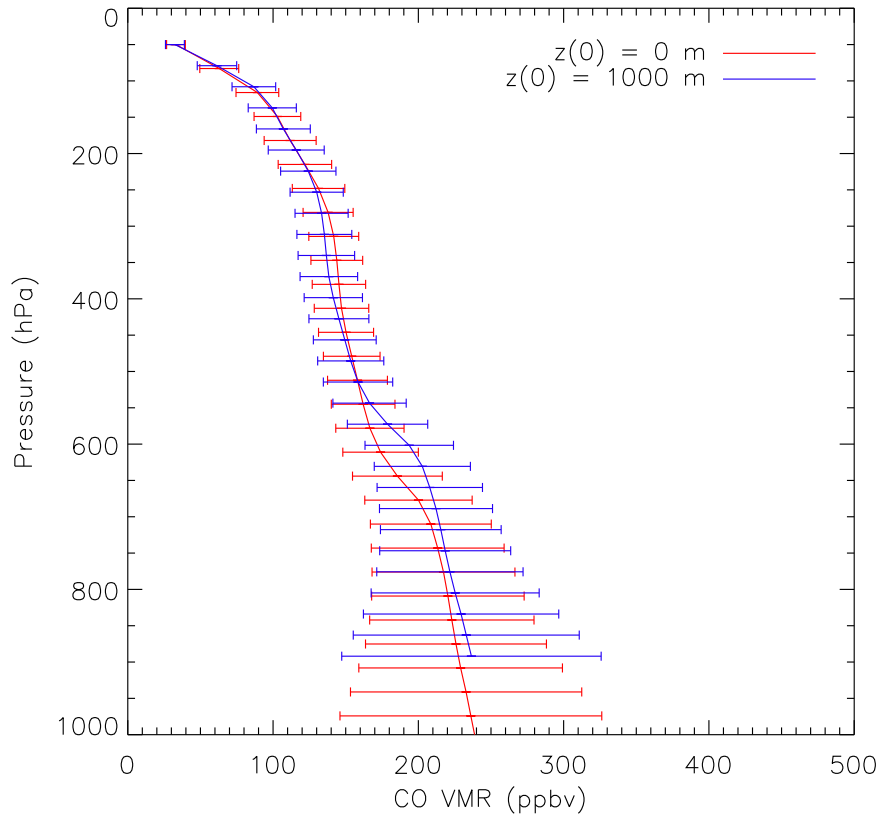


Figure 5.15: The effect of surface elevation on the retrieved CO product. These retrievals were performed on radiances which had been simulated using mid-latitude atmospheric conditions during the nighttime, a surface emissivity of 0.98, and a surface elevation of 1000 m.

is as representative of the truth as is possible, with the significance of an accurate surface emissivity further emphasised by the inclusion of a solar term (not shown).

Section 5.3.4.2 explained how the ULIRS incorporates a spatially well defined topographic map to determine the surface elevation for each IASI IFOV, and then how that information is used to adjust the pressure levels for the retrieval. A sensitivity test was performed to quantify the effect that a poor representation of the topography of the retrieval scene can have on the retrieved CO product, the results of which are shown in Fig. 5.15. These retrievals were performed on radiances which

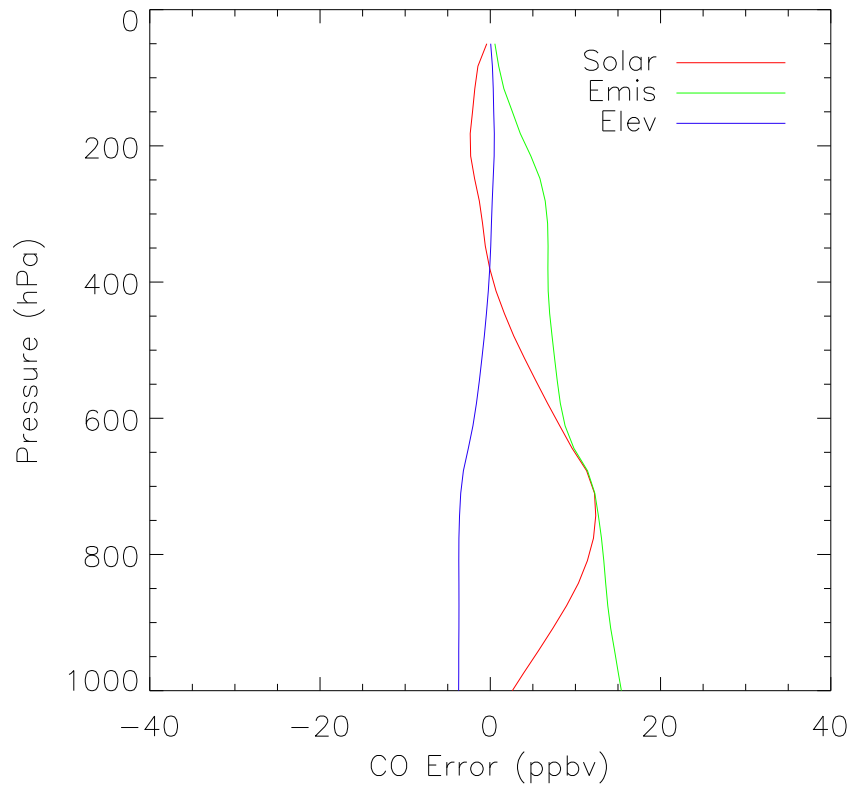


Figure 5.16: The error terms introduced by not accounting for the solar reflected (red), surface emissivity (green) and surface topographic (blue) components. The errors have been calculated using a linear error analysis, as given in Rodgers [2000], using the same simulated retrievals that were used to generate Figs. 5.13 to 5.15.

were simulated using nighttime mid-latitude atmospheric conditions with an enhanced CO concentration, a surface emissivity of 0.98, and a surface elevation of 1000 m. The total column densities are  $5.06 \times 10^{18}$  Molec  $\text{cm}^{-2}$  for the case of an assumed surface elevation of 0 m,  $4.39 \times 10^{18}$  Molec  $\text{cm}^{-2}$  for an elevation of 1000 m, and  $4.39 \times 10^{18}$  Molec  $\text{cm}^{-2}$  for the smoothed truth (which assumed a surface elevation of 1000 m). These results highlight the importance of using a surface elevation which is as accurate a depiction of the true elevation of the IASI IFOV as possible.

A linear error analysis was performed to establish the error terms that are introduced by not accounting for the solar reflected component, surface emissivity, and

topography of the scene, the results of which are shown in Fig. 5.16. This plot was generated from the different parameter errors, which were calculated using the following formula proposed by Rodgers [2000]:

$$\epsilon = \mathbf{G}_\epsilon \mathbf{K}_b (\hat{\mathbf{b}} - \mathbf{b}) \quad (5.10)$$

where  $\epsilon$  is the error associated with the parameter  $\mathbf{b}$ ,  $\mathbf{G}_\epsilon$  is the gain matrix, and  $\mathbf{K}_b$  is the Jacobian for each of the parameters. In order to quantify these error values, the same simulated retrievals (with and without consideration of the appropriate parameters) that were used to produce Figs. 5.13 to 5.15 were run. As can be seen from Fig. 5.16, by not carefully considering the solar reflected term, surface emissivity, and topography of the retrieval scene, significant errors are introduced into the retrieval.

#### 5.4.4.1 Retrievals with IASI Data

To demonstrate the effects of real data, an area was chosen within the study region of Southern Africa in which land variations, emissivity, and solar reflection were all significant. 710 profiles were retrieved in nominally cloud free scenes over the Namibian coastline region for 26 August 2007, and Fig. 5.17 demonstrates the mean differences that are observed in real retrievals by either accounting for or not correctly taking into consideration the three aforementioned parameters. As can be seen from Fig. 5.17(a), neglecting the solar reflected term has a very real and significant effect on the retrieved CO profiles. Figure 5.17(b) shows that assuming a surface emissivity of 1 also introduces a significant effect on the retrieved CO profiles, and this effect is obviously pronounced over regions of low emissivity. As can be seen from Fig. 5.17(c) the surface topography is also significant, in terms of the effect that it has on the retrieved product. Over 99% of the retrieved profiles converged within 10 iterations, with the mean number of iterations between 3 and 4.

Whilst every care has been taken to ensure that the solar reflected term, surface emissivity and topography of the scene have been correctly taken into account in the retrieval scheme, they cannot be known exactly, and as such will introduce a forward model parameter bias. These errors are considered separately from those earlier defined as  $\epsilon_{\text{param}}$ , and in order to quantify them, it is necessary to perform a linear error analysis, as given by Eq.5.10, using a representative uncertainty for each

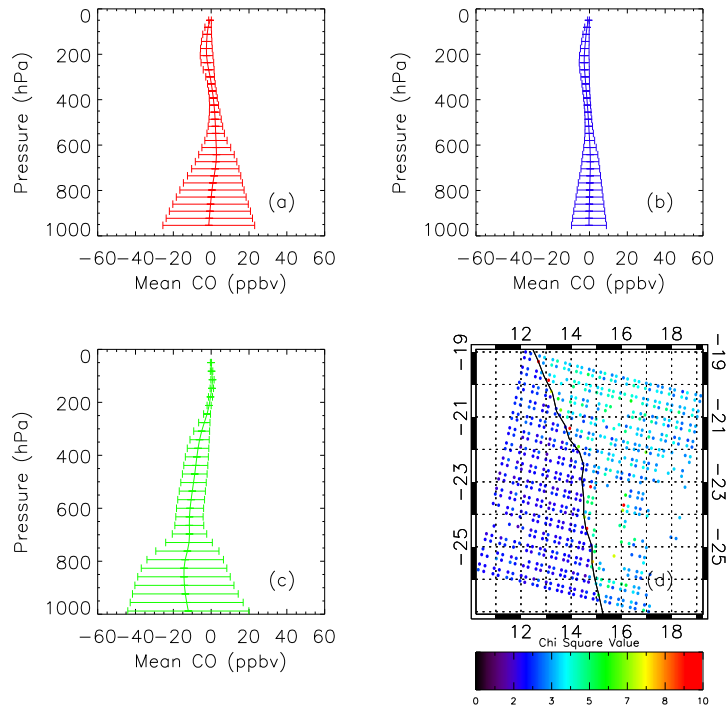


Figure 5.17: The effect of different parameters on the retrieved CO profile (horizontal lines on the profiles indicate the standard deviation): (a) the mean solar reflected term difference (retrieval with solar reflected term - retrieval without solar reflected term) in the CO profile; (b) the mean emissivity difference (retrieval with UW emissivity - retrieval with assumed emissivity of 1) in the CO profile; (c) the mean surface topography difference (retrieval with USGS topography - retrieval with assumed surface elevation of 0 m) in the CO profile; and (d) the region over which the mean differences and standard deviations have been calculated, also plotted is the chi squared value of the retrieval.

of the parameters under consideration. For the error in the solar reflected term  $\epsilon_{\text{sol}}$  the dominant error source comes from the assumption of the surface albedo, and is thus determined by the uncertainty of the surface emissivity  $\epsilon_{\text{emis}}$ . An uncertainty of 5% is assigned to the surface emissivity (and hence also the solar reflected term), with an uncertainty of 7% being assigned to the topography of the scene. The uncertainty in the topography  $\epsilon_{\text{elev}}$  was derived by dividing the globe into 12 km “pseudo-IASI” pixels, and then calculating the standard deviation within each pixel as a fraction of

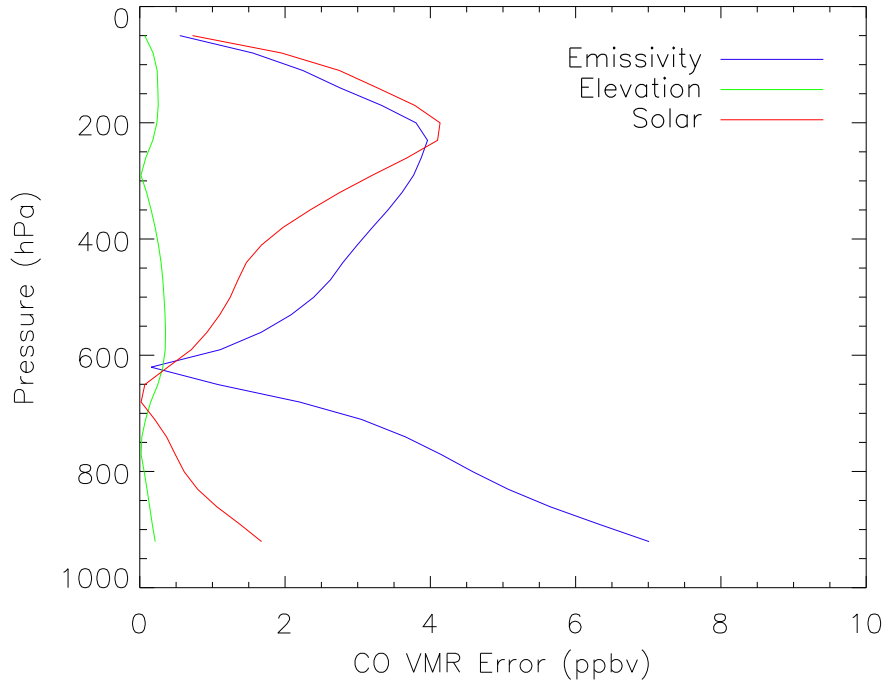


Figure 5.18: An error budget, as in Fig. 5.12 (b), but showing the error associated with the surface emissivity (blue), solar reflected term (red), and scene topography (green).

the assigned surface elevation. Once these values had been assigned, a detailed error budget for each retrieval could be calculated. Figure 5.18 shows these parameter errors for the retrieved scene shown in Fig. 5.12(b), and as can be seen they are much smaller than the measurement and smoothing errors shown in Fig. 5.12(b), but are not negligible and so must still be taken into account when calculating the total error, which is one of the outputs of the ULIRS product. A full ULIRS retrieval, using these associated error statistics, and for the region shown in Fig. 5.17(d) was performed, the results for which are tabulated in Table 5.1, where  $\epsilon_{\text{ran}}$  is now defined as the total error from  $\epsilon_{\text{smooth}}$ ,  $\epsilon_{\text{meas}}$ ,  $\epsilon_{\text{param}}$ ,  $\epsilon_{\text{emis}}$ ,  $\epsilon_{\text{sol}}$ , and  $\epsilon_{\text{elev}}$ .

	$\hat{\mathbf{x}}$	$\mathbf{x}_a$	$\epsilon_a$	$\epsilon_{\text{sys}}$	$\epsilon_{\text{ran}}$	$\epsilon_{\text{smooth}}$	$\epsilon_{\text{meas}}$	$\epsilon_{\text{param}}$	$\epsilon_{\text{emis}}$	$\epsilon_{\text{sol}}$	$\epsilon_{\text{elev}}$
<b>500 hPa<sup>a</sup></b>											
Mean	104.69	118.12	38.30	3.51	21.53	19.26	7.33	2.69	1.57	3.63	0.18
Sigma	29.11	2.48	3.07	1.31	3.67	2.13	3.21	0.98	1.05	2.96	0.15
<b>200 hPa<sup>a</sup></b>											
Mean	78.34	99.90	24.72	4.13	16.10	14.31	6.54	0.80	1.81	1.16	0.34
Sigma	23.74	1.94	1.15	1.64	1.08	1.07	0.49	0.32	0.97	1.32	0.35
<b>TC<sup>b</sup></b>											
Mean	2.33	2.41	0.90	0.15	0.56	0.45	0.22	0.07	0.05	0.14	0.01
Sigma	0.59	0.29	0.16	0.04	0.22	0.17	0.08	0.05	0.05	0.15	0.01

<sup>a</sup> units of ppbv

<sup>b</sup> units of  $1 \times 10^{18}$  Molec  $\text{cm}^{-2}$

Table 5.1: Mean and one sigma standard deviations of the retrieved CO product and associated a priori and error terms. These statistics have been produced using a full ULIRS retrieval over the region illustrated in Fig. 5.17(d), and correspond to the profile values at 500 hPa and 200 hPa, as well as a total column density (TC). The terms used in the table are as follows:  $\hat{\mathbf{x}}$ , retrieved value;  $\mathbf{x}_a$ , a priori value;  $\epsilon_{\text{sys}}$ , total systematic error,  $\epsilon_{\text{ran}}$ , total random error;  $\epsilon_{\text{smooth}}$ , smoothing error;  $\epsilon_{\text{meas}}$ , measurement error;  $\epsilon_{\text{param}}$ , forward model parameter error;  $\epsilon_{\text{emis}}$ , error in the surface emissivity;  $\epsilon_{\text{sol}}$ , error in the solar reflected term;  $\epsilon_{\text{elev}}$ , error in the surface topography.

## 5.5 Full Retrieval Simulations

In order to assess the suitability of the ULIRS for retrieving tropospheric CO profiles and columns from IASI measured radiances, a series of simulations were performed. These involved using the RFM to simulate spectra for a variety of scenarios, and then analysing the differences between the retrieved state vector  $\hat{\mathbf{x}}$ , and the smoothed true state vector, as given by Eq. 5.9.

A set of CO, water vapour and temperature profiles were provided by the CAMELOT (Chemistry of the Atmosphere Mission concEpts and sentineL Observation Techniques) study [Levelt et al., 2009], which were produced using the TM3 CTM model [Heimann and Korner, 2003]. There were 16 different atmospheric schemes used in the CAMELOT study, ranging from a Siberian permafrost to a polluted Pacific region, and the scenarios which were chosen for testing the ULIRS were those which corresponded to: a tropical background; tropical BB over a landmass; tropical BB over the ocean; and a subtropical background region. These scenarios were chosen so as to best test the ULIRS’ ability to accurately retrieve CO products over the Southern Africa region, so as to be consistent with the rest of this study; these sensitivity studies are thus performed in correspondence to the mean CO a priori profile shown in Fig. 5.5.

Different atmospheric spectra were simulated using the RFM and the CAMELOT derived profiles, with a realistic random noise component ( $\pm 2 \text{ nW/cm}^2/\text{cm}^{-1}/\text{sr}$ ) From these simulated spectra the ULIRS attempted to retrieve the true CO profile, as given by the CAMELOT profiles, for a variety of scenarios. For each scenario the retrieval process was repeated a number of times, so as to account for the random noise component that was added to the simulated spectra and profiles, with a mean ideal profile and a mean retrieved profile then being compared. The DFS for the retrievals ranged between 1 and 2, indicating that the retrieved CO product provides 1 to 2 pieces of information on the vertical profile. One may thus expect good information on some vertically weighted column but not on gradients. Applying the  $\mathbf{A}$  of the retrieved product to the true CAMELOT profile, via Eq. 5.9 produces a profile that is what IASI would see in the absence of any retrieval bias.

The first set of simulations that were carried out involved the retrieval of a set of CO profiles, providing that the water vapour and temperature profiles were well represented by the a priori information. As can be seen from Fig. 5.6, for all of the different CAMELOT scenarios which were retrieved, the difference between the ideal smoothed profile (given by Eq. 5.9) and the retrieved profile is very small, and certainly the two profiles always agree to within the posterior error. The ideal and retrieved profiles have similar vertical gradients but this merely reflects the a priori information. More instructive is that for all of the scenarios the total CO columns

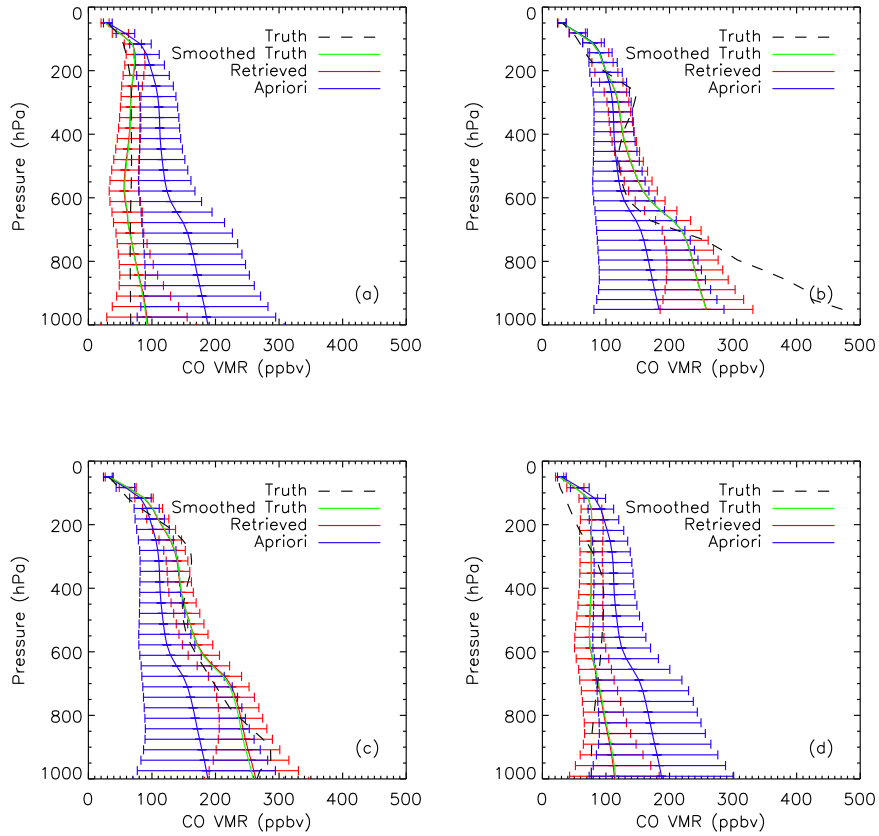


Figure 5.19: Retrieved CAMELOT profiles for a variety of scenarios, in which the a priori water vapour and temperature are well known (i.e. equal to those given by the CAMELOT profiles), the surface elevation is 0 m, and the surface emissivity is 0.98. The different CAMELOT scenarios and the amount by which the tropospheric CO columns (retrieved - smoothed truth) differ by are given as: (a) tropical background region, 0.11 %; (b) tropical BB over land,  $-0.09\%$ ; (c) tropical BB over ocean 0.68 %; and (d) subtropical background region  $-0.70\%$ .

are similar, with less than a 1 % bias for IASI in all cases. It is also important to note that there has been a significant (up to 60 %) reduction in the error, as is evident by comparing the a priori to the posterior error bars.

Following the simulation where the true water vapour and temperature profiles were well represented by the a priori, retrievals were performed where either the a priori water vapour or temperature profiles were up to 5 % different from the truth,

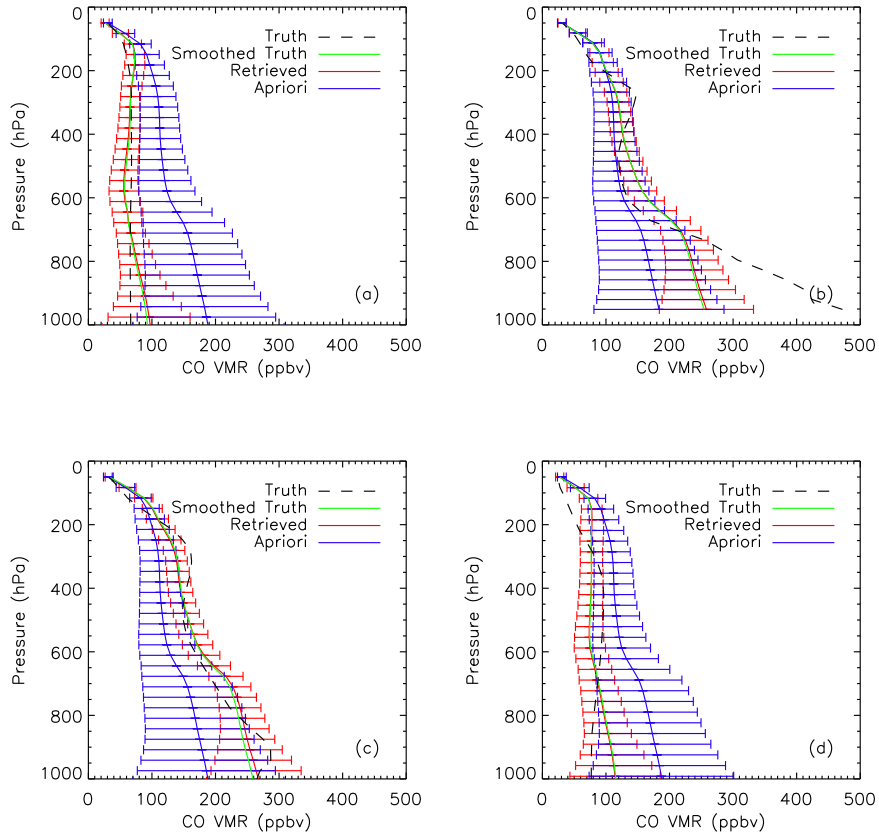


Figure 5.20: Retrieved CAMELOT profiles, as for Fig. 5.6, but with the a priori surface temperature, water vapour and temperature profiles differing from the truth by a  $\pm 5\%$  random error at each of the retrieval pressure levels. The tropospheric CO columns differ (retrieved - truth) by: (a)  $-0.75\%$ ; (b)  $0.46\%$ ; (c)  $1.16\%$ ; and (d)  $-0.55\%$

sy

across the whole profile, in these situations (not shown) the ULIRS still produced retrievals with less than a 3% bias. Even in the case where the a priori water vapour and temperature profiles, as well as the surface temperature were significantly different from the truth, the ULIRS was able to retrieve a very good approximation of the true CO profile, as is demonstrated in Fig. 5.20, with the bias in IASI being less than 2% for every simulation. In addition to this, for each of the different scenarios, over 99% of the retrieved profiles converged within 10 iterations.

## 5.6 Summary

This chapter presented a new retrieval scheme for tropospheric CO, using measured radiances from the IASI onboard the MetOp-A satellite in the  $4.7\ \mu\text{m}$  TIR spectral region. The ULIRS is an optimal estimation retrieval scheme, which utilises equidistant pressure levels and a floating pressure grid based on topography. It makes use of explicit digital elevation and emissivity information, and incorporates a correction for solar surface reflection in the daytime with a high resolution solar spectrum. The retrieval scheme has been assessed through a formal error analysis, via the simulation of surface effects and by an application to real IASI data over a region in Southern Africa. The ULIRS enables the retrieval of between 1 and 2 pieces of information about the tropospheric CO vertical profiles, with peaks in the sensitivity at approximately 5 and 12 km. Typical errors for the African region relating to the profiles are found to be  $\sim 20\%$  at 5 and 12 km, and on the total columns to be approximately 24%. These errors include a smoothing term; neglecting the smoothing error the total random errors are found to be  $\sim 10\%$  at 5 and 12 km, and on the total columns to be approximately 12%. Finally the performance of the ULIRS was shown for a range of simulated geophysical conditions.

As mentioned, the peak sensitivity of the ULIRS is at approximately 5 and 12 km; however the sensitivity to the retrieved profile is variant upon the retrieval scene. As demonstrated by Fig. 5.11, the ULIRS has an increased sensitivity over the land compared to the ocean, and the same is also the case in terms of over night and day retrievals (with a greater sensitivity to the surface during the daytime because of the increased thermal contrast). On average the DFS for the data studied so far range between 0.99 and 2.29, and so it is apparent that the smoothing error term (i.e. the error introduced because the retrieval is an estimate of the true state which has been smoothed by an averaging kernel) dominates the retrieved product. As is evident from Figs. and 5.20 this means that the ULIRS is able to accurately retrieve a smoothed truth profile, but that in terms of absolute truth there is more reliability in the retrieved total column product. It should also be noted that whilst Figs. and 5.20 indicate that the retrieved profile is able to move significantly far from the a priori, this has not yet been tested for a scenario in which there are very low atmospheric

CO concentrations.

The ULIRS CO retrieved product must be compared with other measurements of CO to ensure that the results are representative of the truth. This will be dealt with in Chapter 6, where the ULIRS CO product is compared with the operational product from the MOPITT instrument.

# Chapter 6

## A comparison of CO Data sets from the IASI and MOPITT instruments

### 6.1 Introduction

As discussed in Chapter 1, IASI is only one of many nadir-viewing instruments that make use of the thermal infrared bands at  $4.7\ \mu\text{m}$ . The objective of this chapter is to assess the consistency between the MOPITT and ULIRS retrieved IASI data (hereafter referred to simply as the IASI data set), in order to verify the reasonable performance of the IASI data and identify causes for bias in the retrievals. This analysis takes advantage of the existing validation heritage of the MOPITT data set, which has been operational for over a decade. The work reported in this chapter also represents the first evaluation of IASI data with both the MOPITT V3 and the V4 products, with comparisons performed both in profile and column space.

This chapter is organised as follows. Section 6.2 introduces the MOPITT instrument and presents in detail the retrieval algorithm of the MOPITT CO product, in particular highlighting the similarities and differences between the V3 and V4 operational products. Section 6.3 presents the results of an intercomparison between the IASI and MOPITT instruments and their retrieved CO products, with Sec. 6.4 highlighting the importance of understanding the role of the a priori information in

each of the retrieval schemes. Finally Sec. 6.5 discusses a methodology for reducing the smoothing bias between the two sets of observations.

## **6.2 MOPITT CO Retrievals**

### **6.2.1 MOPITT**

A summary of the main characteristics of the MOPITT instrument is given below; for a full description of the instrument see e.g. Drummond and Mand [1996]. MOPITT is a nadir sounding instrument which measures upwelling infrared radiation in both the 4.7  $\mu\text{m}$  and 2.3  $\mu\text{m}$  spectral bands; it uses gas correlation spectroscopy using Pressure Modulation Cells (PMCs) and Length Modulation Cells (LMCs) to calculate total column amounts and profiles of CO in the lower atmosphere. MOPITT was launched on board the Terra satellite in 1999, with an equator crossing time of 10:30 LST  $\pm$  26 min; a total scanning angle of  $\pm$  26° in each swath, combined with a 22 by 22 km horizontal resolution allows MOPITT to generate a global map of CO once every three days. At the time of this thesis work, no MOPITT retrievals had been performed using the 2.3  $\mu\text{m}$  spectral region and the MOPITT products are based on utilisation of the 4.7  $\mu\text{m}$ ; recently, [Worden et al., 2010] have published the first results using the MOPITT 2.3  $\mu\text{m}$  band. Whilst MOPITT utilises a slightly different technique to IASI in its measurements of TOA radiances, the sensitivity of the two instruments are determined by the same factors; namely the spectral resolution, SNR and viewing geometry.

### **6.2.2 Retrieval Setup**

The MOPITT “version 3” (V3) product first became available in 2002, and was the first data set to offer truly long-term and global coverage about the distribution of tropospheric CO. The characteristics of this data set are given in detail by Deeter et al. [2003], but to summarise they include: (1) an OEM retrieval algorithm, which utilises an operational radiative transfer model (MOPFAS) [Edwards et al., 1999] based on prelaunch laboratory measurements of instrument parameters as its forward model; (2) a fixed 7-level pressure grid (floating surface level, 850 hPa, 700 hPa, 500 hPa,

350 hPa, 250 hPa, 150 hPa); (3) a global a priori profile and covariance matrix for all retrievals; and (4) a state vector which consists of a CO profile, given in terms of a Volume Mixing Ratio (VMR), a surface temperature and a surface emissivity.

A full description of the MOPITT “version 4” (V4) product is given by Deeter et al. [2010]. As with the V3 data set, the V4 algorithm is based on an OEM retrieval technique, using MOPFAS as the forward model. There are however significant differences between the V3 and V4 algorithms, and some of these are now discussed. Whereas the V3 state vector represented the CO vertical profile as a set of VMR values, the V4 state vector represents the CO profile as a set of  $\log(\text{VMR})$  values; it was found that the use of a VMR probability distribution function in V3 occasionally resulted in unrealistic negative VMR values, and so by representing the CO profile in  $\log(\text{VMR})$  space in the V4 product, these negative values were eliminated. The motivation for using the  $\log(\text{VMR})$  state vector for V4 was thus to avoid these negative values, and also to provide a greater consistency with observations. In addition to this, the V4 state vector expresses the CO profile on a 10-level pressure grid (floating surface level followed by nine uniformly spaced levels from 900 to 100 hPa) instead of the seven-level grid used for V3; this change to an equidistant pressure grid was implemented because a retrieval grid with uniform grid spacing (in pressure units) simplifies the physical interpretation of the retrieval, as was discussed in Sec. 5.3.2.2.

For the V4 product some changes to the MOPFAS radiative transfer model were also made in comparison to that used in the V3 algorithm. In extremely polluted conditions, V3 retrievals sometimes failed because they exceeded the upper CO concentration limit of MOPFAS. For the V4 product the MOPFAS forward model was therefore modified to allow for retrievals with significantly higher values, with the number of training profiles expanded from 58 to 116. In the original set of training profiles only two profiles were included that had a CO surface concentration of greater than 300ppbv [Edwards et al., 1999]. The added atmospheres were derived by scaling the original training set profiles by a factor of two. As part of its processing, MOPFAS also incorporates models of the physical states of the MOPITT LMCs and PMCs, and for the V4 algorithm, both the PMC and LMC models have been updated for consistency with the actual on-orbit cell pressure and temperature values observed during the mission. Specifically, the pressure and temperature values that are used to

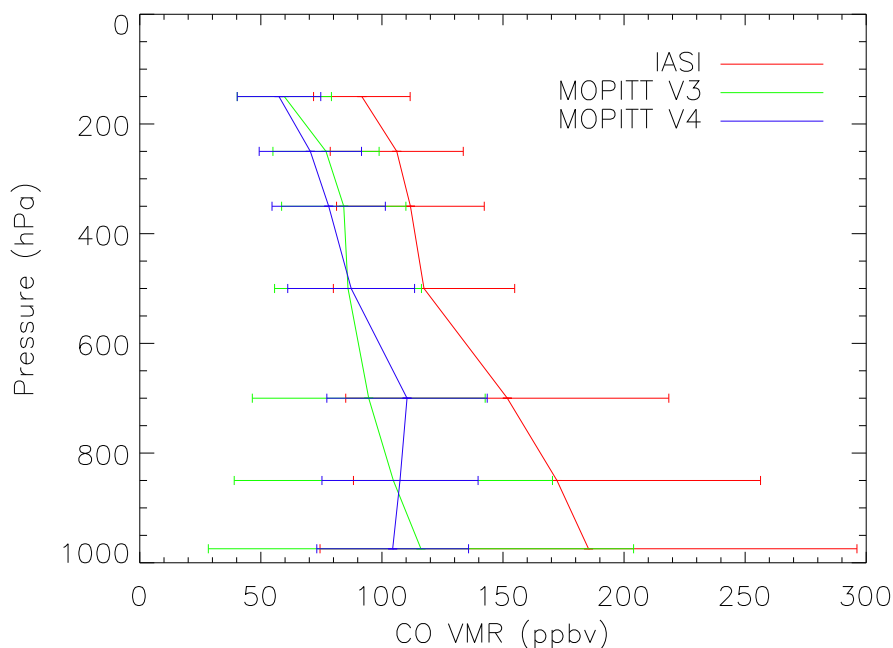


Figure 6.1: IASI and MOPITT V3 a priori profile and associated errors (i.e. the diagonal of the a priori covariance matrix), as well as the MOPITT V4 a priori profile averaged over the region shown in Fig. 6.4 for 1 September 2007. The profiles have all been interpolated onto the MOPITT V3 pressure grid for ease of reference

model the LMCs in MOPFAS are now time-mean values, whilst the shapes and relative phases of the PMC pressure and temperature cycles remain unchanged. These updated models also reflect instrumental modifications performed after the failure of one of MOPITT’s two coolers which occurred on 7 May 2001.

One of the most significant differences between the MOPITT V3 and V4 retrieval algorithms is the choice of the a priori profiles and covariance matrices. In the MOPITT V3 product, a global a priori profile was employed for all retrievals; as discussed in Sec.5.3.3.3, this ensures that any features in the retrieved CO actually correspond to information in the measurements. However, it is also true that using a global a priori can sometimes yield large systematic differences between the “true” CO concentration and the retrieved value, at levels where the weighting functions exhibit low sensitivity. In an attempt to reduce these a priori-related errors, V4 a priori profiles are based on a monthly climatology from the global CTM MOZART-4 (Model for

OZone And Related chemical Tracers, version 4) [Emmons et al., 2010], where for each retrieval, the climatology is spatially and temporally interpolated to the time and location of the observation. Like in V3, the V4 algorithm uses a global a priori covariance matrix, but sets the diagonal elements to a fractional VMR variability of 30 %, and assumes a smoothing length of 100 hPa [Deeter et al., 2010]; these values have been chosen based on analyses of aircraft in situ data sets at individual MOPITT validation sites. This relatively small value for the smoothing length acts to reduce the projection of information from levels where the MOPITT weighting functions are relatively strong (e.g., the mid-lower troposphere) to levels where the weighting functions are relatively weak (e.g., the surface). An example of the differences between the V3 and V4 a priori profiles and covariances matrices is plotted in Fig. 6.1.

### 6.2.3 Comparison of MOPITT V3 and V4 Averaging Kernels

Figure 6.2 shows a plot of the averaged daytime and oceanic MOPITT V3 and V4 averaging kernels ( $\mathbf{A}^{\text{MOP3}}$  and  $\mathbf{A}^{\text{MOP4}}$ ) for 1 September 2007 over the region shown in Fig. 6.4 (hereafter referred to as the Southern Africa region), at each of the pressure levels for the relevant retrieval grid, and illustrates how the retrieved CO profiles in MOPITT V3 and V4 exhibit different sensitivities to the true profile. It is also important to note that  $\mathbf{A}^{\text{MOP3}}$  and  $\mathbf{A}^{\text{MOP4}}$  do not represent the same quantity:  $\mathbf{A}^{\text{MOP3}}$  is  $d\hat{\mathbf{x}}/d\mathbf{x}$ , whereas  $\mathbf{A}^{\text{MOP4}}$  is  $d\log(\hat{\mathbf{x}})/d\log(\mathbf{x})$ . To the first order the V3 and V4 averaging kernels can be converted using the following relationship:

$$\frac{d\log(\hat{\mathbf{x}})}{d\log(\mathbf{x})} = \left(\frac{\mathbf{x}}{\hat{\mathbf{x}}}\right) \frac{d\hat{\mathbf{x}}}{d\mathbf{x}}. \quad (6.1)$$

Because of the large variations in the averaging kernel matrices between day and night, and over land and ocean, it is important to consider each of these cases separately. If these different scenarios are not analysed individually then there are too many factors that must be accounted for to permit a meaningful analysis, such factors include: varying thermal contrast; varying CO distributions; varying a priori; and varying surface pressures. Similarly, significant latitudinal effects can result in tropical retrievals being quite different from polar retrievals (see e.g. Fig 5.11), and this means that any conclusions will be more justifiable if a specific latitudinal zone

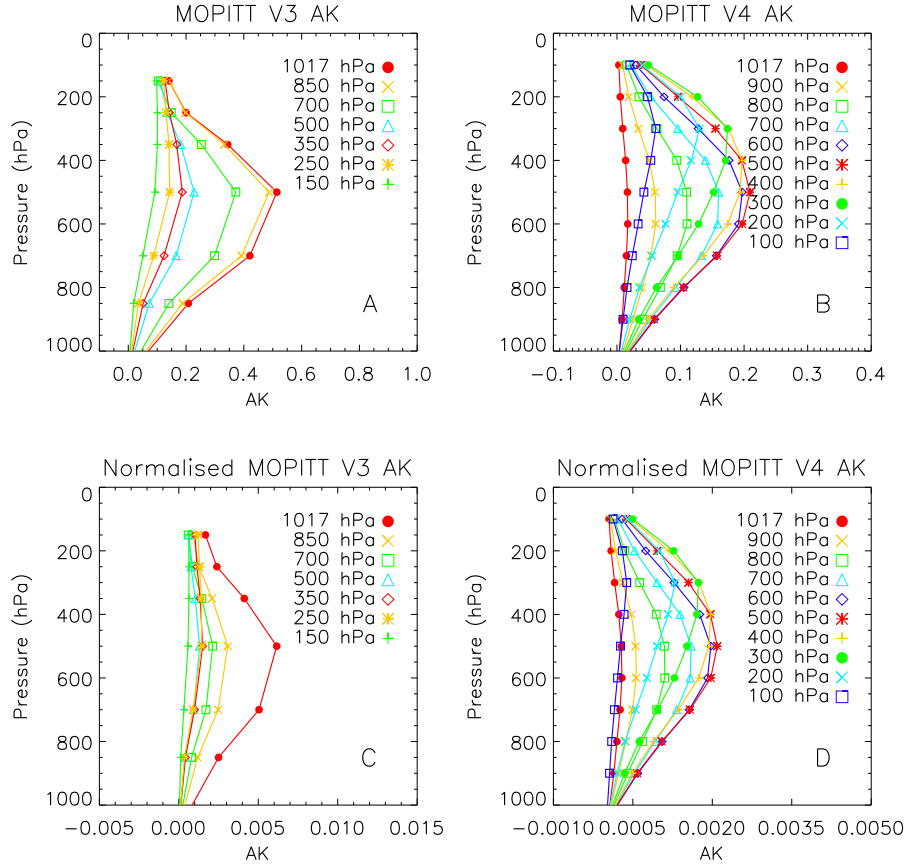


Figure 6.2: Averaged daytime and oceanic averaging kernels for 1 September 2007 over Southern Africa, for: (A) MOPITT V3 ( $\mathbf{A}^{\text{MOP3}}$ ); (B) MOPITT V4 ( $\mathbf{A}^{\text{MOP4}}$ ); (C) pressure-layer-normalised averaging kernels for MOPITT V3 ( $\mathbf{A}_N^{\text{MOP3}}$ ); and (D) pressure-layer-normalised averaging kernels for MOPITT V4 ( $\mathbf{A}_N^{\text{MOP4}}$ ). The MOPITT V3 averaging kernels are in normal space, whereas the MOPITT V4 averaging kernels relate to  $\log(\text{VMR})$  values, and the units of the pressure-layer-normalised averaging kernels are  $\text{hPa}^{-1}$ .

or region, rather than a global data set, is analysed.

The main reason for performing this analysis over the Southern Africa region was because this is the region over which the ULIRS was characterised (see Chapter 5). Over Southern Africa, especially during the fire season (which typically lasts from late July to early November [Giglio et al., 2006]), there is also a large variety in the different CO atmospheric scenarios; Southern Africa thus represents a region over which a wide

variety of CO profiles can be observed, but which should not be adversely affected by latitudinal effects. It has been shown previously [see e.g. Deeter et al., 2007b] that the thermal contrast has a large effect on the MOPITT averaging kernels, therefore the main comparison presented in this study has been carried out during daytime over the ocean, where the effects of the thermal contrast are minimised.

As the averaging kernels are strongly dependent upon the different pressure grids that are used in each of the retrieval schemes, to make a consistent comparison, the pressure-layer-normalised averaging kernels are generated (see Fig. 6.2) using the following equation, taken from Ho et al. [2009]:

$$\mathbf{A}_N^{i,j} = \frac{\mathbf{A}^{i,j}}{\Delta P^i}, \quad (6.2)$$

where  $i$  and  $j$  are indexes of column and row elements of  $\mathbf{A}$  and  $\mathbf{A}_N$ , and  $\Delta P^i$  is the pressure thickness of the layer corresponding to column index  $i$ .

#### 6.2.4 Comparison of MOPITT V3 and V4 Retrievals

The mean CO profiles of the MOPITT V3 and MOPITT V4 retrieval algorithms, over the ocean and for the daytime of 1 September 2007 over the Southern Africa region (see Fig. 6.4) are shown in Fig. 6.3. It can be seen that the largest differences (approximately 70 ppbv) between the MOPITT V3 and V4 CO concentrations occur at the surface, whilst the smallest differences occur between 400 and 600 hPa.

The differences between the MOPITT V3 and MOPITT V4 retrieved profiles shown in Fig. 6.3 are consistent with the results of Deeter et al. [2010], with the mean V3 and V4 retrieved profiles similar in the upper troposphere, and differing greatly in the lower troposphere. One of the major reasons for the observed differences between the MOPITT V3 and V4 profiles is the use of different a priori statistics (i.e. different a priori profiles and covariance matrices). As the V3 algorithm uses a global a priori CO profile for all of its retrievals, the V3 a priori covariance matrix is related to the global variability of CO concentrations, whereas in V4, the a priori covariance matrix describes the fractional variability compared to the local a priori profile (which can be different for each retrieval). This means that there is a much larger variability in the off-diagonal elements of the V3 a priori covariance matrix, in comparison to those used in the V4 algorithm, hence the correlation length for the MOPITT V3

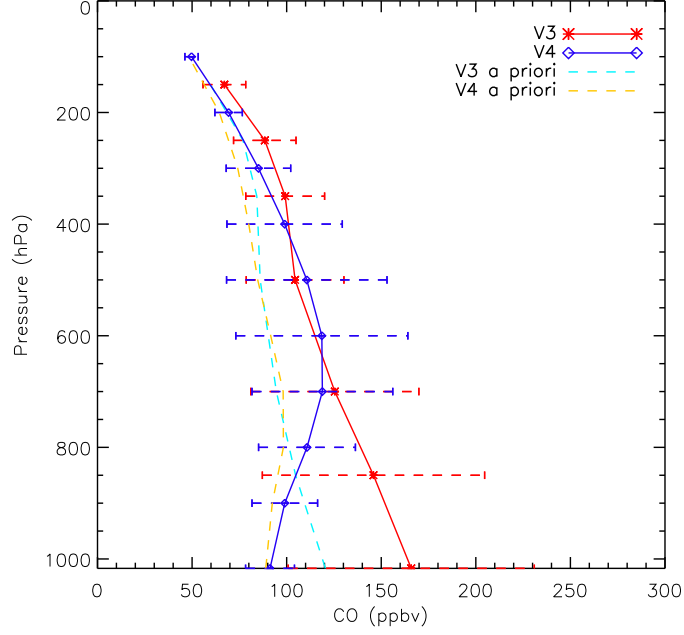


Figure 6.3: MOPITT V3 and V4 mean CO profiles (solid red line and blue line, respectively) and standard deviation relative to their means (dashed horizontal lines) for 1 September 2007 over the Southern Africa region, for the daytime and over the ocean . The MOPITT V3 a priori profile (dashed turquoise line), and mean MOPITT V4 a priori profile (dashed yellow line) used in the retrievals are also shown.

retrievals is longer than for the V4 retrievals ( 500 and 100 hPa, respectively), where the V3 correlation length has been calculated by computing the delta-pressure for which the off-diagonal element of the covariance matrix was found to be  $1/e^2$  times the corresponding diagonal element (Merritt Deeter, personal communication, 2010). The correlation length effectively determines the vertical influence for a change in the concentration of CO at a specific pressure level. This means that for large correlation lengths, retrievals at pressure levels that are insensitive to CO can be strongly influenced by more sensitive levels. One example of where this “false influence” can occur is for scenes with a low-thermal contrast, and hence a lack of sensitivity to the surface; in such scenes a large correlation length can result in the projection of

CO features from the mid-troposphere, where there is an increased sensitivity, to the surface. Such a phenomena could well be responsible for the results seen in Fig. 6.3, with the large differences at the surface being a direct result of the MOPITT V3 being falsely influenced by CO features above 850 hPa.

Another possible cause of the differences between the V3/V4 retrieved profiles is the use of lognormal statistics in the MOPITT V4 retrieval algorithm. Deeter et al. [2007a] showed that the assumption of Gaussian VMR variability in the MOPITT V3 retrieval algorithm is inconsistent with in-situ data sets, and leads to positive retrieval bias in especially clean conditions (e.g., VMR values less than 60 ppbv). As V4 retrievals use a state vector based on  $\log(\text{VMR})$  they are therefore not subject to this effect. A further source of the difference between the MOPITT V3 and V4 data sets is the change in retrieval bias due to drifts in the MOPITT LMCs and PMCs (see Sec. 6.2.2), which are corrected for in the V4 retrieval algorithm, but not in the V3. Emmons et al. [2009] found that the long-term changes in the instrument cell parameters produce a retrieval bias drift on the order of 1 ppbv/yr in the upper troposphere; this bias drift is weaker in the lower and middle troposphere.

### 6.3 Comparison of IASI and MOPITT CO

MOPITT is on board the Terra satellite, which is on a different orbit to MetOp, it is therefore not possible to find exact coincidences between IASI and MOPITT measurements. Thus, to ensure a reasonable coincidence criteria and sample size, only IASI and MOPITT retrievals that correspond spatially to within 50 km, and which differ on a temporal timescale by at most 90 min are considered for this intercomparison; 90 min was chosen, because it allowed for the maximum amount of data to be collated whilst minimising the effects of transportation. The IASI retrievals were further filtered by using the Root Mean Square (RMS) difference between simulated and observed spectra, as well as the  $\chi^2$  value of the retrieval (given by the normalised form of Eq. 2.52). Only retrievals which had a RMS of less than  $3.5 \text{ nW/cm}^2/\text{cm}^{-1}/\text{sr}$  and a  $\chi^2$  of less than 3.5 were considered for the comparison. Any IASI and MOPITT matches where the surface pressures used in the retrieval process differed by more than 20 hPa were also neglected.

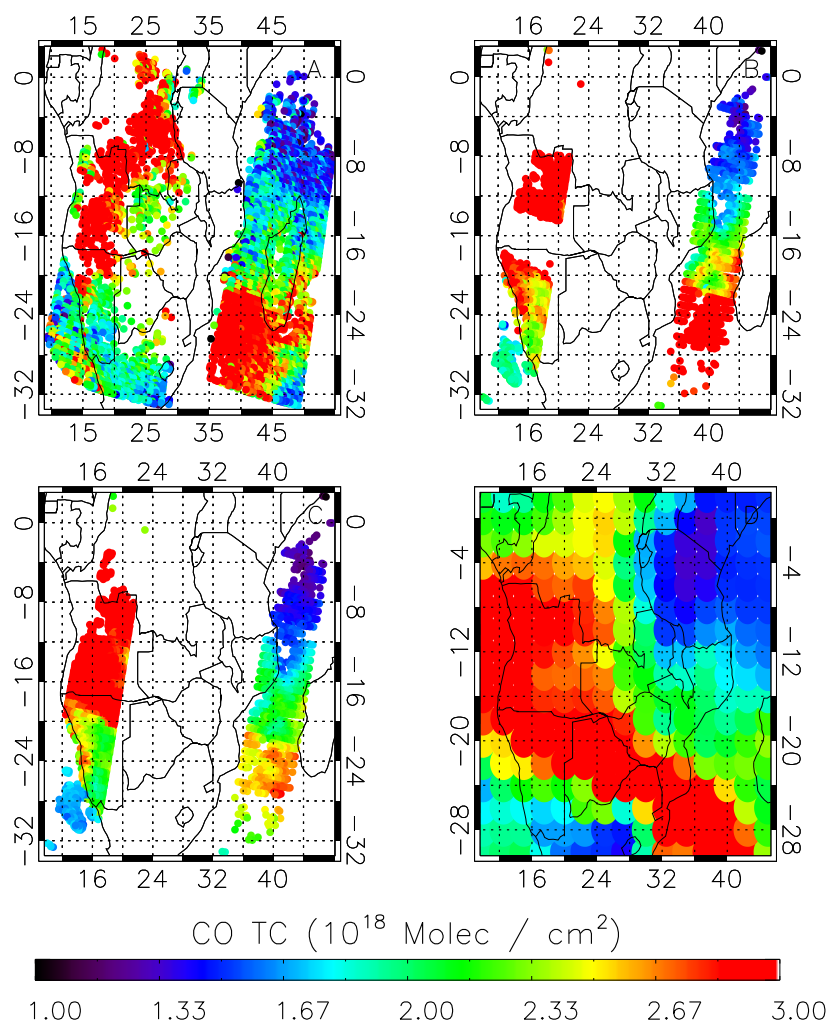


Figure 6.4: CO total column density over Southern Africa during the daytime of 1 September 2007: (A) IASI; (B) MOPITT V3; (C) MOPITT V4; and (D) GEOS-Chem.

The region considered for comparison, along with the retrieved CO total column densities for each of the algorithms is shown in Fig. 6.4. As was discussed in Sec. 6.2.3 it is important to consider the day/night and land/ocean retrievals separately, and the remainder of the figures in this study are for the comparison between daytime retrievals over the ocean.

The IASI and MOPITT retrieval algorithms are set up on pressure grids which differently sample the troposphere, thus the IASI retrievals which were on the pressure

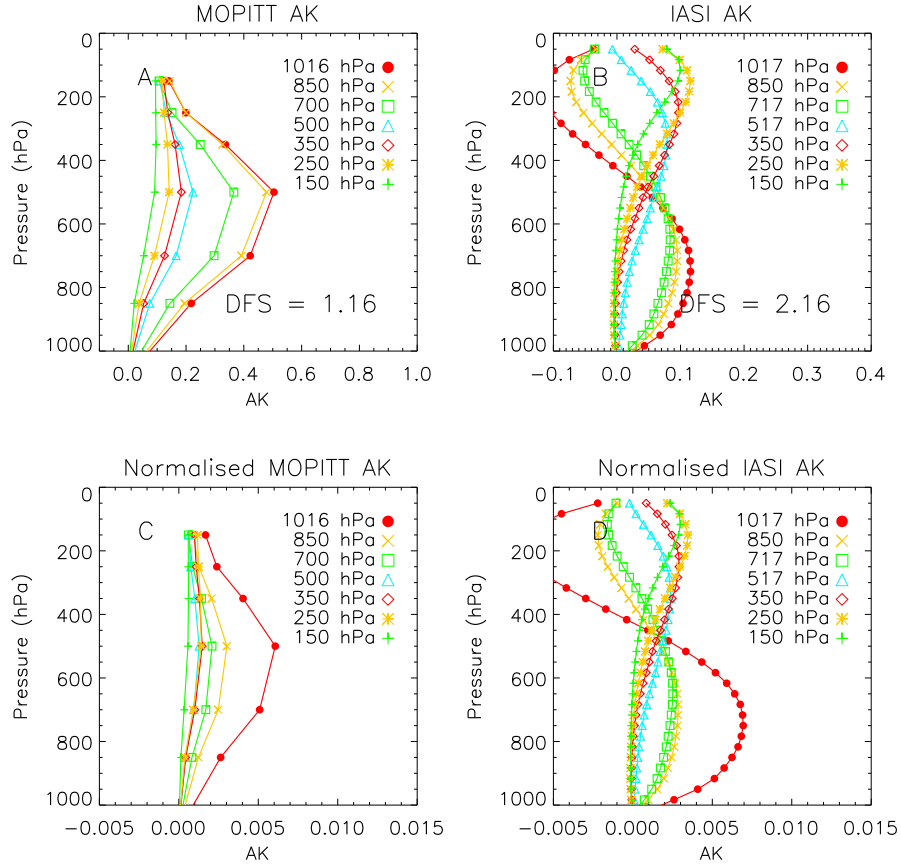


Figure 6.5: Daytime and ocean averaging kernels over the Southern Africa region for 1 September 2007, for: (A) MOPITT V3 ( $\mathbf{A}^{\text{MOP3}}$ ) at MOPITT V3 pressure levels; (B) IASI ( $\mathbf{A}^{\text{IASI}}$ ) at the IASI pressure levels closest to the MOPITT V3 pressure levels; (C) pressure-layer-normalised averaging kernels for MOPITT V3 ( $\mathbf{A}_N^{\text{MOP3}}$ ); and (D) pressure-layer-normalised averaging kernels for IASI ( $\mathbf{A}_N^{\text{IASI}}$ ). The units of the pressure-layer-normalised averaging kernels are  $\text{hPa}^{-1}$ .

levels closest to those of the corresponding MOPITT pressure levels were selected for comparison. The MOPITT V3 ( $\mathbf{A}^{\text{MOP3}}$ ) and IASI averaging kernels ( $\mathbf{A}^{\text{IASI}}$ ) at retrieval pressure levels close to those of MOPITT V3 are shown in Fig. 6.5, whilst the MOPITT V4 ( $\mathbf{A}^{\text{MOP4}}$ ) and IASI averaging kernels ( $\mathbf{A}^{\text{IASI}}$ ) at retrieval pressure levels closest to those of MOPITT V4 are shown in Fig. 6.6. These mean averaging kernels ( $\mathbf{A}^{\text{MOP3}}$ ,  $\mathbf{A}^{\text{MOP4}}$  and  $\mathbf{A}^{\text{IASI}}$ ) correspond to daytime, oceanic averages from MOPITT and IASI for 1 September 2007 over the Southern Africa region shown in

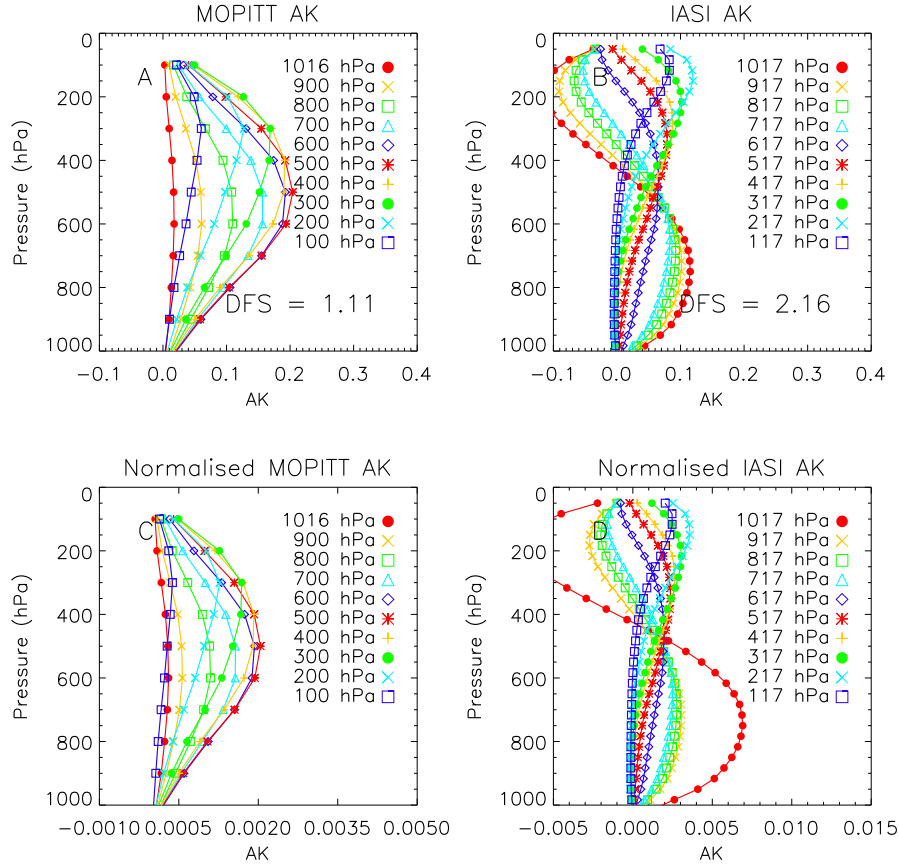


Figure 6.6: Daytime and ocean averaging kernels over the Southern Africa region for 1 September 2007, for: (A) MOPITT V4 ( $\mathbf{A}^{\text{MOP}4}$ ) at MOPITT V4 pressure levels; (B) IASI ( $\mathbf{A}^{\text{IASI}}$ ) at the IASI pressure levels closest to the MOPITT V4 pressure levels; (C) pressure-layer-normalised averaging kernels for MOPITT V4 ( $\mathbf{A}_N^{\text{MOP}4}$ ); and (D) pressure-layer-normalised averaging kernels for IASI ( $\mathbf{A}_N^{\text{IASI}}$ ). The units of the pressure-layer-normalised averaging kernels are  $\text{hPa}^{-1}$ .

Fig. 6.4. As with the differences between  $\mathbf{A}^{\text{MOP}3}$  and  $\mathbf{A}^{\text{MOP}4}$ , the different magnitudes between  $\mathbf{A}^{\text{MOP}}$  and  $\mathbf{A}^{\text{IASI}}$  are mainly due to the different pressure layer thicknesses of the retrieval grids used by MOPITT V3/V4 (7/10 layers) and IASI (30 layers). In addition to this, whilst the IASI and MOPITT V3 averaging kernels both represent  $d\hat{\mathbf{x}}/d\mathbf{x}$ , the MOPITT V4 averaging kernels correspond to  $d\log(\hat{\mathbf{x}})/d\log(\mathbf{x})$ .

The MOPITT V3 and IASI mean CO profiles and standard deviation relative to their means are shown in Fig. 6.7(A), at MOPITT V3 pressure levels for the 1

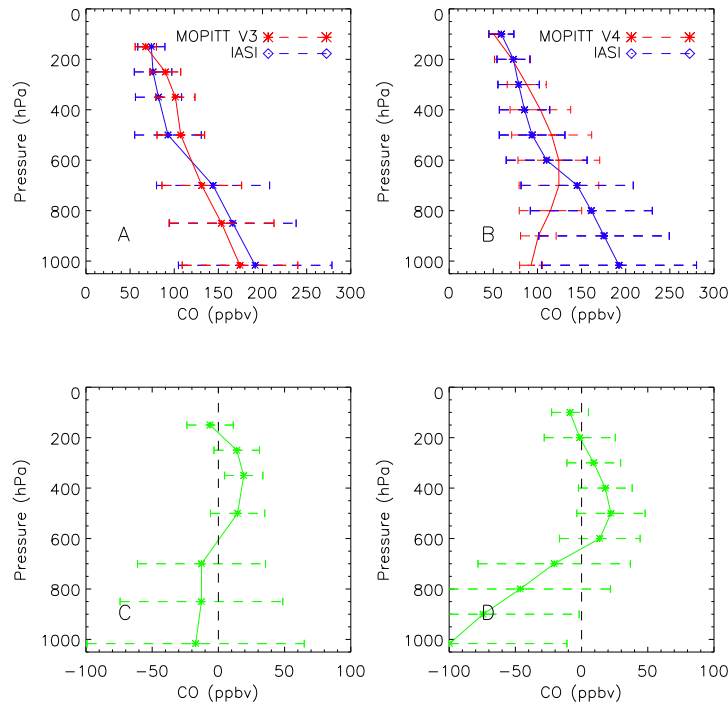


Figure 6.7: (A) MOPITT V3 and IASI CO mean profiles (solid red line and blue line, respectively) and standard deviation relative to their means (dashed lines); (B) MOPITT V4 and IASI CO mean profiles (solid red line and blue line, respectively) and standard deviation relative to their means (dashed lines); (C) the mean difference between MOPITT V3 CO and IASI CO (solid green line) and the standard deviation (dashed green line) relative to the mean; and (D) the mean difference between MOPITT V4 CO and IASI CO (solid green line) and the standard deviation (dashed green line) relative to the mean. The IASI CO retrievals closest to the MOPITT pressure levels are used here, and all comparisons are for over the ocean and during the daytime of 1 September 2007, over the Southern Africa region

September 2007, over the Southern Africa region for the daytime over the ocean. As can be seen from Fig. 6.7(C),  $\mathbf{x}^{\text{IASI}}$  overestimates  $\mathbf{x}^{\text{MOP3}}$  at pressure levels greater than 500 hPa, and is an underestimate at lower pressures. The results from the intercomparison of IASI ( $\mathbf{x}^{\text{IASI}}$ ) and MOPITT V3 ( $\mathbf{x}^{\text{MOP3}}$ ) CO are summarised in Table 6.1.

Figure 6.7(B) shows the MOPITT V4 and IASI mean CO profiles and standard deviation relative to their means, at MOPITT V4 pressure levels for the 1 September 2007 over the Southern Africa region. The differences between the two products are depicted in Fig. 6.7(D), with large apparent discrepancies between the mean IASI and MOPITT V4 CO profiles below 800 hPa symptomatic of the difference in the relative correlation lengths of the two different retrieval algorithms. As was discussed in Sec. 6.2.4 the correlation length used in the MOPITT V4 algorithm is 100 hPa and the a priori profile is based on modelled data that is spatially and temporally interpolated to the retrieval scene. As the IASI retrieval scheme uses a constant a priori profile, and has a smoothing length of approximately 400 hPa (again estimated by computing the delta-pressure for which the off-diagonal element of the covariance matrix was found to be  $1/e^2$  times the corresponding diagonal element), it is more prone to being influenced by mid-tropospheric CO events, to which it has a greater sensitivity compared to the surface (as can be seen from Figs. 6.5 and 6.6). The results from the intercomparison of IASI ( $\mathbf{x}^{\text{IASI}}$ ) and MOPITT V4 ( $\mathbf{x}^{\text{MOP4}}$ ) CO are summarised in Table 6.2.

The results presented in Fig. 6.7 indicate that with respect to the effect of projection of information in the mid-troposphere to the surface, the IASI retrievals more closely resemble the MOPITT V3 than the V4 retrievals. This is to be expected given the similarity in the smoothing lengths of the IASI and MOPITT V3 a priori covariance matrices (400 and 500 hPa, respectively, in comparison to 100 hPa for the MOPITT V4 algorithm), as well as the fact that the diagonal elements of the a priori covariance matrix are similar for IASI and MOPITT V3, in comparison to those for MOPITT V4 (see horizontal error bars in Fig.6.1). It should also be noted that the differences between the MOPITT V3 and V4 retrieved profiles that can be inferred from Fig. 6.7 are the same as those shown in Fig. 6.3.

## 6.4 Comparison of IASI and MOPITT CO Using the Same A Priori

It is instructive to investigate whether the differences observed between  $\mathbf{x}^{\text{IASI}}$  and  $\mathbf{x}^{\text{MOP}}$  are due to the choice of a priori used by each of the retrieval schemes. A useful

	$\mathbf{x}^{\text{MOP3}} - \mathbf{x}^{\text{IASI}}$ (N=987)	$\mathbf{x}^{\text{MOP3}'} - \mathbf{x}^{\text{IASI}}$ (N=974)	$\delta_{\text{MODEL}}$ (N=975)	$\mathbf{x}^{\text{MOP3}'} - \mathbf{x}^{\text{IASI}'}$ (N=972)	$\delta_{\text{MODEL}'}$ (N=972)
850 hPa					
Mean (ppbv)	-12.8 (61.4)	-14.1 (62.9)	-30.3 (18.5)	11.2 (39.1)	7.3 (14.6)
Bias (%)	-7.7 (36.9)	-8.5 (37.8)	-18.7 (11.4)	8.0 (27.8)	5.9 (11.8)
500 hPa					
Mean (ppbv)	14.5 (19.1)	8.1 (20.5)	7.0 (7.1)	5.7 (12.8)	3.6 (5.5)
Bias (%)	15.6 (20.5)	8.8 (22.1)	8.0 (8.1)	6.0 (13.4)	4.1 (6.3)
250 hPa					
Mean (ppbv)	13.9 (16.8)	17.9 (18.3)	17.2 (10.2)	1.5 (8.8)	1.5 (2.1)
Bias (%)	18.2 (22.0)	23.6 (24.1)	23.3 (13.8)	1.6 (9.5)	1.7 (2.4)
Total column					
Absolute Bias (%)	1.2 (20.3)	2.4 (20.4)	1.8 (6.1)	6.4 (17.5)	4.0 (7.3)

Table 6.1: Mean and percentage biases for IASI and MOPITT V3 CO profiles, as well as the mean absolute total column biases between the two products, for daytime over the oceanic Southern Africa region on 1 September 2007. N represents the number of retrievals, and the parentheses denote the standard deviations relative to the mean. Note also that the percentage biases represent the ratio to the mean IASI value.

way to examine this problem, is to use the same a priori profile and covariance for both the MOPITT and IASI retrievals. In order to do this the IASI a priori profiles and covariance matrices were integrated into the MOPITT V3 and V4 retrieval algorithms.

The differences between the IASI ( $\mathbf{x}^{\text{IASI}}$ ) and “adjusted” MOPITT ( $\mathbf{x}^{\text{MOP3}'}$ ) profiles shown in Fig. 6.8(C) are similar to the differences between the IASI and MOPITT V3 profiles (Fig. 6.7(C)), which is to be expected given the similarities in the smoothing length and a priori covariance matrices of the IASI and MOPITT V3 retrieval algorithms. Figure 6.8(D) also demonstrates that  $\mathbf{x}^{\text{IASI}}$  and  $\mathbf{x}^{\text{MOP4}'}$  are in better agreement, particularly in the lower troposphere, compared to the differences between  $\mathbf{x}^{\text{IASI}}$  and  $\mathbf{x}^{\text{MOP4}}$  (Fig. 6.7(D)). This result is mainly explained by the fact that both retrievals now use the same a priori statistics, in particular utilising an

	$\mathbf{x}^{\text{MOP4}} - \mathbf{x}^{\text{IASI}}$ (N=1041)	$\mathbf{x}^{\text{MOP4}'} - \mathbf{x}^{\text{IASI}}$ (N=1038)	$\delta_{\text{MODEL}}$ (N=1042)	$\mathbf{x}^{\text{MOP4}'} - \mathbf{x}^{\text{IASI}'}$ (N=1042)	$\delta_{\text{MODEL}'}$ (N=1038)
900 hPa					
Mean (ppbv)	-74.4 (72.8)	-28.9 (66.7)	-41.9 (35.9)	3.1 (26.9)	3.5 (8.1)
Bias (%)	-42.4 (41.5)	-16.5 (38.0)	-24.3 (20.8)	2.2 (18.7)	2.8 (6.3)
500 hPa					
Mean (ppbv)	22.2 (25.4)	2.0 (19.8)	3.2 (4.2)	2.1 (12.0)	4.2 (6.3)
Bias (%)	23.6 (27.0)	2.2 (21.0)	3.6 (4.8)	2.3 (12.7)	4.8 (7.2)
200 hPa					
Mean (ppbv)	-1.4 (18.6)	13.5 (18.6)	14.3 (11.2)	0.5 (5.8)	2.4 (3.5)
Bias (%)	-1.9 (25.6)	18.5 (25.5)	20.2 (15.9)	0.5 (6.8)	2.9 (4.2)
Total column					
Absolute Bias (%)	14.0 (22.0)	5.6 (20.3)	18.4 (9.3)	2.9 (14.7)	2.5 (3.2)

Table 6.2: Same as Table 6.1, but for IASI and MOPITT V4 CO retrievals.

identical correlation length, meaning that the surface retrievals are equally affected by the influence of mid-tropospheric events. The results from the intercomparison between the IASI and adjusted MOPITT V3 and V4 CO products are summarised in Tables 6.1 and 6.2 respectively.

The differences between the MOPITT V3 and V4 retrieved profiles in Fig. 6.8 are significantly less than the differences between those shown in Fig. 6.7; this indicates that some of the differences between the operational MOPITT V3 and V4 retrieved products can be explained by the different a priori statistics used in each of these schemes.

### 6.4.1 Smoothing Bias

Whilst the IASI and MOPITT products have now been retrieved using the same a priori information, there still exist differences in the measurement sensitivity, i.e.

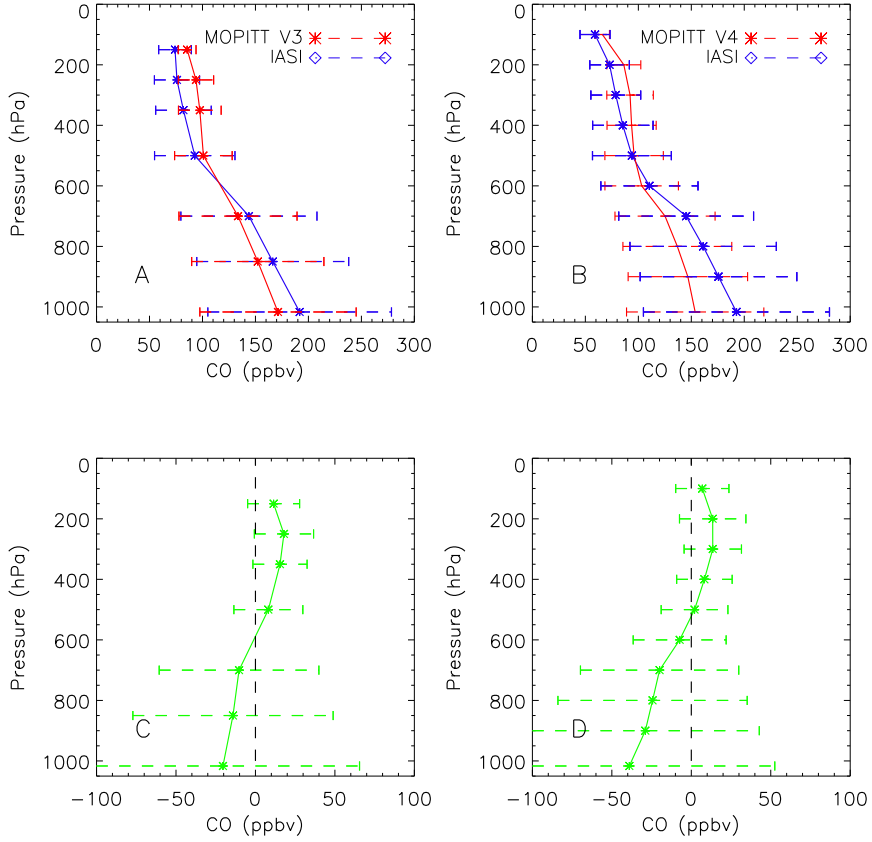


Figure 6.8: Same as Fig. 6.7, except for  $\mathbf{x}^{\text{MOP}}$  and  $\mathbf{x}^{\text{IASI}}$ : (A) adjusted MOPITT V3 and IASI CO mean profiles; (B) adjusted MOPITT V4 and IASI CO mean profiles; (C) the mean difference between adjusted MOPITT V3 CO and IASI CO profiles; and (D) the mean difference between adjusted MOPITT V4 CO and IASI CO profiles.

weighting functions and noise, of the retrievals. The retrieved state vector can be written as a weighted mean of the true profile ( $\mathbf{x}_{\text{true}}$ ) and the a priori profile ( $\mathbf{x}_{\text{a}}$ ) [Rodgers and Connor, 2003]. In the case of IASI retrievals this can be written as:

$$\mathbf{x}^{\text{IASI}} = \mathbf{A}^{\text{IASI}} (\mathbf{x}_{\text{true}} - \mathbf{x}_{\text{a}}^{\text{IASI}}) + \mathbf{x}_{\text{a}}^{\text{IASI}} + \epsilon^{\text{IASI}}, \quad (6.3)$$

whilst for the MOPITT retrievals (V3 and V4):

$$\mathbf{x}^{\text{MOP}} = \mathbf{A}^{\text{MOP}} (\mathbf{x}_{\text{true}} - \mathbf{x}_{\text{a}}^{\text{MOP}}) + \mathbf{x}_{\text{a}}^{\text{MOP}} + \epsilon^{\text{MOP}}, \quad (6.4)$$

where  $\epsilon$  represents the error in the retrieved profiles due to both random and systematic errors in the measured signal and in the algorithm's forward model [Rodgers

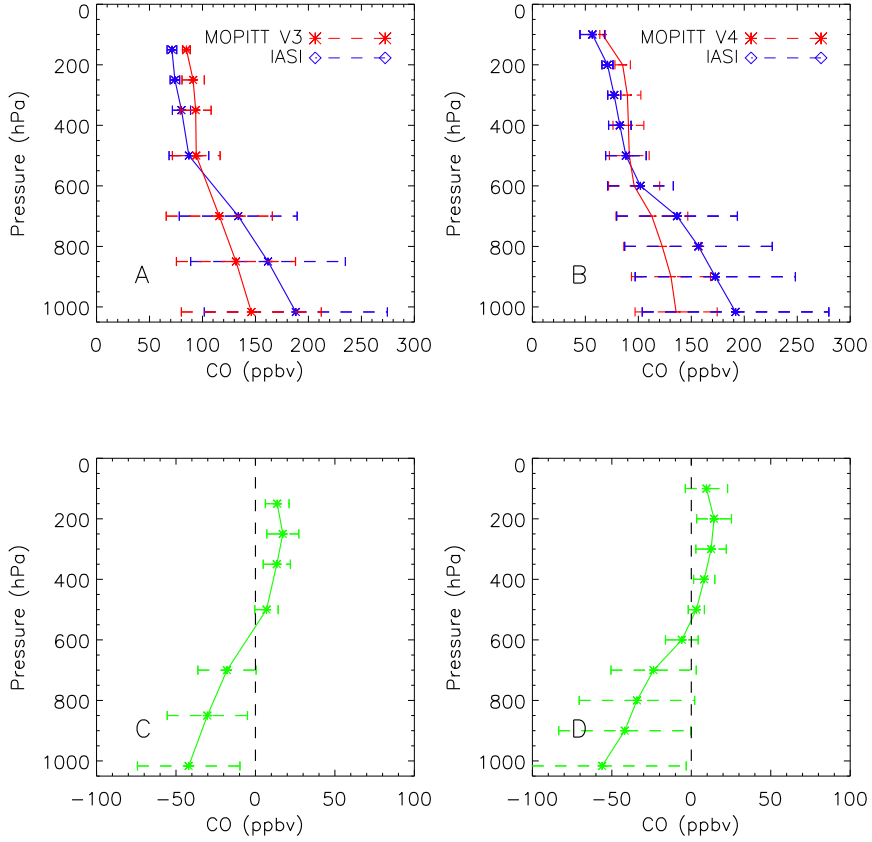


Figure 6.9: Same as Fig. 6.7, except for  $\mathbf{x}_{\text{MODEL}}^{\text{MOP}'}$  and  $\mathbf{x}_{\text{MODEL}}^{\text{IASI}}$ : (A) adjusted MOPITT V3 and IASI CO mean profiles; (B) adjusted MOPITT V4 and IASI CO mean profiles; (C) the mean difference between adjusted MOPITT V3 CO and IASI CO profiles; and (D) the mean difference between adjusted MOPITT V4 CO and IASI CO profiles. (A) and (B) are in relation to the retrieval of a true profile, as provided by GEOS-Chem.

and Connor, 2003]. By processing the MOPITT retrieval algorithms using the IASI a priori, the modified MOPITT retrieved CO profile,  $\mathbf{x}^{\text{MOP}'}$ , can be written as:

$$\mathbf{x}^{\text{MOP}'} = \mathbf{A}^{\text{MOP}'} (\mathbf{x}_{\text{true}} - \mathbf{x}_{\text{a}}^{\text{IASI}}) + \mathbf{x}_{\text{a}}^{\text{IASI}} + \epsilon^{\text{MOP}'}, \quad (6.5)$$

where  $\mathbf{A}^{\text{MOP}'}$  represents the adjusted MOPITT (V3 and V4) averaging kernel matrices.

Differences between  $\mathbf{x}^{\text{IASI}}$  and  $\mathbf{x}^{\text{MOP}'}$  can be characterised from Eqs. 6.3 and 6.5. Further insight into differences in the smoothing effect of the two retrievals (the

smoothing bias) can be obtained by examining what happens when the averaging kernels for each instrument are applied to a true profile (thus simulating the effect of retrieval characteristics on the retrieved profiles). For this study the truth is represented by  $2.5^\circ$  by  $2^\circ$  gridded output from the GEOS-Chem (v7.04.10) CTM (Bey et al. [2001] and <http://www.GEOS-Chem.org/>). GEOS-Chem is a global 3-D CTM for atmospheric composition that principally uses meteorological input from the Goddard Earth Observing System (GEOS) of the NASA global modelling and assimilation office; in this study inventories such as the Global Fire Emissions Data Base (GFED) [Van Der Werf et al., 2006] were used to generate the free run GEOS-Chem CO profiles,  $\mathbf{x}^{\text{GEOS}}$ , with the closest  $\mathbf{x}^{\text{GEOS}}$  to the collocated IASI and adjusted MOPITT CO profiles being used for this comparison; the GEOS-Chem total column densities for the studied region are shown in Fig. 6.4(D).

$\mathbf{x}_{\text{MODEL}}^{\text{IASI}}$  and  $\mathbf{x}_{\text{MODEL}}^{\text{MOP}'}$  have been calculated from Eqs. 6.3 and 6.5, respectively, with  $\mathbf{x}_{\text{true}}$  given by  $\mathbf{x}^{\text{GEOS}}$ . In the absence of any other biases,  $\mathbf{x}_{\text{MODEL}}^{\text{MOP}'}$  and  $\mathbf{x}_{\text{MODEL}}^{\text{IASI}}$  represent the “best possible” retrieval of the GEOS-Chem profiles by the adjusted MOPITT and IASI algorithms, respectively. The results from the intercomparison between the expected smoothing biases  $\delta_{\text{MODEL}}$  MOPITT V3 and V4 CO products are summarised in Tables 6.1 and 6.2 respectively.

As can be seen from Figs. 6.8 and 6.9, and also from Tables 6.1 and 6.2, the differences between  $\mathbf{x}_{\text{MODEL}}^{\text{MOP}'}$  and  $\mathbf{x}_{\text{MODEL}}^{\text{IASI}}$  are of a very similar magnitude to those that are observed between  $\mathbf{x}^{\text{IASI}}$  and  $\mathbf{x}^{\text{MOP}'}$ . Retrieving GEOS-Chem modelled profiles in this manner has therefore shown that many of the observed differences between the IASI and adjusted MOPITT retrievals can be explained by the smoothing bias.

## 6.5 Comparison with Reduced Smoothing Error

The results of Sec. 6.4.1 indicate that the differences between  $\mathbf{x}^{\text{MOP}'}$  and  $\mathbf{x}^{\text{IASI}}$  are a result of the smoothing bias. The direct comparison between the products includes a contribution from smoothing error, even when the same a priori is used for the retrievals of both instruments to be compared. This arises from the non-identical weighting functions and error covariances of the two instruments. Ho et al. [2009] proposed a methodology in which the averaging kernels of one retrieval scheme are

used to smooth the retrieved data set from the other set of measurements, providing that both retrievals utilise the same set of a priori statistics. With the caveat that this “double smoothing” of the truth will serve to smooth away some of the intrinsic information contained within the retrieved data set, this section discusses such a method, the justification for its use, and the results that are obtained.

### 6.5.1 Methodology

Rodgers and Connor [2003] showed that the effect of different averaging kernels can be reduced if the retrieval of one instrument is simulated using the retrieval of another. For profiles used in this study, the number of DFS for the MOPITT retrievals were found to be comparable to, yet usually smaller than, that of IASI. The DFS for IASI over the oceanic Southern Africa region during the daytime were found to range from 1.34 to 2.53, whereas those corresponding to  $A^{\text{MOP3'}}$  and  $A^{\text{MOP4'}}$  were found to range from 0.99 to 2.29 and from 0.95 to 2.00, respectively.

Providing that common a priori statistics are used in the retrievals, Rodgers and Connor [2003] states that:

$$\mathbf{x}^{\text{IASI}'} = \mathbf{A}^{\text{MOP}''} (\mathbf{x}_{\text{IASI}} - \mathbf{x}_{\text{a}}^{\text{IASI}}) + \mathbf{x}_{\text{a}}^{\text{IASI}}, \quad (6.6)$$

where  $\mathbf{A}^{\text{MOP}''}$  is  $\mathbf{A}^{\text{MOP}'}$ , but converted onto the same pressure grid as that used by IASI, and  $\mathbf{x}^{\text{IASI}'}$  now represents the retrieved IASI profile, smoothed using  $\mathbf{A}^{\text{MOP}''}$ .

From Eqs. 6.3, 6.5, and 6.6, the difference between  $\mathbf{x}^{\text{IASI}'}$  and  $\mathbf{x}^{\text{MOP}'}$  can be written as:

$$\mathbf{x}^{\text{MOP}'} - \mathbf{x}^{\text{IASI}'} = (\mathbf{A}^{\text{MOP}''} - \mathbf{A}^{\text{MOP}''} \mathbf{A}^{\text{IASI}}) (\mathbf{x}_{\text{true}} - \mathbf{x}_{\text{a}}^{\text{IASI}}) + \epsilon^{\text{MOP}'} - \mathbf{A}^{\text{MOP}'} \epsilon^{\text{IASI}}. \quad (6.7)$$

Providing that the  $\mathbf{A}^{\text{MOP}''} - \mathbf{A}^{\text{MOP}''} \mathbf{A}^{\text{IASI}}$  term is small, Eq. 6.7 should represent the difference between the MOPITT systematic error and the vertical IASI smoothed systematic error. As can be seen from Figs. 6.10 and 6.11, the DFS for  $\mathbf{A}^{\text{MOP}''} - \mathbf{A}^{\text{MOP}''} \mathbf{A}^{\text{IASI}}$  are on average 0.07 and 0.03 for the MOPITT V3 and V4 retrievals, respectively. As this difference quantity is larger for the MOPITT V3 comparisons, it makes the results of  $\mathbf{x}^{\text{MOP}'} - \mathbf{x}^{\text{IASI}'}$  more difficult to interpret than for the corresponding IASI and V4 analysis.

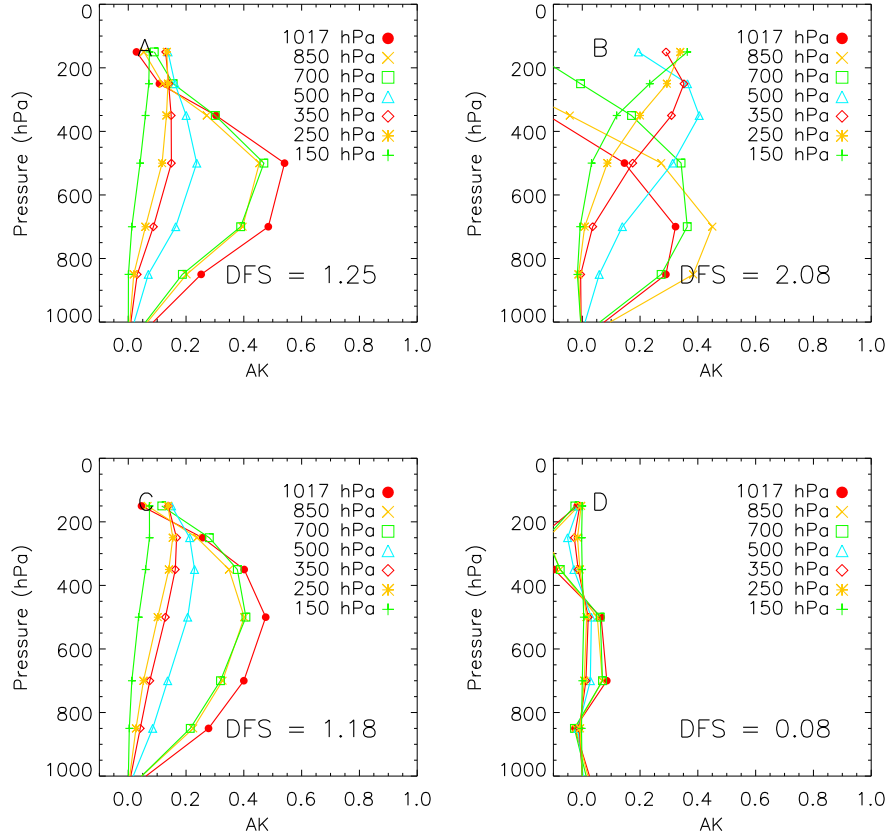


Figure 6.10: Daytime and ocean averaging kernels over the Southern Africa region for 1 September 2007, for: (A) adjusted MOPITT V3 averaging kernels converted onto the IASI pressure grid  $\mathbf{A}^{\text{MOP3}^{\text{r}}}$ ; (B) IASI averaging kernels at pressure levels closest to the MOPITT V3 pressure levels  $\mathbf{A}^{\text{IASI}}$ ; (C)  $\mathbf{A}^{\text{MOP3}^{\text{r}}} \mathbf{A}^{\text{IASI}}$ ; and (D)  $\mathbf{A}^{\text{MOP3}^{\text{r}}} - \mathbf{A}^{\text{MOP3}^{\text{r}}} \mathbf{A}^{\text{IASI}}$

## 6.5.2 Results

Application of the above process to a representative true profile is important in order to demonstrate that the smoothing error terms have been very much reduced. Again, GEOS-Chem CO profiles, were used for this comparison, with the smoothing bias now represented by  $\delta_{\text{MODEL}'}$ . It should be noted that  $\delta_{\text{MODEL}'}$  represents the expected smoothing bias for  $\mathbf{x}^{\text{IASI}'}$  and  $\mathbf{x}^{\text{MOP}'}$ , whilst  $\delta_{\text{MODEL}}$  represents the expected smoothing bias for  $\mathbf{x}^{\text{IASI}}$  and  $\mathbf{x}^{\text{MOP}}$ . As can be seen from Fig. 6.13, the smoothing error across the profiles, in the case of both the MOPITT V3 and V4 comparisons is small.

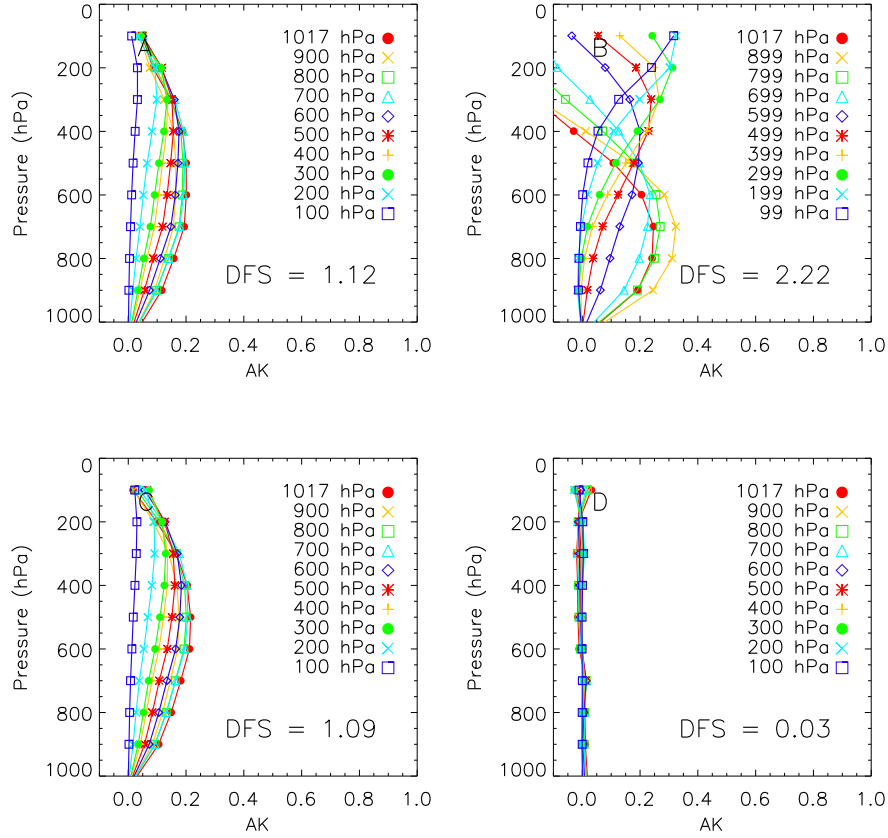


Figure 6.11: Daytime and ocean averaging kernels over the Tropical Africa region for 1 September 2007, for: (A) adjusted MOPITT V4 averaging kernels converted onto the IASI pressure grid  $\mathbf{A}^{\text{MOP4}'}$ ; (B) IASI averaging kernels at pressure levels closest to the MOPITT V4 pressure levels  $\mathbf{A}^{\text{IASI}}$ ; (C)  $\mathbf{A}^{\text{MOP4}'} \mathbf{A}^{\text{IASI}}$ ; and (D)  $\mathbf{A}^{\text{MOP4}'} - \mathbf{A}^{\text{MOP4}'} \mathbf{A}^{\text{IASI}}$

By comparing Figs. 6.13 and 6.9 it can be seen that the application of Eq. 6.6 has significantly reduced the expected smoothing bias.

Figure 6.12 compares the mean values for  $\mathbf{x}^{\text{IASI}'}$ ,  $\mathbf{x}^{\text{MOP3}'}$ , and  $\mathbf{x}^{\text{MOP3}'} - \mathbf{x}^{\text{IASI}'}$ , for each MOPITT V3 pressure level for 1 September 2007 for the daytime over the oceanic Southern Africa region. An offset between the total column densities of 6.32% was also computed, and a correlation coefficient between the IASI and MOPITT V3 total columns of 0.86 is comparable to the correlation coefficient between the IASI operational and MOPITT V3 column amounts of 0.87 that was observed by George et al. [2009]. Over ocean and during the daytime, the MOPITT V3 CO profile appears

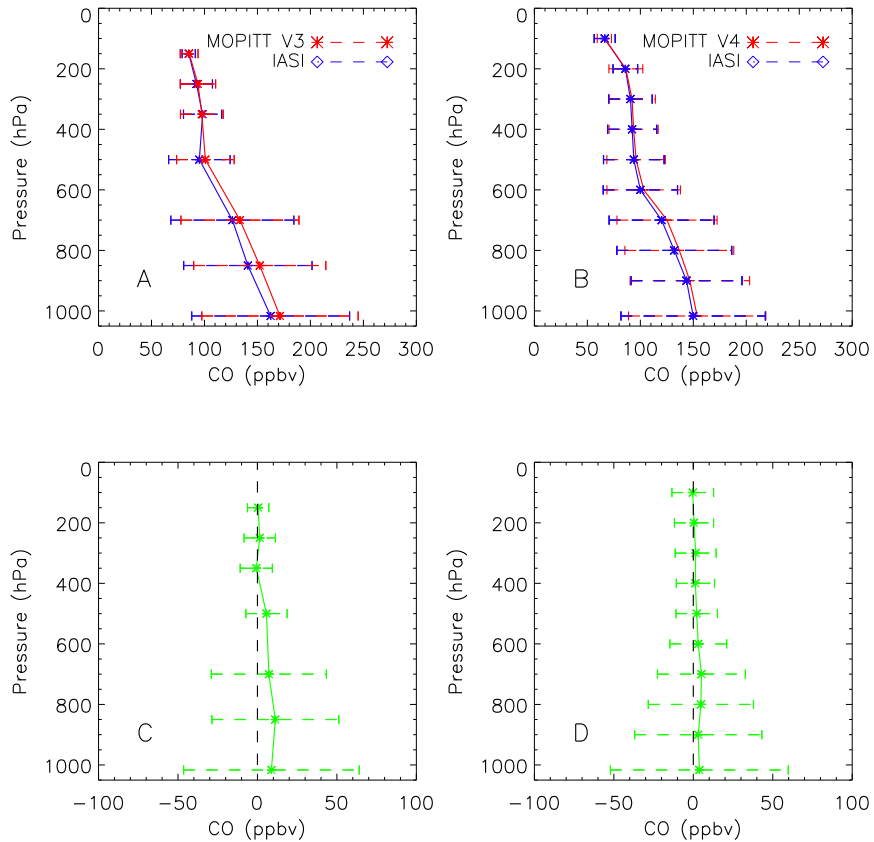


Figure 6.12: Same as Fig. 6.7, except for  $\mathbf{x}^{\text{MOP}}$  and  $\mathbf{x}^{\text{IASI}}$ : (A) adjusted MOPITT V3 and smoothed IASI CO mean profiles; (B) adjusted MOPITT V4 and smoothed IASI CO mean profiles; (C) the mean difference between adjusted MOPITT V3 CO and smoothed IASI CO profiles; and (D) the mean difference between adjusted MOPITT V4 CO and smoothed IASI CO profiles.

to be an overestimate of the IASI retrieved profile in the mid-lower troposphere.

Figure 6.12 also compares the mean values for  $\mathbf{x}^{\text{IASI}}$ ,  $\mathbf{x}^{\text{MOP4'}}$ , and  $\mathbf{x}^{\text{MOP4'}} - \mathbf{x}^{\text{IASI}}$ , for each MOPITT V4 pressure level. As can be seen from this figure, there is excellent agreement between  $\mathbf{x}^{\text{IASI}}$  and  $\mathbf{x}^{\text{MOP4'}}$  across the profile. The results of the comparison between the adjusted MOPITT V4 and the smoothed IASI products are summarised in Table 6.2. The agreement between the smoothed IASI and adjusted MOPITT V4 total column densities is also high (with a mean absolute difference of 4.21%), and there is a correlation coefficient between the column amounts for  $\mathbf{x}^{\text{IASI}}$  and  $\mathbf{x}^{\text{MOP4'}}$  of

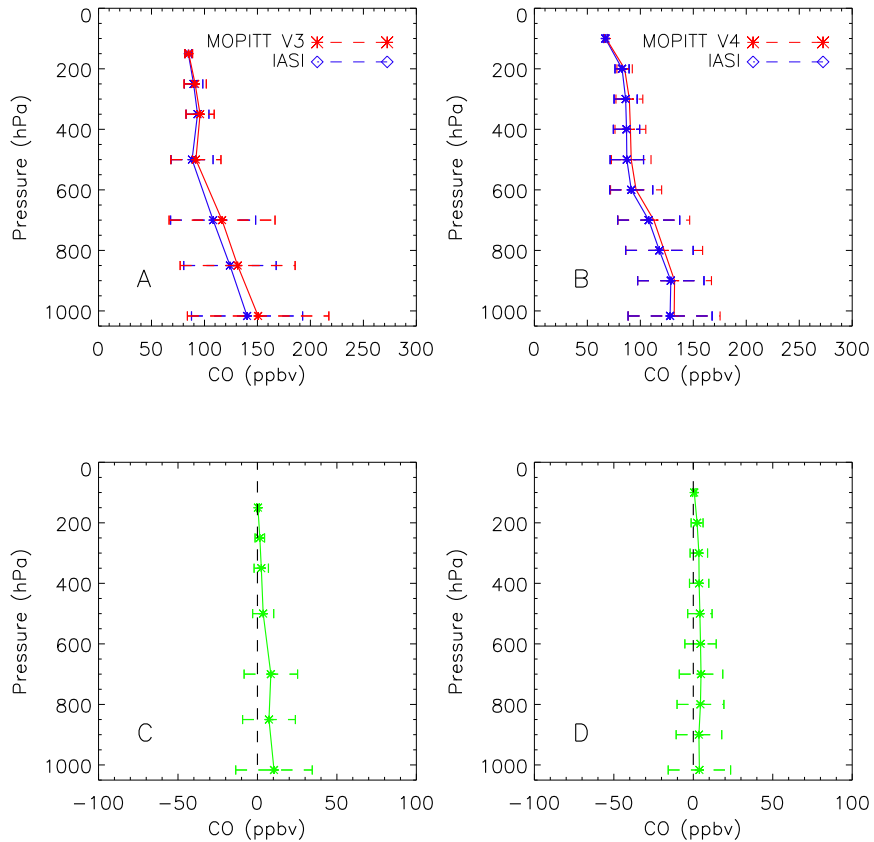


Figure 6.13: Same as Fig. 6.7, but for  $\mathbf{x}_{\text{MODEL}}^{\text{MOPIT}'}$  and  $\mathbf{x}_{\text{MODEL}}^{\text{IASI}}$ : (A) adjusted MOPITT V3 and smoothed IASI CO mean profiles; (B) adjusted MOPITT V4 and smoothed IASI CO mean profiles; (C) the mean difference between adjusted MOPITT V3 CO and smoothed IASI CO profiles; and (D) the mean difference between adjusted MOPITT V4 CO and smoothed IASI CO profiles. (A) and (B) are in relation to the retrieval of a true profile, as provided by GEOS-Chem.

0.86. The results of this comparison indicate that for the data studied, over ocean and during the daytime, the IASI and MOPITT V4 data sets are in very good agreement.

Tables 6.3 and 6.4 summarise the values for  $\mathbf{x}^{\text{MOPIT}'} - \mathbf{x}^{\text{IASI}'}$ , along with the expected smoothing bias ( $\delta_{\text{MODEL}'}$ ) for the 1 September 2007 over the region shown in Fig. 6.4 for the daytime/ocean, nighttime/ocean, and nighttime/land scenarios. The results for the daytime/land scenario are not shown as there were insufficient coincident data points from which to draw conclusions from. It should also be noted that only profiles

	day and	ocean	night and	ocean	night and	land
	$\mathbf{x}^{\text{MOP3'}} - \mathbf{x}^{\text{IASI'}} \delta_{\text{MODEL}'}$		$\mathbf{x}^{\text{MOP3'}} - \mathbf{x}^{\text{IASI'}} \delta_{\text{MODEL}'}$		$\mathbf{x}^{\text{MOP3'}} - \mathbf{x}^{\text{IASI'}} \delta_{\text{MODEL}'}$	
	(N=972)	(N=972)	(N=908)	(N=908)	(N=711)	(N=710)
850 hPa						
Mean	11.2 (39.1)	7.3 (14.6)	11.5 (38.8)	1.2 (7.4)	28.7 (44.1)	19.1 (29.7)
(ppbv)						
Bias (%)	8.0 (27.8)	5.9 (11.8)	9.7 (32.9)	1.1 (7.0)	15.8 (24.3)	11.4 (17.7)
500 hPa						
Mean	5.7 (12.8)	3.6 (5.5)	12.0 (8.1)	1.2 (2.8)	8.6 (13.1)	-0.6 (5.6)
(ppbv)						
Bias (%)	5.8 (13.4)	4.1 (6.3)	15.2 (10.2)	1.6 (3.7)	8.3 (12.5)	-0.7 (6.0)
250 hPa						
Mean	1.5 (8.8)	1.5 (2.1)	6.3 (13.4)	-0.1 (1.5)	7.5 (11.0)	-1.5 (4.9)
(ppbv)						
Bias (%)	1.6 (9.5)	1.7 (2.4)	7.6 (16.3)	-0.1 (1.8)	8.0 (11.8)	-1.7 (5.7)
Total column						
Absolute	6.4 (17.5)	4.0 (7.3)	10.4 (14.4)	0.8 (4.4)	13.0 (14.9)	3.7 (6.7)
Bias (%)						

Table 6.3:  $\delta\mathbf{x}_{\text{BIAS}}$  for IASI and MOPITT V3 CO retrievals for different scenarios.

for which there were retrieved values at each of the fixed MOPITT pressure levels were chosen, and as much of the Southern Africa land region has a surface pressure of less than 900 hPa (but greater than 850 hPa) this resulted in a large discrepancy in the number of MOPITT V3 and V4 comparisons over land during the nighttime. The comparisons show that for V4 data, the anticipated differences due to smoothing error are very small. Therefore, any biases observed are likely to be intrinsic, non-retrieval, systematic biases between MOPITT and IASI, which on average across the profile appear to be less than 4%. The results for V3 are less easy to interpret but would be consistent with systematic biases of up to 10%. As the MOPITT V4 product has been shown to be more reliable than the MOPITT V3 product [see e.g. Deeter et al.,

	day and	ocean	night and	ocean	night and	land
	$\mathbf{x}^{\text{MOP4}'} - \mathbf{x}^{\text{IASI}'} \delta_{\text{MODEL}'}$					
	(N=1038)	(N=1038)	(N=925)	(N=925)	(N=211)	(N=211)
900 hPa						
Mean	3.1 (26.9)	3.5 (8.1)	-3.4 (30.0)	-2.2 (4.4)	-4.9 (48.9)	1.41 (5.6)
(ppbv)						
Bias (%)	2.2 (18.7)	2.8 (6.3)	-2.7 (24.0)	-1.8 (3.6)	-2.7 (27.3)	1.0 (4.2)
500 hPa						
Mean	2.1 (12.0)	4.2 (6.3)	3.9 (8.0)	0.7 (1.9)	3.9 (12.4)	0.6 (3.7)
(ppbv)						
Bias (%)	2.3 (12.7)	4.8 (7.2)	4.9 (10.0)	0.8 (2.4)	3.8 (12.0)	0.7 (4.4)
200 hPa						
Mean	0.5 (5.8)	2.4 (3.5)	4.4 (11.5)	0.5 (1.6)	5.7 (11.0)	0.1 (2.6)
(ppbv)						
Bias (%)	0.5 (6.8)	2.9 (4.2)	5.5 (14.6)	0.6 (2.1)	6.8 (13.1)	0.1 (3.2)
Total column						
Absolute	2.9 (14.7)	2.5 (3.2)	4.5 (14.4)	0.1 (2.1)	7.4 (16.2)	2.1 (4.3)
Bias (%)						

Table 6.4:  $\delta\mathbf{x}_{\text{BIAS}}$  for IASI and MOPITT V4 CO retrievals for different scenarios.

2010], it is encouraging that ULIRS agrees to such a large extent with the MOPITT V4 data set.

## 6.6 Summary

In this chapter, retrievals from the ULIRS presented in Chapter 5 were compared to the MOPITT V3 and V4 data products, in order to assess the performance of the IASI retrieved CO. Considerable differences were observed in a direct comparison between the MOPITT and IASI retrieved data sets, which were shown to arise because of the different a priori statistics used in the retrieval algorithms. The comparisons to IASI

are improved for V4 when the IASI a priori statistics are used in the V4 processing; for V3, there is less of an improvement due to the similarities in the a priori covariance matrices of the V3 and IASI data sets.

By use of a double smoothing methodology, it has been possible to derive retrieved profile comparisons which are much less dependent on smoothing error. For MOPITT V4, the comparison is sufficient to show that MOPITT V4 and IASI CO inter-product biases are less than 4% on average. For MOPITT V3, the results are less easy to compare, but systematic differences appear to be closer to 7%. As there is more confidence in the validity of the MOPITT V4 retrieved CO product these results indicate that the IASI retrievals are very reasonable, and that they compare well to an independent data set with a well established validation heritage.

# Chapter 7

## Top-down and Bottom-up Estimations of CO Emissions from Localised Fires

### 7.1 Introduction

As was discussed in Chapter 1, the powerful role that CO plays in determining the tropospheric concentrations of  $O_3$  and OH (the main oxidising components of the troposphere) implies that models of global atmospheric chemistry should be able to simulate accurate CO concentrations. The complex distribution (both spatial and temporal) of the sources of CO, means that a barrier to the full exploitation of the data in these models is the accurate representation of these sources. The sources of CO are estimated by using either a “bottom-up” (i.e. derived using traditional ground based emissions inventories) or a “top-down” (i.e. derived using measurements of atmospheric concentrations) approach, with CO inversion studies, such as that carried out by Bergamaschi et al. [2000], pointing to significant differences between top-down and bottom-up estimates of regional CO sources.

The purpose of this chapter is to compare the ULIRS’s observations of CO emissions from localised fires to currently available process-based bottom-up inventories. Section 7.2 discusses the bottom-up methodology of estimating CO emissions, whilst

Sec. 7.3 describes how CO emissions can be estimated using a top-down approach, focussing in particular on the utilisation of a simplified approach using the CO product from the ULIRS. The selection of an appropriate fire event for an intercomparison of the top-down and bottom-up estimates of CO emissions, and the results of such a comparison, is discussed in Sec. 7.4. Finally Sec. 7.5 presents a comparison between the ULIRS retrieved CO product and modelled data, in relation to this isolated fire event.

## 7.2 Bottom-up Methodology

Bottom-up emission inventories are produced by using an emission estimation algorithm. The standard method for estimating emissions from BB, in yearly emissions ( $E_{ij}$ , TG/yr) of a gas for vegetation type  $i$  within a grid cell  $j$ , is given by Jain et al. [2006] as:

$$E_{ij} = [A]_{ij} \times [AFL]_{ij} \times [CC]_{ij} \times [EF]_{ij} \quad (7.1)$$

where  $A$  (km<sup>2</sup>) is the total burnt area (or cleared area for croplands) for each vegetation type  $i$  within each grid cell  $j$ ,  $AFL$  (kg dry matter km<sup>-2</sup>) is the Available Fuel Load or burnable plant material for vegetation type  $i$  within each grid cell  $j$ ,  $CC$  (dimensionless fraction) is the Combustion Completeness or efficiency for vegetation type  $i$  within each grid cell  $j$ , and  $EF$  (g species / kg dry matter) is an Emission Factor of a gas for an open fire in ecosystem type  $i$  of grid cell  $j$ .

### 7.2.1 Burnt Area

As Earth-system modelling efforts recognise and include fire disturbance as an important process in the terrestrial carbon cycle, there remains a strong need for long term spatially- and temporally-explicit global burnt area data sets. In response to this need, a growing number of multi-year, satellite-based global burnt area products have been made publicly available over the past several years. These include: 1) the 1 km L3JRC product [Tansey et al., 2008], currently spanning April 2000 to March 2007, and produced from SPOT VEGETATION imagery with a modified version of the Tansey et al. [2004] Global Burnt Area 2000 algorithm; 2) the 1 km GlobCarbon

burnt area product, currently spanning April 1998 to December 2007, derived from SPOT VEGETATION, AATSR-2, and AATSR imagery using a combination of mapping algorithms [Plummer et al., 2006]; and 3) the Roy et al. [2008] 500 m MODIS burnt area product (MCD45A1), generated from Terra and Aqua MODIS imagery and available from mid-2000 through to present. All three data sets map the spatial extent of burnt vegetation (variously referred to as burned areas, burnt areas, burn scars, fire scars, and fire affected areas) at daily temporal resolution. At coarser spatial and temporal scales, Version 2 of the GFED (GFED2) provides monthly global burnt area estimates at  $1^\circ$  spatial resolution from January 1997 to December 2008. In the GFED2 product, burnt area is estimated indirectly using monthly active fire observations from the MODIS, ATSR, and Tropical Rainfall Measuring Mission (TRMM) Visible and Infrared Scanner (VIRS) sensors [Van Der Werf et al., 2006]. Version 3 of the GFED burnt area data set (GFED3) provides global, monthly burnt area aggregated to  $0.5^\circ$  spatial resolution from mid-1996 through to present, and is specifically intended for use within large-scale (typically global) atmospheric and biogeochemical models [Giglio et al., 2010].

Estimates of the total burnt area can vary considerably on continental and smaller scales depending on the model used. The annual global burnt areas for the year 2000 as calculated by the L3JRC, MCD45A1, GlobCarbon, GFED2, and GFED3 data sets were approximately 3.88, 3.44, 3.89, 3.58, and  $3.94 \times 10^{10} \text{ km}^2$  respectively. However, whilst these values agree reasonably well in terms of the total global burnt area product, the discrepancies over regional scales are far larger. Over the African region for example, estimates of the total burnt area for the year 2000 range from the L3JRC value of  $1.59 \times 10^{10} \text{ km}^2$  to the GFED3 estimate of  $2.64 \times 10^{10} \text{ km}^2$ , a difference of  $\sim 67\%$ . These large discrepancies in the burnt area product will have a decided outcome on any bottom-up estimation of CO emissions (see Eq. 7.1). In this study, which deals primarily with fires in the Southern Africa region, the MCD45A1 burnt area product is used to define the area which has been burned by fire. Unlike the L3JRC algorithm, which was initially developed and validated for boreal fires, the MCD45A1 was developed over the African region, with the validation of the MCD45A1 product that was performed by Roy and Boschetti [2009] indicating that it was capable of capturing 75% of the burnt area as detected by the Landsat Enhanced

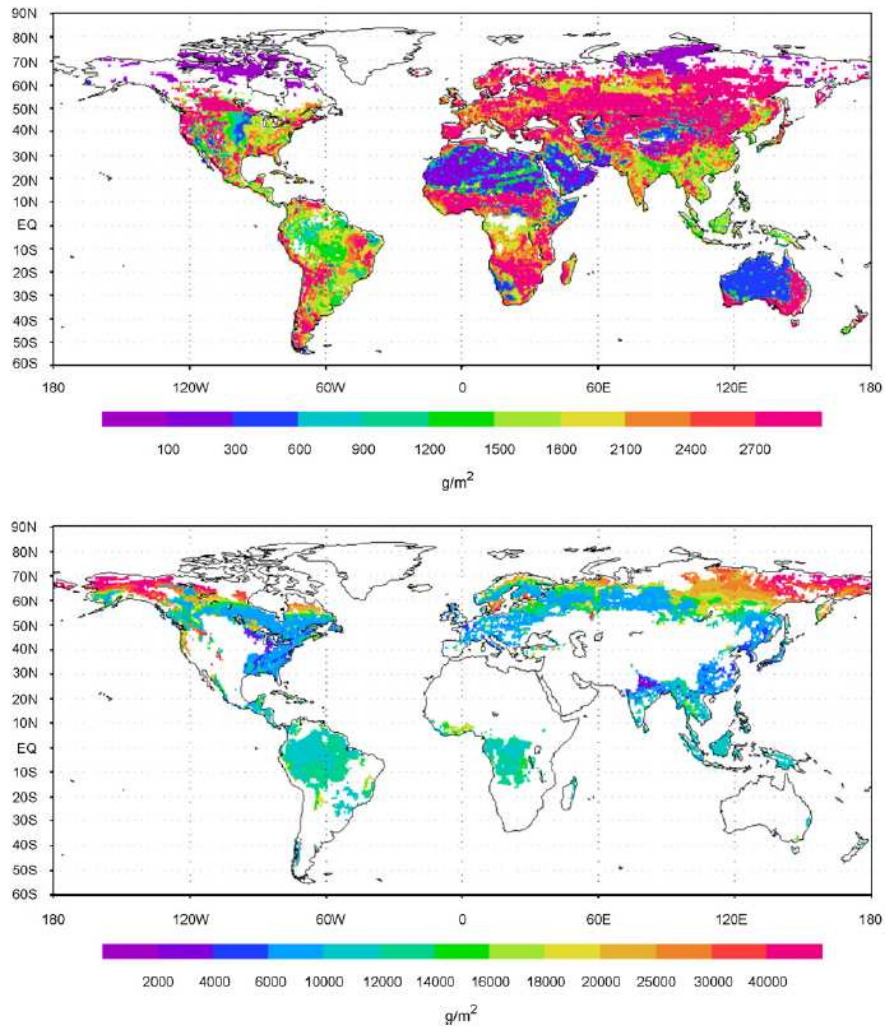


Figure 7.1: ISAM estimated AFL for the year 2000. The top panel shows the AFL for all non-forest ecosystems, and the bottom panel shows the AFL for all forest ecosystems. Figure taken from Jain [2007].

Thematic Mapper Plus (ETM+). [Roy and Boschetti, 2009] found that over the African region at the subcontinental scale, the MCD45A1, GlobCarbon, and L3JRC burnt area products can be expected to capture 75 %, 60 %, and 14 % of the true area burnt, respectively.

### 7.2.2 Available Fuel Load

In this study, the AFL or pre-burnable plant material is calculated using the terrestrial component of the Integrated Science Assessment Model (ISAM) [Jain and Yang, 2005]. This model simulates the carbon fluxes to and from different compartments of the terrestrial biosphere with a  $0.5^\circ \times 0.5^\circ$  spatial resolution. There are a number of features which make the terrestrial component of the ISAM suitable for estimating AFL, these include: 1) separation between ground vegetation and tree parts allows for the distinction between woody and non-woody biomass; 2) consideration is given to biomass burned via land transformation; and 3) the AFL is calculated as a time dependent quantity. Figure 7.1 plots the ISAM estimated global AFL density ( $\text{g m}^{-2}$ ) for forest and non-forest ecosystem types for the year 2000.

Table 7.1 summarises the ISAM model estimated AFL for various regions and across major ecosystem types, as derived by Jain et al. [2006], and it is these values that are used in this study to assign a value for the AFL, depending on the land surface type. Aside from the ISAM there is no consistent global map of AFL available in the open literature, with most of the field experiment studies available having been carried out on specific regions or a country using diverse methods. This results in the uncertainty ranges for the available literature values as being generally quite large, and is why one global model for AFL is used in this study's bottom-up estimations of CO emissions.

### 7.2.3 Combustion Completeness

CC is the fraction of the AFL that is actually combusted, it is a unitless quantity which ranges from 0 to 1 and varies over the course of the fire season, with more complete combustion at the end when fuels have had more time to dry out, as shown by Hoffa et al. [1999] for savanna ecosystems. In general, fine and dry fuels burn more completely than coarse and wet fuels, although CC is highly variable between different fires under different conditions, even in similar vegetation types. In this study, ecosystem types with similar characteristics are grouped together and assigned a CC based on a literature survey carried out by Jain et al. [2006], the results of which are displayed in Table 7.2. Figure 7.2 shows a plot of the global CC for December 2005, as calculated

Region	Tropical	Temperate	Boreal	Total for Forest Ecosystem	Total for Non-Forest Ecosystem
Tropical America	11 277	13 586	n/a	12 297	600
Tropical Africa	12 740	9800	n/a	12 738	756
Tropical Asia	11 061	n/a	n/a	11 061	1370
North America	n/a	14 257	16 803	16 245	1037
Europe	18 333	12 371	10 819	11 520	1837
Former Soviet Union	n/a	14 054	18 347	18 018	1910
North Africa and Middle East	n/a	15 744	n/a	15 744	491
China	12 096	8172	7302	8109	1013
Oceania	11 471	11 941	n/a	11 766	653
<b>Global Total</b>	12 819	12 799	16 379	14 259	1073

Table 7.1: ISAM estimated AFL for forest ecosystems as well as totals for forest and non-forests ecosystems and regions for the year 2000. The values are given in units of  $\text{g m}^{-2}$ , and are taken from Jain et al. [2006].

by the GFED2 data set, and taken from the Oak Ridge National Laboratory Distributed Active Archive Centre (ORAL DACE) website (<http://daac.ornl.gov/>).

## 7.2.4 Emission Factors

EFs are estimations of the amount of a particular species that is emitted relative to some measurement of total burnt material. In this study, all EFs for CO are given in terms of gram of species per kilogram of dry matter (g species per kg dry matter). Natural vegetation-based EFs are used, which have been compiled from several publications for various regions and ecosystems; these values are presented in Table 7.3.

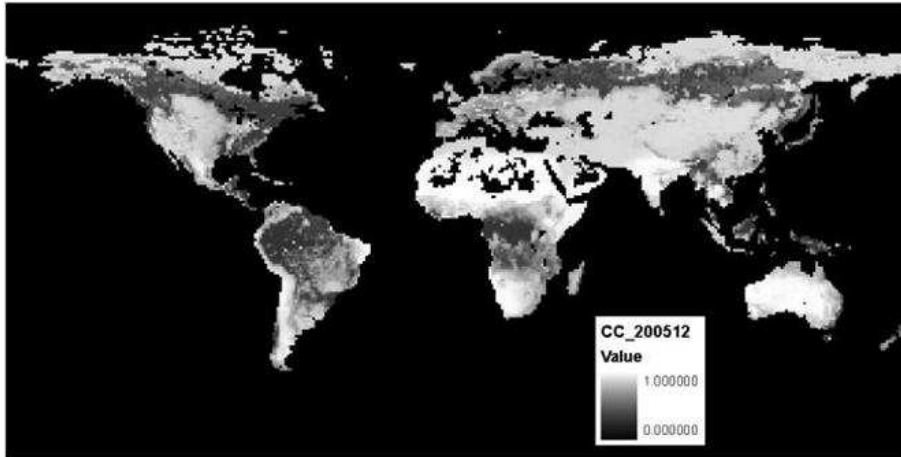


Figure 7.2:  $1^\circ \times 1^\circ$  gridded monthly Combustion Completeness (CC) for December 2005. Figure taken from <http://daac.ornl.gov/>.

### 7.3 Top-down Methodology

The two most important characteristics of the bottom-up approach are the accurate representation of a physical processes and the upscaling of emission inventories to a higher level of aggregation, i.e. to figures which are generally representative for that emission process on a larger scale [Janssen et al., 1999]. In upscaling, the “best available” average EF appropriate to the available statistics is used to aggregate on a national, regional or global scale. This means that on a local scale, regions of significant interest (e.g. a high temperature event anomaly) may be statistically removed when upscaling, which can result in significant uncertainties in the regional estimates of CO sources [Kasibhatla et al., 2002]. A different approach is to use an inverse modelling framework combined with measurements of atmospheric CO to derive estimates of emissions for various source categories [Bergamaschi et al., 2000]. Assuming a linear approach, the measured CO concentrations  $\mathbf{y}$  can be related to the individual source strengths  $\mathbf{x}$  according to:

$$\mathbf{y} = \mathbf{K}\mathbf{x} + \epsilon, \quad (7.2)$$

where  $\mathbf{K}$  is the Jacobian matrix of response functions derived from a CTM, and  $\epsilon$  specifies the uncertainty in the measurement, which in this instance arises from the

Land Cover Type	Combustion Completeness (%)	Source
Tropical evergreen	0.50	Fearnside [2000]
Tropical deciduous	0.50	Fearnside [2000]
Temperate evergreen	0.50	Hoelzemann et al. [2004]
Temperate deciduous	0.50	Hoelzemann et al. [2004]
Boreal	0.50	Hoelzemann et al. [2004]
Savanna	0.75	Average of Ward et al. [1996], Hoffa et al. [1999], and Hély et al. [2003]
Grassland/Pastureland	0.83	Average of Hoffa et al. [1999], and Fearnside [2000]
Shrubland	0.75	Average of Ward et al. [1996], Hoffa et al. [1999], and Hély et al. [2003]
Cropland	0.86	Saarnak et al. [2003]

Table 7.2: Combustion Completeness (CC) for different land cover types. Values are taken from Jain et al. [2006].

errors in the measured atmospheric CO concentrations [Arellano Jr. et al., 2004]. Assuming a Bayesian approach (similar to that for the retrieval of trace gases from TOA radiances described in Chapter 2), the MAP solution to the inverse problem is given by:

$$\hat{\mathbf{x}} = \mathbf{x}_a + (\mathbf{K}^T \mathbf{S}_\epsilon^{-1} \mathbf{K} + \mathbf{S}_a^{-1})^{-1} \mathbf{K}^T \mathbf{S}_\epsilon^{-1} (\mathbf{y} - \mathbf{K} \mathbf{x}_a), \quad (7.3)$$

where  $\mathbf{x}_a$  represents the a priori source strengths,  $\mathbf{S}_\epsilon$  is the observation error covariance matrix, and  $\mathbf{S}_a$  is the a priori error covariance matrix.

### 7.3.1 Simplified Approach

The availability of near-global and long-term CO observations, in conjunction with CTMs, has allowed for the use of inverse methods to constrain CO sources [see e.g. Arellano Jr. et al., 2004]. However, the use of Bayesian inverse methods to estimate regional sources intrinsically involves assessing the robustness of the estimates by

Land Cover Type	Emission Factor <sup>a</sup>
Tropical evergreen	
Tropical America <sup>b</sup>	122.0
Other Regions <sup>c</sup>	104.0
Tropical deciduous	
Tropical America <sup>d</sup>	79.2
Other Regions <sup>c</sup>	104.0
Savanna	
Tropical Africa <sup>e</sup>	67.0
Other Regions <sup>c</sup>	65.0
Grassland/Pastureland/Shrubland/Desert	
Tropical Africa <sup>f</sup>	62.4
Other Regions <sup>c</sup>	65.0
Cropland	
Tropical Africa <sup>g</sup>	117.0
Other Regions <sup>c</sup>	92.0

<sup>a</sup> g species per kg dry matter.

<sup>b</sup> Average of Ferek et al. [1998], Fearnside [2000], and Scholes and Andreae [2000].

<sup>c</sup> Andreae and Merlet [2001].

<sup>d</sup> Average of Ward et al. [1996], Bertschi et al. [2003], Sinha et al. [2003], and Yokelson et al. [2003].

<sup>e</sup> Average of Cofer III et al. [1996], Hao et al. [1996], Scholes et al. [1996], Sinha et al. [2003], and Yokelson et al. [2003].

<sup>f</sup> Average of Scholes et al. [1996], Ward et al. [1996], Korontzi et al. [2003], Sinha et al. [2003], and Yokelson et al. [2003].

<sup>g</sup> Saarnak et al. [2003].

Table 7.3: Emission Factors (EFs) for different land cover types and regions for CO. Values are taken from Jain et al. [2006].

characterising both the measurement and the model errors. Current approaches to characterising the errors in the CTMs are typically provisional [Arellano Jr. and Hess, 2006], and over a localised region there is a relatively small amount of data for the inversion scheme, which makes it difficult to find a constrained solution. A simplified approach for calculating the emissions of CO from a localised fire region over a reasonably short time scale, using ULIRS measured CO concentrations is now presented.

#### **7.3.1.1 Detection of Fires**

The fires that are studied in this chapter have been selected using the ESA WFA, a global collection of hot spots detected using the ATSR-2 instrument from November 1995 to December 2002, and extended using the AATSR since the beginning of 2003 to present [Mota et al., 2006]. The processing consists of detecting hot spots in the thermal bands of the ATSR family of instruments. In particular, the band centred at  $3.7\ \mu\text{m}$  shows the highest sensitivity to surface temperature variations, and two simple “fixed threshold” algorithms have been developed to fully exploit this band. The detection of observations for the WFA is based only on the  $3.7\ \mu\text{m}$  channel, which is highly sensitive to radiation emitted at temperatures from 500 K to 1000 K. Use of nighttime data is meant to minimise false alarms due to sun-glint, reflection off cloud edges, and bright soil surfaces. It is also expected to reduce false alarms caused by hot ground surfaces. However, one limitation of using nighttime data is that it may lead to a possible undersampling of small BB events, which occur mainly during the daytime. Nighttime band  $3.7\ \mu\text{m}$  BT spots are detected according to the following criteria:

- ALGO1: BT saturated (i.e.  $\text{BT} > 312\ \text{K}$ )
- ALGO2:  $\text{BT} > 308\ \text{K}$

The monthly record generated by this processing is given for a spatial resolution of 1 km with a revisit time of  $\sim 3$  days, and is available from the ESA WFA website (<http://dup.esrin.esa.int/ionia/wfa/index.asp>).

### 7.3.1.2 Methodology

Once the fires have been located using the ESA WFA, it is necessary to determine where the plume from the fires has been transported to, so that the boundaries for the region of “enhanced” CO can be set; this is done by performing a trajectory analysis using the Hybrid Single Particle Lagrangian Integrated Trajectory (HYSPLIT) model [Draxler and Hess, 1998]. Once the region of enhanced CO has been selected, a “background” region must also be defined. This region should be chosen so as to best represent what the concentration of CO would have been in the enhanced region in the absence of any fires. Once these two regions have been selected, the CO burden from the fires in the enhanced region is calculated by computing the mean CO concentration over the enhanced region, and subtracting from this the mean CO background concentration. This then gives a mean value for the CO burden in units of Molec cm<sup>-2</sup>, which is converted to total Molec of CO by multiplying by the area of the enhanced region, and then finally into units of Tg by dividing by the Avogadro constant ( $6.02 \times 10^{23}$  mol<sup>-1</sup>), and multiplying by the molecular weight of CO (28 g).

Figure 7.3 illustrates the enhanced and background regions chosen for such a comparison, in the Southern Hemisphere Africa (SHA) region for 1 September 2007. Three distinct regions are shown in Fig. 7.3: the solid blue box represents a region in SHA for which the ESA WFA has detected a number of fires (as indicated by black triangles); the dashed blue box indicates the region over which the plume from any of the fires in the solid blue box has travelled, according to an analysis carried out using the HYSPLIT trajectory model (see Fig. 7.4); and the red box represents a background region, so chosen because it is unaffected by the plume from the fire region, yet sufficiently close on both a temporal and spatial scale so as to give a good indication of the typical background values of CO in the enhanced region.

Figure 7.6 shows a map of the different land types over this region, as classified by ESA’s Globcover project. The map was generated using 19 months worth of data from Envisat’s Medium Resolution Imaging Spectrometer (MERIS) instrument, working in full resolution mode to provide a spatial resolution of 300 m, with data collected between December 2004 and June 2006. There are 22 different land cover types shown in the map, including croplands, wetlands, forests, artificial surfaces, water bodies and permanent snow and ice, details of which can be found in Arino

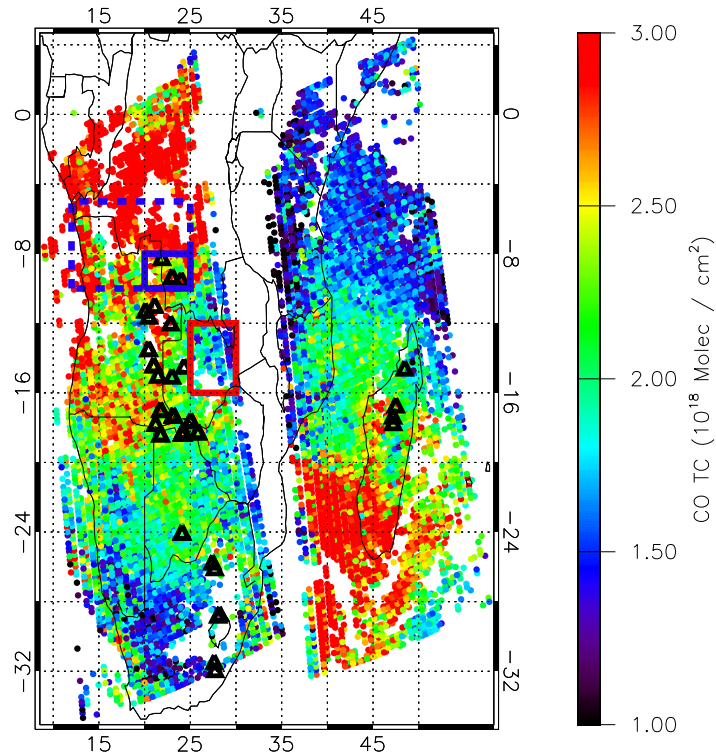


Figure 7.3: ULIRS nighttime total CO retrievals for 1 September 2007 over the SHA region; the black triangles represent fires, as determined by the ESA WFA (ALGO1). The solid red box shows the area used to determine the average background value, the solid blue box indicates the region used for determining the fire source locations, and the dashed blue box indicates the region that bounds the emissions from these fires, as determined by the HYSPLIT trajectory model (see Fig. 7.4).

et al. [2008]. As can be seen from Fig. 7.6 the land types bounded by the background (solid red box) and enhanced regions (dashed blue box) are similar. In order for this simplified top-down approach to be valid it is important that this is the case, so that: 1) anthropogenic sources of CO are correctly accounted for; and 2) the differing emissivities and observed thermal contrasts are not seen to bias the retrieval.

The HYSPLIT model was run using a matrix trajectory, with the multiple source locations chosen so as to sample the region that was selected for this analysis, i.e. the

NOAA HYSPLIT MODEL  
 Forward trajectories starting at 0000 UTC 01 Sep 07  
 GDAS Meteorological Data

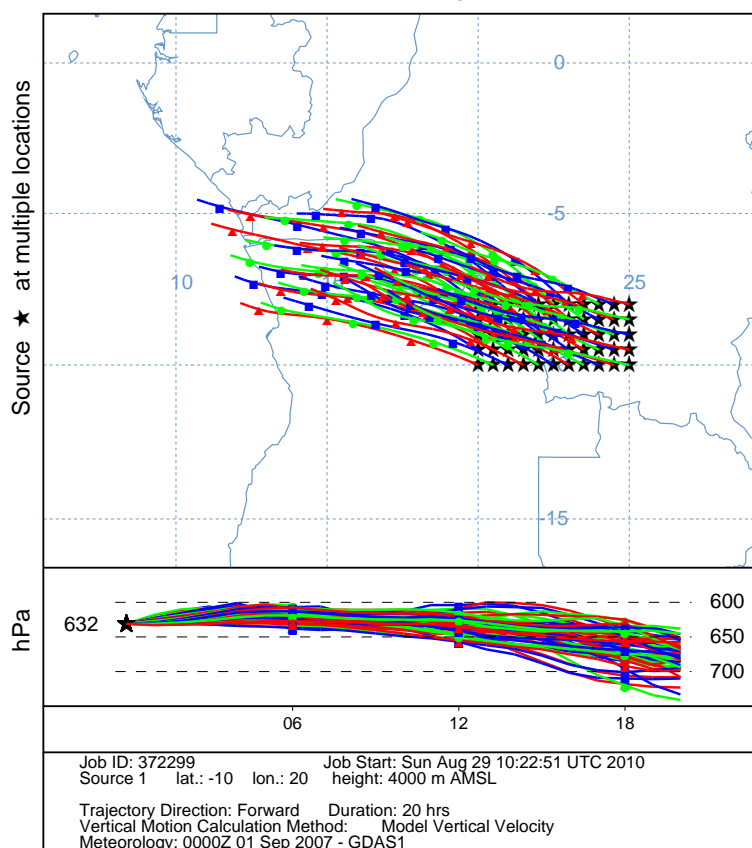


Figure 7.4: HYSPLIT trajectory analysis for 1 September 2007 over the region of interest indicated by the solid blue box in Fig. 7.3. The run was started at 00:00 on 1 September 2007 and run for 20 hours. The stars indicate the multiple source locations, and the height of the plume is plotted in terms of pressure and time since release. A plume injection height of 4000 m above sea level was used.

area bounded by the solid blue box in Fig. 7.3; the trajectory analysis was performed over a time period of 20 hours from 00:00 on 1 September, as the IASI measurements in this region were made between 19:00 and 20:00 UTC, and a plume injection height of 4000 m was chosen based on an analysis of the range of top heights of the aerosol layers, as shown in Fig. 7.5. The aerosol top heights were determined using the vertical feature mask as measured by the Cloud Aerosol Lidar and Infrared Pathfinder Satellite Observations (CALIPSO) space-borne lidar instrument [Winker et al., 2003],

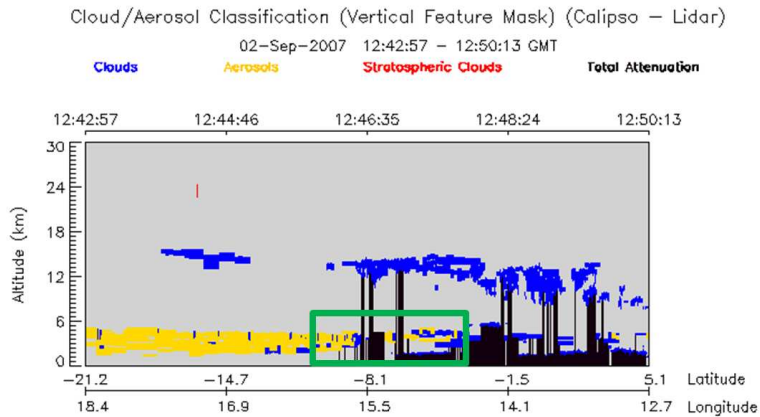


Figure 7.5: CALIPSO vertical feature mask for 2 September 2007 over the SHA region. The green box indicates the enhanced region (dashed blue box) shown in Fig. 7.3

assuming that the aerosol is a good marker of the fire emissions. This analysis was performed using data and visualisation from the Giovanni online data system [Acker and Leptoukh, 2007]. No spatially coincident data for the fire region existed for the 1 September 2007, and so measurements from the 2 September were used instead. The justification for a plume injection height of 4000 m is further verified by the work of Labonne et al. [2007], who found that the plume injection height of SHA fires ranges (on average) from 3000 to 4500 m.

### 7.3.1.3 Results

By using the ULIRS CO retrieved product, and the methodology outlined in Sec. 7.3.1.2, the simplified top-down approach estimates that a total of 0.28 Tg to 0.32 Tg CO has been emitted by the fires bound by the blue box in Fig. 7.3, from the time of burning to the time of measurement. The burden is calculated by computing the mean number of moles of CO in the enhanced region (total column density multiplied by area) and subtracting the mean number of pseudo background moles of CO in the enhanced region (i.e. the mean total column density of the background region multiplied by the area of the enhanced region). The range of values corresponds to the error in the ULIRS retrieved CO total column density product.

The background may be over-evaluated, but this effect will be compensated for by the lack of sensitivity of the ULIRS to the surface, which is weakened because

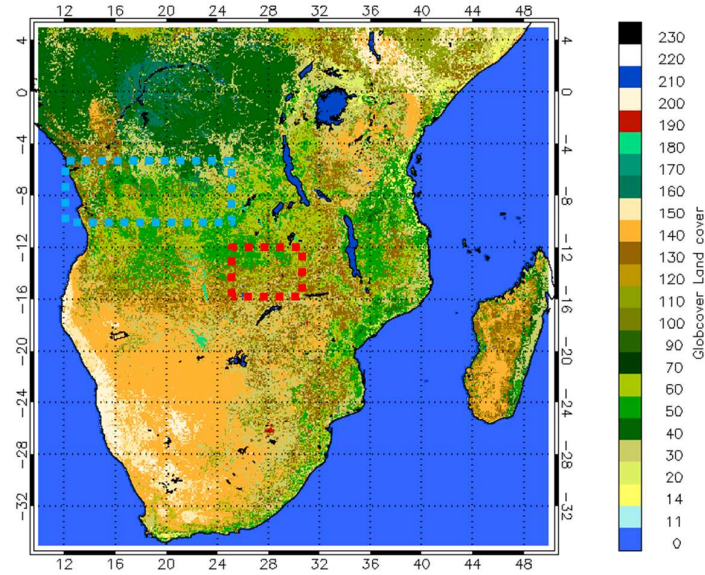


Figure 7.6: Globcover land type map over the SHA region; the dashed red and blue boxes corresponds to the areas of background and enhanced CO, respectively as shown in Fig. 7.3. The values correspond to the 22 different land cover types, as outlined in Arino et al. [2008].

the observations were performed at night where there is a reduced thermal contrast. Whilst deriving the concentration amounts from the ULIRS total column densities mean that the results should not be biased by the IASI instrument’s sensitivity to different parts of the atmosphere, the reduced thermal contrast at nighttime is still likely to result in an underestimated total, meaning that the value inferred should be on the low end of the actual CO emissions.

According to the Emission Database for Global Atmospheric Research Fast Track (EDGAR FT) 2000 anthropogenic emission inventory [Olivier et al., 2005], the total anthropogenic emissions over this same region are 9.72 Tg CO per year. This fire event would then correspond, in terms of pollution emitted, to  $\sim 3\%$  of the total annual anthropogenic activities in only one day.

Using the methodology and values outlined in Sec. 7.2, as well as MODIS land type map, a bottom-up estimate of the CO emissions for 1 September 2007, from the time of burning to the time of the IASI observation, yielded a value of 0.08 Tg for the

Methodology	CO Emissions (Tg)
Top-down	0.28-0.32
Bottom-up (MODIS BA)	0.08
EDGAR	0.03

Table 7.4: Estimates of CO emissions for a SHA fire event on 1 September 2007. The EDGAR value corresponds to the mean daily anthropogenic emissions, and is included for comparative purposes.

region bound by the blue box in Fig. 7.3. The estimates for the CO emissions from this SHA fire event are tabulated in Table 7.4.

The large discrepancies between these top-down and bottom-up estimates can be explained in part because of the limitations of the simplified top-down approach. The main drawbacks of this methodology are that the enhancement as seen from the observed concentrations (or burden) may not necessarily be the same as the emission, since some of the emissions might have been either: 1) lofted on a different trajectory or injected in the atmosphere quite differently than that which was assumed in the trajectory model; 2) removed from the atmosphere via chemical reactions (e.g. with OH); or 3) deposited prior to the location of observation from other sources of CO nearby.

Accurately accounting for the trajectory of the plume, to ensure that the correct enhanced region is chosen, can be done by performing a number of different trajectory analyses, with varying plume injection heights. Such an analysis will give a greater degree of confidence in the selection of the enhanced region. As this study is currently only interested in the CO burden from the fires over a relatively short time period (typically a few days), the issue of the chemical removal of CO from the atmosphere is not crucial because of the lifetime of CO, which at approximately 2 to 3 months is much longer than the timescales being considered for study. The main limitation of this simplified top-down approach is therefore in its inability to correctly differentiate between the “background concentrations”, “fresh plumes” and “aged-plumes”. This inaptitude in the simplified model for properly accounting for transport processes is discussed in Sec. 7.4. A further possible cause of the discrepancies between the

top-down and bottom-up estimations of CO emissions from fires is the production of CO from the oxidation of co-emitted Volatile Organic Compounds (VOCs), such as Formaldehyde [see e.g. Stavrakou et al., 2009], with bottom-up estimations of the CO emissions from fires failing to take these VOC emissions into account.

## 7.4 Isolated Fire Event

The simplified top-down estimation of CO emissions from fires that was outlined in Sec. 7.3.1.2 assumes that any enhancement in CO has come only from the considered fires; it does not fully take into account the effects of transportation. Transportation means that the CO burden for the SHA fire event that was calculated in Sec. 7.3.1.3 was probably an overestimation, as some of the CO burden will have been related to other recent fire and CO emitting events. This is especially true for the event that is shown in Fig. 7.3, as it occurs in the middle of the SHA fire season, which typically lasts from late July to early November [Giglio et al., 2006]. Therefore there are lots of nearby fire events (as is evident from the number of ESA WFA detected fires in Fig. 7.3), emissions from which could easily be transported into the region. Figure 7.7 shows a backward trajectory plot produced using HYSPLIT, run over the enhanced region (dashed blue box) shown in Fig. 7.3 for 20 hours, from 20:00 on 1 September 2007, and which illustrates how the CO burden in the enhanced region is not entirely related to the fires for which the emissions have supposedly been calculated, i.e. the air in the enhanced region (dashed blue box in Fig. 7.3) has not come exclusively from the studied fire region (solid blue box in Fig. 7.3), and has in fact also come from other regions which also contain fire-events during the specified time period (as indicated by the black triangles in Fig. 7.3). During this time period, which is in the peak of the SH BB season, the calculation of the CO burden for a fire event in SHA is further complicated because of the long range transportation of CO emissions from South America [Gloude-mans et al., 2006].

In order to circumvent the effect of transportation, the simplified top-down approach would ideally be first applied to an isolated fire event, i.e. one which occurs in a region otherwise unaffected by short- and long-range transport from other CO sources. As previously discussed, the main fire season in SHA lasts from late July

NOAA HYSPLIT MODEL  
 Backward trajectories ending at 2000 UTC 01 Sep 07  
 GDAS Meteorological Data

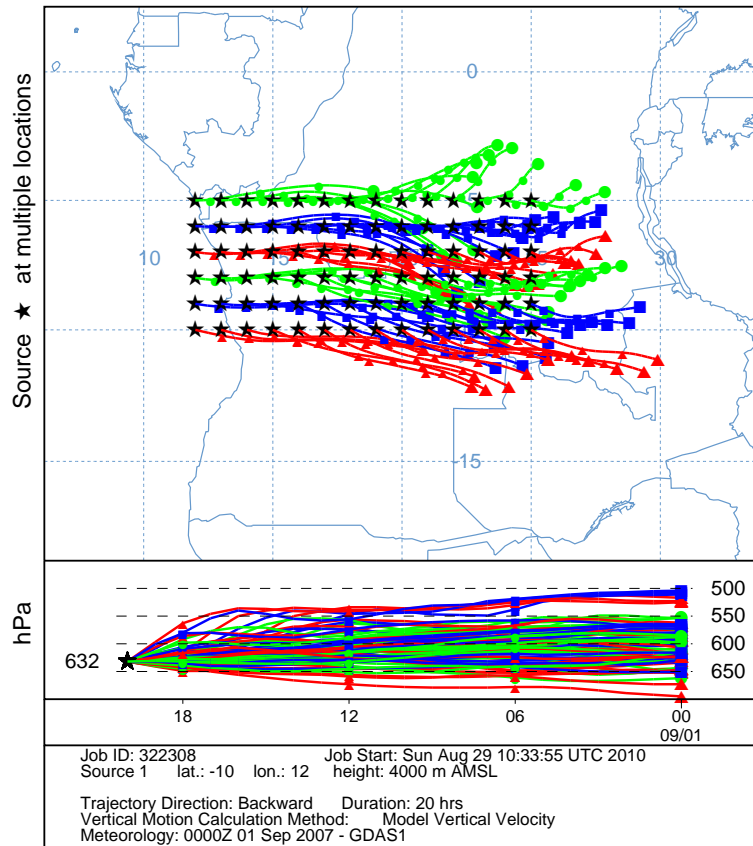


Figure 7.7: Backwards HYSPLIT trajectory analysis for 1 September 2007 over the enhanced region (dashed blue box) shown in Fig. 7.3. The run was started at 20:00 on 2 September 2007 and run backwards for 24 hours.

until early November, and so any fire event in this region that is to be considered isolated should occur outside of this time frame. An ideal fire event for which to estimate the CO emissions using the simplified top-down approach would consist of a number of localised fires that burn strongly over a small period of time, and which occur over a region that is not influenced by the transportation of CO from any other sources.

On 6 February 2009 two isolated fire events occurred in Western South Africa. Near Cape Town over 90 fires, fanned by gale force winds, raged throughout the day leading to an estimated 20 000 ha being burnt [McKune and Johns, 2009]; whilst a

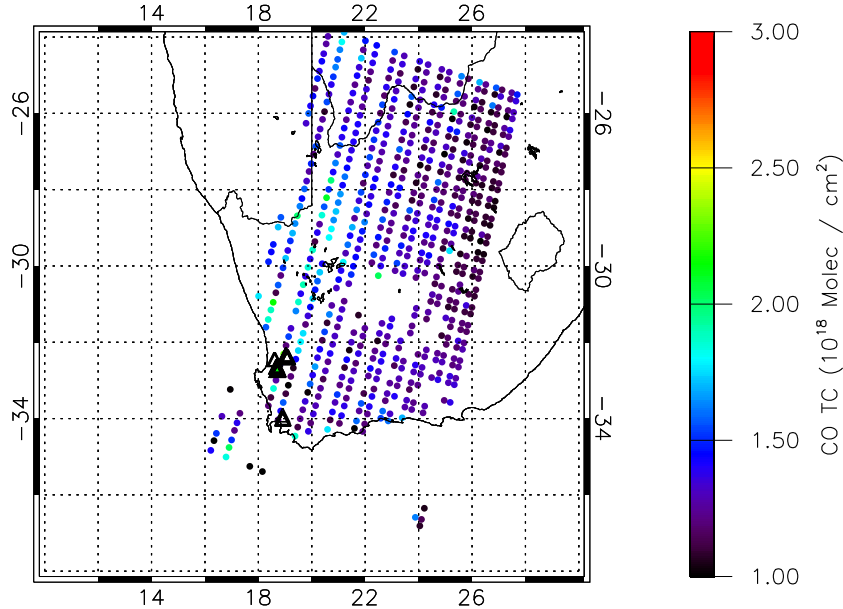


Figure 7.8: ULIRS daytime total CO total column density for 6 February 2009 at approximately 07:10 over South Africa. The black triangles represent the 7 February fires, as determined by the ESA WFA (ALGO1), and are shown here for reference.

second set of fires brought about by falling rocks in the Cederberg Wilderness Area in the Western Cape of the country were also recorded. These fires, as detected by the ESA WFA are shown in Fig. 7.8, which also plots the daytime ULIRS CO total column density for 6 February 2009; these retrievals correspond to measurements made between approximately 07:10 and 07:15 UTC, which is before the fires had begun to burn, as such it gives a good indication as to typical background levels of CO in this region.

Figure 7.9 plots the daytime ULIRS total column density for 7 February 2009; these retrievals correspond to measurements made between approximately 06:50 and 08:30 UTC. In Fig. 7.9 the solid red box now represents the area in which the fires occur; and the dashed red box the area of enhanced CO from the fire plumes, as determined by HYSPLIT. The HYSPLIT analysis shown in Fig. 7.10 shows the modelled plume trajectory for the region of the isolated fire event (solid red box in Fig. 7.9) assuming a plume injection height of 4000 m. Based on CALIPSO data (shown in

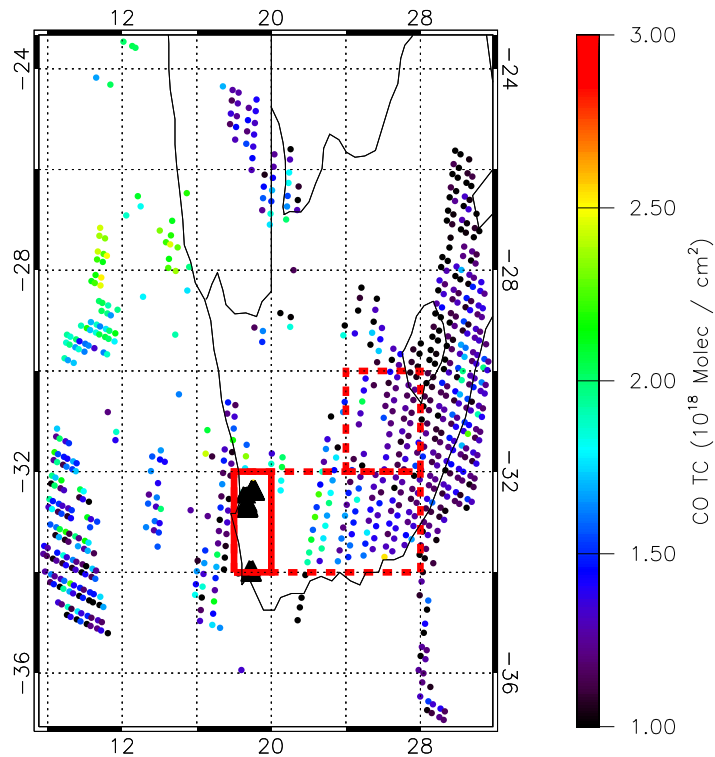


Figure 7.9: ULIRS daytime total CO retrievals for 7 February 2009 over the SHA region. These measurements were made between approximately 06:50 and 08:30; the black triangles represent fires, as determined by the ESA WFA (ALGO1). The solid red box indicates the region used for determining the fire source locations, and the dashed red box denotes the region that bounds the emissions from these fires, as determined by the HYSPLIT trajectory model (see Fig. 7.10).

Fig.7.11), a number of trajectory analyses were carried out with plume injection heights ranging from 2 to 4 km, so as to ensure that the trajectory of transport from this isolated fire event was correctly accounted for. No spatially coincident CALIPSO data for the fire region existed for the 7 September 2009 and that is why measurements from the 6 September were used. The background concentrations of CO were calculated over the enhanced region (dashed red box in Fig. 7.9) but for 6 September 2007. This was because, as can be seen from Fig. 7.12, there is no nearby background

NOAA HYSPLIT MODEL  
 Forward trajectories starting at 0700 UTC 06 Feb 09  
 GDAS Meteorological Data

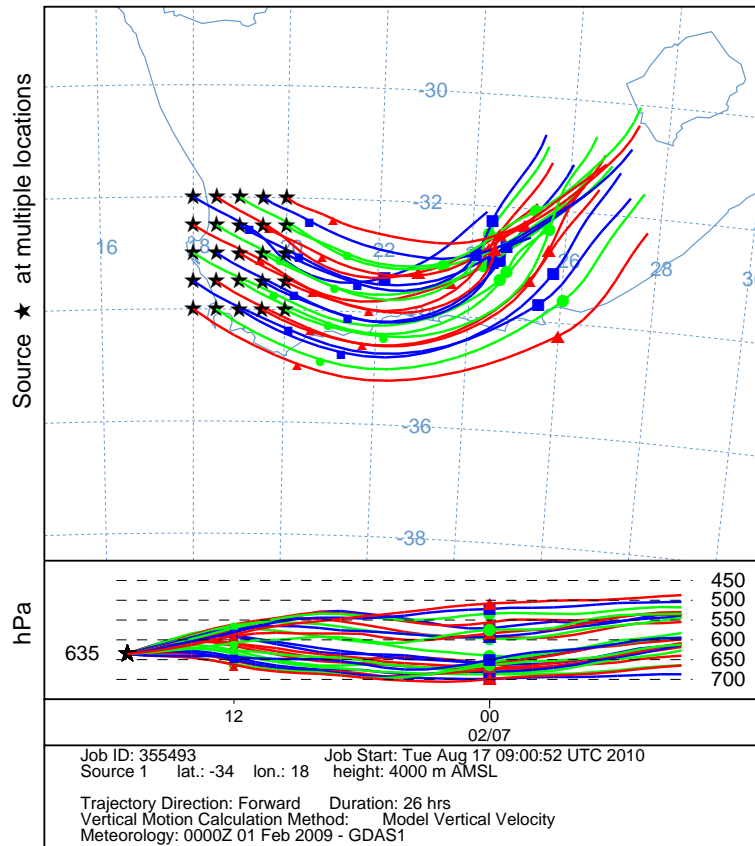


Figure 7.10: HYSPLIT trajectory analysis for 7 February 2009 over the region of interest indicated by the solid red box in Fig. 7.9. The run was started at 07:00 on 6 February 2009 and run for 26 hours. The stars indicate the multiple source locations, and the height of the plume is plotted in terms of pressure and time since release. A plume injection height of 4000 m above sea level was used.

region that is suitable in terms of the distribution of land cover type, and the isolated nature of the event means that the temporal difference should not introduce any artifacts or bias.

In order to confirm that the region of enhanced CO (dashed red box in Fig. 7.9) is due to the emissions from those fires which occurred on 6 February, a backwards trajectory analysis was performed using HYSPLIT, the results of which are shown in Fig. 7.13; this demonstrates that the region of enhanced CO under consideration

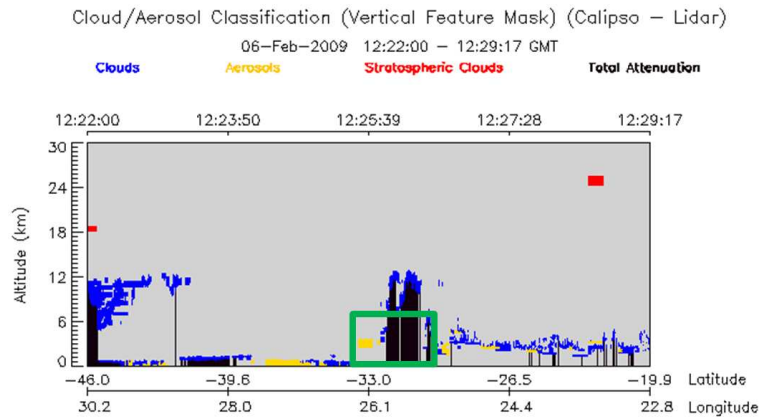


Figure 7.11: CALIPSO vertical feature mask for 6 February 2009 over South Africa. The green box indicates the enhanced region (dashed red box) shown in Fig. 7.9

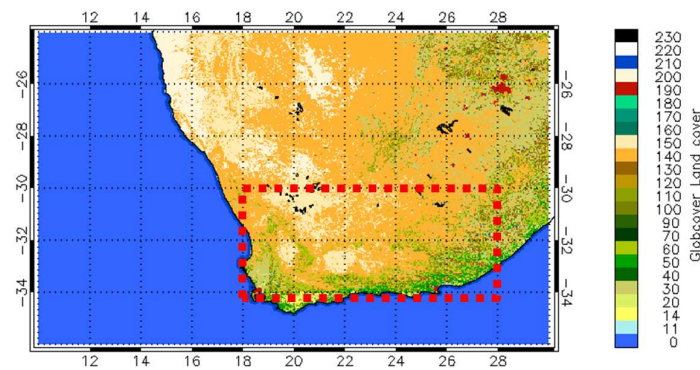


Figure 7.12: Globcover land type map over South Africa; the dashed red box corresponds to the area of enhanced CO, as shown in Fig. 7.9. The values correspond to the 22 different land cover types, as outlined in Arino et al. [2008].

can be directly traced back to the region of the isolated fire event (solid red box in Fig. 7.9). The hypothesis that this is truly an isolated fire event is given further credence by knowing that no fires in this region were recorded by the ESA WFA in the whole of the preceding month.

NOAA HYSPLIT MODEL  
 Backward trajectories ending at 0900 UTC 07 Feb 09  
 GDAS Meteorological Data

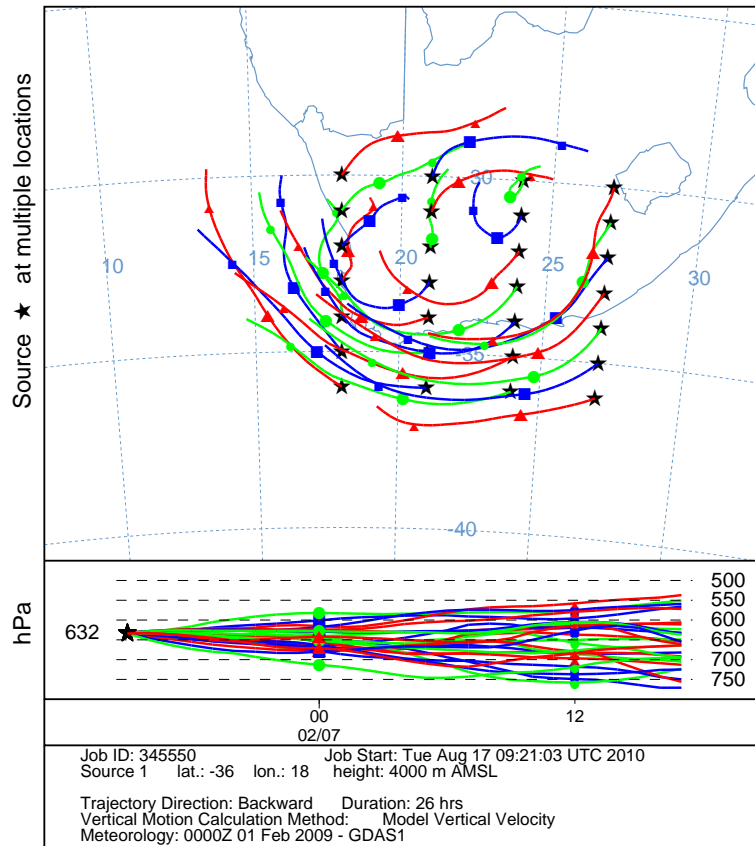


Figure 7.13: Backwards HYSPLIT trajectory analysis for 7 February 2009 over the enhanced region (dashed red box) shown in Fig. 7.9. The run was started at 09:00 on 7 February 2009 and run backwards for 26 hours.

### 7.4.1 Top-down Estimate

The simplified top-down approach estimates that a total of between 0.02 and 0.03 Tg CO has been emitted by the fires bound by the solid red box in Fig.7.9 from the time of burning to the time of measurement. The EDGAR FT 2000 anthropogenic emission inventory estimates the total anthropogenic emissions over the same region at 0.63 Tg CO per year, meaning that this fire event would correspond, in terms of pollution emitted, to approximately 3 - 4% of the total annual anthropogenic activities for the same region in only one day. These estimates for the CO emissions from this isolated fire event are tabulated in Table 7.5.

Methodology	CO Emissions (Tg)
Simplified Top-down	0.02-0.03
Bottom-up (MODIS BA)	0.0007
EDGAR	0.0017

Table 7.5: Estimates of CO emissions for the isolated fire event on 6 February 2009. The EDGAR value corresponds to the mean daily anthropogenic emissions, and is included for comparative purposes.

### 7.4.2 Bottom-up Estimate

Using the same methodology discussed in Sec. 7.3.1.3, a bottom-up estimate of the CO emissions for 7 February 2009 yielded a value of 0.0007 Tg for the region indicated by the solid red box in Fig.7.9. In comparison, the GFED3 gives a total of 0.0430 Tg for the same region, for the month of February 2009. However, it is not instructive to calculate a daily mean from this monthly GFED3 value, as such a value would not take into account the effects of transportation from fires and other CO emitting events during this time period. Whilst the ESA WFA indicates that the fires occurring on the 6 February are the only major fire event for this region over the entire month, the monthly GFED3 estimate may well be biased by emissions from long-range transport.

### 7.4.3 Discrepancies

Whilst differences between top-down and bottom-up estimates of CO emissions are to be expected [see e.g. Bergamaschi et al., 2000], the large discrepancies shown in Table 7.5 indicate that either the bottom-up methodology is underestimating the emissions, or the simplified top-down methodology is overestimating the emissions, or both. The top-down approach has endeavoured to ensure that the CO burden that has been calculated is truly representative of the emissions from the isolated fire event, and whilst it is still possible that this value may be an overestimation of the truth, the very low value for the bottom-up estimation of CO emissions, for a region where there is known to be fires, indicates that the bottom-up estimation of the CO emissions from the fire is a large underestimation of the truth. It was thought

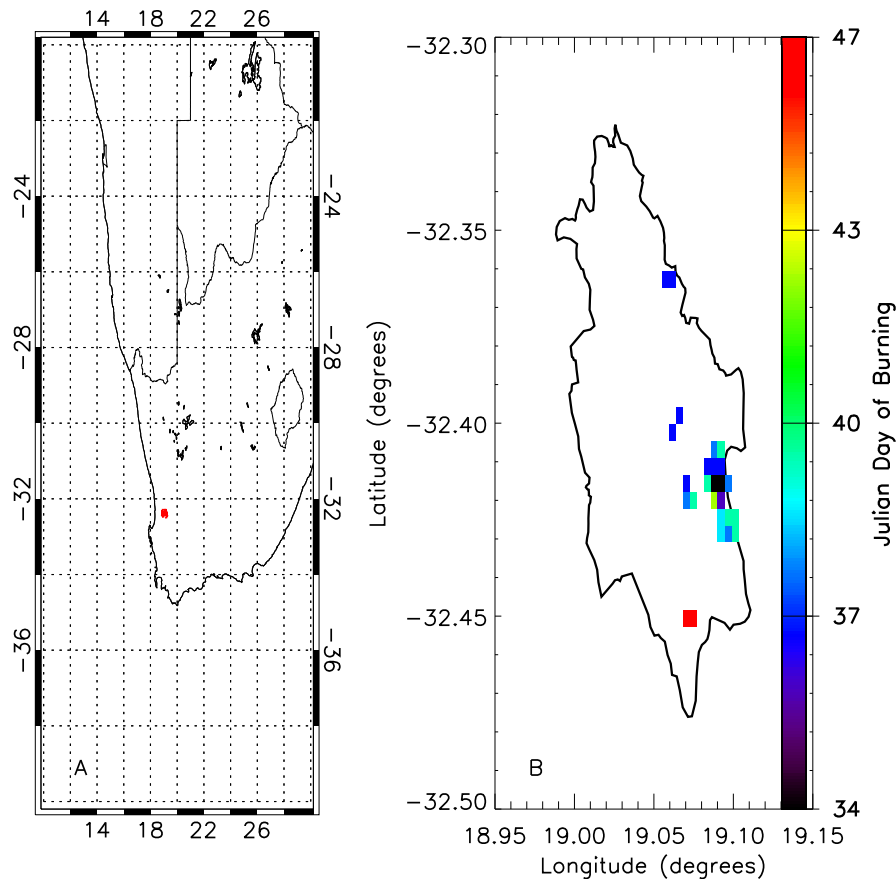


Figure 7.14: A: Location of Cederberg Wilderness fire (red) relative to SHA. B: The outline shows the in situ burnt area map of the February 2009 fire in the Cederberg Wilderness Area of South Africa, with the MCD45A1 detected fires for the month of February 2009 represented by the coloured squares.

that part of this underestimation was because of the delay that is associated with active fires and burnt area products, however a calculation of the CO emissions using MCD45A1 burnt area for the days proceeding the fire event yielded similar results.

In a study of the Greek wildfires of 2007, Turquety et al. [2009] found that bottom-up estimates of CO emissions from the fires were 23% lower compared to the CO burden derived from their IASI observations. By recalculating the bottom-up emissions based on in-situ measurements of the total burnt area, rather than using a satellite derived product (such as MCD45A1) they observed a discrepancy of less than 8%, i.e. the insensitivity of the remote sensing measurements to the true extent of the

	<b>MODIS</b>	<b>In situ</b>
Burnt Area (ha)	650	11 302
CO Emissions (Tg)	$2.33 \times 10^{-3}$	$2.67 \times 10^{-2}$

Table 7.6: In situ and MODIS derived Burnt Area and CO emissions for a fire in the Cederberg Wilderness Area of South Africa. The fire began burning on 6 February 2009.

burnt area resulted in an underestimation in the emissions.

In situ data for the burnt area of one of the fires in the Cederberg Wilderness Area has been provided by the Scientific Services team at CapeNature, a public institution with the statutory responsibility for biodiversity conservation in the Western Cape region of South Africa (see <http://www.capenature.org.za> for more details). Figure 7.14 shows the in situ measurements of the fire, as well as showing the MCD45A1 detected fires for the month of February 2009 in this region. Whilst it is difficult to prescribe a set burning time for the fire, a liberal estimate of one month still shows that the MCD45A1 algorithm does a poor job in correctly accounting for the burnt area of this isolated fire region. As can be seen from Fig.7.14, the MCD45A1 algorithm is only able to account for approximately 6% of the area that was actually burnt during this fire event, leading to an underestimation in the emitted CO of over 91%, as summarised in Table 7.6. This new bottom-up emission estimate was calculated using the same values of the AFL, CC, and EF for the relevant land types of the burnt area, and highlights the large discrepancies between the in situ and satellite derived burnt area products, and the effect that this difference has on the bottom-up CO emission estimates. Whilst this comparison between in situ and satellite derived burnt area has been done over a month, it gives a general indication as to the difficulty remote sensing measurements have in accounting for the total burnt area for an isolated fire. This supports the hypothesis that the bottom-up estimate for the CO emissions from the fire region of the Western Cape (solid red box in Fig. 7.9) is potentially a large underestimation of the actual CO emissions.

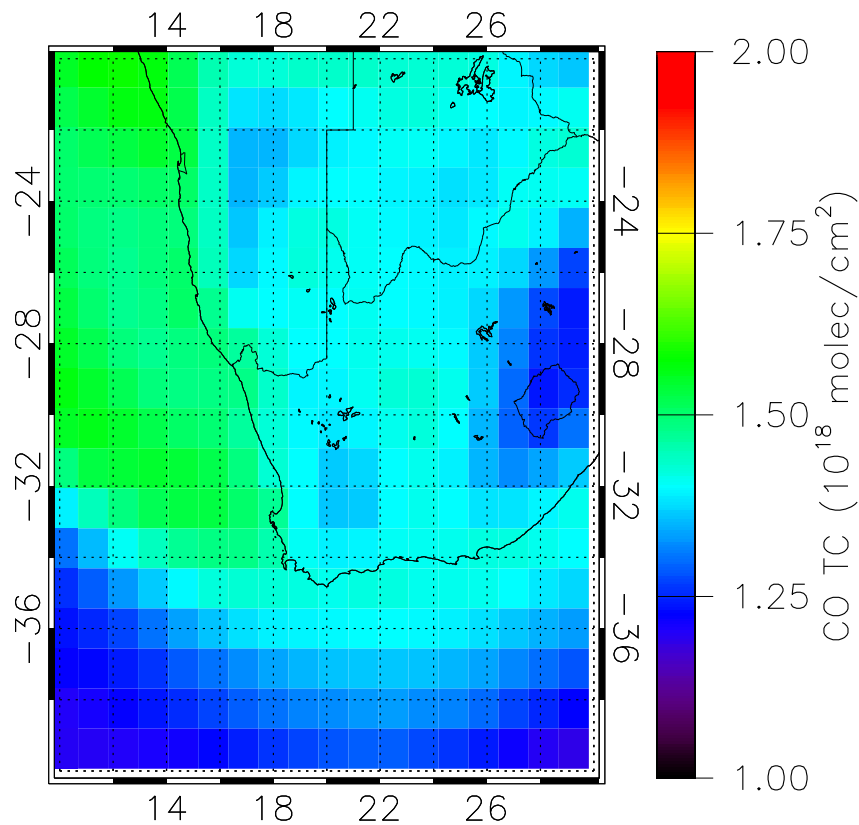


Figure 7.15: GEMS re-analysis CO total column density over the Western Cape region of South Africa, for 6 February 2009 on a  $1.125^\circ \times 1.125^\circ$  grid.

## 7.5 Comparison with Modelled Data

As an intermediary between the simplified top-down approach presented here and that of a full Bayesian inversion scheme, the ULIRS derived CO product has been compared to that from a study which assimilates both modelled and satellite retrieved products. The EU-funded GEMS (Global and regional Earth-system Monitoring using Satellite and in-situ data) project was developed as a comprehensive data analysis and modelling system for monitoring the global distribution of atmospheric constituents important for climate, air quality and UV radiation [Hollingsworth et al., 2008]. As part of the project a pre-operational data assimilation and forecasting system for aerosols, greenhouse gases and chemically reactive gases was developed,

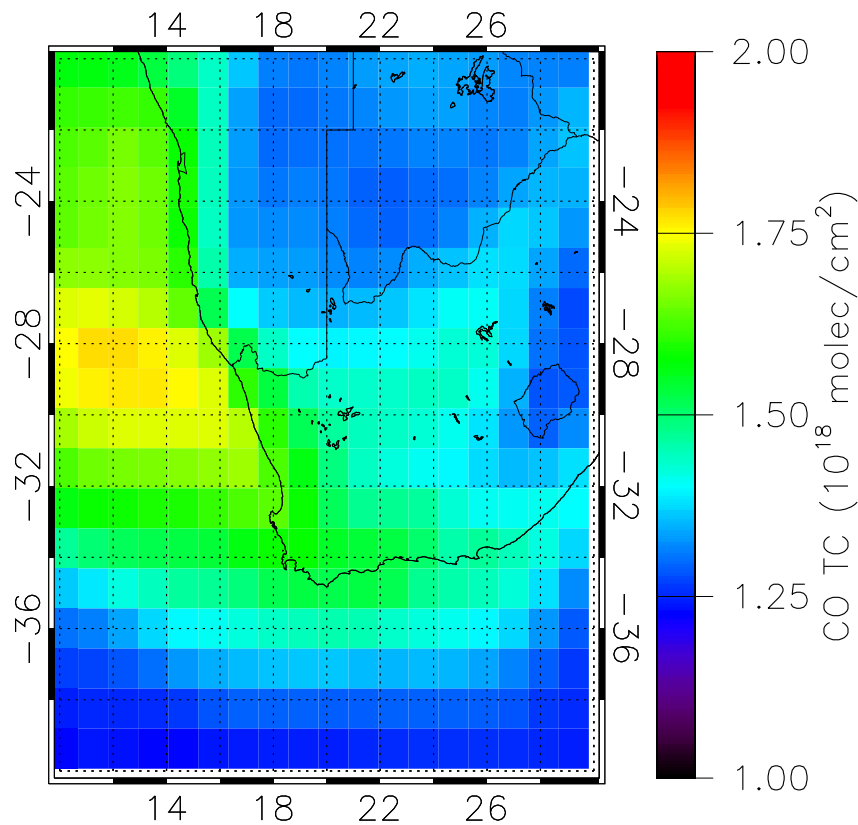


Figure 7.16: GEMS re-analysis CO total column density over the Western Cape region of South Africa, for 7 February 2009 on a  $1.125^\circ \times 1.125^\circ$  grid.

utilising ECMWF's 4D-VAR data assimilation system to assimilate satellite observations of atmospheric composition at the global scale. In this case, CO total column densities over land and between  $65^\circ$  N and  $65^\circ$  S, retrieved using the MOPITT V3 algorithm were used. Maps of the GEMS re-analysis CO total column density over the Western Cape region of South Africa, for 6 and 7 February 2009 are shown in Figs. 7.15 and 7.16, respectively. In comparison to Fig. 7.15, Fig. 7.16 shows an enhancement in CO over the Western Cape region of South Africa, but as can be seen from Fig. 7.17 this appears to be an artefact of transportation from North Africa, rather than a direct consequence of the fire events on 6 February in that region.

On both continental and regional scales the CO budget in Africa is dominated by fires. Fresh tropical BB plumes are usually confined within the boundary layer

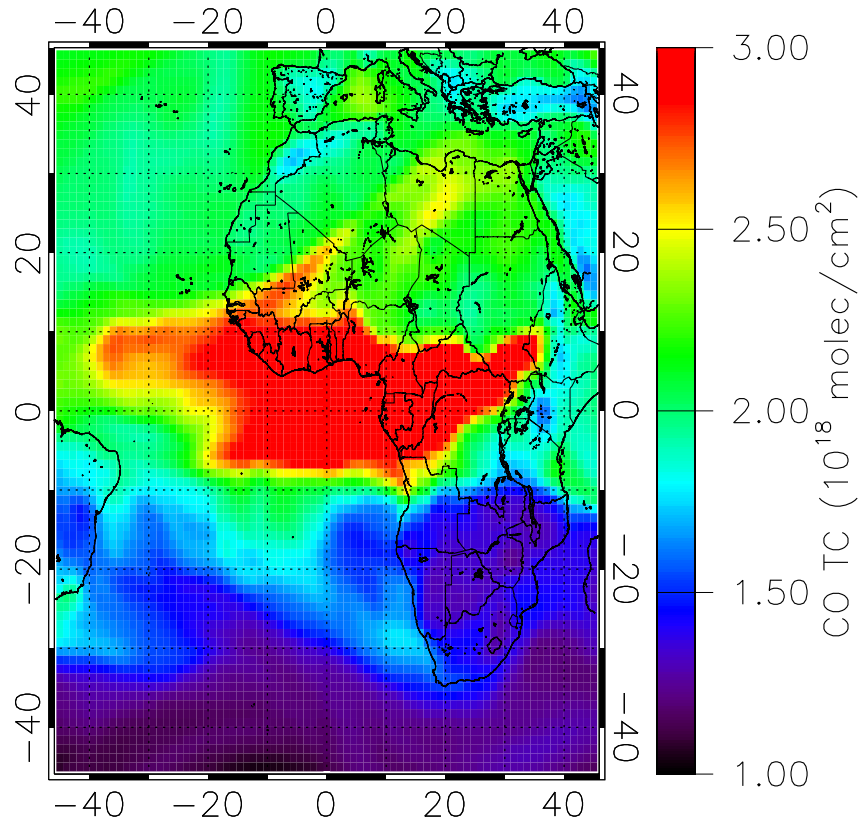


Figure 7.17: GEMS re-analysis CO total column density over the African region, for 7 February 2009 on a  $1.125^\circ \times 1.125^\circ$  grid. Note the different scale of the colour bar in comparison to Figs. 7.15 and 7.16.

[see e.g. Labonne et al., 2007] and may leave the African continent at low elevation [Garstang, 1988], meaning that by the time the plumes reach the free troposphere, they may be well depleted in CO [Mauzerall et al., 1998]. As a result, BB induces large gradients in the CO vertical profiles over tropical lands [see e.g. Yokelson et al., 2003]. Depending on the thermal contrast at the surface, the MOPITT instrument has some sensitivity to lower tropospheric CO [Deeter et al., 2007b], but cannot capture these steep gradients. Therefore, MOPITT provides only coarse spatial information about the CO emissions from fires, which could be responsible for a nonrepresentational CO total column density in the GEMS reanalysis. Future studies are needed to assess if the ULIRS data would improve on this assimilation, although the results of the

Western Cape study discussed in Sec. 7.4 would seem to indicate that the ULIRS is sensitive to fire events. Another factor which must also be considered is the early overpass of the IASI spacecraft during daytime (09:30 LST), as this does not favour the observation of the PBL which develops mostly in the afternoon.

## 7.6 Summary

This chapter has presented a description of how bottom-up and top-down estimates of CO emissions from fires are calculated, and has also discussed a new methodology for estimating CO emissions from a localised fire using the ULIRS CO product. The benefits of this simplified top-down approach, in comparison to a full Bayesian inversion scheme are that it is computationally more efficient, and that it is not affected by the necessary simple parameterisations of the errors inherent in CTMs. The major limitation to this simplified top-down approach is that it does not account for transportation from other CO emitting events, and as such it can only be reliably applied to isolated fire events.

A comparison between a bottom-up and a simplified top-down estimate of CO emissions, from an isolated fire event in Western South Africa on 6 February 2009 revealed large differences between the values derived using these two approaches. This large discrepancy prompted a detailed study into a comparison between remote sensing and in situ measurements of the burnt area for a relatively small and isolated fire. The inability of the MCD45A1 algorithm to correctly account for the true extent of the burning over this studied region, as given by an in situ map of the area burnt by the fire, pointed to the bottom-up estimate of CO emissions being an underestimation of the truth. This study highlighted the need for a better understanding of how the burnt area for reasonably small-scale isolated fire events is calculated from remote sensing measurements.

SHA is affected by large wild fires during the fire season, but the associated emissions for isolated fire events are not always included in modelled data, this was demonstrated by considering the GEMS modelled data of the isolated fire event in Western South Africa on 6 February 2009. Further work is needed to ascertain whether

integrating the ULIRS retrieved CO product would improve the accuracy in modelling such events, although given the lifetime of CO (approximately 2 months in the troposphere), at least a few months of the ULIRS derived CO product would be required, over a much larger spatial zone than the region of interest for the emissions. Ultimately, the ULIRS retrieved CO product would be incorporated into a 4D-Var assimilation such as GEMS, and an assessment as to how this product would inform on such an assimilation should be carried out.

# Chapter 8

## Conclusions and Future Work

This final chapter summarises how the aims of this thesis were successfully achieved and provides some of the key findings. Recommendations relating to future work are also discussed.

The key results of this thesis include:

- A demonstration that the IASI is radiometrically accurate to  $<0.3\text{ K}$ , in band 1 of the IASI instrument, over the 245 to 300 K temperature, and also in the  $4.7\ \mu\text{m}$  spectral region; this is less than the original 0.5 K requirement in the IASI Science Plan.
- It is shown that large retrieval errors and biases of up to 15% across the profiles and total columns are introduced by not including a solar reflected term, wavelength dependant surface emissivity, and detailed scene topography. The development and implementation of a new retrieval scheme, the ULIRS, which converts IASI TOA radiances into a CO product, and which incorporates these three terms is presented.
- The ULIRS enables the retrieval of between 1 and 2 pieces of information about the tropospheric CO vertical profiles, with peaks in the sensitivity at approximately 5 and 12 km. In the absence of a smoothing error, typical random errors over the African region relating to the profiles are found to be  $\sim 10\%$  at 5 and 12 km, and on the total columns to be  $\sim 12\%$ .

- The first detailed comparison of IASI data with the MOPITT retrieved CO product; these infer that the ULIRS CO retrievals are very reasonable, with low systematic biases apparent between the ULIRS and V4 in the study region. The majority of the profile differences are shown to be due to different a priori and measurement sensitivities.

Finally this chapter also includes a short discussion on future satellite mission proposals, and comments upon the suitability of these missions for continuation of the work in this thesis.

## 8.1 Radiometric Accuracy of the IASI Instrument

Chapter 4 presented an intercomparison between IASI and AATSR measured BTs in the 11 and 12  $\mu\text{m}$  regions, and concluded that there was an AMD between the two sets of measurements (IASI-AATSR) of  $-0.04\text{ K}$  and  $0.22\text{ K}$  for the 11 and 12  $\mu\text{m}$  channels respectively, for clear sky conditions. The random error on the mean of the average differences was also found to be relatively small, with a conservative estimate of the bias uncertainty in the AMD taken to be  $0.04\text{ K}$  for both channels. Furthermore, the results show a remarkable consistency, particularly for the combination of clear sky and fully-cloudy data, for which there are a larger number of matches and a wider temperature range than for the clear sky only comparisons. Absolute differences at 11  $\mu\text{m}$  are less than  $0.1\text{ K}$  for all cases, and for 12  $\mu\text{m}$  shift from  $0.22\text{ K}$  for clear sky, to  $0.34\text{ K}$  for all match-ups; this shift may in part be due to the temperature range of the intercomparison, which extends below that for which the AATSR is understood to be linearly radiometrically calibrated (265 to 305 K). As the AATSR is calibrated to a radiometric accuracy of  $30\text{ mK}$ , these results indicate that the IASI instrument has a radiometric accuracy of better than  $0.1\text{ K}$  at 11  $\mu\text{m}$ , over the 245 to 300 K temperature range. The result for the offset at 12  $\mu\text{m}$  independently supports the need for a possible correction to the AATSR 12  $\mu\text{m}$  spectral filter function.

The intercomparison between the IASI and AATSR gave a direct quantification for the radiometric accuracy in band 1 of the IASI instrument. As the radiometric calibration error between any 2 bands of the IASI instrument is known to be  $< 0.1\text{ K}$ , it can be stated with some confidence that the radiometric accuracy of the IASI

instrument is  $<0.3$  K in the  $4.7\ \mu\text{m}$  region, over the 245 to 300 K temperature range for which this intercomparison was conducted. This is better than the radiometric accuracy of approximately 0.5 K that was originally stipulated as part of the IASI Science Plan, and has important implications for the retrieval of atmospheric CO information, which utilises this part of the spectra.

### 8.1.1 Future Work

Whilst this study has considered a large number of IASI and AATSR measured BTs, across a wide temporal range, it is by no means exhaustive. Initial studies have indicated that the orbital tracks of the Envisat and MetOp-A satellites, combined with the requirement of a temporal resolution of less than thirty minutes and an absolute difference in the satellite zenith angles of less than  $1^\circ$ , result in a statistically significant data set being available on average less than once a month. The next step in the continuation of this work is thus to extend the intercomparison to include all of the coincident dates from the beginning of the IASI mission to the present, which is thought to be in the region of 30. Such a long-spanning comparison should also highlight any possible seasonal dependency in the intercomparison. The extension of the intercomparison to include fully cloudy scenes was discussed in Chapter 4, however care must be taken when considering measured BTs which extend beyond the range for which the AATSR instrument is known to be linearly calibrated. Any BTs which extend beyond this range must factor in the non-linearity correction for the AATSR, or must be neglected entirely.

Another interesting study would be to perform an intercomparison between the AATSR and IASI measured BTs in the  $3.7\ \mu\text{m}$  region. This would then give further information as to the radiometric accuracy of the IASI instrument in band 3. The major drawback with this approach is that part of the IASI spectra would need to be modelled, as the spectral response function goes beyond the spectral range of the IASI instrument. The possible errors that this would introduce are the reasons why this approach has not been adopted here, but future work could be carried out to ascertain the degree of error that would be introduced by modelling that part of the spectrum.

As previously alluded to, the current spectral response function for the  $12\ \mu\text{m}$

channel of the AATSR instrument is now believed to be incorrect, with initial reports indicating that this has resulted in a negative bias of approximately 0.2 K for the AATSR measured BTs in this channel. The work carried out in this study has been shown to independently verify this result, and it is hypothesised that when the new spectral response function has been verified and made public, that the intercomparison between the IASI and AATSR measured BTs in the 12  $\mu\text{m}$  channel will come into agreement with the results obtained for the 11  $\mu\text{m}$  channel.

The AATSR should continue to provide very high quality data until 2013, following the recent extension of the ESA's Envisat mission. The first of the next generation of ATSR instruments, the Sea and Land Surface Temperature Radiometers (SLSTR), is planned to be in operation towards the end of 2013 or, more likely, in 2014. Although agencies and climate scientists are clear about the need to maintain a continuous climate record, there is the strong possibility of a data gap, and thus the need for a comparison point for radiometric calibration to bridge this gap between the AATSR and the SLSTR missions. The results presented in this thesis confirm the possible strategy of using IASI to fulfil this need. Furthermore, the methodology of intercomparison that has been presented in this thesis can be applied to the future IASI instruments onboard the MetOp-A and MetOp-B satellites, as understanding how the three IASI instruments are calibrated relative to one another will be vital.

## 8.2 Retrieval of CO

Chapter 5 discussed in detail the ULIRS, a new retrieval scheme for converting IASI TOA radiances into CO profile and total column amounts. The ULIRS incorporates the Oxford RFM as a forward model, and makes use of the spectral interval 2143 to 2181  $\text{cm}^{-1}$ . A CO a priori profile and covariance matrix were constructed using over 8000 profiles from the TOMCAT CTM, which incorporates a wide variety of CO scenarios, and are representative of an entire year (2004), so as to allow for any seasonal effects. The three main features that exemplify the ULIRS are: a spatially precise surface emissivity and topography of the IFOV, and a quantified solar component, which makes use of the ACE-FTS atlas of the IR solar spectrum. A linear error analysis was performed to establish the error terms that are introduced by not

accounting for these parameters in the retrieval process, with errors of up to 15 % across the profile being observed.

A thorough characterisation of the retrievals has shown that the high quality TOA radiances measured by the IASI instrument enable the retrieval of between 1 and 2 pieces of information about the tropospheric CO vertical profiles. The first piece of information is located in the lower-middle troposphere (at approximately 5 km) and the second one in the UTLS (at approximately 12 km). A full error analysis has shown that the main source of error is the smoothing error, with an added contribution from the measurement error in the lower-middle troposphere. Typical errors for the African region relating to the profiles are found to be  $\sim 20\%$  at 5 and 12 km, and on the total columns to be approximately 24 %. These errors include a smoothing term; neglecting the smoothing error the total random errors are found to be  $\sim 10\%$  at 5 and 12 km, and on the total columns to be approximately 12 %.

The sensitivity of the ULIRS was investigated by assessing the retrieval of a number of profiles provided by the CAMELOT mission, with the ULIRS retrievals found to introduce a bias of no more than 3 % for a thorough consideration of simulations.

### 8.2.1 Future Work

The validity of the choices made in constructing the ULIRS have been discussed thoroughly in this thesis, with sensitivity tests and simulations demonstrating that it is able to provide a detailed and well characterised CO product. Although the ULIRS provides a high quality CO product, an improvement that could be made would be to incorporate a hyper-spectral surface emissivity product, such as that which has recently been developed by Eva Borbas at the University of Wisconsin-Madison Space Science and Engineering Centre (UW-SSEC). Such an inclusion must be carefully incorporated however, as the RFM is limited to the use of a monochromatic emissivity product.

Whilst the ULIRS was never designed to retrieve at operational speeds (or near real time), the computational efficiency of the scheme could certainly be improved, so that localised regions spanning a wide temporal range could be retrieved more rapidly. Again, part of the limitations to this improvement in retrieval speed come from the current choice of forward model, as the RFM is unable to use appropriate

approximations and pre-computed Look-Up Tables (LUTs) for the ULIRS' choice of retrieval parameters. This is a further indication that the investigation of a possible replacement for the RFM would be a worthwhile study. One possible candidate is the Radiative Transfer Model for TOVS (RTTOV) [Saunders et al., 1999], which expresses the transmittances of atmospheric gases as a function of profile dependent predictors, and which is very computationally efficient. Eventually the ULIRS should be modified so as to allow the user to select from a variety of forward models, should they so wish.

The simulations carried out on the ULIRS have given some indication as to the retrieval biases; however, in order to account for these fully it is necessary to validate the retrieved product with real measurements, and whilst an intercomparison of ULIRS and MOPITT retrieved CO (see Sec. 8.3) has verified this in terms of other independent satellite measurements, it is vital that the ULIRS retrieved product is compared to ground-based and aircraft, remote sensing and in situ measurements, so as to inform on any biases within the retrieval scheme in comparison to the best perceived "truth". In addition to these validation studies it would be instructive to perform an in-depth analysis to compare and contrast the ULIRS and the operationally retrieved IASI CO product, available from the LATMOS (Laboratoire Atmosphères, Milieux, Observations Spatiales) research group [see e.g. Turquety et al., 2009].

### **8.3 Satellite Intercomparison of CO**

Chapter 6 presented an intercomparison between the ULIRS CO product and that which was retrieved operationally using the MOPITT instrument; with the comparison being carried out for both the V3 and the V4 MOPITT data sets. To account for the different a priori information in IASI and MOPITT retrievals, IASI a priori profiles and covariance matrices were applied to a modified operational MOPITT retrieval algorithm. The resulting differences were similar to those expected from the smoothing biases of the two instruments, which was characterised using modelled CO data from the GEOS-Chem CTM. A smoothing of the IASI retrieved profile using the MOPITT averaging kernels resulted in retrieved profile comparisons which were much less dependent on smoothing error. This methodology was found to be more

reliable for the comparison with the MOPITT V4 product, where MOPITT V4 and IASI CO biases were found to be less than 4% on average. These results indicated that the ULIRS CO retrievals were reasonable, and agreed well with an independent data set.

### 8.3.1 Future Work

Only one day (1 September 2007) has been selected for this study, which has also been limited to the sub-Saharan Africa region. The next step in the continuation of this work would be to extend the intercomparison over a larger temporal range, and to different regions. Initially the intercomparison should be widened to incorporate dates from the different seasons, as it would be interesting to see how the IASI and MOPITT CO products compared during a period that was not affected by biomass burning. Such a study would also enable the identification of any inter-annual variability between the two data sets, which could then be explored further by carrying out an intercomparison for extended time periods; obviously such a study would be reliant upon an improvement in the computational efficiency of the ULIRS, as outlined in Sec. 8.2.1. With a larger data set it would also be possible to quantify how the observed differences between the IASI and MOPITT data sets compare to the instrument-related biases that are expected between the MOPITT V3 and V4 products.

One of the interesting results to arise from the work carried out in this comparison, was that the IASI instrument appears to display a greater vertical sensitivity to CO in comparison to MOPITT, as is evident from MOPITT having less DFS than IASI over the region considered for this analysis. It is hypothesised that this is because of the different measurement techniques that the two instruments utilise, however this needs to be validated using more data, as if this is so then it recommends the use of FTS over PMC based instrumentation for future CO retrievals.

## 8.4 Top-down and Bottom-up Estimates of CO Emissions

Chapter 7 presented a simplified top-down methodology for estimating CO emissions from a localised fire, by directly utilising the ULIRS CO product. This approach is beneficial in comparison to a full Bayesian inversion scheme as it is unaffected by errors in the CTM, as well as being more computationally efficient. The main limitation of this simplified approach is that it does not fully account for transport processes, and thus can only be reliably applied to an isolated event. The approach developed in this thesis could be used to provide a basis for local verification of bottom-up and top-down estimates of CO emissions.

Chapter 7 also discussed a comparison between a bottom-up and simplified top-down estimate of CO emissions from an isolated fire event in Western South Africa on 6 February 2009, with large differences found to exist between these two values. As the event was shown to be truly isolated, it was hypothesised that the bottom-up approach was an underestimation of the truth. Further investigation showed this to be the case, as the satellite derived burnt area product used in the bottom-up approach was found to largely underestimate that provided by in situ measurements.

### 8.4.1 Future Work

There are two discrepancies that have been studied in Chapter 7 of this thesis: 1) the difference between a simplified top-down and bottom-up approach to estimating the CO emissions from a localised fire; and 2) the difference between satellite derived and in situ burnt area maps for small isolated fires. In order to further understand the causes of these differences, so that they can (if possible) be rectified, it will be necessary to study a number of isolated fire events, and to compare not only the top-down and bottom-up estimations of CO emissions, but also the burnt area product as derived from satellites, and as measured on the ground. One other feature that must be considered in the simplified top-down estimate is the role of clouds. The ULIRS is optimised for cloud-free conditions, and so this means that data which has been flagged as cloudy is not considered when calculating the CO burden from the ULIRS

derived product. This may lead to a misrepresentation of the true extent of the CO emissions from the fire, either through a reduction in the dataset, or because the data which has been flagged as cloudy is actually a plume from the fire.

Ultimately, the ULIRS retrieved CO product would be incorporated into a 4D-Var assimilation such as GEMS, and an assessment as to how this product would inform on such an assimilation should be carried out. By assimilating a few months of the ULIRS derived CO product over a much larger region than the region of interest for the emissions, to ensure that the domain boundaries are well constrained, it is believed that the CO emissions from these isolated fires could be better accounted for; such a large number of retrievals would obviously require an improvement in the computational efficiency of the ULIRS.

## 8.5 Future Missions

The MetOp-A satellite is due to be in service until at least 2020, this means that there should be over a decade of continuous data from the current IASI instrument, from which long-term climatological trends of atmospheric CO and the emissions from fires should be observable. The MetOp-B, due to be launched in mid 2012, and MetOp-C, to be launched in the 2016/2017 time frame, satellites will also have IASI instruments mounted upon them; this means that as well as extending the data record there will be long periods of overlap, which will be vital in assessing the validation and calibration of the different IASI instruments.

Other future missions designed to improve upon our understanding of the vertical distribution of CO include the PREMIER (PRocess Exploration through Measurements of IR and millimetre-wave Emitted Radiation) instrument, which is one of three candidates for ESA's seventh Earth Explorer mission, to be launched around 2016. Its objective is to understand the many processes that link trace gases, radiation, chemistry and climate in the atmosphere - concentrating on the processes in the UTLS region. PREMIER aims to achieve its objectives by implementing two major innovations: (1) the first satellite FTIR limb-imager, with integrated cloud/aerosol imaging, and (2) the first satellite Millimetre-Wave Limb-Sounder (MWLS) optimised for upper-troposphere sounding. The FTIR instrument's shortwave limit is currently

$\sim 6 \mu\text{m}$ , which is well outside of the  $4.7 \mu\text{m}$  ( $4200 \text{ cm}^{-1}$ ) band, and so will not be used for CO observations. However, the MWLS will make measurements at the 346 GHz CO absorption line, which is  $\sim 6$  stronger than the one at 231 GHz that is currently used to make CO observations by the MLS. The observation of this stronger line feature, coupled with the use of a 14 element array, rather than a single limb-scanning receiver, mean that the information on CO in the upper troposphere that is provided by the PREMIER mission should be a great improvement on that currently obtainable by the MLS.

ESA is currently developing five new missions called Sentinels, specifically for the operational needs of the joint European Commission-ESA Global Monitoring for Environment and Security (GMES) programme. A Sentinel-5 precursor mission is planned to launch in 2014, to avoid data gaps between Envisat and Sentinel-5 (planned launch date of 2019), and will be devoted to atmospheric monitoring. The Sentinel-5 precursor is a UV-VIS-NIR-SWIR spectrometer and will operate in a nadir observation mode, in LEO, with global daily coverage, and a ground pixel size of  $7 \text{ km}^2$ . It will make use of the  $4198$  to  $4320 \text{ cm}^{-1}$  spectral band to make global observations of atmospheric CO, and aims to be radiometrically accurate to better than  $\sim 2\%$ . As measurements made in the  $4200 \text{ cm}^{-1}$  band require sunlight, the temporal and spatial resolution of the instrument will be reduced.

There is a limitation to the temporal frequency that can be achieved by satellites in LEO, and this appears to be approximately 1 per day at the equator. A geostationary orbit, where the same part of the planet is in view at any time, would greatly improve the temporal resolution, to about 10 to 100 min. The downside of this technique is that a network of satellites is required for the coverage to be truly global. An example of a geostationary based instrument designed for making observations of atmospheric CO is the Geostationary Coastal and Air Pollution Events (GEO-CAPE) mission, which has been recommended for launch in the 2013 to 2016 time frame by the National Research Council in the US. GEO-CAPE consists of three instruments in geosynchronous Earth orbit near  $80^\circ \text{ W}$  longitude: a UV-VIS-NIR wide-area imaging spectrometer ( $7 \text{ km}^2$  nadir pixel), capable of mapping North and South America from  $45^\circ \text{ S}$  to  $50^\circ \text{ N}$  at approximately hourly intervals; a steerable high-spatial-resolution ( $250 \text{ m}$ ) event-imaging spectrometer with a  $300 \text{ km}$  field of view; and an IR correlation

radiometer, which makes use of both the 4.7  $\mu\text{m}$  and the 2.3  $\mu\text{m}$  spectral bands, for the mapping of CO over a field consistent with the wide-area spectrometer.

In order to produce the most reliable maps of global CO, it will be necessary to use a combination of LEO and geostationary satellites, which make use of both the 4.7  $\mu\text{m}$  and the 2.3  $\mu\text{m}$  spectral bands. For example, a geostationary based instrument situated over the Atlantic Ocean would be able to map the outflow of fires from South America to Southern Africa with a high temporal frequency, but in the case of observing emissions from boreal fires in the former USSR, instruments situated in a LEO would be required, because of the high viewing angles that would be required for geostationary observations [Drummond, 2002]. The continued importance of LEO observations have lead to the development of a new generation IASI instrument, which will be flown onboard the post-EPS program, from 2019 onwards [Phillips et al., 2007].

## 8.6 Closing Remarks

The work undertaken in this thesis has demonstrated that the IASI instrument is performing with a better radiometric accuracy than was originally anticipated. It has also been shown that by carefully considering the TOA radiances measured by IASI, information about the atmospheric composition of CO can be inferred, providing that careful consideration is given to the selection and integration of a priori and auxiliary data sets. These initial results compare well to other independent data sets with a long term heritage and, combined with the long lifetime of the IASI mission, indicate that measurements made using the IASI instrument can be used as a long term data record for calibration, validation, and climatological purposes.

## ACKNOWLEDGEMENTS FOR PROVISION OF DATA AND FUNDING

This work was funded by a Natural Environment Research Council (NERC) studentship at the University of Leicester, UK.

IASI has been developed and built under the responsibility of the Centre National d'Etudes Spatiales (CNES, France). It is flown onboard the MetOp satellites as part of the EUMETSAT Polar System. The IASI L1 data used in this thesis have been provided by EUMETSAT's online archive, UMARF. The MOPITT data was obtained from the NASA Langley Research Center Atmospheric Science Data Centre, USA, with further analysis performed on some of the data sets by Merritt Deeter at the Atmospheric Chemistry Division of the National Centre for Atmospheric Research (NCAR), USA.

The AATSR data used in this study were provided by ESA and the NERC Earth Observation Data Centre (NEODC). The AATSR is a nationally provided payload instrument on ESA's Envisat satellite, which was funded by the UK Department of Environment, Food and Rural Affairs (DEFRA), and is now funded by the Department of Energy and Climate Change (DECC), in support of their programme in climate prediction and research, with additional contributions from NERC, UK, & CSIRO, Australia.

The author gratefully acknowledges the NOAA Air Resources Laboratory (ARL) for the provision of the HYSPLIT transport and dispersion model and READY website (<http://www.arl.noaa.gov/ready.php>). GEMS data came courtesy of the Monitoring Atmospheric Composition and Climate (MACC) project, delivered as a component of Europe's GMES initiative. Some of the analyses and visualisations used in this thesis were produced with the Giovanni online data system, developed and maintained by the NASA GES DISC.

The author would like to thank Peter Bernath at The University of York for the use of ACE solar spectra, Nigel Richards and Martyn Chipperfield at University of Leeds for TOMCAT data, Paul Palmer and Siegfried Gonzi at The University of Edinburgh for GEOS-Chem data, and the NEODC for access to ECMWF data.

# Bibliography

- Acker, J. G. and Leptoukh, G. [2007], ‘Online analysis enhances use of NASA Earth Science Data’, *Eos* **88**(2).
- Andreae, M. O. and Merlet, P. [2001], ‘Emission of trace gases and aerosols from biomass burning’, *Global Biogeochemical Cycles* **15**(4), 955–966.
- Arellano Jr., A. F. and Hess, P. G. [2006], ‘Sensitivity of top-down estimates of CO sources to GCTM transport’, *Geophysical Research Letters* **33**(21), L21807.
- Arellano Jr., A. F., Kasibhatla, P. S., Giglio, L., van der Werf, G. R. and Randerson, J. T. [2004], ‘Top-down estimates of global CO sources using MOPITT measurements’, *Geophysical Research Letters* **31**(1), L01104 1–5.
- Arino, O., Bicheron, P., Achard, F., Latham, J., Witt, R. and Weber, J. . [2008], ‘Globcover: The most detailed portrait of Earth’, *European Space Agency Bulletin* **2008**(136), 24–31.
- Aumann, H. H. and Pagano, T. S. [2008], Using AIRS and IASI data to evaluate absolute radiometric accuracy and stability for climate applications, *in* ‘Society of Photo-Optical Instrumentation Engineers (SPIE) Conference Series’, Vol. 7085.
- Barret, B., Turquety, S., Hurtmans, D., Clerbaux, C., Hadji-Lazaro, J., Bey, I., Auvray, M. and Coheur, P. . [2005], ‘Global carbon monoxide vertical distributions from spaceborne high-resolution FTIR nadir measurements’, *Atmospheric Chemistry and Physics* **5**(11), 2901–2914.
- Bates, T., Kelly, K., Johnson, J. and Gammon, R. [1995], ‘Regional and seasonal variations in the flux of oceanic carbon to the atmosphere’, *Journal of Geophysical Research* **79**, 23093–23101.

- Bergamaschi, P., Hein, R., Heimann, M. and Crutzen, P. J. [2000], ‘Inverse modeling of the global CO cycle 1. inversion of CO mixing ratios’, *Journal of Geophysical Research D: Atmospheres* **105**(D2), 1909–1927.
- Bertschi, I., Yokelson, R. J., Ward, D. E., Babbitt, R. E., Susott, R. A., Goode, J. G. and Hao, W. M. [2003], ‘Trace gas and particle emissions from fires in large diameter and belowground biomass fuels’, *Journal of Geophysical Research D: Atmospheres* **108**(13).
- Bey, I., Jacob, D. J., Yantosca, R. M., Logan, J. A., Field, B. D., Fiore, A. M., Li, Q., Liu, H. Y., Mickley, L. J. and Schultz, M. G. [2001], ‘Global modeling of tropospheric chemistry with assimilated meteorology: Model description and evaluation’, *Journal of Geophysical Research D: Atmospheres* **106**(D19), 23073–23095.
- Blumstein, D., Chalon, G., Carlier, T., Buil, C., Hébert, P., Maciaszek, T., Ponce, G., Phulpin, T., Tournier, B., Siméoni, D., Astruc, P., Clauss, A., Kayal, G. and Jegou, R. [2004], IASI instrument: Technical overview and measured performances, *in* M. Strojnik, ed., ‘Society of Photo-Optical Instrumentation Engineers (SPIE) Conference Series’, Vol. 5543.
- Bovensmann, H., Burrows, J. P., Buchwitz, M., Frerick, J., Nol, S., Rozanov, V. V., Chance, K. V. and Goede, A. P. H. [1999], ‘SCIAMACHY: Mission objectives and measurement modes’, *Journal of the Atmospheric Sciences* **56**(2), 127–150.
- Bowman, K. [2006], ‘Transport of carbon monoxide from the tropics to the extratropics’, *Journal of Geophysical Research* **111**, D02107.
- Bowman, K. and Cohen, P. [1997], ‘Interhemispheric exchange by seasonal modulation of the hadley circulation’, *Journal of Atmospheric Science* **54**, 2045–2059.
- Camy-Peyret, C. and Eyre, J. [1998], IASI science plan, Technical report, ISSWG.
- Ceccherini, S. and Ridolfi, M. [2010], ‘Technical note: Variance-covariance matrix and averaging kernels for the levenberg-marquardt solution of the retrieval of atmospheric vertical profiles’, *Atmospheric Chemistry and Physics* **10**(6), 3131–3139.

- Chalon, G., Cayla, F. and Diebel, D. [2001], IASI : An advance sounder for operational meteorology, *in* ‘Proceedings of the 52nd Congress of the International Astronautical Federation (IAF), Toulouse, France, 1-5 October’.
- Chipperfield, M. P. [2006], ‘New version of the TOMCAT/SLIMCAT off-line chemical transport model: Intercomparison of stratospheric tracer experiments’, *Quarterly Journal of the Royal Meteorological Society* .
- Clerbaux, C., Boynard, A., Clarisse, L., George, M., Hadji-Lazaro, J., Herbin, H., H., D., Pommier, M., Razavi, A., Turquety, S., Wespes, C. and Coheur, P.-F. [2009], ‘Monitoring of atmospheric composition using the thermal infrared IASI/MetOp sounder’, *Atmospheric Chemistry and Physics* **9**(16), 6041–6054.
- Cofer III, W. R., Levine, J. S., Winstead, E. L., Cahoon, D. R., Sebacher, D. I., Pinto, J. P. and Stocks, B. J. [1996], ‘Source compositions of trace gases released during African savanna fires’, *Journal of Geophysical Research D: Atmospheres* **101**(19), 23597–23602.
- Deeter, M., Edwards, D., Gille, J., Emmons, L., Francis, G., Ho.S.-P., Mao.D., Masters, D., Worden, H. and Drummond, J. [2010], ‘The MOPITT version 4 CO product: Algorithm enhancements, validation, and long-term stability’, *Journal of Geophysical Research D: Atmospheres* **115**.
- Deeter, M. N., Edwards, D. P. and Gille, J. C. [2007a], ‘Retrievals of carbon monoxide profiles from MOPITT observations using lognormal a priori statistics’, *Journal of Geophysical Research D: Atmospheres* **112**(11).
- Deeter, M. N., Edwards, D. P., Gille, J. C. and Drummond, J. R. [2007b], ‘Sensitivity of MOPITT observations to carbon monoxide in the lower troposphere’, *Journal of Geophysical Research D: Atmospheres* **112**(24).
- Deeter, M. N., Emmons, L. K., Francis, G. L., Edwards, D. P., Gille, J. C., Warner, J. X., Khattatov, B., Ziskin, D., Lamarque, J. ., Ho, S. ., Yudin, V., Atti, J. ., Packman, D., Chen, J., Mao, D. and Drummond, J. R. [2003], ‘Operational carbon monoxide retrieval algorithm and selected results for the MOPITT instrument’, *Journal of Geophysical Research D: Atmospheres* **108**(14), ACH 1–1 – ACH 1–11.

- Dinguirard, M. and Slater, P. N. [1999], ‘Calibration of space-multispectral imaging sensors: A review’, *Remote Sensing of Environment* **68**(3), 194–205.
- Draxler, R. R. and Hess, G. D. [1998], ‘An overview of the HYSPLIT-4 modelling system for trajectories, dispersion and deposition’, *Australian Meteorological Magazine* (4), 295–308.
- Drummond, J. R. [2002], The future of carbon monoxide measurements in the troposphere, *in* ‘International Geoscience and Remote Sensing Symposium (IGARSS)’, Vol. 2, pp. 1099–1101.
- Drummond, J. R. and Mand, G. S. [1996], ‘The measurements of pollution in the troposphere (MOPITT) instrument: Overall performance and calibration requirements’, *Journal of Atmospheric and Oceanic Technology* **13**(2), 314–320.
- Dudhia, A. [2000], ‘Michelson interferometer for passive atmospheric sounding (MIPAS) reference forward model (RFM)’, *Software User’s Manual* .
- Duncan, B., Logan, J., Bey, I., Megretskaia, I., Yantosca, R., Novelli, P., Jones, N. and Rinsland, C. [2007], ‘Global budget of CO, 1988 - 1997: Source estimates and validation with a global model’, *Journal of Geophysical Research D: Atmospheres* **112**(22).
- Edwards, D. P. [1992], ‘GENLN2: A general line-by-line atmospheric transmittance and radiance model’, *NCAR Tech.Note, NCAR/TN-367+STR* .
- Edwards, D. P., Halvorson, C. M. and Gille, J. C. [1999], ‘Radiative transfer modeling for the EOS Terra satellite measurement of pollution in the troposphere (MOPITT) instrument’, *Journal of Geophysical Research D: Atmospheres* **104**(D14), 16755–16775.
- Edwards, P. G., Berruti, B., Blythe, P., Callies, J., Carlier, S., Fransen, C., Krutsch, R., Lefebvre, A. ., Loiselet, M. and Stricker, N. [2006], ‘The MetOp satellite’, *European Space Agency Bulletin* (127), 8–16.

- Emmons, L. K., Edwards, D. P., Deeter, M. N., Gille, J. C., Campos, T., Ndlec, P., Novelli, P. and Sachse, G. [2009], ‘Measurements of pollution in the troposphere (MOPITT) validation through 2006’, *Atmospheric Chemistry and Physics* **9**(5), 1795–1803.
- Emmons, L. K., Walters, S., Hess, P., Lamarque, J.-F., Pfister, G. G., Fillmore, D., Granier, C., Guenther, A., Kinnison, D., Laepple, T., Orlando, J., Tie, X., Tyndall, G., Wiedinmyer, C., Baughcum, S. L. and Kloster, S. [2010], ‘Description and evaluation of the model for ozone and related chemical tracers, version 4 (MOZART-4)’, *Geoscientific Model Development* (3), 43–67.
- ESA [2008], ‘AATSR: Product handbook’.  
**URL:** <http://www.leos.le.ac.uk/aatsr/whatis/handbook.html>
- Fearnside, P. M. [2000], ‘Global warming and tropical land-use change: Greenhouse gas emissions from biomass burning, decomposition and soils in forest conversion, shifting cultivation and secondary vegetation’, *Climatic Change* **46**(1-2), 115–158.
- Ferek, R. J., Reid, J. S., Hobbs, P. V., Blake, D. R. and Liousse, C. [1998], ‘Emission factors of hydrocarbons, halocarbons, trace gases and particles from biomass burning in Brazil’, *Journal of Geophysical Research D: Atmospheres* **103**(D24), 32107–32118.
- Garstang, M. [1988], ‘Trace gas exchanges and convective transports over the Amazonian rain forest’, *Journal of Geophysical Research* **93**(D2), 1528–1550.
- George, M., Clerbaux, C., Hurtmans, D., Turquety, S., Coheur, P.-F., Pommier, M., Hadji-Lazaro, J., Edwards, D. P., Worden, H., Luo, M., Rinsland, C. and McMillan, W. [2009], ‘CO distributions from the IASI/METOP mission: evaluation with other space-borne remote sensors’, *Atmospheric Chemistry and Physics* **9**(21), 8317–8330.
- Giglio, L., Csiszar, I. and Justice, C. O. [2006], ‘Global distribution and seasonality of active fires as observed with the Terra and Aqua Moderate Resolution Imaging Spectroradiometer (MODIS) sensors’, *Journal of Geophysical Research G: Biogeosciences* **111**(2).

- Giglio, L., Randerson, J. T., Van Der Werf, G. R., Kasibhatla, P. S., Collatz, G. J., Morton, D. C. and Defries, R. S. [2010], ‘Assessing variability and long-term trends in burned area by merging multiple satellite fire products’, *Biogeosciences* **7**(3).
- Gloude-mans, A. M. S., Krol, M. C., Meirink, J. F., De Laat, A. T. J., Van Der Werf, G. R., Schrijver, H., Van Den Broek, M. M. P. and Aben, I. [2006], ‘Evidence for long-range transport of carbon monoxide in the Southern Hemisphere from SCIAMACHY observations’, *Geophysical Research Letters* **33**(16).
- Hadji-Lazaro, J., Clerbaux, C., Couvert, P., Chazette, P. and Boone, C. [2001], ‘Cloud filter for CO retrieval from IMG infrared spectra using ECMWF temperatures and POLDER cloud data’, *Geophysical Research Letters* **28**(12), 2397–2400.
- Hamilton, J. F., Allen, G., Watson, N. M., Lee, J. D., Saxton, J. E., Lewis, A. C., Vaughan, G., Bower, K. N., Flynn, M. J., Crosier, J., Carver, G. D., Harris, N. R. P., Parker, R. J., Remedios, J. J. and Richards, N. A. D. [2008], ‘Observations of an atmospheric chemical equator and its implications for the tropical warm pool region’, *Journal of Geophysical Research D: Atmospheres* **113**(20).
- Hao, W. M., Ward, D. E., Olbu, G. and Baker, S. P. [1996], ‘Emissions of CO<sub>2</sub>, CO, and hydrocarbons from fires in diverse African savanna ecosystems’, *Journal of Geophysical Research D: Atmospheres* **101**(19), 23577–23584.
- Hase, F., Wallace, L., McLeod, S. D., Harrison, J. and Bernath, P. [2010], ‘The ACE-FTS atlas of the infrared solar spectrum’, *Journal of Quantitative Spectroscopy and Radiative Transfer* **111**.
- Heimann, M. and Korner, S. [2003], ‘The global atmospheric tracer model TM3: Model description and users manual release 3.8a’, *Max Planck Institute for Biogeochemistry (MPIBGCC)* (5).
- Hély, C., Alleaume, S., Swap, R. J., Shugart, H. H. and Justice, C. O. [2003], ‘SAFARI-2000 characterization of fuels, fire behavior, combustion completeness, and emissions from experimental burns in infertile grass savannas in western zambia’, *Journal of Arid Environments* **54**(2), 381–394.

- Henault, F., Buil, C., Chidaine, B. and Scheidel, D. [1998], Spaceborne infra-red interferometer of the IASI instrument, *in* M. Strojnik Scholl and B. F. Andresen, eds, ‘Society of Photo-Optical Instrumentation Engineers (SPIE) Conference Series’, Vol. 3437.
- Ho, S. ., Edwards, D. P., Gille, J. C., Luo, M., Osterman, G. B., Kulawik, S. S. and Worden, H. [2009], ‘A global comparison of carbon monoxide profiles and column amounts from tropospheric emission spectrometer (TES) and measurements of pollution in the troposphere (MOPITT)’, *Journal of Geophysical Research D: Atmospheres* **114**(21).
- Hobbs, P. V. [2000], *An Introduction to Atmospheric Chemistry*, Cambridge University Press.
- Hoelzemann, J. J., Schultz, M. G., Brasseur, G. P., Granier, C. and Simon, M. [2004], ‘Global Wildland Fire Emission Model (GWEM): Evaluating the use of global area burnt satellite data’, *Journal of Geophysical Research D: Atmospheres* **109**(14).
- Hoffa, E. A., Ward, D. E., Hao, W. M., Susott, R. A. and Wakimoto, R. H. [1999], ‘Seasonality of carbon emissions from biomass burning in a Zambian savanna’, *Journal of Geophysical Research D: Atmospheres* **104**(D11), 13841–13853.
- Hollingsworth, A., Engelen, R. J., Textor, C., Benedetti, A., Boucher, O., Chevallier, F., Dethof, A., Elbern, H., Eskes, H., Flemming, J., Granier, C., Kaiser, J. W., Morcrette, J. ., Rayner, P., Peuch, V. ., Rouil, L., Schultz, M. G. and Simmons, A. J. [2008], ‘Toward a monitoring and forecasting system for atmospheric composition: The GEMS project’, *Bulletin of the American Meteorological Society* **89**(8), 1147–1164.
- Holloway, T., Levy II, H. and Kasibhatla, P. [2000], ‘Global distribution of carbon monoxide’, *Journal of Geophysical Research* **105**, 12123–12147.
- IGAC [2003], *Atmospheric Chemistry in a Changing World*, Spinger.
- Illingworth, S. M., Remedios, J. J. and Parker, R. J. [2009], ‘Intercomparison of integrated IASI and AATSR calibrated radiances at 11 and 12  $\mu\text{m}$ ’, *Atmospheric Chemistry and Physics* **9**, 6677–6683.

- IPCC [2007], ‘Changes in atmospheric constituents and in radiative forcing’, *Climate Change 2007 The Physical Science Basis* p. 147.
- Jain, A. K. [2007], ‘Global estimation of CO emissions using three sets of satellite data for burned area’, *Atmospheric Environment* **41**(33), 6931–6940.
- Jain, A. K., Tao, Z., Yang, X. and Gillespie, C. [2006], ‘Estimates of global biomass burning emissions for reactive greenhouse gases (CO, NMHCs, and NO<sub>x</sub>) and CO<sub>2</sub>’, *Journal of Geophysical Research D: Atmospheres* **111**(6).
- Jain, A. K. and Yang, X. [2005], ‘Modeling the effects of two different land cover change data sets on the carbon stocks of plants and soils in concert with CO<sub>2</sub> and climate change’, *Global Biogeochemical Cycles* **19**(2), 1–20.
- Janssen, L. H. J. M., Olivier, J. G. J. and Van Amstel, A. R. [1999], ‘Comparison of CH<sub>4</sub> emission inventory data and emission estimates from atmospheric transport models and concentration measurements’, *Environmental Science and Policy* **2**(3), 295–314.
- Jiang, J. and Livesey, N. a. [2007], ‘Connecting surface emissions, convective uplifting, and long-range transport of carbon monoxide in the upper troposphere: New observations from the aura microwave limb sounder’, *Geophysical Research Letters* **34**, L18812.
- Justice, C. O., Vermote, E., Townshend, J. R. G., Defries, R., Roy, D. P., Hall, D. K., Salomonson, V. V., Privette, J. L., Riggs, G., Strahler, A., Lucht, W., Myneni, R. B., Knyazikhin, Y., Running, S. W., Nemani, R. R., Wan, Z., Huete, A. R., Van Leeuwen, W., Wolfe, R. E., Giglio, L., Muller, J. ., Lewis, P. and Barnsley, M. J. [1998], ‘The moderate resolution imaging spectroradiometer (MODIS): Land remote sensing for global change research’, *IEEE Transactions on Geoscience and Remote Sensing* **36**(4), 1228–1249.
- Kanakidou, M. and Crutzen, P. [1999], ‘The photochemical source of carbon monoxide: Importance, uncertainties and feedbacks’, *Chemosphere: Global Change Science* **1**, 91–109.

- Kasibhatla, P., Arellano, A., Logan, J. A., Palmer, P. I. and Novelli, P. [2002], ‘Top-down estimate of a large source of atmospheric carbon monoxide associated with fuel combustion in asia’, *Geophysical Research Letters* **29**(19), 6–1.
- Kirsch, A., Schomburg, B. and Berendt, G. [1988], ‘The Backus-Gilbert method’, *Inverse Problems* **4**, 771–83.
- Kobayashi, H., Shimota, A., Kondo, K., Okumura, E., Kameda, Y., Shimoda, H. and Ogawa, T. [1999], ‘Development and evaluation of the interferometric monitor for greenhouse gases: A high-throughput Fourier-transform infrared radiometer for nadir Earth observation’, *Applied Optics* **38**(33), 6801–6807.
- Korontzi, S., Justice, C. O. and Scholes, R. J. [2003], ‘Influence of timing and spatial extent of savanna fires in southern Africa on atmospheric emissions’, *Journal of Arid Environments* **54**(2), 395–404.
- Labonne, M., Bron, F. M. and Chevallier, F. [2007], ‘Injection height of biomass burning aerosols as seen from a spaceborne lidar’, *Geophysical Research Letters* **34**(11).
- Larar, A. M., Smith, W. L., Zhou, D. K., Liu, X., Revercomb, H., Taylor, J. P., Newman, S. M. and Schlssel, P. [2010], ‘IASI spectral radiance validation inter-comparisons: Case study assessment from the JAIVEx field campaign’, *Atmospheric Chemistry and Physics* **10**(2).
- Levelt, P., Veefkind, J., Kerridge, B., Siddans, R., de Leeuw, G., Remedios, J. and Coheur, P. [2009], CAMELOT final report, issue 1, Technical report, ESA.
- Llewellyn-Jones, D., Edwards, M. C., Mutlow, C. T., Birks, A. R., Barton, I. J. and Tait, H. [2001], ‘AATSR: Global-change and surface-temperature measurements from ENVISAT’, *ESA Bulletin* **105**, 11–21.
- Mason, I. M., Sheather, P. H., Bowles, J. A. and Davies, G. [1996], ‘Blackbody calibration sources of high accuracy for a spaceborne infrared instrument: The along track scanning radiometer’, *Applied Optics* **35**(4), 629–639.

- Mauzerall, D. L., Logan, J. A., Jacob, D. J., Anderson, B. E., Blake, D. R., Bradshaw, J. D., Heikes, B., Sachse, G. W., Singh, H. and Talbot, B. [1998], ‘Photochemistry in biomass burning plumes and implications for tropospheric ozone over the tropical South Atlantic’, *Journal of Geophysical Research D: Atmospheres* **103**(D7), 8401–8423.
- McKune, C. and Johns, L. [2009], ‘South Africa: Ninety fires in one day’, *Cape Argus* **Feb.**
- McMillan, W. W., Barnet, C., Strow, L., Chahine, M. T., McCourt, M. L., Warner, J. X., Novelli, P. C., Korontzi, S., Maddy, E. S. and Datta, S. [2005], ‘Daily global maps of carbon monoxide from NASA’s Atmospheric Infrared Sounder’, *Geophysical Research Letters* **32**(11), 1–4.
- Merchant, C. J., Simpson, J. J. and Harris, A. R. [2003], ‘A cross-calibration of GMS-5 thermal channels against ATSR-2’, *Remote Sensing of Environment* **84**(2), 268–282.
- Migeotte, M. [1949], ‘The fundamental band of carbon monoxide at 4.7  $\mu\text{m}$  in the solar spectrum’, *Physical Review* **75**, 1108–1109.
- Mittaz, J. and Harris, A. [2009], A new physical calibration for the AVHRR instrument series, in ‘2009 EUMETSAT Meteorological Satellite Conference’, EUMETSAT.
- Monks, P. [2005], ‘Gas-phase radical chemistry in the troposphere’, **34**, 376–395.
- Mota, B. W., Pereira, J. M. C., Oom, D., Vasconcelos, M. J. P. and Schultz, M. [2006], ‘Screening the esa atsr-2 world fire atlas (1997-2002)’, *Atmospheric Chemistry and Physics* **6**(5), 1409–1424.
- Mutlow, C. T., Zavody, A. M., Barton, I. J. and Llewellyn-Jones, D. T. [1994], ‘Sea surface temperature measurements by the along-track scanning radiometer on the ERS 1 satellite: early results’, *Journal of Geophysical Research* **99**, 22,575–22,588.
- Nedelec, P., Cammas, J., Thouret, V., Athier, G., Cousin, J., Legrand, C., Abonnel, C., Lecoœur, F., Cayez, G. and Marizy, C. [2003], ‘An improved infrared carbon monoxide analyser for routine measurements aboard commercial airbus aircraft:

- technical validation and first scientific results of the MOZAIC III campaign’, *Atmospheric Chemistry and Physics* **3**, 1551–1564.
- Novelli, P. [1998a], ‘CO in the atmosphere: measurement techniques and related issues’, *Chemosphere: Global Change Science* **1**, 115–126.
- Novelli, P. C., Masarie, K. A. and Lang, P. M. [1998b], ‘Distributions and recent changes of carbon monoxide in the lower troposphere’, *Journal of Geophysical Research D: Atmospheres* **103**(D15), 19015–19033.
- Noyes, E. J. [2005], An Investigation Into the Accuracy of Surface Temperature Retrievals From the AATSR, PhD thesis, University of Leicester.
- Olivier, J., van Aardenne, J., Dentener, F., Ganzeveld, L. and Peters, J. [2005], ‘Recent trends in global greenhouse gas emissions: regional trends and spatial distribution of key sources’, *Non-CO<sub>2</sub> Greenhouse Gases (NCGG-4)* p. 325330.
- Peterson, A., Warneke, T., Lawrence, M., Notholt, J. and Schrems, O. [2008], ‘First ground-based FTIR observations of the seasonal variation of carbon monoxide in the tropics’, *Geophysical Research Letters* **35**, L03813.
- Phillips, P. L., Schlüssel, P., Accadia, C. J., Munro, R., Wilson, J. J. W., Perez-Albinana, A. and Banfi, S. [2007], Definition of mission requirements for the follow-on eumetsat polar system, *in* ‘Society of Photo-Optical Instrumentation Engineers (SPIE) Conference Series’, Vol. 6744.
- Phulpin, T., Blumstein, D., Prel, F., Tournier, B., Prunet, P. and Schlüssel, P. [2007], Applications of IASI on MetOp-A: First results and illustration of potential use for meteorology, climate monitoring and atmospheric chemistry, *in* M. D. Goldberg, H. J. Bloom, A. H. Huang and P. E. Ardanuy, eds, ‘Society of Photo-Optical Instrumentation Engineers (SPIE) Conference Series’, Vol. 6684, pp. 66840F–66840F.
- Plummer, S., Arino, O., Simon, M. and Steffen, W. [2006], ‘Establishing a Earth observation product service for the terrestrial carbon community: The globcarbon initiative’, *Mitigation and Adaptation Strategies for Global Change* **11**(1), 97–111.

- Reichle Jr., H. G., Anderson, B. E., Connors, V. S., Denkins, T. C., Forbes, D. A., Gormsen, B. B., Langenfelds, R. L., Neil, D. O., Nolf, S. R., Novelli, P. C., Pougatchev, N. S., Roell, M. M. and Steele, L. P. [1999], ‘Space shuttle based global CO measurements during April and October 1994, MAPS instrument, data reduction, and data validation’, *Journal of Geophysical Research D: Atmospheres* **104**(D17), 21443–21454.
- Remedios, J. J., Leigh, R. J., Waterfall, A. M., Moore, D., Sembhi, H., Parkes, I., Greenhough, J., Chipperfield, M. and Hauglustaine, D. [2007], ‘MIPAS reference atmospheres and comparisons to v4.61/v4.62 MIPAS level 2 geophysical data sets’, *Atmospheric Chemistry and Physics Discuss.* **7**, 9973–10017.  
**URL:** <http://www.atmos-chem-phys-discuss.net/7/9973/2007/>
- Rinsland, C. P., Luo, M., Logan, J. A., Beer, R., Worden, H., Rider, D., Osterman, G., Gunson, M., Eldering, A., Goldman, A., Shephard, M., Clough, S. A., Rodgers, C., Lampel, M. and Chiou, L. [2006], ‘Nadir measurements of carbon monoxide distributions by the Tropospheric Emission Spectrometer instrument onboard the Aura spacecraft: Overview of analysis approach and examples of initial results’, *Geophysical Research Letters* **33**(22).
- Rodgers, C. [2000], *Inverse Methods for Atmospheric Sounding: Theory and Practice*, World Scientific.
- Rodgers, C. D. and Connor, B. J. [2003], ‘Intercomparison of remote sounding instruments’, *Journal of Geophysical Research D: Atmospheres* **108**(3), ACH 13–1 – ACH 13–14.
- Rothman, L. S., Gordon, I. E., Barbe, A., Benner, D. C., Bernath, P. F., Birk, M., Boudon, V., Brown, L. R., Campargue, A., Champion, J. ., Chance, K., Coudert, L. H., Dana, V., Devi, V. M., Fally, S., Flaud, J. ., Gamache, R. R., Goldman, A., Jacquemart, D., Kleiner, I., Lacome, N., Lafferty, W. J., Mandin, J. ., Massie, S. T., Mikhailenko, S. N., Miller, C. E., Moazzen-Ahmadi, N., Naumenko, O. V., Nikitin, A. V., Orphal, J., Perevalov, V. I., Perrin, A., Predoi-Cross, A., Rinsland, C. P., Rotger, M., imeckov, M., Smith, M. A. H., Sung, K., Tashkun, S. A., Tennyson, J., Toth, R. A., Vandaele, A. C. and Vander Auwera, J. [2009], ‘The HITRAN

- 2008 molecular spectroscopic database', *Journal of Quantitative Spectroscopy and Radiative Transfer* **110**(9-10), 533–572.
- Roy, D. P. and Boschetti, L. [2009], 'Southern africa validation of the MODIS, L3JRC, and GlobCarbon burned-area products', *IEEE Transactions on Geoscience and Remote Sensing* **47**(4), 1032–1044.
- Roy, D. P., Boschetti, L., Justice, C. O. and Ju, J. [2008], 'The collection 5 MODIS burned area product - Global evaluation by comparison with the MODIS active fire product', *Remote Sensing of Environment* **112**(9), 3690–3707.
- Saarnak, C. F., Nielsen, T. T. and Mbow, C. [2003], 'A local-scale study of the trace gas emissions from vegetation burning around the village of Dalun, Ghana, with respect to seasonal vegetation changes and burning practices', *Climatic Change* **56**(3), 321–338.
- Sanhueza, E., Scharffe, D., Lobert, J. and Crutzen, P. [1998], 'Carbon monoxide uptake by temperate forest soils: The effects of leaves and humus layers', *Tellus* **50**, 51–58.
- Saunders, R., Matricardi, M. and Brunel, P. [1999], 'An improved fast radiative transfer model for assimilation of satellite radiance observations', *Q.J.Roy.Meteor.Soc.* **144**, 1547–1558.
- Scholes, M. and Andreae, M. O. [2000], 'Biogenic and pyrogenic emissions from Africa and their impact on the global atmosphere', *Ambio* **29**(1), 23–29.
- Scholes, R. J., Ward, D. E. and Justice, C. O. [1996], 'Emissions of trace gases and aerosol particles due to vegetation burning in southern hemisphere Africa', *Journal of Geophysical Research D: Atmospheres* **101**(19), 23677–23682.
- Seemann, S. W., Borbas, E. E., Knuteson, R. O., Stephenson, G. R. and Huang, H. . [2008], 'Development of a global infrared land surface emissivity database for application to clear sky sounding retrievals from multispectral satellite radiance measurements', *Journal of Applied Meteorology and Climatology* **47**(1), 108–123.

- Seinfeld, J. [1986], *Atmospheric Chemistry and Physics of Air Pollution*, John Wiley and Sons.
- Siméoni, D., Astruc, P., Miras, D., Alis, C., Andreis, O., Scheidel, D., Degrelle, C., Nicol, P., Bailly, B., Guiard, P., Clauss, A., Blumstein, D., Maciaszek, T., Chalon, G., Carlier, T. and Kayal, G. [2004], Design and development of IASI instrument, Vol. 5543, pp. 208–219.
- Siméoni, D., Singer, C. and Chalon, G. [1997], ‘Infrared atmospheric sounding interferometer’, *Acta Astronautica* **40**(2-8), 113–118.
- Singh, H., Brune, W., Crawford, J., Fuelberg, H. and Jacob, D. [2004], The intercontinental chemical transport experiment - phase B (INTEX-B): An update, Technical report, NASA.
- Sinha, P., Hobbs, P. V., Yokelson, R. J., Bertschi, I. T., Blake, D. R., Simpson, I. J., Gao, S., Kirchstetter, T. W. and Novakov, T. [2003], ‘Emissions of trace gases and particles from savanna fires in southern Africa’, *Journal of Geophysical Research D: Atmospheres* **108**(13).
- Smith, D. L., Delderfield, J., Drummond, D., Edwards, T., Mutlow, C. T., Read, P. D. and Toplis, G. M. [2001], ‘Calibration of the AATSR instrument’, *Advances in Space Research* **28**(1), 31–39.
- Stavrakou, T., Müller, J. ., De Smedt, I., Van Roozendael, M., Van Der Werf, G. R., Giglio, L. and Guenther, A. [2009], ‘Evaluating the performance of pyrogenic and biogenic emission inventories against one decade of space-based formaldehyde columns’, *Atmospheric Chemistry and Physics* **9**(3), 1037–1060.
- Strabala, K. I., Ackerman, S. A. and Menzel, W. P. [1994], ‘Cloud properties inferred from 8-12  $\mu\text{m}$  data’, *Journal of Applied Meteorology* **33**(2), 212–229.
- Swinerton, J., Linnebom, V. and Lamontagne, R. [1970], ‘The ocean, a natural source of carbon monoxide’, *Science* **167**, 984–986.

- Szopa, S., Hauglustaine, D. and Ciais, P. [2007], ‘Relative contributions of biomass burning emissions and atmospheric transport to carbon monoxide interannual variability’, *Geophysical Research Letters* **34**, L18810.
- Tansey, K., Grgoire, J. ., Defourny, P., Leigh, R., Pekel, J. ., van Bogaert, E. and Bartholom, E. [2008], ‘A new, global, multi-annual (2000-2007) burnt area product at 1 km resolution’, *Geophysical Research Letters* **35**(1).
- Tansey, K., Grgoire, J. ., Stroppiana, D., Sousa, A., Silva, J., Pereira, J. M. C., Boschetti, L., Maggi, M., Brivio, P. A., Fraser, R., Flasse, S., Ershov, D., Binaghi, E., Graetz, D. and Peduzzi, P. [2004], ‘Vegetation burning in the year 2000: Global burned area estimates from SPOT VEGETATION data’, *Journal of Geophysical Research D: Atmospheres* **109**(14).
- Taylor, J. A., Zimmerman, P. R. and Erickson, D. J. [1996], ‘A 3-D modelling study of the sources and sinks of atmospheric carbon monoxide’, *Ecological Modelling* **88**(1-3), 53–71.
- Thompson, A. M. [1992], ‘The oxidizing capacity of the Earth’s atmosphere: Probable past and future changes’, *Science* **256**(5060), 1157–1165.
- Turquety, S., Hurtmans, D., Hadji-Lazaro, J., Coheur, P.-F., Clerbaux, C., Josset, D. and Tsamalis, C. [2009], ‘Tracking the emission and transport of pollution from wildfires using the IASI CO retrievals: analysis of the summer 2007 greek fires’, *Atmospheric Chemistry and Physics* **9**, 4897–4913.
- Twomey, S. [1977], *Introduction to the mathematics of inversion in remote sensing and indirect measurement*, Dover Publications Inc., New York.
- Van Der Werf, G. R., Randerson, J. T., Giglio, L., Collatz, G. J., Kasibhatla, P. S. and Arellano Jr., A. F. [2006], ‘Interannual variability in global biomass burning emissions from 1997 to 2004’, *Atmospheric Chemistry and Physics* **6**(11), 3423–3441.
- Velazco, V., Notholt, J., Warneke, T., Lawrence, M., Bremer, H., Drummond, J., Schulz, A., Krieg, J. and Schrems, O. [2005], ‘Latitude and altitude variability

- of carbon monoxide in the Atlantic detected from ship-borne Fourier transform spectrometry, model, and satellite data’, *Journal of Geophysical Research D: Atmospheres* **110**(9), 1–12.
- Walker, J. and Dudhia, A. [2009], Use of the RFM to model IASI spectra, Technical report, Oxford.
- Wallace, J. M. and Hobbs, P. V. [2006], *Atmospheric Science - an Introductory Survey*, Elsevier.
- Wang L., X. Wu, Y. L. S.-H. S. M. G. and Cao, C. [2009], ‘Comparison of AIRS and IASI radiance measurements using GOES imagers as transfer radiometers’, *Journal of Applied Meteorology and Climatology* .
- Ward, D. E., Hao, W. M., Susott, R. A., Babbitt, R. E., Shea, R. W., Kauffman, J. B. and Justice, C. O. [1996], ‘Effect of fuel composition on combustion efficiency and emission factors for African savanna ecosystems’, *Journal of Geophysical Research D: Atmospheres* **101**(19), 23569–23576.
- Wigley, T., Smith, S. and Prather, M. [2002], ‘Radiative forcing due to reactive gas emissions’, *J. Climate* **15**, 2690–2696.
- Winker, D. M., Pelon, J. and McCormick, M. P. [2003], The calipso mission: Spaceborne lidar for observation of aerosols and clouds, *in* ‘Society of Photo-Optical Instrumentation Engineers (SPIE)’, Vol. 4893, pp. 1–11.
- Worden, H., Deeter, M., Edwards, D., Gille, J., Drummond, J. and Nédélec, P. [2010], ‘Observations of near-surface carbon monoxide from space using MOPITT multi-spectral retrievals’, *Journal of Geophysical Research D: Atmospheres* **in preparation**.
- Yokelson, R. J., Bertschi, I. T., Christian, T. J., Hobbs, P. V., Ward, D. E. and Hao, W. M. [2003], ‘Trace gas measurements in nascent, aged, and cloud-processed smoke from African savanna fires by airborne Fourier transform infrared spectroscopy (AFTIR)’, *Journal of Geophysical Research D: Atmospheres* **108**(13).

Zavody, A. M., Mutlow, C. T. and Llewellyn-Jones, D. T. [2000], ‘Cloud clearing over the ocean in the processing of data from the along-track scanning radiometer (ATSR)’, *Journal of Atmospheric and Oceanic Technology* **17**(5), 595–615.